CARBON-OXYGEN EQUILIBRIUM AND HOMOGENEOUS NUCLEATION OF CARBON MONOXIDE BUBBLES IN LEVITATED MOLTEN IRON

Nagy Hamed El-Kaddah

A thesis submitted for the degree of Doctor of Philosophy of the University of London and for Diploma of Imperial College

November 1975

John Percy Research Group in
Process Metallurgy,
Imperial College of Science and
Technology,
London S.W.7.

Abstract

The work described was concerned with the study of carbon-oxygen reactions in levitated molten iron. The convective heat transfer around levitated drops was investigated in all convective regimes, forced, natural and combined. The effect of steep temperature gradients on the segregation of $CO-CO_2$ gas mixtures due to thermal diffusion was also studied. The equilibria of the Fe-C and Fe-C-O systems with $CO-CO_2$ gas mixtures were studied. It was possible by the use of high pressure to study the Fe-C equilibrium over a wide range of carbon. The effect of carbon on the activity coefficient of oxygen in molten iron was measured by maintaining the same oxygen activity (defined by P_{CO_2}/P_{CO}) and varying the carbon activity by changing the total pressure. The kinetics of carburization and decarburization of Fe-C alloys with $CO-CO_2$ gas mixtures at high pressure were also investigated. Homogeneous nucleation of carbon monoxide gas bubbles in molten iron (one single phase) was also studied. Supersaturation of carbon monoxide in the melt was acheived by a rapid drop in the ambient gas pressure. Dissolved oxygen was found to play an important role in nucleation. The critical supersaturation pressures required for CO nucleation were obtained as a function of oxygen activity.

Contents

INTRODUCTION

This work was aimed at obtaining a better understanding of the carbon-oxygen reaction in molten iron. This reaction is the most important in the steel-making process and in solidification of rimming steel. The mechanisms of carbon-oxygen reaction in molten iron vary widely from one process to another, but all processes can be classified from the physical point of view into two categories:

1 Reaction at a gas-liquid interface

2 Reaction with spontaneous formation of carbonmonoxide bubbles.

To understand such reactions the equilibrium of carbon and oxygen in liquid iron must be determined first.

This work was carried out on levitated molten iron drops under controlled carbon and oxygen potential in the gas phase using $CO-CO_2$ gas mixtures under pressure. The work is mainly concerned with:

a) Carbon oxygen equilibrium in molten iron.

b) The time to establish this equilibrium.

c) Homogeneous nucleation of carbonmonoxide bubbles in liquid iron.

Advanced techniques were used to closely define and control the pressure, specimen temperature during reaction, pressure change and the rapid processes occurring during reaction.

This thesis has been divided into chapters each of which is a self-contained unit describing a particular topic. The first chapter deals with the basic experimental technique and the second with transport phenomena in the gas phase: heat transfer, mass transfer and thermal diffusion. These must be understood and calculated so we can define our system. Chapter 3 deals with the study of the carbon-oxygen equilibrium in molten iron over a wider range of carbon and oxygen than any other previous work.. The next chapter treats the kinetics of carburization and decarburization of liquid iron-carbon drops with $CO-CO_2$ gas mixtures. Chapter 5 deals with homogeneous nucleation of carbonmonoxide bubbles in molten iron.

CHAPTER 1

EXPERIMENTAL TECHNIQUE

1-1 Electromagnetic Levitation

This technique allows heating and melting of a freely supported conducting material in a high frequency alternating electromagnetic field.

The levitation technique has been established and used successfully as a laboratory tool in physico-chemical studies. The experimental aspects of levitation melting and its field of application have been discussed in review articles by Jenkins et al (1), Peifer (2) and Rostron (3).

The levitation technique offers:

a) Well-defined geometry of the liquid

b) Homogeneity of the melt due to the small size of the specimen.

c) Rapid attainment of equilibrium in gas-liquid metal systems.

d) No contamination from a container.

In addition of these advantages levitation at high pressure, as used in this study, overcomes the disadvantages of relatively high vaporization rate and difficulty in temperature control of metal drops.

1-2 High pressure levitation apparatus

A photograph of the apparatus is given in fig. (1.1).

1-2.1 The high frequency generator

In this work levitation was carried out by a 10KW, 450 kHz "J.J. Induction" generator. The control of the generator power output, and hence the specimen temperature within the temperature range obtainable using a particular coil, has proved to be the keystone to adequate experimental work in the whole field covered by this project. This was acheived through the use of a "Eurotherm" temperature controller equipment linked between the temperature measuring device and the generator. This gave better results than manual control of the power. The principles of the high frequency generator, and the automatic control equipment with its specification are given in Appendix (1)

1-2.2 Levitation coils

A $\frac{2}{16}$ inch silver tubing of 0.01 inch wall thickness was used in constructing levitation coils. A number of successful levitation coil designs have been reviewed (1). Two designs were chosen for use in the present work and are shown in fig. (1-2). They gave high lifting force and excellent lateral stability. Coil (a) in fig. (1-2) consisted of seven turns. The two lower turns being wound co-planar, while the next three formed a cone of 30° with the inner lower turn, which was 17.5mm diameter. Two reverse turns of 17.5mm inner diameter were place above the cone. Coil (b) in the same figure consisted of two sets of co-planar turns of 17.5mm inner diameter and a similar set of reverse turns above. Coil (a) produced lower temperature than coil (b), under the same conditions. The two coils

.../...

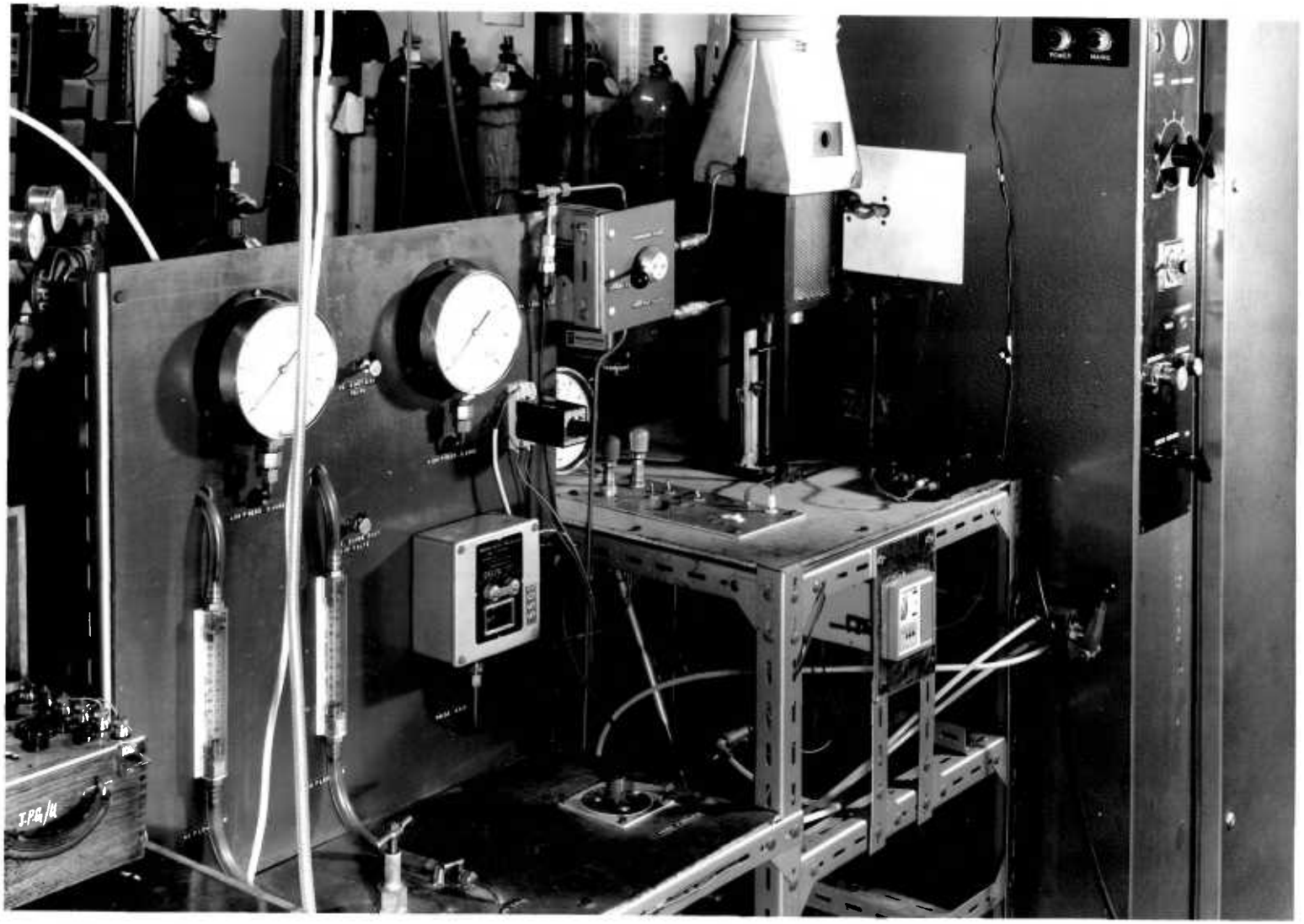

Fig. (1-1) Photograph of apparatus

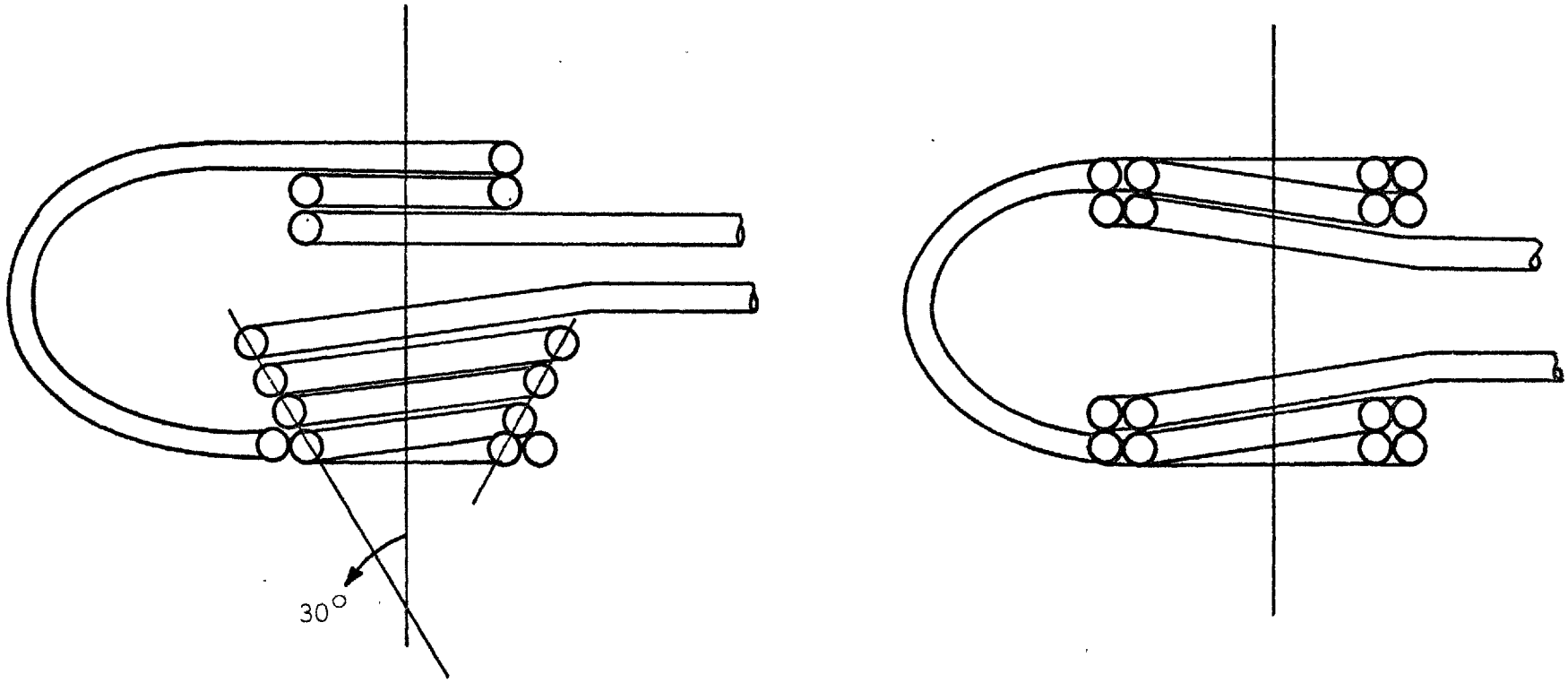

(a) (b)

Fig (1-2)

Levitation Coil Assemblies

used in this work

allowed the temperature to be controlled within the required limits of 1450-1750°C at any pressure above five atmospheres.

1-2.3 Design of high pressure levitation cell (HPLC)

The following points were considered in the design of the HPLC.

1) Ability to withstand pressures up to 100 atmosphere.
2) It must contain all the facilities to introduce the specimen into the coil, and to deoxidise and quench the levitated specimen under pressure.
3) It must contain facilities for the observation of the nucleation process.

There are two approaches to the design of the HPLC, either the levitated drop can be contained within an insulating tube which can withstand the pressure and passes through the turns of the coil, or the coil and the levitated drop can both be enclosed inside a pressure chamber.

The first approach was adopted because it offered a simpler, more compact design. Recrystallized alumina tube of 17.5mm outer diameter and 12.5mm inner diameter was a suitable size for levitation and calculations showed that it could withstand internal pressures of 100 atmosphere with a safety factor of eight. Testing of tube, from Thermal Syndicate, was carried out using a high pressure system.

working up to 160 atmosphere and showed no failure of the tubes. However it was found that 'Purox' tubes failed above 50 atmosphere. The inherent disadvantage of recrystallised alumina , which is its bad thermal shock resistance, caused some failures during runs when the molten iron hit the tube. This problem was minimised by testing the tubes before use and by accurate adjustment of the levitation coil. In the following paragraphs the main features of the design are described.

A photograph of the HPLC is given in fig. (1-3) and a drawing of a cross-section in fig. (1-4). The levitation cell consisted essentially of two stainless steel square plates fixing and sealing each end of the alumina tube by Wilson seals. Four stainless steel rods were used to hold and align the two plates. An observation window was fixed on the top plate. On the lower one was a turn-table which rotated inside a fitting flange. The turntable allowed four 'stations' to be rotated to positions either directly below the alumina tube or the lid. The 'stations' were used to contain the specimen, the deoxidiser, quenching mould and a prism. The turn-table was rotated by a lever fixed to a shaft on its axis. The shaft also sealed the turn-table by circumferential O-rings. A ball-bearing was located under the turn-table for smooth rotation under pressure.

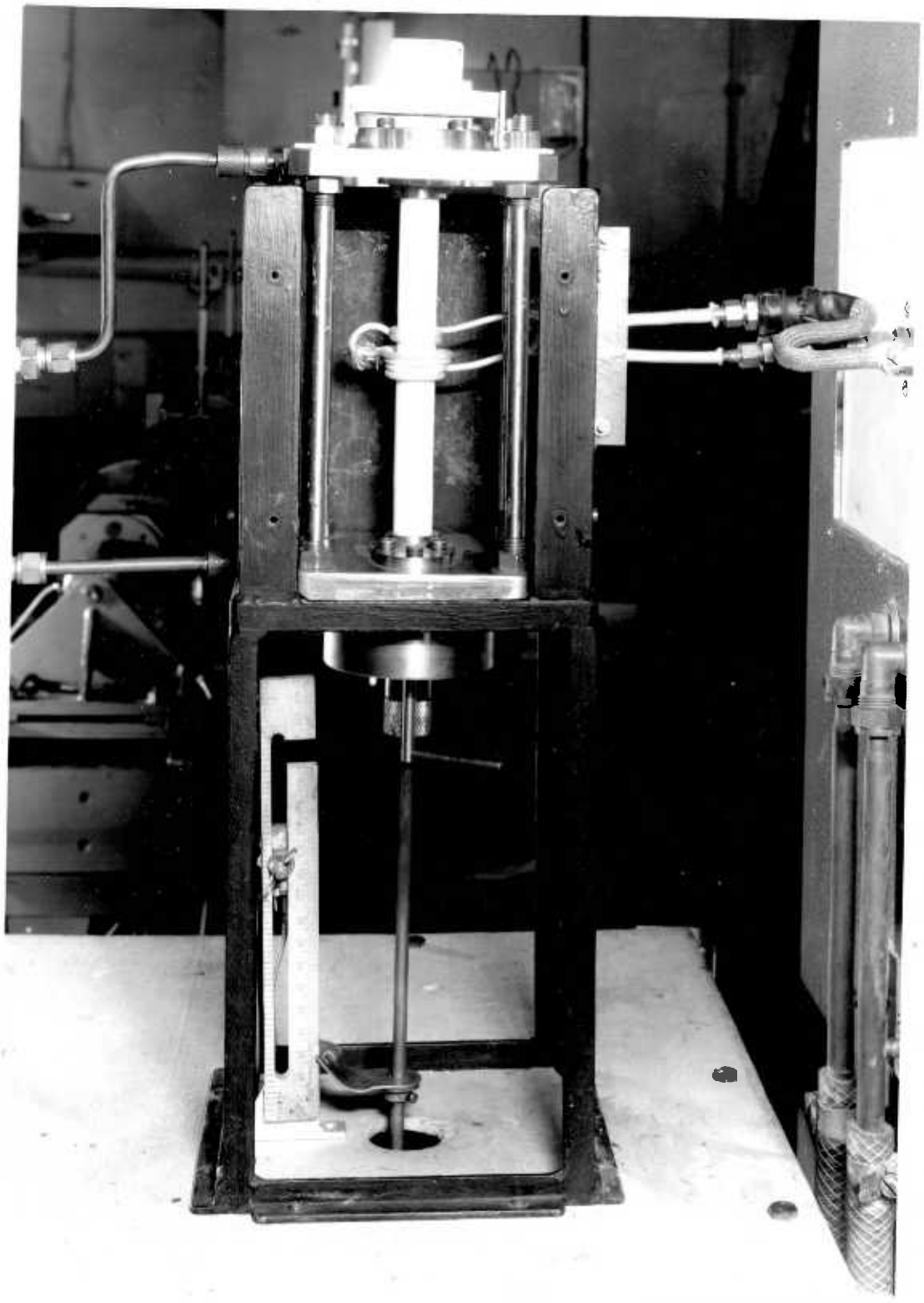

Fig. (1-3) Photograph of HPLC.

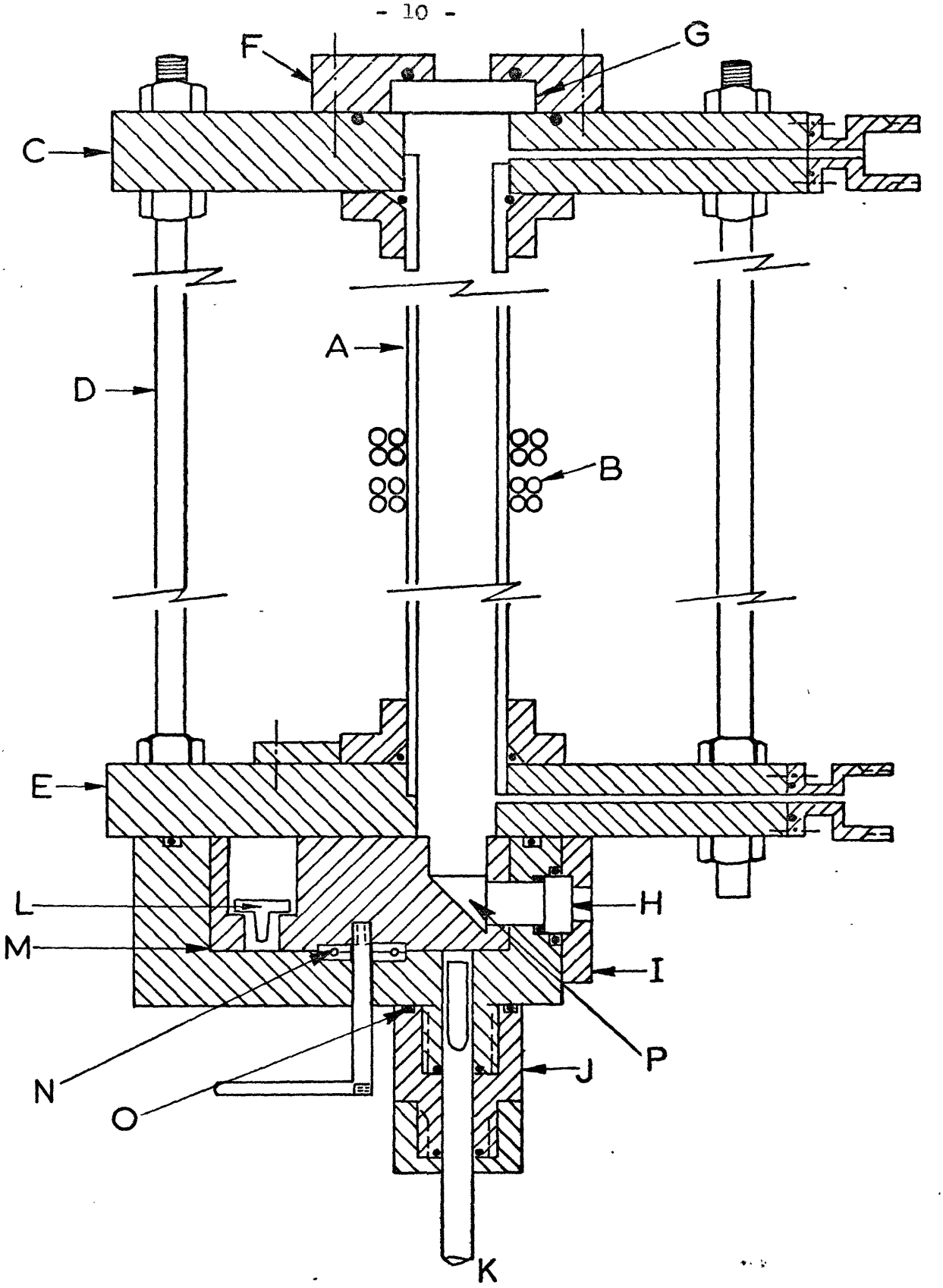

Fig (1-4) Details of HPLC Design

A Alumina tube
B Levitation coil
C Top plate
D Holding rods
E Bottom plate
F Upper glass disc flange
G Upper glass disc flange
H Lower glass disk
I Lower glass disk flange
J Bottom flange
K Push rod
L Platform
M Turning table
N Thrust ball bearing
O O-ring
P Prism

The specimens were raised up to the coil by a push rod. The push rod was made of brass and had a "Perspex" end to minimise the induced current. It was manipulated by a pneumatic cylinder which was connected to a five-port valve to control its movement. Another observation window was placed on the bottom fitting, for observation of the specimen via the prism mounted in the turn table.

The dimensions of each part of the HPLC were calculated using a safety factor of six (4). Some advantages of the design are listed below:

1) The alumina tube could be easily replaced.
2) The specimen could be placed into the HPLC without dismantling it.
3) The apparatus was simple to operate and was flexible for equilibrium, kinetic and nucleation work.

1-2.4 Gas train

In carrying out experiments in which gases are to be used under pressures up to 100 atmospheres it is possible to obtain compressed gas in cylinders above that pressure. In this work gas cylinders were used as reservoirs to furnish the desired pressure by means of a "Hoke" precision high pressure regulator which had a maximum delivery pressure of 2000 psi. The outlet pressurised gas flowed through $\frac{1}{4}$ inch half-hard copper tubing. The pressure was measured by a series of 'Barnet' stock and test gauges as

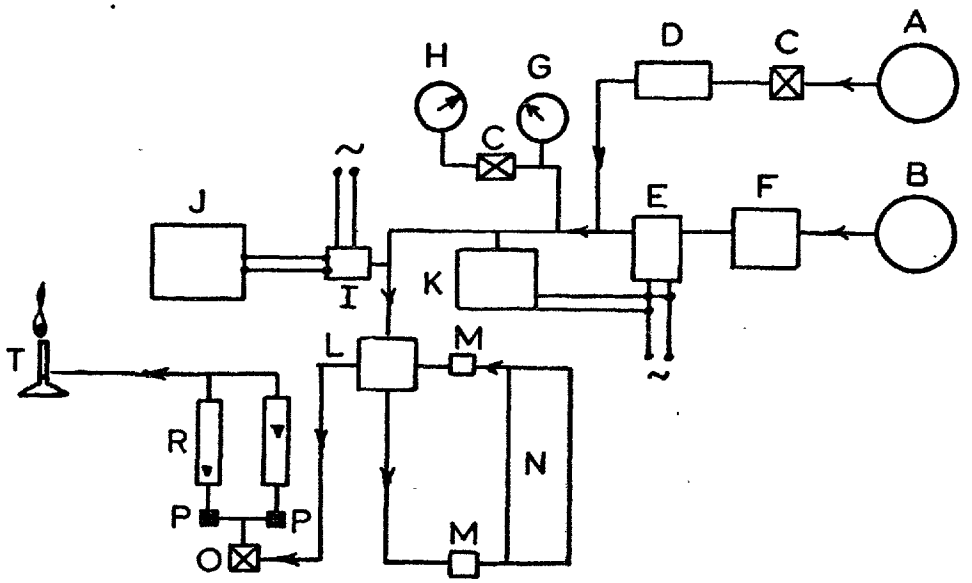

Fig (1-5) Gas Train

A Inert gas cylinder
B Reacting gas cylinder
C Shut of valve
D Check valve
E Solenide valve
F High pressure regulator
G High pressure gauge
H Low pressure gauge
I pressure transducer
J Chart recorder
K Pressure switch
L 4-way ball valve
M Filter
N HPLC
O High pressure needle valve
P Shut off valve
R Rotometer
T Bunsen burner

well as a 'Bell and Howell' pressure transducer (0-1500 psiA type 4-366). Stock gauges (0-1600) psi and (0-500)psi were used as an indication, and the test gauges (0-50 atm.A.No. T 6718R and 1-20 atm.A.No. T 3726) gave accurate reading.

The gas flow past the levitated drop could be changed from upward to downward flow by a four-way ball valve. However the upward flow was used in all the experiments. Since the possibility of failure of the alumina tube existed, a high pressure solenoid valve (normally closed) was fixed after the pressure regulator and linked with a differential pressure switch.

The gas flow rate was controlled at the end of the high pressure line by a high pressure needle valve. The flow rate was measured at atmospheric pressure by calibrated "Rotameters".

Low pressure line for helium connected to the HPLC was protected when high pressure gas was introduced into the HPLC by a check valve. A sketch of the gas train is shown in fig. (1-5).

1-3 Operation of the apparatus

Apart from simple operations such as levitating the specimen, there were a number of techniques which were either developed during this work or were of such importance

as to merit detailed discussion. Those techniques which were common to a number of the investigations reported in this thesis are described in the following sections to avoid unnecessary duplication later. Techniques relevant to only one investigation are described in the appropriate chapter.

The basic operations in using the apparatus are listed here. They were:

1) Setting the generator's output power either manually or automatically.
2) Adjusting the pressure range in the differential pressure switch according to the required working pressure.
3) Flushing out the air from the gas train and HPLC by helium.
4) Temperature measurement through the lower observation window after the specimen was levitated in helium.
5) Introducing the appropriate gas at the required pressure by the pressure regulator after switching on the power to the pressure switch to open the solenoid valve (normally closed). The flow rate was then adjusted at this pressure by means of the high pressure needle valve.
6) Depressurising the HPLC was carried out by closing the solenoid valve and bleeding the gas through the needle valve.

7) When the pressure dropped to a predetermined low pressure helium flowed into the system.

8) Quenching of the specimen by raising the copper mould was accompanied by automatic switch-off of the power from the generator.

1-4 Temperature measurement

In the levitation of metal droplets, where the use of a thermocouple is difficult and inappropriate, optical pyrometers are used to measure the surface temperature.

Temperatures were measured with a "Milletron" two-colour optical pyrometer (TCP). The TCP gives the measured temperature as a meter reading and millivolt output. It was calibrated under black body condition by the manufacturers and the measured temperature by TCP will be true if the object to be measured behaves as a black or grey body. This temperature will be independent of any radiation attenuating material in its optical path only if the material affects the intensity of both colours equally.

Liquid iron does not behave as a grey body, so it is necessary to calibrate the TCP against some standard in the HPLC since the calibration must include the effect of transmittance of both colours by the glass disc and the prism. This was done by determining the melting point of spec-pure iron (1535^{o}C) during melting and solidification.

The reading of the TCP was different, as expected, and the difference was used to obtain the true temperature of liquid iron and iron-carbon alloys from the TCP reading.

The temperature measurements were carried out through the lower observation window and the prism in the turn table had to be changed from time to time by another one. It was found that the TCP read 20^{o} too high with one batch of prisms and 40^{o} too high with another, at the melting point of the iron. So calibration was regularly carried out when the prism was changed.

Because of uncertainty of the calibration at higher temperature, the accuracy decreased as the measured temperature moved away from the calibration point. However, in much of this work the important thing was to maintain the temperature constant at a fixed value. The actual value of the temperature was less important. It will be shown later that temperature was accurate within $\pm$ $10^{o}C$.

1-5 Materials

Spec-pure iron rods supplied by Johnson Matthey and Company Limited were used in this work. Iron carbonyl powder (MR grade) and electrografitic carbon blocks (EY9106 grade) were used in the preparation of iron-4.5% carbon alloy by the same technique as described by Robertson (5).

Materials	C ppm	Si ppm	Mn ppm	Ti, V ppm	Ca ppm	Ni& Mo ppm	Cr ppm	Fe ppm	Al ppm	O ppm	Ca, Mg, B ppm
Spec pure iron-1	-	1	2	-	1	-	1	bla.	-	60	<1
Spec pure iron-2	-	3	1	-	1	-	1		-		<2
iron carbonyl powder (MR grade)	600	-	-	-	-	500	-	bla	-	-	-
Electro graphite carbon blocks (EY9106 grade)	bal.	<50	<1	<50	<1	<50	-	<100	<50		<200
Aluminium wire	-	-	-	-	10	-	-	7	bla.	-	32

Table (1-1)

Materials used during this work

Gases	CO	CO_2 Vol %	O_2 ppm	N_2 ppm	H_2 ppm	H_2O dew point ^oC	Hydrocarbons ppm
CO-0.75% CO_2		0.76	<20	960	300	-60	<10
CO-1% CO_2		1.1	<20	853	<20	-69	43
CO-2% CO_2		1.9	22		<1		22.5
CO-2% CO_2		2.15	110	849	<20	-67	40
CO-2.5% CO_2		2.3	<20		<20		
CO-3% CO_2		2.9	<20		<20		
CO-4% CO_2		4.58	83	953	<20	-68	42
CO-8% CO_2		8.21	31	1220	145	-57	44
Argon HP			3.45		6	-80	

Table (1-2)

Gases used during this work

The compositions of these materials are given in table (1.1).

High purity $CO-CO_2$ gas mixtures were used in the experiments. The carbon-dioxide and the impurities in each cylinder are summarised in table (1.2). Forming gas (10% H_2 and 90% N_2) was deoxidised and dried by passing it through "Deoxo" catalyst (D type) and molecular sieve 3A in a high pressure vessel before entering the HPLC.

1-6 Carbon analysis

The analyses of carbon were performed by the author, using the conventional gravimetric combustion method, in which the sample was held at 1100°C in a stream of purified oxygen and the evolved carbon-dioxide was adsorbed by soda asbestos and weighed. In this work micro analytical reagents were used.

British Chemical Standard samples, number 01, 215, 172, and 23711 containing 2.79, 0.936, 0.333, and 0.105 wt% carbon respectively were used to check the accuracy of the technique.

CHAPTER 2

TRANSPORT PHENOMENA IN GASES FLOWING AROUND THE LEVITATED DROPS

2-1 Introduction

This chapter describes the work carried out on transport phenomena in gases initially at room temperature flowing around a levitated molten iron drop which has approximately the shape of a sphere. The information obtained from this work is the foundation of understanding and defining the reaction at the interface between $CO-CO_2$ gas mixtures and the levitated specimens.

Two problems were experimentally investigated, the convective heat transfer in an inert atmosphere and thermal diffusion in the $CO-CO_2$ binary gas mixtures. The analogy between heat and mass transfer was used to predict the convective mass transfer at low mass transfer rate.

2-2 Convective heat transfer

2-2.1 Introduction

Heat transfer between the flowing gas at room temperature and levitated molten iron was studied experimentally over a wide range of pressure (1-100 atmospheres) and flow rate (15-60 s.l.m.) in argon. At low pressures (up to 15 atmosphere) forced convection was the dominant heat transfer mechanism. By increasing the pressure the density of the gas phase was increased and the buoyancy effect determined the flow pattern, so that natural convection became the heat transfer mechanism. There was of course an intermediate regime of combined forced and natural convection.

The results obtained for forced convection, natural convection and in the combined regime were for a laminar boundary layer, with variable physical properties. The criteria for the regions in which the flow could be classed as purely free, purely forced, or combined were also defined.

2-2.2 Theoretical consideration of the problem

Convective heat transfer from a surface to a flowing gas can take place by two mechanisms.

a) Molecular conduction within the fluid

b) Energy transport created by the motion of "fluid particles".

The heat transfer rate can be evaluated by solving the equation of motion (Navier-Stokes equation) and the energy equation under the constraint of conservation of mass (continuity equation). There is no exact solution of these equations for flow around spheres. The approximate solution of the equations, simplified through the idea of the boundary layer (6), is insufficient to permit complete theoretical analysis for flow over a sphere in which the flow separates at some point on the surface. The only approach available in such cases is to use formulae produced from correlations of the experimental results.

Dimensional analysis of the basic equations (6,7) identifies the parameters that dominate the heat transfer. It is recognised that the following dimensionless groups:

$$Re,\ Gr/Re^2,\ 1/Re.Pr \text{ and } E$$

define the dimensionless mean heat transfer coefficient Nu_m and the solution may be represented as

$$Nu_m = f\ (Re,\ Pr,\ Gr,\ E) \qquad (2\text{-}1)$$

When special solutions are considered, one or more of the dimensionless groups disappear. The Eckert number (E) is only important when the velocity of the flowing gas approaches the sonic velocity. The dependence on Grashof number ceases when buoyancy forces are small compared with

inertial forces, and equation (2-1) yields, for forced convection:

$$Nu_m = f\ (Re,\ Pr) \qquad (2\text{-}2)$$

for natural convection equation (2-1) becomes:

$$Nu_m = f\ (Gr,\ Pr) \qquad (2\text{-}3)$$

2-2.3 Previous work

The rate of heat transfer from a sphere has been extensively studied because of its importance in many chemical engineering problems. The work was carried out in the following regimes:

a) Radial molecular conduction
b) Forced convection
c) Natural convection
d) Combined forced and natural convection

a) Radial molecular conduction

This occurs when there is no relative motion between the fluid and the sphere (i.e. Gr = Re = 0). At the steady-state condition the analytical solution of radial heat conduction gives (8)

$$Nu_m = 2 \qquad (2\text{-}4)$$

Equation (2-4) has been verified experimentally (9, 10).

b) Forced convection

The published work on heat transfer to gases or liquids from spheres in the range $10 < Re < 10^4$ are extensive. A number of correlations have been proposed to fit the experimental results. A simple and general form of these equations, which is based on equation (2-2), is

$$Nu_m = B\ Re^n\ Pr^m \qquad (2-5)$$

In the absence of natural convection, some correlations include the contribution of molecular radial conduction in order to be valid for the limiting case when Re = 0, but there is no theoretical basis for including such a term. The expression is then given as

$$Nu_m = 2 + BRe^n \cdot Pr^m \qquad (2-6)$$

The exponents of Re and Pr are either evaluated experimentally or taken as 0.5 and 0.33 respectively, these being the values obtained in the theoretical analysis for the front half of a sphere (11).

Rowe et al (12) reviewed these correlations. They found from their work and some other previous published work that the constant "B" depends on the fluid medium. Their finding was 0.69 for air and 0.79 for water with 0.5 and 0.33 for the exponents.

The turbulent transfer through the wake in separated flow is not amenable to theoretical treatment. By correlating the results on the local heat transfer to the rear half of spheres, White and Churchill (13) suggested that the transfer rates in separated flow are proportional to Re and that the overall transfer coefficient can be represented by

$$Nu_m = B\, Re^{\frac{1}{2}}\, Pr^{\frac{1}{3}} + C\, Re\, Pr^{\frac{1}{3}} \qquad (2\text{-}7)$$

From there own results and other available data (14, 15), Lee and Barrow (16) showed that the transfer through the wake is proportional to Re with a power of 0.78 ($Re > 2000$) and the ratio of mean transfer of heat (or mass) at the front over that at the rear of the sphere is

$$Nu_{mf}/Nu_{mr} = 22.8\, Re^{-0.28} \qquad (2\text{-}8)$$

At lower Re the mean transfer in the separated flow can be represented as

$$Nu_{mr} = f(Re^{0.55}) \qquad 100 < Re < 500 \qquad (2\text{-}9)$$

and

$$Nu_{mr} = f(Re^{n}) \qquad 500 < Re < 2000 \qquad (2\text{-}10)$$

where n increases with Re and varies from 0.5 - 0.78

c) Natural convection

In natural convection the approximate solution (17, 18) gives the function of equation (2-3) as

$$Nu = A\ (Gr.Pr)^{1/4} \qquad (2\text{-}11)$$

The value of A obtained by Merck and Prins (17) depends on Pr and for air is 0.474 and reaches 0.558 in high Pr fluids. Few correlations were obtained from the experimental results in air. They are given in the following table:

Author	Correlation	Range
Mathers et al (10)	$Nu_m = 2 + 0.282(Gr.Pr)^{0.37}$	$Gr.Pr. < 10^2$
Mathers et al (10)	$Nu_m = 2 + 0.5(Gr.Pr)^{0.25}$	$10^2 < Gr.Pr < 10^6$
Yuge (19)	$Nu_m = 2 + 0.392(Gr)^{0.25}$	$1 < Gr < 10^5$
Broham et al (20)	$Nu_m = 0.513(Gr.Pr)^{0.25}$	$3x10^6 < Gr < 8x10^6$

Table 2-1

Correlations for natural convection in air

d) Combined forced and natural convection

McAdams (21) suggested that the higher of the two values predicted from the correlations of forced and natural convection alone be employed in evaluation of the

heat transfer rate. Steinberger and Treybal (22) used linear addition of natural and forced convection to correlate vast quantities of the data. They obtained:

$$Nu_m = 2.0 + 0.547\ (Gr.Pr)^{1/4} + 0.357\ Re^{0.62}\ Pr^{.31} \qquad (2\text{-}12)$$

Yuge (19) carried out experiments which were aimed at studying the combined effect in cross, opposed and parallel flow. He showed that the contributions of the two effects were not additive, and that the heat transfer rate depended on the direction of the flow. He proposed a graphical procedure to predict the heat transfer rate for each case.

Pei et al (23, 24) analysed their results on the basis of approximate solution of the boundary layer equations which showed that Gr/Re^2 is the only criterion which defines the combined regime. They presented their results as a plot of Gr/Re^2 against $Nu/Re^{\frac{1}{2}}$ for parallel and opposing flow.

2-2.4 Experimental technique

The steady state temperature of a levitated specimen in an inert gas is determined by the balance between the heat generated in the specimen by eddy currents and heat lost by convection and radiation. We may therefore write:

$$Q_{EC} + Q_{CONV} + Q_{RAD} = 0 \qquad (2\text{-}13)$$

$$Q_{EC} = h_m A\ (T_s - T_b) + eA\sigma(T_s^4 - T_b^4) \qquad (2\text{-}14)$$

Q_{EC} cannot be easily measured directly. However, it was possible, through mathematical manipulation of equation (2-14), to obtain quantitative values on heat transfer rate from temperature measurements at different flow conditions, as long as Q_{EC} remained constant.

Constant power input to the specimen (Q_{EC}) during the whole period of the run was achieved by fixing the manual power control at a certain position. A number of early runs were conducted at fixed power and gas flow rates for periods of up to one hour and they showed that temperature remained constant within $\pm$ 2°C.

One gram specimens of spec-pure iron were used. They were levitated in forming gas for ten minutes to make sure that the specimen surface was absolutely clean. Argon was used in this work. Temperature readings from the TCP were corrected as described in section (1-4).

2-2.5 Results

Two sets of experiments were performed in which temperature measurements were made at steady state. The results are given in table (2.2) and a typical plot of temperature against pressure at different flow rates is given in fig. (2.1). It is shown that up to 8 atmospheres the temperature is only a function of flow rate (forced

convection regime) while above 40 atmospheres the flow rate has no effect on the temperature (natural convection regime). Obviously between 8 and 40 atmospheres we are in the combined regime.

Another two runs were carried out to study forced convection at high flow rates (20 - 60 s.l.m.) at 2 atmospheres. The results are given in table (2.3).

The approach velocity of the gas flow was corrected for tube blockage due to the levitated specimen by the use of the mean flow area (25, 26) which gives the corrected velocity as:

$$V_c/V = 1/(1 - 2d^2/5D^2) \qquad (2\text{-}15)$$

Film properties of the gas were used, using the arithmetic mean temperature to account for the variable properties in the boundary layer. The formulae used to calculate the dimensionless groups are given in Appendix 2. The film temperature was always about $1100^{\circ}K$. In this work the forced convection was studied over a range of $150 < Re < 500$, while for natural convection Gr was in the range of $8 \times 10^3 - 2 \times 10^6$.

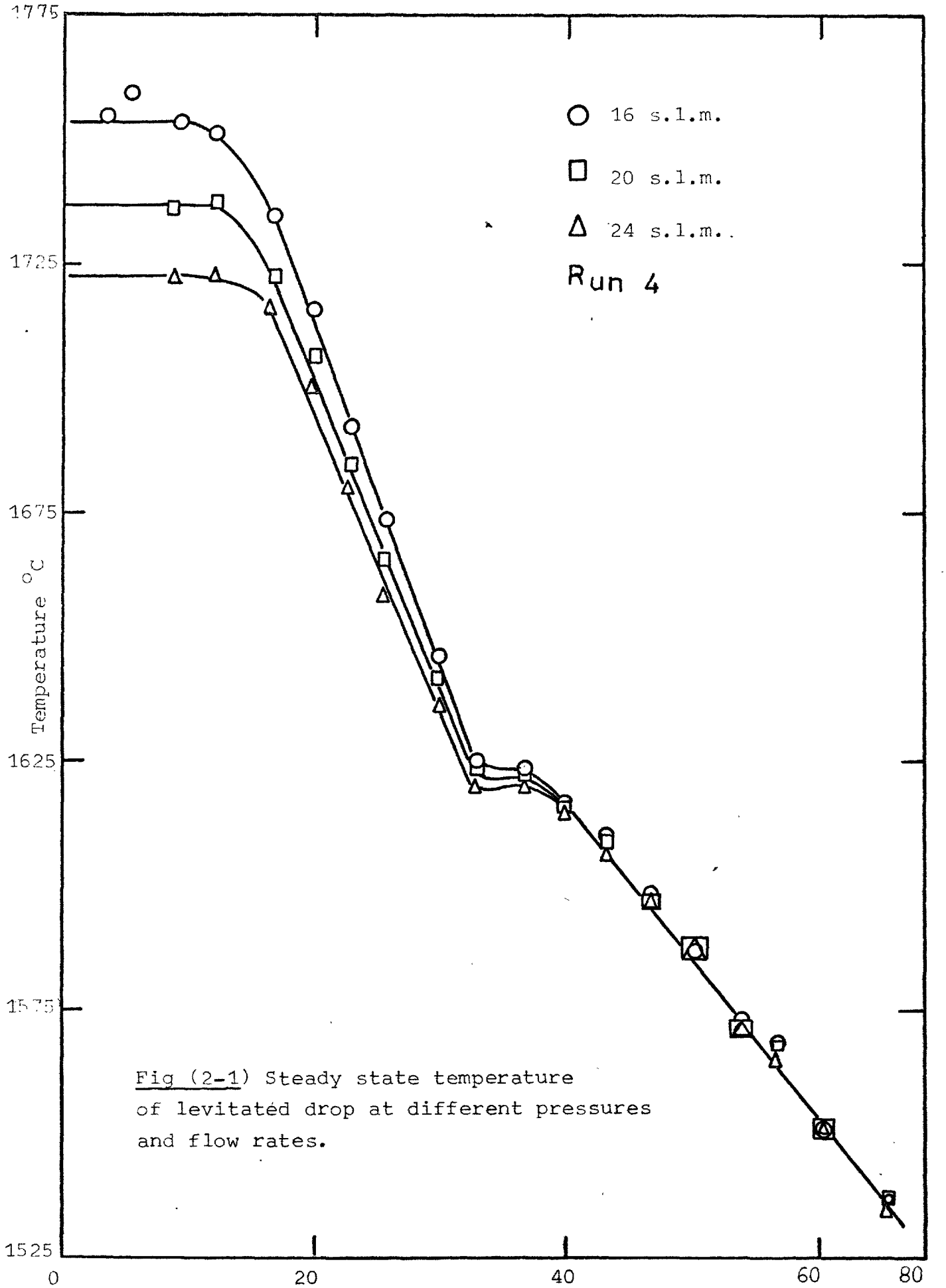

Fig (2-1) Steady state temperature of levitated drop at different pressures and flow rates.

Pressure atmosphere	Flow rate s.l.m.	Drop temperature °C
Run 4		
65.79	20.98	1540
65.64	16.30	1539
65.33	24.00	1537
60.48	24.79	1553
60.19	20.90	1553
60.30	16.21	1554
56.53	16.30	1571
56.32	20.83	1570
56.22	21.43	1567
53.72	24.79	1574
53.67	21.05	1573
53.77	16.48	1575
49.82	16.42	1589
49.67	21.20	1588
49.56	24.39	1589
46.65	24.39	1600
46.70	20.91	1600
46.81	16.35	1601
43.01	16.21	1611
42.91	20.55	1612
42.80	24.39	1608
39.88	24.29	1617
39.90	20.83	1618
40.05	16.30	1619
36.25	16.57	1626
36.18	20.93	1623
36.12	24.39	1622
33.25	24.00	1622
33.34	20.69	1625
33.58	16.13	1627
29.59	16.17	1648
29.53	20.69	1644
29.46	24.00	1639
25.71	24.19	1660
25.82	20.69	1668
26.03	16.30	1676
22.74	16.39	1695
22.68	20.83	1687
22.53	24.00	1682

continued

Table (2-2)

Results of heat transfer from a one gram drop to argon at different pressures and flow rates

Pressure atmosphere	Flow rate s.l.m.	Drop temperature °C
19.60	24.29	1702
19.79	20.55	1709
19.55	16.34	1718
19.44	16.36	1737
16.27	20.69	1724
16.13	24.00	1719
11.96	24.19	1725
12.17	20.41	1739
12.52	16.13	1753
9.32	16.30	1755
8.99	20.98	1738
8.72	24.00	1724
5.12	16.48	1762
3.52	16.31	1557
Run 5		
95.56	20.83	1577
95.18	24.19	1577
95.08	16.76	1577
88.68	16.39	1599
88.54	21.43	1596
88.40	24.46	1590
81.97	24.19	1607
82.05	21.27	1605
82.16	16.48	1603
74.52	16.60	1622
74.46	21.05	1617
74.35	23.81	1617
68.70	23.81	1637
68.76	20.48	1637
68.86	16.48	1639
61.06	16.16	1665
60.95	20.69	1663
60.90	24.19	1663
55.46	20.68	1682
55.36	24.79	1684
55.63	16.66	1687
50.08	17.37	1690
50.03	21.38	1698
49.92	24.59	1702
45.28	24.79	1718
45.39	20.83	1717
45.55	16.57	1716
39.34	16.36	1728
39.26	20.83	1725
39.14	24.79	1729

Table (2-2)
(continued)

Pressure atmosphere	Flow rate s.l.m.	Drop temperature °C
34.44	25.00	1734
34.49	21.77	1734
34.72	16.62	1737
29.67	16.76	1754
29.56	20.83	1750
29.41	24.69	1745
24.49	24.79	1788
24.68	20.68	1797
24.87	16.66	1802
19.44	16.79	1818
19.38	20.91	1811
19.21	24.19	1808
13.88	25.00	1813
14.11	20.55	1823
14.37	16.39	1830
16.61	16.58	1842
10.32	20.69	1826
10.04	24.29	1812
7.19	16.57	1845

Table (2-2)
(continued)

flow rate s.l.m.	temperature °C
Run 6	
24.09	1782
28.09	1770
31.98	1760
36.05	1753
39.68	1742
43.60	1735
47.62	1725
51.90	1716
56.28	1707
Run 7	
24.17	1770
27.73	1758
30.55	1746
35.88	1732
40.00	1721
43.73	1712
47.69	1700

Table (2-3)

Results of heat transfer from one gram drops to argon at 2 atmospheres total pressure

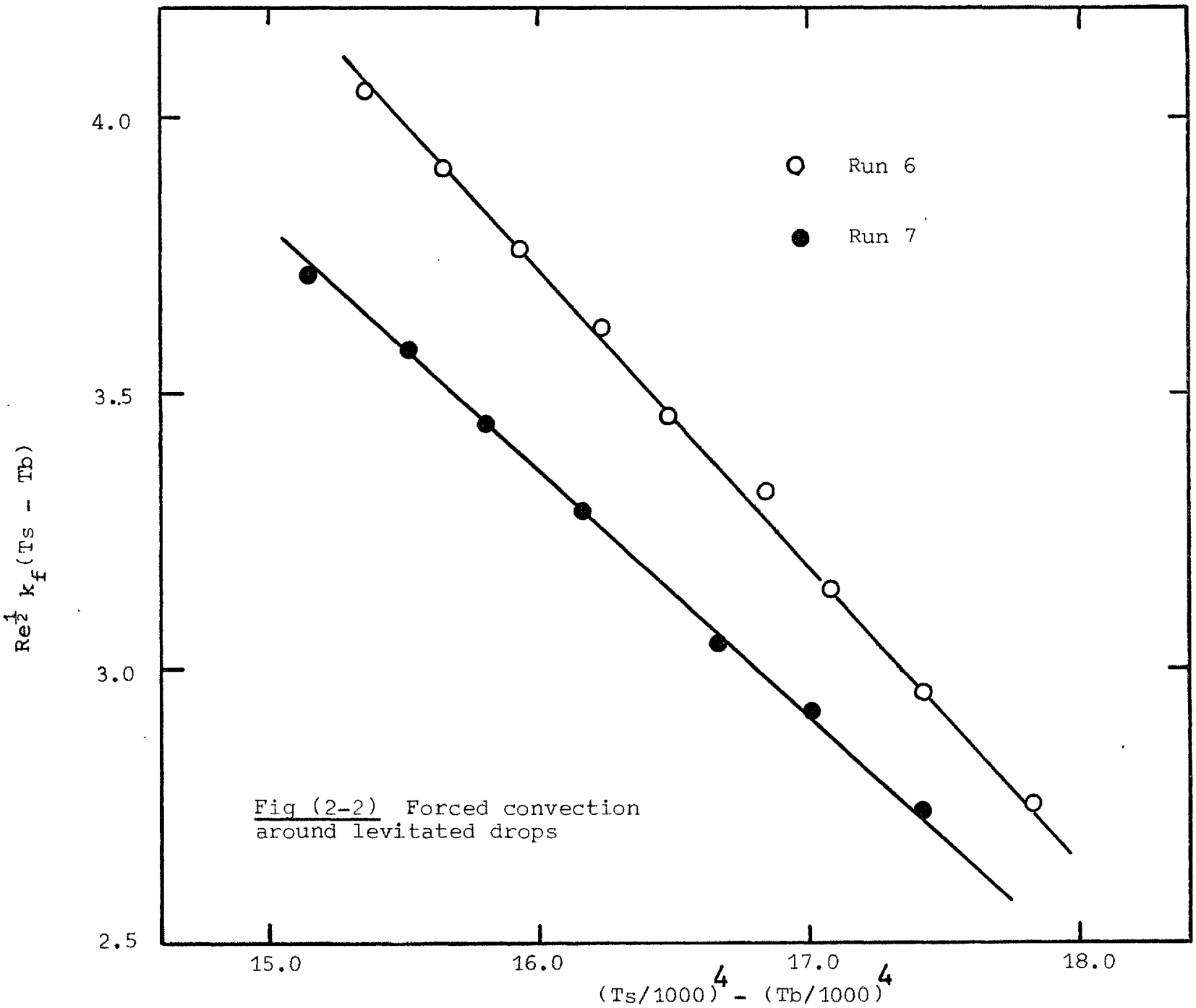

Fig (2-2) Forced convection around levitated drops

2-2.6 Evaluation of the results

The forced convection runs were solved first and the correlation obtained for this regime was used to evaluate the heat generated in the specimens Q_{EC}. The heat transfer rate in natural convection and combined parallel flow were then calculated and correlated for each regime.

a) Forced convection

The correlation of forced convection proposed has the general simple form of equation (2-5)

$$Nu_m = B\ Re^{0.5}\ Pr^{0.33} \qquad (2\text{-}17)$$

The power of Reynolds and Prandtl numbers used in equation (2-17) are based on theory. This equation does not include the contribution of radial conduction (Nu = 2 at Re = 0).

Introducing equation (2-17) to equation (2-14) we get

$$(T_s^4 - T_b^4) = B\ Re^{\frac{1}{2}}\ Pr^{\frac{1}{3}}\ k_f(T_s - T_b)/de\sigma + Q_{EC}/e\sigma A$$

Plotting $\left[(T_s/1000)^4 - (T_b/1000)^4\right]$ against $k_f\ Re^{\frac{1}{2}}\ (T_s - T_b)$ gives a straight line of scope $BPr^{\frac{1}{3}}/de\sigma'$, fig. (2-2) where σ' is $\sigma \times 10^{12}$.

The value of B was evaluated for each run and a mean

value was taken. The emissivity was assumed independent of temperature and of value 0.4 (27). The correlation obtained for forced convection was:

$$Nu_m = 0.8\ Re_f^{\frac{1}{2}}\ Pr_f^{\frac{1}{3}} \quad 150 < Re < 500 \qquad (2\text{-}19)$$

In the forced convection part of the high pressure runs the heat input was calculated using equation (2-19) and an emissivity of 0.4 to evaluate Q_{CONV}. The calculations at different values of the flow rate yielded a constant value for Q_{EC} within less than 0.5%.

b) Natural convection

Convective heat transfer coefficients were calculated and hence Nu was obtained for each point. The dependence of heat transfer rate was taken to be proportional to $(Gr.Pr)^{1/4}$, as indicated by theory for a simple laminar boundary layer. The results were plotted as Nu_m against $(Gr.Pr)^{1/4}$. The best fitting of the results, fig. (2-3), has the following form:

$$Nu = 0.78\ (Gr.Pr)^{1/4} \qquad (2\text{-}20)$$

c) Combined forced and natural convection

Heat transfer coefficients and Nusselt number were calculated as for natural convection (the same run). To verify the theory, all the results were plotted as $Nu/Re^{\frac{1}{2}}$

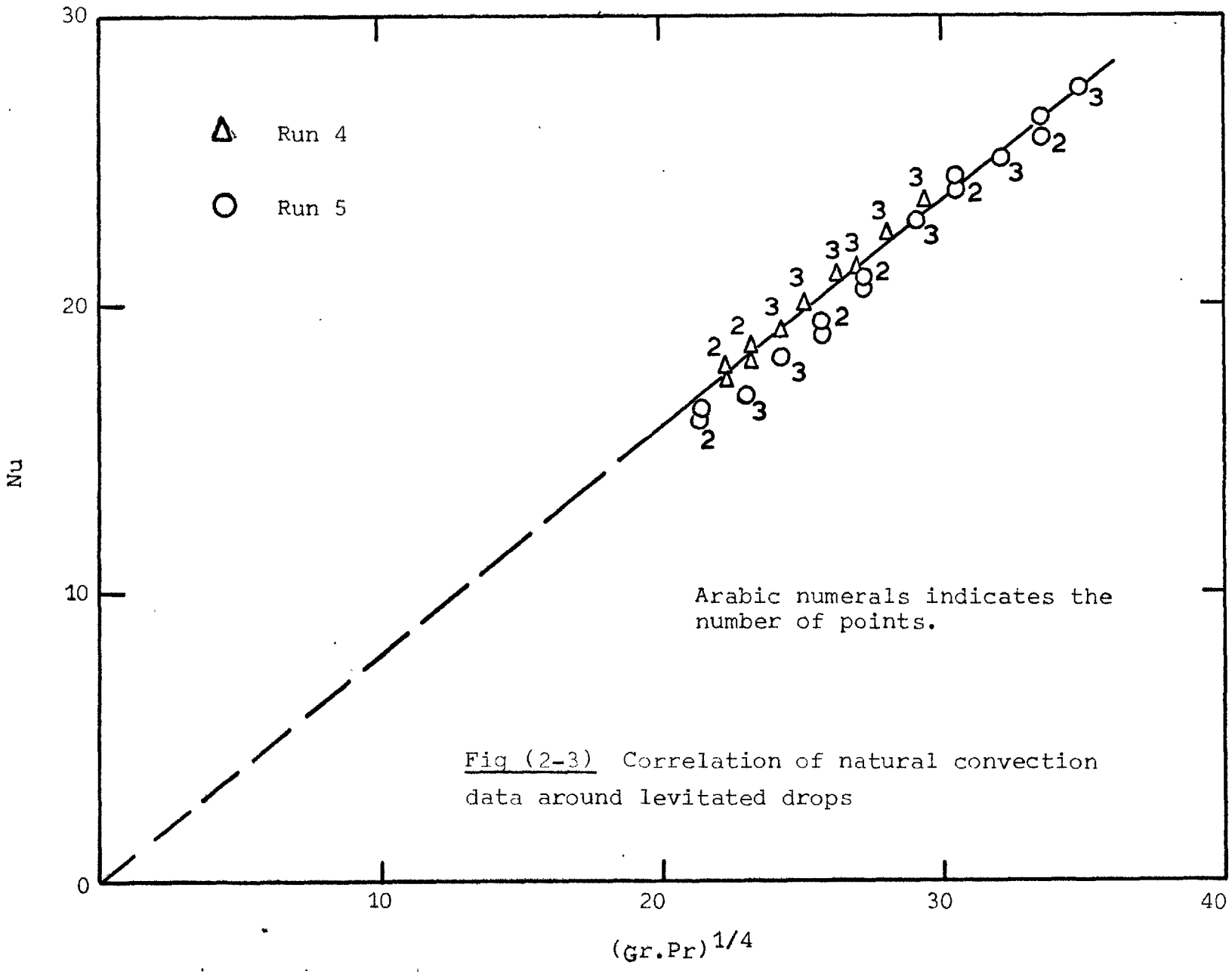

Fig (2-3) Correlation of natural convection data around levitated drops

against Gr/Re^2, fig. (2-4). The combined regime was observed at $1.3 < Gr/Re^2 < 7$. The results were scattered around the natural convection extrapolation, and no definite conclusion can be drawn about the transition from natural to forced convection.

2-3 Thermal diffusion in $CO-CO_2$ gas mixtures

2-3.1 Introduction

The levitation technique is characterized by large temperature gradient at the surface of the drop. This induced thermal diffusion in the bulk gas mixture of $CO-CO_2$, along the temperature gradient. The surface concentration of $CO-CO_2$ was measured at the graphite saturation using the equilibrium data for the reaction

$$C_{(graphite)} + CO_2 = 2CO \qquad (2-21)$$

and the graphite solubility in liquid iron.
The measured thermal diffusion parameters were compared with those predicted by the rigorous kinetic theory of gases and the measured values for $N_2 - CO_2$ mixtures.

2-3.2 Some theoretical aspects of thermal diffusion

a) Mass Transfer and thermal diffusion

Thermal diffusion in gases was predicted theoretically by Enskog and Chapman through their development of the rigorous kinetic theory of gases (28, 29). Mass flux

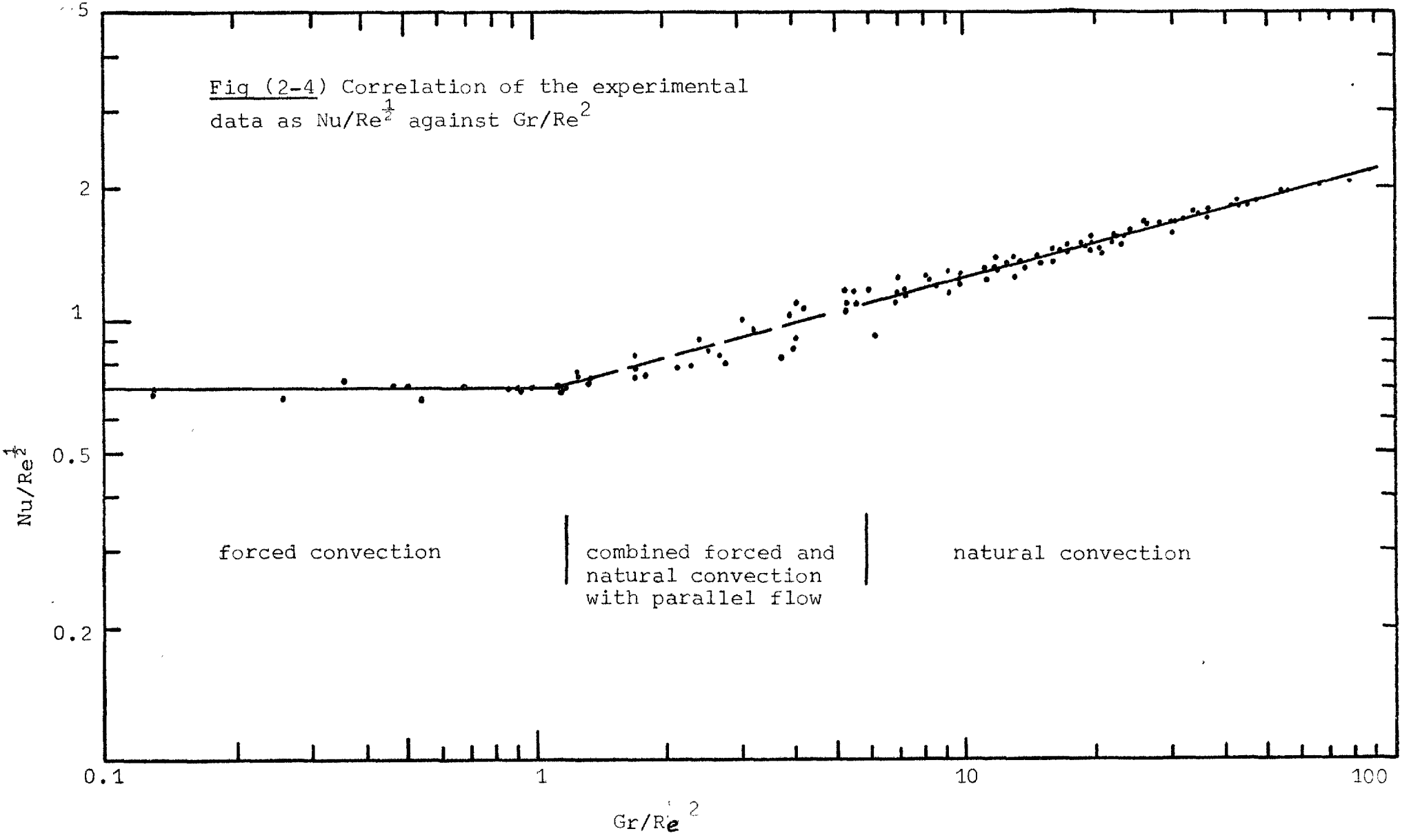
Fig (2-4) Correlation of the experimental data as Nu/Re^1/2 against Gr/Re^2
5
2
1
0.5
0.2
Nu/Re^1/2
forced convection
combined forced and natural convection with parallel flow
natural convection
0.1
1
10
100
Gr/Re^2

defined in terms of the gradient of various physical properties was obtained as the on basis of this theory, as

$$J_i = n_i m_i \bar{V}_i = \frac{n^2}{\rho} \sum_{j=1} m_i m_j D_{ij} d^j - D_i^T \frac{\partial \ln T}{\delta r} \qquad (2\text{-}22)$$

The symbol d^j includes the gradients of mole fraction and pressure and also the effect of the external forces acting on the molecules and represented as

$$d^j = \frac{\delta}{\delta r}\left(\frac{n_j}{n}\right) + \left[\left(\frac{n_j}{n} - \frac{n_i m_j}{\rho}\right)\right]\frac{\delta \ln P}{\delta r} - \frac{n m_j}{P \rho}\left[\frac{\rho}{m_j} X_j - \sum_{K=1} n_K X_K\right] \qquad (2\text{-}23)$$

For binary gas mixtures, under no external effect and constant pressure, equation (2-22) may be simplified as

$$J_1 = n_1 m_1 \bar{V}_1 = \frac{n^2}{\rho} m_1 m_2 D_{12} \frac{\delta}{\delta r}\left[\frac{n_2}{n}\right] - D_1^T \frac{\delta \ln T}{\delta r} \qquad (2\text{-}24)$$

Since $n_1 + n_2 = n$ and $\sum J = 0$ it follows that $D_{12} = D_{21}$ and $D_1^T = -D_2^T$. Equation (2-23) can be represented as

$$\bar{V}_1 - \bar{V}_2 = -\frac{n^2}{n_1 n_2} D_{12}\left\{\frac{\delta}{\delta r}\left(\frac{n_1}{n}\right) + K_T \frac{\delta \ln T}{\delta r}\right\} \qquad (2\text{-}25)$$

Where $K_T = \rho D_1^T / n^2 m_1 m_2 D_{12}$

This quantity is known as the thermal diffusion ratio. When the equilibrium has been established so that the diffusion velocity of each component is equal, we obtain

$$\frac{\delta}{\delta r}\left(\frac{n_1}{n}\right) = -K_T \frac{\delta}{\delta r} \ln T \qquad (2\text{-}26)$$

The thermal diffusion ratio is now defined so that when K_T is positive component 1 moves to the cold region and when K_T is negative it moves to the hotter region. Thermal diffusion ratio is a function of concentration and temperature and integration of equation (2-26) is very complicated. However the change in concentration is so small that the variation of K_T may be neglected and the variation of temperature can be approximated by using a mean temperature value, so we obtain

$$-K_{(T_f)} = \Delta(n_1/n)/\ln\ (T_s/T_b) \qquad (2\text{-}27)$$

Equation (2-26) was used in this work to calculate $K_{(T_f)}$ from experimental results on separation of the CO-CO_2 binary gas mixtures. The experimental value of $K_{(T_f)}$ was used to define two quantities, the thermal diffusion factor and thermal separation ratio R_T. They are defined as

$$\alpha = K_{(T_f)}{}_{expt} / X_1 X_2 \qquad (2\text{-}28)$$

$$R_T = K_{(T_f)}{}_{expt} / k_{(T_f)rig.sph.} \qquad (2\text{-}29)$$

The quantity (α) is used because it is very nearly independent of concentration, while (R_T) is a measure of the extent to which the intermolecular forces decrease the thermal diffusion below that of the maximum value for ideal hard molecules of rigid spheres.

b) Diffusion phenomena in gases

Despite the satisfactory state of the rigorous kinetic theory of gases, the simple physical interpretation of diffusion (especially thermal diffusion) does not appear through the mathematical derivation. For this reason several attempts have been made to explain these phenomena.

A simple physical explanation based on the concept of mean free path (30), was attempted by Gillespie (31) and Furth (32). Inspite of their success in obtaining some formal relationships (equation (2-24)) and some conclusions about thermal diffusion which correspond with those of the kinetic theory of gases, their explanation fails in detail. For example the prediction of the mutual diffusion coefficient is contradicted by experiments. The fact is that the mean free path does not provide a correct physical approach to diffusion problems, as it does for viscosity and thermal conductivity (30, 33).

This is because the mean free path method is only a good representation of transport processes in which all the collisions between molecules play an important part. This is true of viscosity and thermal conductivity, but not of diffusion phenomena where it is the collisions between unlike molecules which are of main importance.

The momentum transfer method developed by Maxwell and Stefan was suggested by Frankel (34) and elaborated by Furry (33) to provide an elementary explanation of the phenomena of mutual diffusion and thermal diffusion. This approach gives essentially correct results for the mutual diffusion coefficient. The treatment of thermal diffusion combines the momentum transfer method for molecular flow with the mean free path method for the energy flow by thermal conduction due to the temperature gradient. An elementary description of thermal diffusion following that given by Frankel is included in Appendix (3).

The following conclusions were drawn for thermal diffusion:

1) The light molecules tend to concentrate in the hot region.
2) A difference in size of the molecules contributes to thermal diffusion. For equal mass molecules the smaller accumulate in the hot region.

3) This phenomenon is peculiarly sensitive to the precise form of the molecular interaction law. For example if the molecules act as a point centre of repulsion ($F = Cr^{-\delta}$, where r is the distance between the centre of the molecules), the direction of thermal diffusion changes if the dependence of repulsive force on the distance is more or less than by the inverse fifth power (Maxwellian molecules) at which the thermal diffusion vanishes. The magnitude of thermal diffusion is at a maximum for a rigid sphere molecules ($\delta = \infty$).

4) Thermal diffusion ratio is concentration dependent. The maximum separation is obtained at about equal concentrations.

5) The present incomplete knowledge of intermolecular forces and the use of semi-empirical laws, obtained from both experimental observation (viscosity measurements) and theoretical considerations, limits the application of the kinetic theory of gases in predicting thermal diffusion for polyatomic molecules, which have internal degrees of freedom.

c) Pressure dependence of thermal diffusion

The results of the kinetic theory of gases are not applicable at high pressures where its assumptions cannot be applied. However the argument based on the principle

of corresponding states proposed by Van de Waals, gives a practical method for determining pressure dependence of transport properties. The principle of corresponding states implies that all substances obey the same relations in terms of reduced variables. According to this principle measured properties of one substance at different pressure and temperature represented as reduced variables may be used to predict the properties of other substances under conditions where no data exist and no satisfactory theoretical treatment may be applied.

Few experimental results on the effect of pressure are available for transport properties except for viscosity (29). However these data were used as a qualitative method to predict deviations from the kinetic theory of gases.

2-3.3 Previous work

Thermal diffusion in binary gas mixtures around levitated drops has been studied by Sunderland et al (35). Their technique was to measure the equilibrium sulphur content of iron drops in H_2-H_2S gas mixtures during reaction of sulphurization of iron,

$$H_2 + \underline{S} \rightleftharpoons H_2S \qquad (2\text{-}30)$$

and compare it with the availiable equilibrium data. Larche and McLean (36) were not able to detect thermal diffusion in CO-CO_2 gas mixture by measuring the oxygen content dissolved

in molten iron at equilibrium using the equilibrium data of the reaction

$$CO + \underline{O} \rightleftharpoons CO_2 \qquad (2\text{-}31)$$

since the equilibrium data available were not of sufficient precision.

Conventional techniques to produce separation of the components in a gas mixture using two bulbs at different temperature, and the methods of analysis of the gas mixtures, have been reviewed by Ibbs and Grew (37).

No work has been reported on the study of CO-CO_2 gas mixtures using the conventional techniques. However the experimental data of thermal diffusion in N_2-CO_2 gas, which is available in the literature, was used as an alternative for CO-CO_2 mixtures since N_2 has the same molecular weight as CO and nearly the same viscosity and thermal conductivity, which reflect the similarity between the two fields of force.

Grew et al (38) measured the separation of 49.7% CO_2 in N_2 by the two bulb method in which one of the bulbs was at a temperature of 293°K while the other was at temperatures in the range of 165° to 1167°K. They found that above 736°K the thermal diffusion factor remained constant. Humphreys and Gray (39) carried out measurements over a temperature

range of 300 to 800°K with a reference temperature of 306.7°K and a wide range of composition (10-90% CO_2). The agreement between their results at 50% CO_2 with those by Grew et al (30) was remarkable above 700°K and differed only marginally at lower temperatures. They also observed that decreasing CO_2 % increased the thermal diffusion factor. The work of Becker (40) on thermal diffusion of N_2-CO_2 gas mixture is of particular interest, since he studied the effect of pressure on the separation. The apparatus was two steel bulbs, they were kept at 287° and 427°K. He found on 48% CO_2-N_2 mixture at pressures ranging from 3-80 atmosphere, that the thermal diffusion factor increased by increasing pressure and the increase was eight fold over that range.

The results of these investigations are given in the following table:

Author	Pressure atm	X_{CO_2}	Temp range °(K)	α	R_T
Grew et al (38)	1	0.497	465-1167	0.092	0.39
Humphreys et al (39)	1	0.1	500-700	0.109	
	1	0.5	500-700	0.089	0.377
	1	0.9	500-700	0.076	
Becke (40)	3	0.48	427	0.05	
	26			0.124	
	52			0.252	
	81			0.402	

Table (2-4)

Measurements of thermal diffusion in N_2-CO_2 gas mixtures

2-3.4 Experimental technique

This section describes the measurement of the thermal diffusion effect in the temperature gradient around the drop in the $CO-CO_2$ gas mixtures used in this work. This involved measuring the pressure and temperature at which graphite saturation occurred in each gas mixture. Two techniques were used.

In the first technique visual observation was used to detect the appearance of the graphite phase floating on the surface of the specimen. This was confirmed by a sudden temperature drop of the specimen because of the higher emissivity of the graphite. A specimen of spec-pure iron weighing about one gram was levitated in $CO-CO_2$ gas mixtures at high pressure at 1560°C. After sufficient time for the equilibrium to be established at that temperature, the specimen temperature was dropped in 5°C steps every 5 minutes approximately, until graphite was observed. This procedure is illustrated graphically in fig. (2-5).

The second technique was more reliable and accurate than the first one. The equilibrium carbon was measured along the line A-A in fig. (2-5) at 20°C intervals through a number of equilbrium runs. The graphite saturation temperatures were obtained by extrapolating the results to the graphite solubility limit, line B-B on fig. (2-5). An additional check on carbon analyses using the combustion method was done by measuring the weight change of the spec-pure

iron specimen after the equilibrium run. The calculated value represents the minimum carbon on the specimen, because of loss of weight due to vaporisation. Fortunately high pressure cuts the vapourisation rate (molecular diffusivity in the gas phase is inversely proportional to pressure), and the accuracy of estimation of carbon by weighing was 0.03 w/o carbon.

The accuracy of setting the temperature was $\pm$ 2°C using the automatic temperature control system, and the temperature reading of TCP was corrected from the calibration. Since most of the experiments were carried out at temperatures lower than the melting point of pure iron, the runs were started at 1560°C for 5 minutes, which was enough time for the CO-CO_2 gas mixtutes to "pump" a lot of carbon into the specimen (see chapter 4).

2-3.5 Results

The temperature of graphite formation and hence the composition of CO-CO_2 gas mixture at the hot surface of the molten drops was obtained using three CO-CO_2 gas mixtures of 2.15%, 1.10% and 0.76% CO_2 in CO and at pressures ranging from 70-84 atmospheres.

Surface concentrations were calculated from the established thermodynamic data of the graphite reaction with CO-CO_2 (41)

$$CO_2 + C_{graphite} \rightleftharpoons 2CO \qquad (2\text{-}32)$$

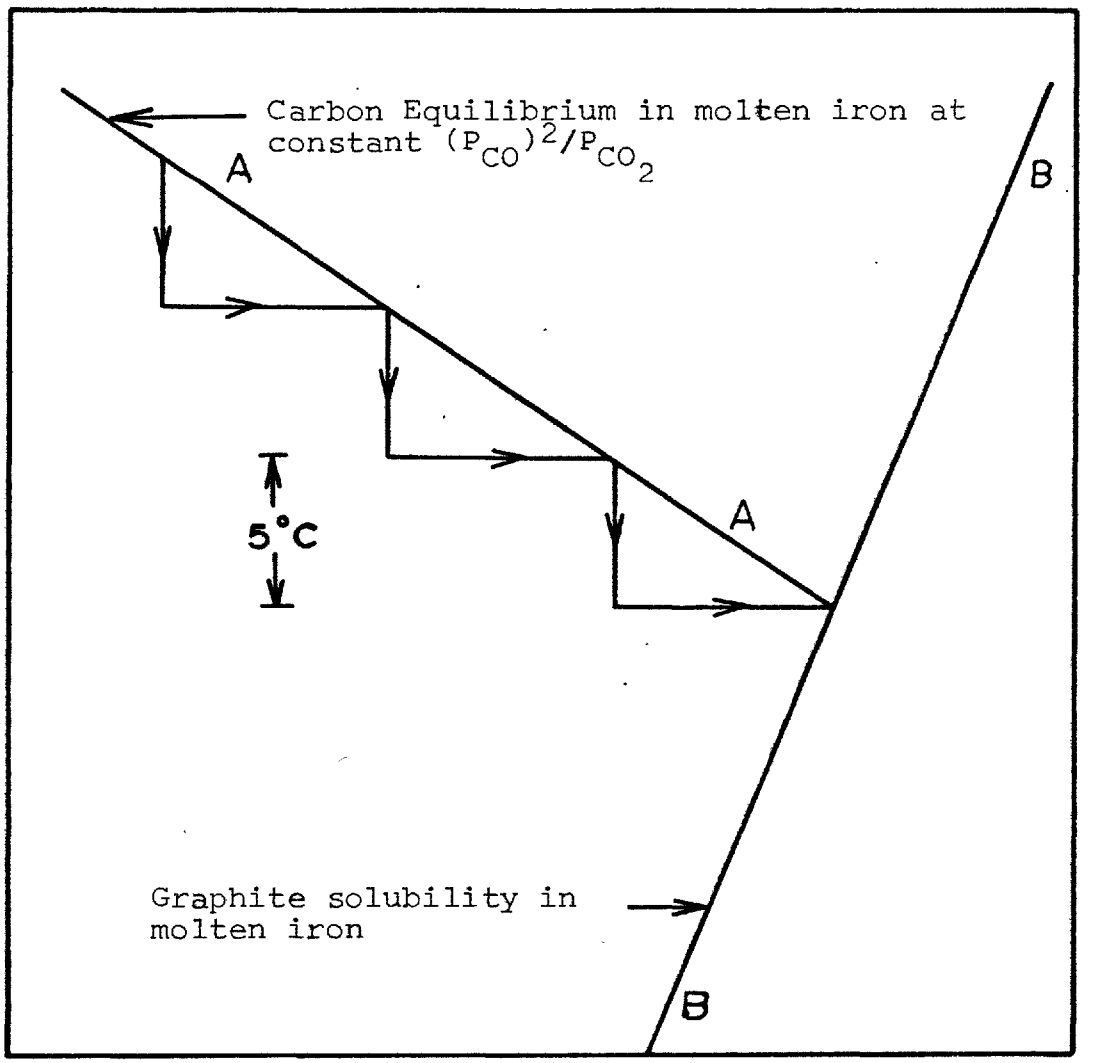

Fig (2-5)

Schematic representation of the approach toward the graphite solubility in molten iron

$$K = (P_{CO})^2/P_{CO_2} \qquad (2\text{-}33)$$

Visual observation method

Gas mixtures of 2.15% and 1.1% CO_2 at 80.22 and 83.7 atmospheres respectively were used. The calculated surface gas compositions were 2.05% and 1.07% CO_2 respectively. The results are given in table (2-5).

Equilibrium method

The solubility of graphite in liquid iron was measured accurately in the course of establishing the Fe-C phase diagram, and can be represented according to Chipman et al (42) as

$$\%C = 1.34 + 2.54 \times 10^{-3}\ t(^{o}C) \qquad (2\text{-}34)$$

The results of 1.1% and 0.76% CO_2 at 80.9 and 70.13 atmospheres respectively were extrapolated to the graphite saturation line as shown in fig. (2-6). The values of carbon saturation for these mixtures and pressures for an iso-thermal system were calculated from equation (2-33) and (2-34) and are shown along the line of saturation in the same figure. The results of each set may be extrapolated as straight lines, see fig. (2-6).

Segregation of the gas mixture was confirmed again and 1.07% and 0.72% CO_2 were obtained at the surface for 1.1% and 0.76% CO_2 bulk gas respectively. The experimental

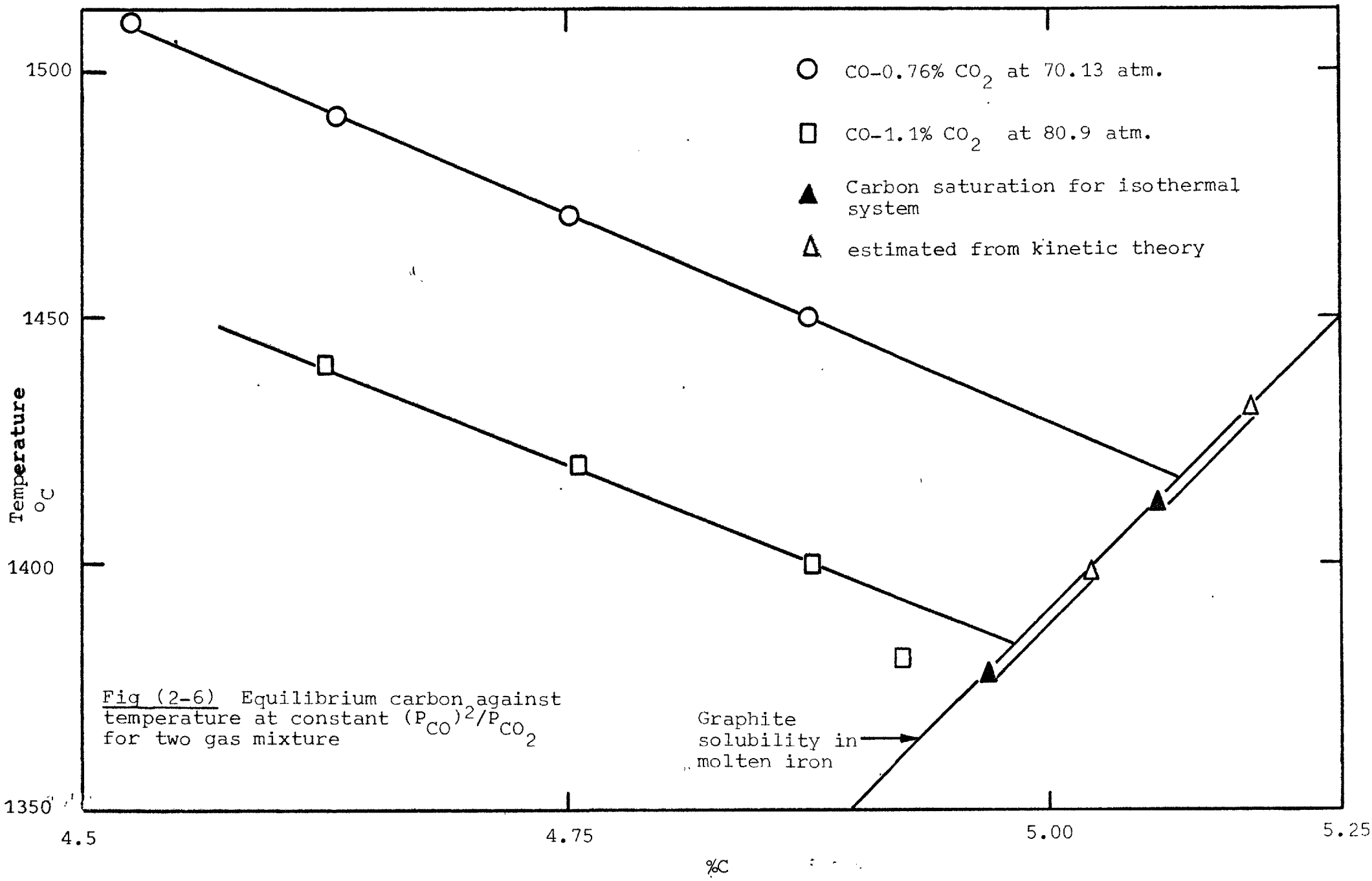

Fig (2-6) Equilibrium carbon against temperature at constant $(P_{CO})^2/P_{CO_2}$ for two gas mixture

conditions and the results are summarised in table (2-6).

2-3.6 Evaluation of the results

Segregation of $CO-CO_2$ gas mixture was observed around the levitated drop-due to a temperature gradient. Before carrying out any calculation on thermal diffusion using equation (2-27), which is given in section (2-3.2), the concentration and temperature gradient in the gas phase must be examined around the levitated drop. For convective flow around the drop under the experimental condition, heat and mass flux occur through their corresponding gradients in the laminar boundary layer. The relative thickness of these boundary layers is defined by the ratio Prandtl to Schmidt number (Lewis number). For $CO-CO_2$ gas mixtures at the mean temperature this ratio is nearly unity, which implies that the thermal and diffusion boundary layers were coincident. Equation (2-25) is therefore valid and can be used to evalute thermal diffusion ratio $K_{(T)}$. Calculation of thermal diffusion factor α, and separation factor R_T was carried using equations (2-28) and (2-29). The results of thermal diffusion ratio $K_{(T_f)}$, factor α, and separation factor R_T are given in table (2-7). Calculated values from the kinetic theory of gases using Lennard-Jones (6-12) and elastic rigid sphere models of inter-molecular forces are included in table(2-7). Some details of these calculations are given in Appendix (4).

Run	Gas mixture	Pressure atm.	Approach gas temperature °C	Observed graphitization temperature °C
C2	CO-2.15% CO_2	80.22	50	1335
C3	CO-1.1% CO_2	83.7	50	1435

Table (2-5)

Measurements of Thermal diffusion using visual observation technique

Run	Gas mixture	Pressure atm.	Approach gas temp.	Drop temp °C	w/o carbon
C4	CO-1.1% CO	80.81	50	1490	4.624
C5	"	80.899	50	1450	4.895
C6	"	81.029	50	1470	4.756
C7	"	81.31	50	1430	4.926
C8	"	81.10	50	1425	4.896
C9	"	81.09	50	1430	4.917
Graphitization temperature = 1433°C					
C14	CO-0.076% CO_2	70.13	50	1560	4.528
C15	"	70.13	50	1540	4.610
C16	"	70.13	50	1540	4.634
C17	"	70.13	50	1520	4.759
C18	"	70.13	50	1520	4.769
C19	"	70.13	50	1500	4.90
G20	"	70.13	50	1500	4.88
Graphitization temperature = 1467°C					

Table (2-6)

Measurements of thermal diffusion using equilibrium technique

The measured thermal diffusion factors using different gas mixtures under different experimental conditions showed a good agreement. This was evidence of the accuracy of these measurements, particularly temperature measurements. It should be pointed out that a $\pm$ 2°C error in temperature reading from the TCP, and temperature fluctuations, which are inevitable in any high temperature studies, make the thermal diffusion factor subject to an error of $\pm$ 50%. This amplification is mainly due to the sensitive dependence on temperature of the equilibrium constant of the β graphite reaction with $CO-CO_2$ gas mixtures. On the other hand the same error in temperature measurement lead to only a very small error in actual CO/CO_2 ratio, about $\pm$ 0.5% relative error for a 1% CO_2 gas mixture.

The fact that reasonable values were obtained for α and .. particularly that α was found to be approximately the same under different conditions, suggests that the error in temperature measurement may have been well below the $\pm$10°C which was estimated conservatively as the accuracy of the TCP (see section 1-4).

Mixtures	Press. atm.	$k_{(T_f)} \times 10^3$			α			R_T
		experimental	Theoretical		experimental	Theoretical		
			LJ (6-12)	rigid sphere		LJ (6-12)	rigid sphere	
CO-0.076% CO_2	70.13	0.143	0.855	1.36	0.0190	0.113	0.181	0.11
CO-1.1% CO_2	80.90	0.269	1.232	1.967	0.0247	0.113	0.181	0.137
CO-1.1% CO_2	83.70	0.139	1.232	1.967	0.0128	0.113	0.181	0.071
CO-2.15% CO_2	80.22	0.476	2.37	3.813	0.0227	0.113	0.181	0.125

Table (2-7)

Experimental and theoretical values

of thermal diffusion for CO-CO_2 gas mixtures

2-4 Discussion

2-4.1 Convective heat transfer

The work presented in this chapter relates the convective heat transfer from a levitated drop to a gas around it. This particular system differs from the previously studied systems. The differences are listed below:

1) Characteristics of levitated drops

The levitated drops are not perfectly spherical, but are slightly egg-shaped. The drops sometimes show a slight bulk rotation about a vertical axis at around 4 revs/s. The induced currents cause a movement of the surface but the directions of movement have not been defined. These characteristics are well illustrated by Robertson (5).

2) Steep temperature gradient in the boundary layer

The temperature of the approaching gas (room temperature about 20°C) increases toward the droplet temperature (about 1700°C) in the boundary layer around the drop. The physical properties of the gas (density, viscosity, thermal conductivity, ...) vary markedly while in many previous studies such variations are negligible because their work was carried out near room temperature.

In the following paragraphs we compare the heat transfer rate from levitated drops with steep temperature gradients with previous studies on spheres, with comparatively gentle gradients in the boundary layer.

a) Forced convection

Proposed heat transfer correlations for heat transfer from a sphere by forced convection are summarised in fig. (2-7). The band within which all the correlations lie is due to accuracy limits of the experimental techniques ($\pm$ 10 - 20%), and to the over simplification of the Re, Pr function equation (2-5) (12). The correlation obtained during this work, equation (2-19), is also shown in fig. (2-7). It lies near the upper limits, so it generally predicts relatively high mass transfer rate. Despite the differences mentioned in section (2-4.1), equation (2-19) is evidently suitable for spheres where there is a steep temperature gradient in the gas boundary layer in the range $150 < Re < 500$ as well as levitated drops.

The value of the B in equation (2-19) depends on the value taken for the total emissivity. This value is 0.4 and is within $\pm$ 10%. It is clear from the success of the correlation over a wide range of temperature and in the calculation of values of Q_{EC} which lead to a consistent picture for natural convection, that $B = 0.8$ must be correct within about 20%.

The fact that total pressure had no effect on temperature up to 8 atmospheres is a critical test which proves that natural convection does not contribute to heat transfer until a particular value of Gr/Re^2 is reached.

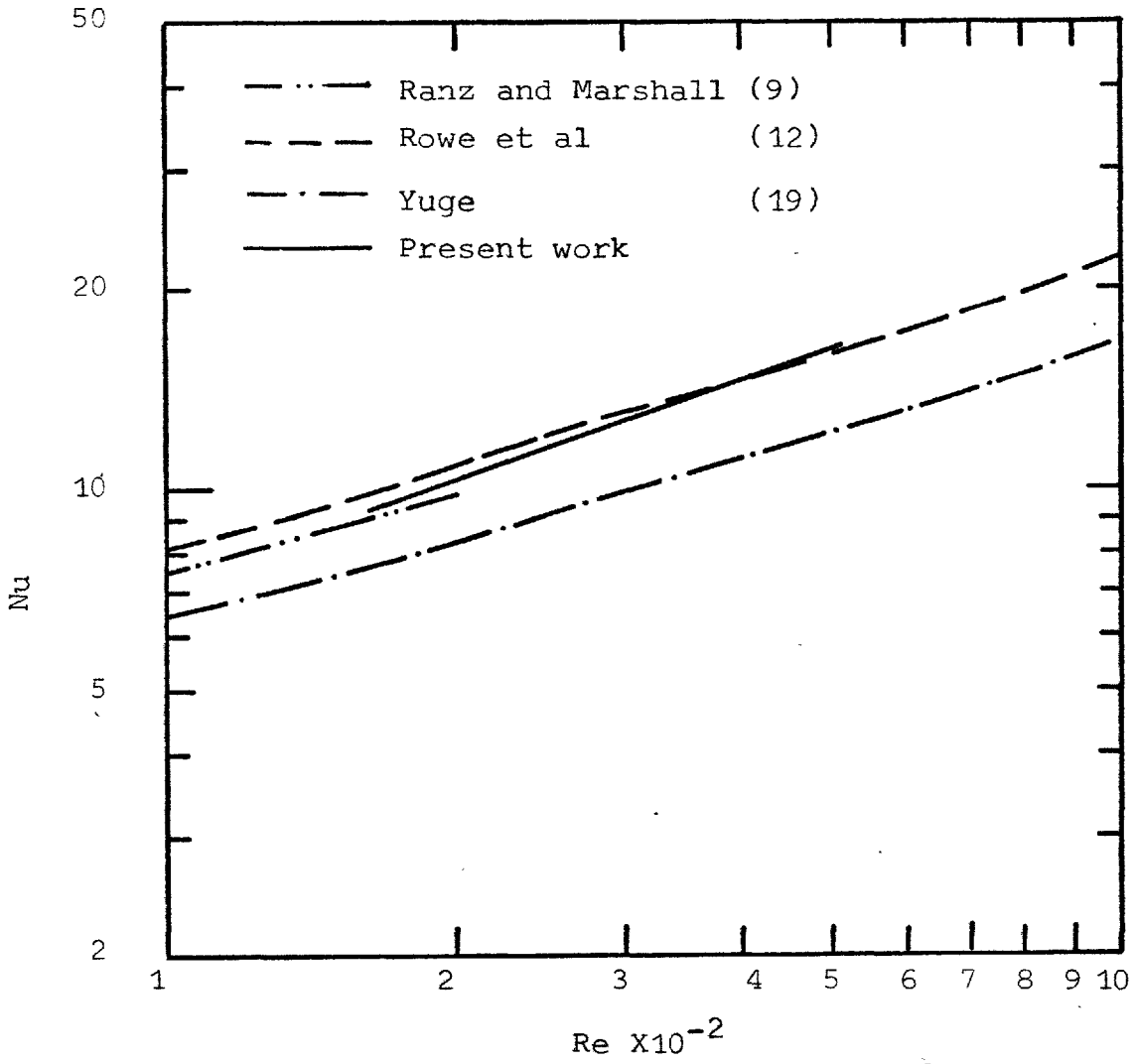

Fig (2-7) Heat transfer
from spheres in forced convection
by various investigations, (Pr = 0.67)

b) Natural convection

Measurements of rates of heat transfer by natural convection in the present work, equation (2-20), are in good agreement with the previous studies within the accuracy limits of the experimental techniques of ± 10 - 20% fig. (2-8). This again confirms the fact that levitated drops can be treated as spheres and the large temperature gradients can be allowed for by using mean values for the physical properties in the boundary layer. However the obtained correlation equation (2-8) which covers a wider range of Gr than any other availiable correlations, showed higher heat transfer rate than the other correlations, particularly at higher Grashof number.

The accuracy of this correlation could be within ± 20% due to the same reasons mentioned in forced convection. However an excellent agreement was obtained when used for mass transfer (see section (4-5)). Forced convection had no contribution on heat transfer rate after a particular value of Gr/Re^2 is reached, from the fact that flow rate had no effect on temperature above 40 atmospheres.

c) Transition between forced and natural convection

Pei and coworkers determined the transition regime for $0.05 < Gr/Re^2 < 100$ (24) with natural convection contributing less than 10% for $0.05 < Gr/Re^2 < 0.3$, and $0.3 < Gr/Re^2 < 35$ (23). In this work the transition occurred for

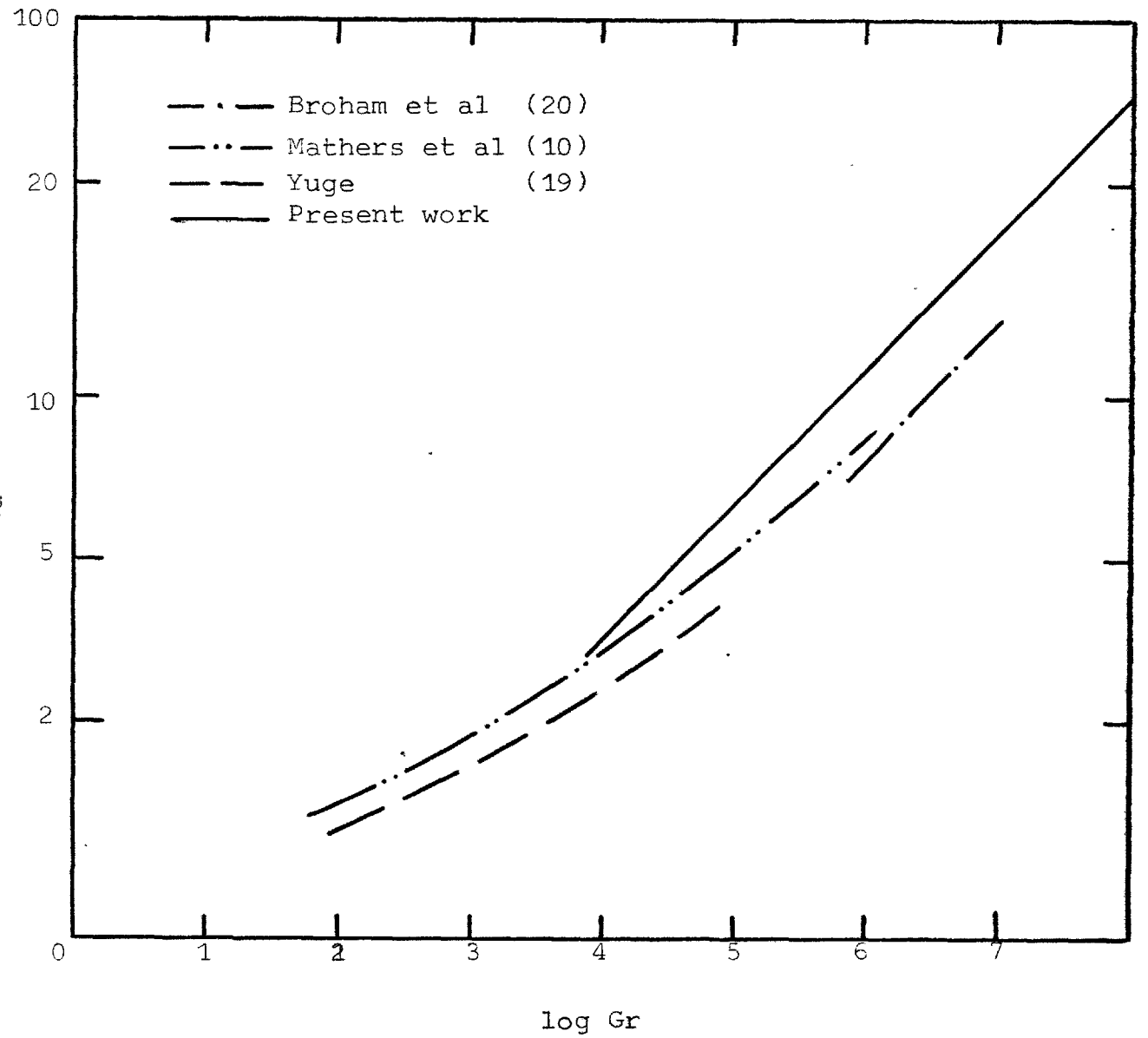

Fig (2-8) Heat transfer from spheres in natural convection by various investigations (Pr = 0.67)

$1.3 < Gr/Re^2 < 7$. The limits of the transition regime are obviously difficult to measure accurately, particularly using our technique where a large proportion of the heat transfer occurs by radiation.

In the transition regime the forced and natural components are definitely not arithmetically additive, and despite the scatter of the results, it can be represented by pure natural convection. This is in support of the suggestion by McAdams (21) for treating convection effects in the transition region. The previous works by Pei and coworkers (23, 24) and Yuge (19) reached the conclusion that behaviour in the transition regime is nonadditive, but they reported that the transition between forced and natural convection is gradual in the case of parallel flow.

2-4.2 Convective mass transfer

Boundary layer equations for mass transfer based on the assumption of constant properties of the fluid and low mass transfer rate i.e. the velocity at and normal to the surface approach zero, have an analogous form to the heat transfer equations (7).

As would be expected from the analogy between heat and mass transfer, the mass transfer correlations around levitated drops may be represented as:

Forced convection:

$$Sh = 0.8\ Re^{\frac{1}{2}}Pr^{\frac{1}{3}} \qquad (2\text{-}35)$$

Natural convection:

$$Sh = 0.78\ (Gr.Sc)^{1/4} \qquad (2\text{-}36)$$

In the case of mass transfer, the buoyancy term $(g(\rho_s - \rho_b))$ is not only dependent on the temperature gradient, but also on the concentration gradient. The overall Grashof number Gr' is defined as (10).

$$Gr' = Gr_{12} + (Sc/Pr)^{\frac{1}{2}} Gr$$

where Gr_{12} is the Grashof number for mass transfer, and is defined as,

$$Gr_{12} = \rho_f^2 g d^3 \zeta\ (X_{1s} - X_{1b})/\mu^2_f \qquad (2\text{-}37)$$

where $\zeta = -1/\rho\ (\delta\rho/\delta X_A)_{T,P}$ and equal to $(M_2 - M_1)/(M_1X_{1f} + M_2X_{2f})$ for ideal gases and Gr is Grashof number for heat transfer.

With steep temperature gradients around the levitated drop, the contribution of the Grashof number for mass transfer to the overall Grashof number is generally small. For example for binary CO - CO_2 gas mixtures reacting with a levitated drop ($\Delta T \simeq 1700$) with maximum driving force ($\Delta X = 1$), the Grashof number for mass transfer contributes to the overall Grashof number by 20% . This changes the value of Sherwood number by 5%.

The criteria for the transition regime should be the same as that for heat transfer i.e. $1.3 < Gr'/Re^2 < 7$. There has been much controversy in the literature (43, 44) over the use of the Steinberger and Treybal correlation (22) where natural and forced contributions are added in a linear fashion at all values of Gr/Re^2. This is obviously not correct in all cases. The correct approach is to vary total pressure with Re constant, and this will show whether natural convection is contributing to the rate and will allow the evalution of the Gr/Re^2 values for various regimes.

2-4.3 Thermal diffusion in CO - CO_2 gas mixture

The main object of this study is to provide quantitative data on thermal separation of the CO-CO_2 gas mixtures around levitated drops. This provides a more accurate estimate of the gas composition at the surface of the drop for thermodynamic and kinetic studies. Although these thermal diffusion measurements are not as accurate as those using the two bulb method, they provide the first data on thermal diffusion in CO-CO_2 gas mixtures. The thermal diffusion factor α for dilute CO-CO_2 gas mixtures ($\%CO_2 \longrightarrow 0$) is constant and independent of the pressure in the pressure range 70 - 84 atmospheres. The following paragraphs discuss the effect of pressure on thermal diffusion, and the validity of these results at lower pressures.

Thermal diffusion is pressure independent from the rigorous kinetic theory of gases, provided that this pressure

is not so high that the postulates on which this theory is based become invalid.

Using the principle of corresponding states it is possible to show that pressures of up to 100 atmospheres at the mean temperature ($T \sim 1000^{\circ}K$) have no effect on the viscosity of dilute CO_2 in CO gas mixtures. It is therefore a reasonable assumption that the kinetic theory of gases is valid up to 100 atmospheres and that the thermal diffusion ratio is independent of pressure.

Becker (40) showed that non-ideality of gases in a mixture will lead to a separation with temperature gradient irrespective of any thermal diffusion process. Therefore if this separation is ascribed to thermal diffusion and included in the thermal diffusion factor the thermal diffusion factor will show a change with pressure. On the basis of this idea, he explained the measured increase of the thermal separation of gases by pressure (40). Since the CO-CO_2 gas mixtures used were very dilute in CO_2 (partial pressure of CO_2 about one atmosphere), so any deviation of CO_2 from ideal behaviour was negligible.(45). Carbon monoxide behaves as an ideal gas up to 100 atmospheres at $300^{\circ}K$ (45). On the basis of this theory it follows that the pressure can have no effect on the thermal diffusion factor of these gas mixtures.

From the above discussion, the pressure has no effect on the thermal separation of the gas mixtures used.

This independence of pressure has been confirmed over the small range of pressure from about 70 to 84 atmospheres.

In comparing experimental results with the predicted values from the kinetic theory of gases at the mean temperature using Lennard-Jones potential for thermal diffusion factor, the measured values are five time lower. Similar ratio is also obtained in comparing the results with measurements in N_2-CO_2 mixtures at a mean temperature of 600°K. Larche and McLean (36) were not able to detect any thermal diffusion in CO-CO_2 gas mixtures using the levitation technique. Such low values for the thermal diffusion factor could be characteristic of the large spatial variation of physical properties in the gasphases and the motion of the gas in the boundary layer. Also the thermal and concentration boundary layer thickness do not exactly coincide. On the other hand, the use of Lennard-Jones potential model (6-12) to predict the thermal diffusion in CO-CO_2 gas mixtures may not be appropriate, although it does describe other transport phenomena well, particularly at low temperatures. The sensitivity of thermal diffusion to the nature of molecular interaction is far greater than for any other transport phenomena, so that the assumption of a (6-12) potential may not be adequate for thermal diffusion. The value obtained for thermal separation factor R_T of about 0.12 indicates that the molecules are soft. This suggests that the repulsive force index is less than 12 as used in the Lennard-Jones potential model.

Accurate measurements on thermal diffusion in $CO-CO_2$ gas mixtures using the bulb method are required to test this hypothesis.

The failure of the $CO-CO_2$ mixtures to give the same values as measured for the N_2-CO_2 mixture may be due to either of the reasons mentioned above i.e. steep gradients or different intermolecular forces.

2-5 Conclusion

The work presented in this chapter is best regarded as a contribution to an understanding of transport phenomena in the gas phase around levitated drops. The high pressure levitation technique was the only suitable technique for this study, and has yielded reliable data that it was not possible to obtain in the previous studies.

Convective heat transfer around the levitated drop was studied in forced, natural, and transition regimes. Heat transfer rates around levitated drops were correlated for forced and natural convection. The criteria for the transition region, in terms of Gr/Re^2, were also defined. The scatter of the results in the transition regime did not allow the analysis of the contribution of both forced and natural convection on the heat transfer rate. However, as a good approximation forced convection can be neglected.

Convective heat transfer from levitated drops and spheres was found to be nearly identical. The correlations

obtained are recommended for levitated drops, and for spheres with steep temperature gradient. Convective mass transfer correlations were proposed based on the analogy between heat and mass transfer at low rates of mass transfer.

Thermal diffusion in $CO-CO_2$ gas mixtures ($CO_2 \longrightarrow 0$) was measured using the levitation technique, and a thermal diffusion factor of 0.022 was obtained. The pressure up to 100 atmosphere was found to have no effect on thermal separation of these gas mixtures. The theoretical value of thermal diffusion factor calculated from the kinetic theory of gases is higher than the obtained value. Since the literature is lacking in reported measurements it is difficult to assess the data. However, the measured value can obviously be used for calculation of thermal separation of $CO-CO_2$ gas mixture around levitated drops in this work.

CHAPTER 3

THERMODYNAMICS OF THE LIQUID Fe-C-O SYSTEM

3-1 Introduction

The equilibria of carbon and oxygen in molten iron are the first steps in understanding the steelmaking process. They have been extensively studied in the laboratory and in the plant. This work was undertaken to investigate two aspects. These were the Fe-C equilibrium over a carbon range far wider than in any other previous investigation, and the effect of carbon on the oxygen concentration in the Fe-C-O system at constant oxygen activity.

This study was carried out at 1550, 1650 and 1750°C, using $CO-CO_2$ mixtures, at pressures up to 70 atmospheres. The information obtained in the work on thermal diffusion was used to define the gas mixture composition at the surface of the drop. The equilibrium was approached from both sides as a check that true equilibrium was acheived.

The previous work was assessed and compared with the present study. The thermodynamic properties of the Fe-C system have been tested with the measurements of the activity of carbon in austenite.

3-2 Previous work

3-2.1 Introduction

There has been an enormous amount of equilibrium work on the molten Fe-C, Fe-O, Fe-C-O systems. A collection of the results obtained has been given by Bodsworth and Bell (46). The results of the previous workers will be compared with this work in the discussion.

3-2.2 Carbon in molten iron

The activity of carbon in molten iron has been measured by studies of the chemical equilibrium of the reaction between gases of known carbon activity and dissolved carbon. Two methods were used, one involving equilibrium with mixtures of CO_2-CO (47-53)

$$C \text{ (in iron)} + CO_2 \rightleftharpoons 2CO \qquad (3\text{-}1)$$

$$K_1 = (P_{CO})^2/P_{CO_2}\, a_c \qquad (3\text{-}1a)$$

and the other with mixtures of H_2 and CH_4 (9)

$$C \text{ (in iron)} + 2H_2 \rightleftharpoons CH_4 \qquad (3\text{-}2)$$

$$K_2 = (P_{CH_4})/(P_{H_2})^2\, a_C \qquad (3\text{-}2a)$$

The study of reaction (3-1) was usually carried out at low carbon concentration since at one atmosphere total pressure for carbon concentration above 1w/o the CO_2/CO ratio must be less than 10^{-3}, and gas mixtures which were so dilute

in CO_2 could have caused a large error (section 3-2.5). Richardson and Dennis(49) did not operate with CO_2/CO less than 10^{-3}, however Ban-Ya and Matoba(51) used ratios as low as 2.5×10^{-4} and claimed that they avoided any serious error. Their work covered the carbon range up to 2 w/o carbon. The earliest work, by Marshall and Chipman(48), used high pressure in order to obtain high carbon potential while maintaining relatively high CO_2/CO ratios. In their furnace the maximum design pressure was 20 atmospheres and they were able to carry out the measurements up to 2.5 w/o carbon at 1550°C.

Turkdogan et al(54) studied the reaction (3-2) which is suitable for high carbon concentration. They were not able to work at low carbon since at one atmosphere CH_4/H_2 must be less than 10^{-4}. Their work was limited to low temperature (1300 - 1500°C) in order to avoid side reactions.

3-2.3 Oxygen in molten iron

In measuring the activity of dissolved oxygen as a function of composition in Fe-O alloys, the oxygen potential in the gas phase was established using either $CO-CO_2$ (45, 48, 51, 52)

$$CO + O(\text{in iron}) \rightleftharpoons CO_2 \qquad (3\text{-}3)$$

$$K_3 = P_{CO_2}/P_{CO}\ a_O \qquad (3\text{-}3a)$$

or H_2 - H_2O gas mixtures (55-59)

$$H_2 + O(\text{iron}) \rightleftharpoons H_2O \qquad (3\text{-}4)$$

$$K_4 = P_{H_2O}/P_{H_2}\, a_O \qquad (3\text{-}4a)$$

The thermodynamic data of the various workers were not in agreement. However, for the dissolved oxygen concentration in the binary system at low oxygen potential at 1550°C, all the values lie within 30ppm. at a total oxygen in the 300ppm. region. This shows that the actual results are in rough agreement, bearing in mind the difficulties in measuring dissolved oxygen, but the scatter can lead to widely different values of thermodynamic properties.

3-2.4 Carbon-oxygen in molten iron

The carbon-oxygen equilibrium in molten iron may be represented as:

$$C(\text{in iron}) + O(\text{in iron}) \rightleftharpoons CO \qquad (3\text{-}5)$$

$$K_5 = P_{CO}/a_O\, a_C \qquad (3\text{-}5a)$$

The equilibrium constant for this reaction was obtained by combining the data either from (47, 48, 51, 53, 60, 61, 62) reaction (3-1) and (3-3) or reaction (3-1) and (3-5) combined with thermodynamic data of the water gas reaction (61).

$$H_2 + CO_2 \rightleftharpoons H_2O + CO \qquad (3\text{-}6)$$

$$K_6 = P_{H_2O} P_{CO} / P_{H_2} P_{CO_2} \qquad (3\text{-}6a)$$

At one atmosphere total pressure of CO and in very dilute solution equation (3-5a) can be used to predict

$$\text{w/o (C) x w/o (O)} = \text{constant} = m \qquad (3\text{-}7)$$

In spite of controversy in the measurement of m at high carbon, the agreement was remarkable between all workers at carbon concentrations below 0.2 w/o carbon, the value of m at 1600°C being between 0.002 and 0.0025.

No reliable measurements of the interaction between oxygen and carbon have been reported, because of sources of experimental error discussed in section (3-2.5).

3-2.5 Discussion of the main sources of error

Whenever measurements of a quantity must be made, there is some degree of uncertainty concerning its true value. The degree of uncertainty varies with the refinement of the technique used, the care taken, and the inherent experimental difficulties. The experimental difficulties have been the reason for the controversy in the measurement of the equilibrium data of carbon and oxygen in binary and ternay alloys with molten iron. The extent of the errors depends primarily on the experimental technique used in these studies. The sources of error may be attributed to the following:

1) Reacting gas mixture

Any removal or addition of a component in a gas mixture used to fix the potential of a component in the liquid will cause an error. This will be particularly serious if the gas phase is dilute in the component which is added or removed e.g. CO_2 in CO at high carbon potentials in molten iron. The following factors are of importance.

a) Impurities in the gas mixture:

This factor has been emphasised by Chipman (63)as a major source of error in the measurement of carbon activities.

b) Stability of the gas mixture at high temperatures:

With very low CO_2 content there is an increased chance of carbon deposition on hot surfaces as the gas enters the hot zone by the reaction

$$2\ CO \rightleftharpoons C_{(gr)} + CO_2 \qquad (3\text{-}8)$$

also at high temperatures loss of methane by formation of C_2H_2 becomes probable since it becomes stable with respect to CH_4 (63).

c) Side reactions:

The side reaction between the oxide crucible and carbon in the melt in the range of low oxygen potential leads to the evolution of CO. This error was fatal when MgO crucibles were used. However this effect was also observed with recrystallised Al_2O_3 crucibles (64).

d) Errors in controlling a constant gas composition and in analysis of very dilute gas mixtures.

2) Thermal diffusion

Thermal diffusion occurs in any system where there are temperature gradients, and leads to a different gas composition at the surface of the melt, than that of the bulk gas. This effect is appreciable for H_2-H_2O gas mixtures and to a lesser extent in CO-CO_2 mixtures.

3) Melt contamination

This may tend to change the actual concentration of the studied components and their activity. The major sources of contamination are the dissolution of the crucible into the melt, and the graphite(61)used in preparing Fe-C alloys.

4) Temperature measurement and temperature fluctuations.

5) Errors in analysis arising from imperfect sampling of inhomogeneous melts after solidification.

6) Accuracy limits of carbon and oxygen analyses.

3-3 Experimental technique

One gram specimens of both specpure iron and the specially prepared iron/4.5% carbon alloy were levitated in $CO-CO_2$ gas mixtures at different pressures ranging from 5 to 70 atmospheres at temperatures of 1550, 1650, and 1750°C for sufficient time to attain the equilibrium.

Quenching was carried out using the following technique in order to minimise any possibility of carbon deposition on the cooling specimen. Quenching the specimen was carried out at the operating pressure in a brass mould and was accompanied by automatic switching off of the high frequency power. When the power was shut off the following events occurred almost instantaneously. The pressure was reduced to atmospheric and helium then flowed through the apparatus through the check value.

Estimation of the carbon concentration in section (2-3.5) was used as a check of the accuracy of carbon analysis by the combustion method.

3-3.1 Deoxidation

In order to obtain accurate results in the equilibrium studies, CO evolution during solidification was eliminated by deoxidizing the specimen just before quenching. For a levitated one gram drop the amount of deoxidizer to be added will be in the order of milligrams. This was acheived by using 0.25mm wires with different lengths.

Deoxidation was carried out by introducing the deoxidizing wire, mounted vertically on a silica platform, into the levitated drop. The wire was sucked into the molten metal by the surface tension force. This technique had advantages that the specimen did not touch the platform and any required amount of the deoxidant could be added.

A large number of deoxidizers are used in steelmaking and the relevant equilibrium data have been established. Aluminium was selected for use in this work. It gave a sound specimen with no sign of CO evolution after quenching and which was therefore suitable for carbon analysis.

3-3.2 Oxygen analysis

The use of one gram specimens made it possible to analyse the whole specimen in order to avoid the problem of segregation during solidification. The analyses was carried out by the vacuum fusion method at Henry Wiggin Company Limited, Hereford.

3-4 Experimental aspects of this work

Levitation melting at high pressure provided an appropriate technique for the study of the equilibrium between the molten Fe-C-O system and $CO-CO_2$ gas mixtures. Lack of agreement between the results of previous workers relates to the experimental difficulties inherent in the conventional crucible technique at atmospheric pressure. In the following paragraphs the advantages and disadvantages of the new technique are given in order to assess the accuracy of the resulting measurements.

3-4.1 Use of high pressure

From the reactions (3-1), the activity of carbon is defined by (3-1a) and it follows that the activity of carbon for a particular CO/CO_2 ratio is proprotional to the total pressure. The use of pressures up to 70 atmospheres allows the use of relatively high CO_2 contents in $CO-CO_2$ mixtures ($CO_2/CO > 7 \times 10^{-2}$) while achieving sufficiently high carbon potentials to study alloys containing up to 4.6 w/o carbon at 1550°C.

Since the oxygen potential in the gas phase is independent of the total pressure used (equation (3-3)), it was possible, by using any one gas mixture, to keep the oxygen potential constant while varying the carbon potential. This made the study of the interaction between carbon and oxygen in molten iron well defined.

3-4.2 Carbon deposition

In the levitation technique errors due to thermal cracking of CO on the hot parts of the apparatus are almost certainly completely eliminated. The only hot parts of the apparatus with which the gas comes into contact are the walls of the alumina tube immediately adjacent to the drop, since both above and below the drop the tube walls are cold. No carbon deposition was observed and even if it did occur it is unlikely that the resulting extra CO_2 would have been able to diffuse across to the levitated drop. Another possible site for cracking was on iron droplets

produced by an enhanced vaporization mechanism. Since enhanced vaporization was a very slow process at high pressure, this effect cannot have been large. The relatively high CO_2 contents used also tend to lessen the effect of any tiny amount of CO cracking.

Some carbon deposition was observed at the outlet gas filter where carbon was able to deposit on the filter medium from the warm gas which has passed over the levitated drop. For this reason continuous flow of fresh gas from the cylinder was used to prevent any error due to change of the gas composition during equilibration.

3-4.3 Thermal diffusion

Thermal diffusion in the gas phase was inevitable in this work. The measurements of thermal diffusion in $CO-CO_2$ gas mixtures (chapter 2) allowed the calculation of the CO/CO_2 ratio at the surface of the drop. The accuracy of the measured thermal diffusion ratio was $\pm$ 50%. This lead to a relative error in the calculated CO/CO_2 ratio of 0.5% for a 1% CO_2 gas mixture, the error increased to 4% for the 8% CO_2 gas mixture.

3-4.4 Deoxidation of the specimen

Specimens containing carbon above 1.7 w/o showed no carbon monoxide evolution on solidifcation using 1.1% CO_2 and 2.15% CO_2 gas mixtures up to 1650°C. Specimens at 1750°C showed no CO evolution at carbon concentration above 2 w/o.

CO evolution on solidification was observed in all other cases and deoxidation of the specimens with aluminium wire was carried out to prevent any error due to losing carbon and oxygen as CO. The mixing time before quenching was about 20 seconds (this was the minimum time in which it was possible to bring down the deoxidizing platform to the turn table and introduce the quenching moulds under the specimen).

The effect of 0.05 w/o aluminium, which was generally added, on the activity of carbon is negligibly small(46), and the short time of mixing was not enough to establish the new equilibrium.

The deoxidation technique was therefore quite satisfactory in enabling accurate carbon concentration to be measured while establishing the iron-carbon equilibrium.

In the case of oxygen the scatter of the results after deoxidation, was quite large. Two major sources of error caused this scatter:

a) Uneven amounts of oxide on the wire.
b) Oxygen absorption by the specimen, during the mixing period.

The first source of error listed was fatal since it lead to a large error - the amount of oxygen on the wire being comparable with that in the drops.

The blank was measured by adding aluminium wires to spec-pure iron drops levitated in hydrogen. The results were given in table (3-1)and showed a variable blank around 100ppm.

The second source of errors due to effect of Al on oxygen activity (66) was examined by measuring the oxygen in quenched and deoxidized specimens containing carbon above 2 w/o. Table (3-2) showed a difference around 190ppm. This makes aluminium wire unsuitable as a deoxidant where oxygen analyses were required for oxygen equilibrium study. However, in the experiments in which the specimens were deoxidized the oxygen blank was taken to be 150ppm.

Run No	wt of spec-pure iron	wt of Aluminium	measured oxygen ppm
B5	0.900	0.0016	94
B6	0.892	0.0016	130

Table (3-1)

Measurements of oxygen blank

Run No	Gas mixture	pressure atm.	oxygen ppm.	Notes
ECO 51	CO-1.9%CO_2	65.8	81	quinched at high pressure with no CO evolution during solidification. Deoxidized with 0.001 gm. Al wire in 0.937 gram drop.
ECO 52		65.3	270	
Oxygen difference = 189 ppm				

Table (3-2)

Effect of dissolved Aluminium

on Oxygen measurements in oxydizing atmosphere

3-4.5 Approach to the equilibrium

The equilibrium carbon was established from two different paths of carbon reactions with $CO-CO_2$ gas mixture (carburization and decarburization). The equilibrium was attained much faster for levitated molten drops than for a metal bath in a crucible because of the small quantity of metal involved, the high surface to volume ratio, and the rapid rates of mass transport in the gas and liquid phases. The levitated specimens reached 99.9% of the equilibrium carbon content within minutes (see kinetic studies in chapter 4). This is to be compared with the times to equilibrium of several hours reported by e.g. Richardson and Dennis (49). The initial concentrations were zero and about 4.5 w/o carbon. The agreement between runs with either alloy was perfect, being within the limits of accuracy of chemical analysis (0.02 w/o C).

Oxygen equilibrium was obtained from carburization and decarburization runs. Fig. (3-1) shows the results for approach to equilibrium from both alloys using 1.9% CO at 65 atmospheres. The equilibrium was approached from both sides and the agreement between the equilibrium oxygen was $\pm$ 2ppm (vacuum fusion analysis limits of error at that concentration).

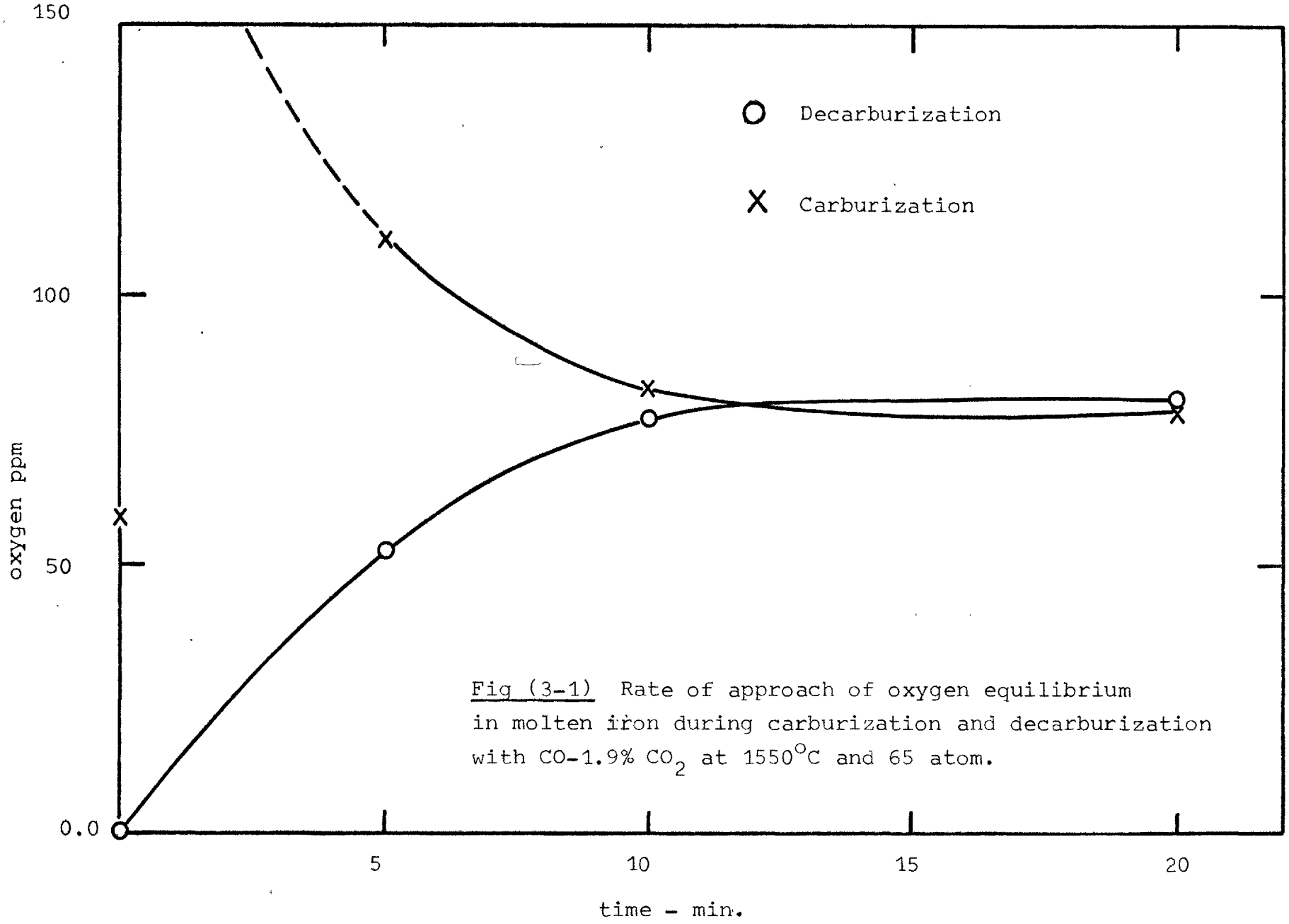

Fig (3-1) Rate of approach of oxygen equilibrium in molten iron during carburization and decarburization with CO-1.9% CO_2 at 1550°C and 65 atom.

3-5 Results

The equilibria for carbon and oxygen in molten iron were determined at 1550, 1650 and 1750°C for the values of oxygen potentials ($RT \ln(x_{CO_2}/x_{CO})$) characterised by the gas mixtures containing 1.1%, 1.9%. 2.15% and 4.58% CO_2 in CO and for carbon potentials ($RT \ln(P_t(x_{CO})^2/x_{CO_2})$) in 1.1%, 2.15%, 4.58% and 8.28% CO_2 in CO gas mixture at pressures ranging from 5 to 70 atmosphere. The experimental results, excluding undeoxidized runs at low carbons and the preliminary runs,are tabulated in Tables (3-3) and (3-4). Table (3-3) gives the results of equilibrium carbon, and they are classified according to the temperature. The oxygen equilibrium results in Table (3-4) are classified according to the gas mixture. The values of corrected gas mixture composition at the surface of the drop due to thermal diffusion are also given.

3-5.1 Carbon results

The relationship between $(P_t(x_{CO})^2/x_{CO_2})$ and the equilibrium carbon expressed in weight per-cent at 1550, 1640, and 1750°C are plotted in fig. (3-2). The measurements covered a wider range (up to 4.5 w/o carbon)* than any other previous work. Nearly the same carbon "potentials" were obtained using different gas compositions and pressures and these gave nearly the same carbon concentration.

*The measurements of equilibrium carbon for thermal diffusion measurements are also included.

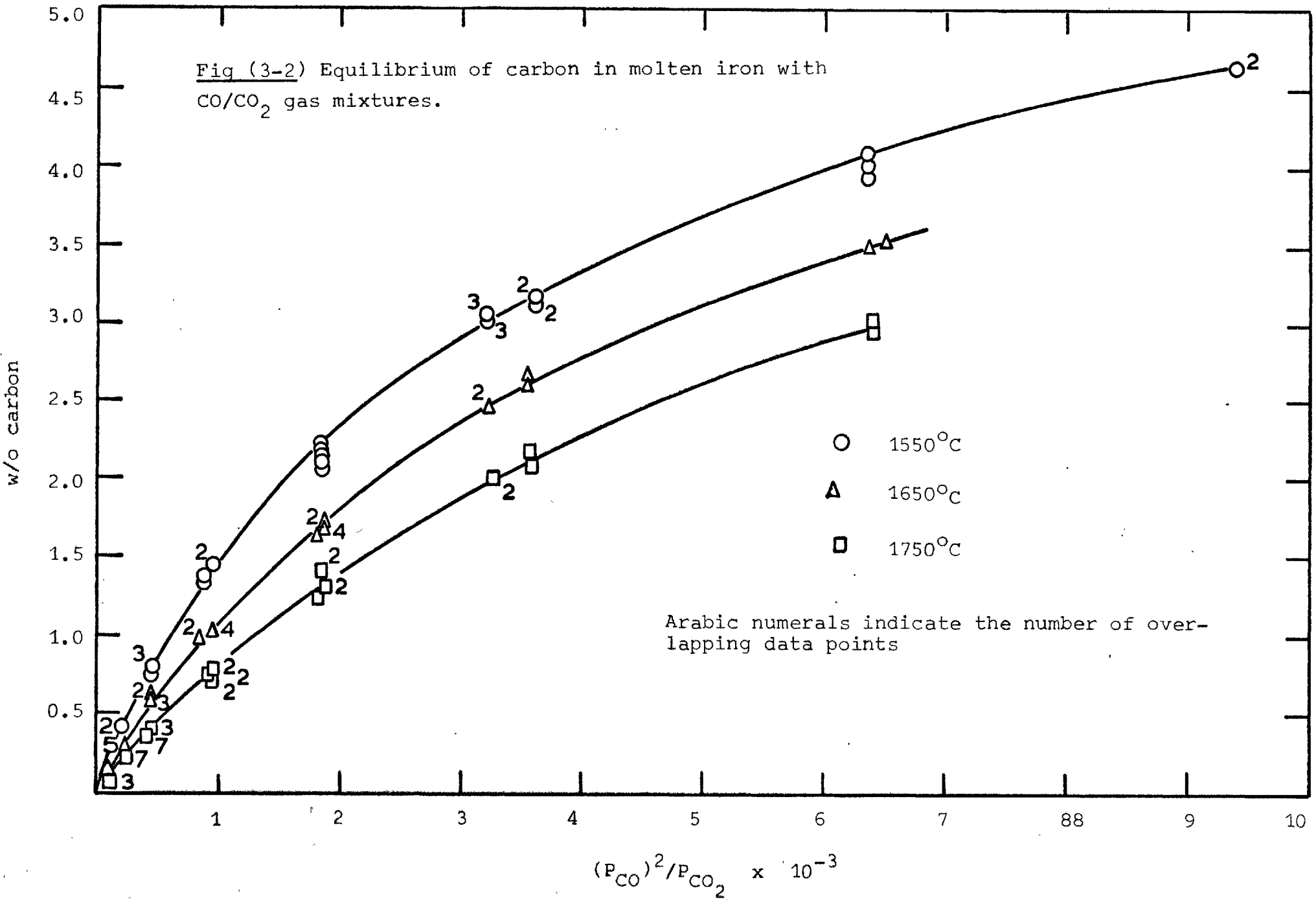
Fig (3-2) Equilibrium of carbon in molten iron with CO/CO2 gas mixtures.
w/o carbon
5.0
4.5
4.0
3.5
3.0
2.5
2.0
1.5
1.0
0.5
1
2
3
4
5
6
7
88
9
10
(PCO)2/PCO2 x 10-3
1550°C
1650°C
1750°C
Arabic numerals indicate the number of overlapping data points

Run number ECO	$CO-CO_2$ mixture	CO_2 Vol %	Pressure	Carbon w/o
1550°C				
ECO 63	CO-1.1% CO_2	1.061	69.716	3.963
64	"	"	69.716	4.024
65	"	"	69.404	4.084
79	"	"	39.308	3.182
80	"	"	39.032	3.154
81	"	"	39.117	3.186
114	"	"	20.20	2.146
115	"	"	20.10	2.041
183	"	"	20.30	2.201
184	"	"	20.50	2.225
87	CO-2.15% CO_2	2.07	69.94	3.095
88	"	"	69.99	3.044
90	"	"	70.21	3.023
104	"	"	39.18	2.248
106	"	"	39.25	2.268
133	"	"	20.15	1.443
134	"	"	20.05	1.441
136	CO-4.58 % CO_2	4.035	40.35	1.351
139	"	"	40.35	1.322
140	"	"	20.10	0.765
143	"	"	20.00	0.730
156	CO-8.21 % CO_2	7.98	40.20	0.814
158	"	"	40.20	0.796
159	"	"	40.35	0.816
209	"	"	19.55	0.427
210	"	"	19.55	0.439
1650°C				
ECO 68	CO-1.1% CO_2	1.060	70.64	3.547
69	"	"	69.695	3.532
77	"	"	38.926	2.631
78	"	"	39.116	2.687
111	"	"	20.30	1.676
112	"	"	20.30	1.660
179	"	"	20.60	1.656
180	"	"	20.40	1.714
187	"	"	10.05	1.025
188	"	"	10.20	1.044
192	"	"	5.00	0.565
193	"	"	5.12	0.569
92	CO-2.15% CO_2	2.074	69.94	2.464
94	"	"	70.05	2.456
99	"	"	39.117	1.679
101	"	"	39.17	1.678
175	"	"	40.15	1.731
128	"	"	20.20	1.040
129	"	"	20.15	1.046

Table (3-3)

Experimental results of $CO-CO_2$ equilibrium with carbon

Run number ECO	$CO-CO_2$ mixture	CO_2 Vol %	Pressure	Carbon w/o
ECO194	$CO-2.15\%\ CO_2$	2.074	10.10	0.544
195	"	"	10.10	0.558
227	"	"	5.0	0.259
228	"	"	5.0	0.290
147	$CO-4.58\%\ CO_2$	4.431	40.00	0.972
149	"	"	40.10	0.976
153	"	"	19.95	0.585
155	"	"	20.00	0.541
204	"	"	10.15	0.307
206	"	"	10.20	0.298
225	"	"	5.00	0.159
160	$CO-8.71\%\ CO_2$	"	40.30	0.571
161	"	"	40.30	0.592
164	"	"	40.30	0.562
165	"	"	40.4	0.540
166	"	"	40.35	0.554
211	"	"	19.55	0.325
213	"	"	19.55	0.300
220	"	"	10.06	0.145
221	"	"	10.08	0.154
$1750^{\circ}C$				
ECO 72	$CO-1.1\%\ CO_2$	1.059	69.83	3.023
73	"	"	70.37	2.953
83	"	"	39.11	2.186
86	"	"	39.18	2.11
119	"	"	20.10	1.246
181	"	"	20.45	1.327
182	"	"	20.50	1.352
185	"	"	10.00	0.765
186	"	"	10.00	0.77
189	"	"	10.10	0.72
190	"	"	5.2	0.428
191	"	"	5.2	0.420
96	$CO-2.15\%\ CO_2$	2.072	70.59	1.999
97	"	"	70.21	2.019
107	"	"	39.38	1.38
109	"	"	39.39	1.418
124	"	"	20.25	0.809
196	"	"	10.18	0.440
197	"	"	10.20	0.405
198	"	"	3.30	0.246
199	"	"	3.27	0.248
200	$CO-4.48\%\ CO_2$	4.426	42.29	0.803
201	"	"	42.21	0.724
202	"	"	19.50	0.412

Table (3-3)
(continued)

Run number ECO	$CO-CO_2$ mixture	CO_2 Vol %	Pressure	Carbon w/o
ECO203	CO-4.48% CO_2	4.426	19.50	0.387
207	"	"	10.05	0.233
208	"	"	10.07	0.234
222	"	"	5.00	0.117
223	"	"	5.00	0.099
117	CO-8.21% CO_2	7.964	40.25	0.471
168	"	"	40.20	0.436
170	"	"	40.30	0.476
171	"	"	40.30	0.417
214	"	"	19.53	0.216
215	"	"	19.50	0.225
219	"	"	10.00	0.105

Table (3-3)
(continued)

Run No.	Starting material	Pressure atm.	temp °C	Estimated carbon w/o	measured oxygen ppm	oxygen in Binary Fe-O system ppm.
CO-1.1% CO_2						
ECO 64	iron	69.716	1550	4.10	43	80-100
65	Fe-C	69.716	"	4.00	62	"
79	iron	39.30	"	3.15	54	"
82	Fe-C	39.10	"	3.14	58	"
113	iron	20.20	"	2.20	77	"
116	Fe-C	20.20	"	2.20	98	"
68	iron	70.64	1650	3.53	74	150-185
70	Fe-C	70.42	"	3.52	94	"
75	"	39.074	"	2.63	100	"
76	iron	38.99	"	2.63	85	"
178	"	40.00	"	2.66	91	"
117	Fe-C	20.20	"	1.72	140	"
118	iron	20.20	"	1.72	130	"
71	iron	70.64	1750	3.00	140	260-330
74	Fe-C	70.37	"	3.02	150	"
84	iron	39.13	"	2.13	150	"
85	Fe-C	39.18	"	2.13	150	"
CO-1.9% CO_2						
ECO 51	iron	66.35	1550	3.15	81	150-190
58	Fe-C	63.16	"	3.05	78	"

Table (3-4)

Results of oxygen equilibrium in ternary Fe-C-O system

Run No.	Starting material	Pressure atm.	temp °C	Estimated carbon w/o	measured oxygen ppm	oxygen in Binary Fe-O system ppm.
CO-2.15% CO_2						
ECO 87	iron	69.94	1550	3.00	100	170-210
89	Fe-C	70.20	"	3.01	110	"
103	iron	39.16	"	2.21	120	"
105	Fe-C	39.22	"	2.21	150	"
172	iron	40.00	"	2.23	110	"
91	iron	70.53	1650	2.50	200	300-380
93	Fe-C	69.9	"	2.48	190	"
100	"	39.17	"	1.68	220	"
102	iron	39.17	"	1.68	210	"
173	"	40.05	"	1.71	210	"
175	"	40.10	"	1.72	210	"
95	iron	70.69	1750	2.02	340	530-670
98	Fe-C	69.6	1750	1.97	350	"
Results of deoxidized specimen with Aluminium wire, Oxygen blank was taken 150 ppm.						
CO-1.1% CO_2						
ECO 121	iron	20.30	1750	1.37	240	260-330
122	Fe-C	20.30	"	1.37	270	"
CO-2.15% CO_2						
ECO 132	iron	20.30	1550	1.46	210	170-210
135	Fe-C	20.30	"	1.46	260	"
127	iron	20.20	1650	1.05	160	390-380
130	Fe-C	20.10	"	1.05	300	"

Table (3-4) continued

Run No.	Starting material	Pressure atm.	temp °C	Estimated carbon w/o	measured oxygen ppm	oxygen in Binary Fe-O system ppm.
ECO 108	iron	39.30	1750	1.35	520	530-670
110	Fe-C	39.30	"	1.35	540	"
123	iron	20.25	"	0.80	520	"
126	Fe-C	20.20	"	0.80	480	"
CO-4.85% CO_2						
ECO 137	Fe-C	40.35	1550	1.35	290	350-440
138	iron	40.35	"	1.35	390	"
142	Fe-C	20.00	"	0.78	400	"
144	iron	20.00	"	0.78	390	"
145	iron	40.00	1650	0.95	690	620-800
148	Fe-C	40.05	"	0.95	700	"
152	iron	20.00	"	0.54	570	"
154	Fe-C	20.00	"	0.54	400	"

Table (3-4) continued

To allow for the small differences in carbon "potential" the carbon percentage read from the best fitting curve at each carbon "potential" was compared with the measured carbon percentage. The difference is given in the last column of table (3-5) and shows that the same carbon potential gave the same carbon percentage within $\pm$ 0.05 w/o. This proves the accuracy and consistency of these measurements.

At the high oxygen potentials used there was no effect of oxygen on the activity of carbon at carbon concentrations greater than 0.4 w/o, as shown in table (3-5) at the extreme cases of high oxygen contents (1650°C and 1750°C). There was not enough data to confirm this conclusion at lower carbon. The results as a whole are markedly consistent.

The best fitting curves, drawn through the data by eye, were expressed as polynomials for convenience in calculations (w/o C) at any value of Z. The weight percent of carbon was expressed as a simple power series expansion in terms of Z (P^2_{CO}/P_{CO_2}) by:

$$\text{w/o (C)} = a_1 Z + a_2 Z^2 + a_3 Z^3 \qquad (3\text{-}9)$$

The degree of the best polynomial was found to vary from one temperature to another and the coefficients a of the power series are given below in Table (3-6). The standard deviation (σ) is also given in each case. As emphasised by Bale and Pelton (66) extrapolation of the results through the polynomial beyond its assigned limits leads to error.

Run No	Gas mixture	$(P_{CO})^2/P_{CO_2}$	carbon w/o	
			measured	Deviation from best fitting curve
1650°C				
ECO 192	CO-1.1% CO_2	456.52	0.565	+0.003
193	"	467.48	0.569	-0.005
194	CO-2.15% CO_2	465.93	0.544	-0.030
195	"	465.93	0.558	-0.016
153	CO-4.58% CO_2	410.39	0.585	+0.074
155	"	411.42	0.541	+0.030
160	CO-8.21% CO_2	427.23	0.571	+0.040
161	"	427.23	0.592	+0.061
164	"	427.23	0.562	+0.031
165	"	428.29	0.540	+0.009
166	"	427.7	0.554	+0.023
1750°C				
ECO 190	CO-1.1% CO_2	475.32	0.428	0.000
191	"	475.32	0.421	-0.007
196	CO-2.15% CO_2	470.1	0.44	+0.014
197	"	471.0	0.405	-0.021
202	CO-4.58% CO_2	401.5	0.411	+0.046
203	"	401.5	0.387	+0.022
117	CO-8.21% CO_2	427.68	0.471	+0.070
168	"	427.68	0.476	+0.075
170	"	426.62	0.437	+0.036
171	"	427.68	0.417	+0.016

Table (3-5)

Comparison of Carbon measurements at constant $(P_{CO})^2/P_{CO_2}$

Temperature / Coefficients	1550°C $\sigma = 3.122 \times 10^{-4}$	1650°C $\sigma = 2.606 \times 10^{-5}$	1750°C $\sigma = 122 \times 10^{-5}$
a_1	2.13589×10^{-3}	1.52192×10^{-3}	9.8621×10^{-4}
a_2	-9.15873×10^{-7}	-7.24998×10^{-7}	-1.84329×10^{-7}
a_3	3.27978×10^{-10}	3.8392×10^{-10}	2.75343×10^{-11}
a_4	-7.53717×10^{-14}	-1.27427×10^{-13}	-2.22971×10^{-15}
a_5	1.00315×10^{-17}	2.3762×10^{-17}	7.0598×10^{-20}
a_6	-7.00057×10^{-22}	-2.30585×10^{-21}	0
a_7	1.97724×10^{-26}	9.08171×10^{-26}	0

Table (3-6)

Coefficients of best fitting curves

at 1550, 1650, and 1750°C

3-5.2 Oxygen results

The reproducibility of the equilibrium oxygen concentration at high carbon concentration (no CO evolution during solidification) was within ± 10ppm at concentrations up to 300ppm. The measured equilibrium oxygen concentration using the using the iron-4.5% carbon alloys were generally 10-20ppm higher than those obtained using spec-pure iron. This may be related to the impurities of the graphite which was used in the preparation of these alloys (see table 1-1). The results with spec-pure iron may be more accurate than with iron-4.5 w/o carbon, since the effect of small quantities of impurities is likely to lead to an increased oxygen content.

The reliable results at high carbon showed that for fixed oxygen potential the oxygen decreased by increasing the carbon in molten iron. In order to check the consistency of these results the equilibrium oxygen for the binary Fe-O system (at zero carbon) was calculated for each oxygen potential from the available thermodynamic data of the other workers. Since their data showed significant differences, calculations were carried out at the higher and lower values of equilibrium constant of oxygen in molten iron, and are shown in table (3-4).

The oxygen concentrations in the binary Fe-O system, at the same oxygen-potential and temperature, are higher than those measured at high carbon. The oxygen contents

increase towards the values in the binary as carbon decreases. Deoxidized specimens at low carbon were corrected for the blank (section 3-4.4) and gave oxygen concentrations within the range reported for the binary, table (3-4). This confirmed the accuracy and consistency of these measurements which show that carbon decreases the oxygen concentration in molten iron at constant oxygen potential.

The product of the equilibrium carbon and oxygen relative to one atmosphere pressure was decreased by increasing carbon, fig. (3-3), and approached the value of 0.002 at very low carbon. This observation is in agreement with laboratory and industrial results at low carbon. The experimental error prevented the evaluation of the effect of temperature on carbon-oxygen product at high carbon. The reaction is weakly exothermic and hence the dependence of the equilibrium constant on temperature is small.

3-6 Evaluation of the thermodynamic data

The equilibrium data were expressed first for infinitely dilute solution as standard state with concentration expressed in weight percent. These data were transferred to other standard states when it was found to be useful.

3-6.1 Equilibrium of $CO-CO_2$ gas mixtures with carbon in molten iron

The equilibrium constant of reaction (3-1) is given by equation (3-1a)

$$C(\text{in iron}) + CO_2 \rightleftharpoons 2CO \qquad (3\text{-}1)$$

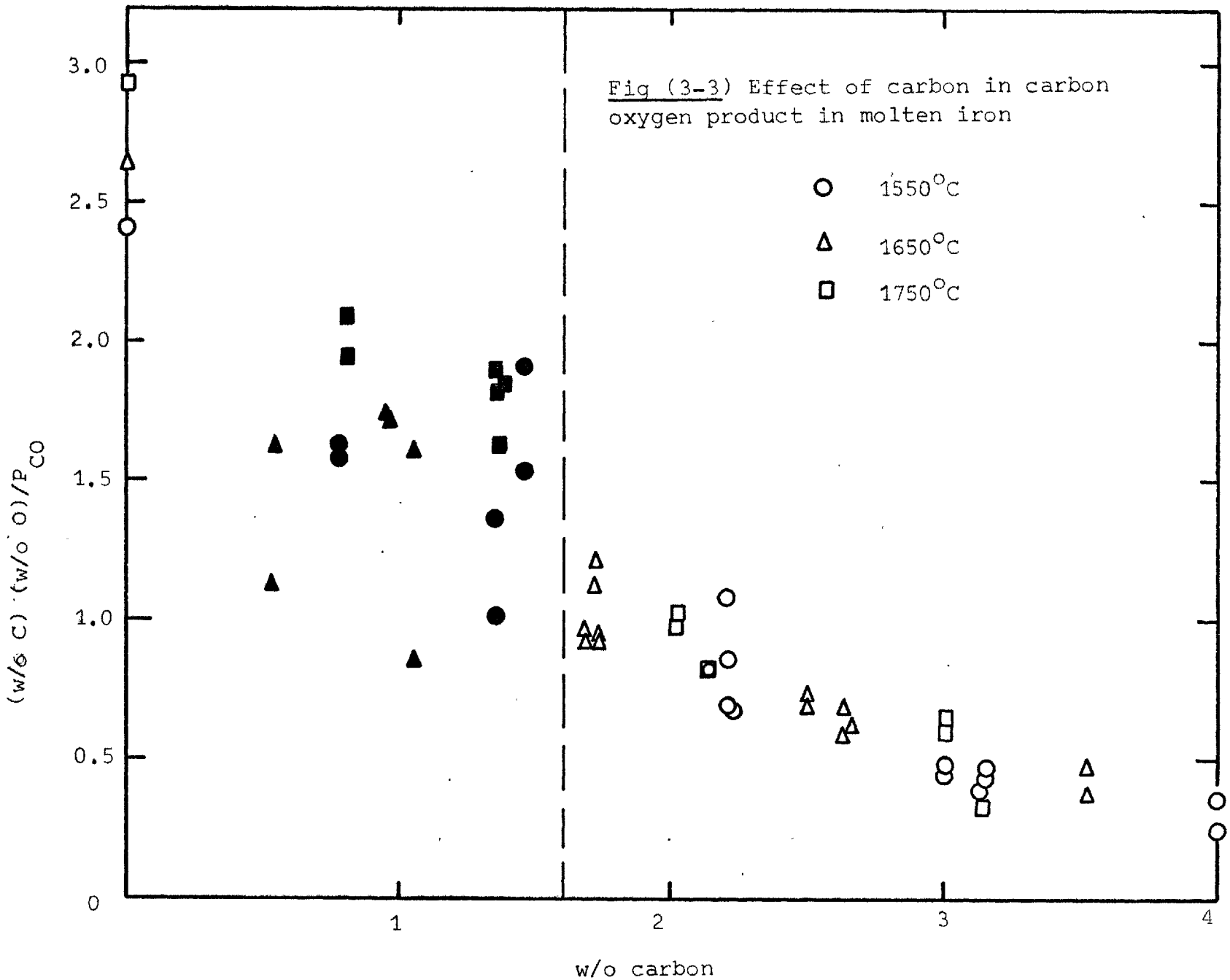

Fig (3-3) Effect of carbon in carbon oxygen product in molten iron

$$K_{1\ (w/o)} = P_t\ (x_{CO})^2/x_{CO_2}\ a_C \qquad (3\text{-}1a)$$

with a_C defined by $a_C/(w/oC) = 1$ at $(w/oC) = 0$ where the activity at any concentration is expressed in the usual form

$$a_C = f_C\ (w/oC) \qquad (3\text{-}10)$$

The apparent equilibrium constant $K'_{1(w/o)}$ is defined by

$$K'_{1\ (w/o)} = P_t\ (x_{CO})^2/x_{CO_2}\ (w/oC) \qquad (3\text{-}11)$$

The data were plotted in the usual form of log $K'_{1(w/o)}$ against (w/oC) at 1550, 1650 and 1750°C in fig. (3-4).

The logarithm of K' showed a non-linear variation with carbon above 3.0 w/o within the experimental error, and is consistent with the approach toward the graphite solubility in liquid iron. The non-linearity is pronouced at 1550°C since the data cover a wide range of carbon. The data below 3.0 w/o were analysed by the method of least mean square to obtain the best line for the linear variation of log $K'_{1(w/o)}$ with (w/oC). The resulting equations are:

$$\text{Log } K'_{1(w/o)(1550^oC)} = 2.62(\pm 0.0068) + 0.135(\pm 0.0039)(w/oC) \qquad (3\text{-}12)$$

$$\text{Log } K'_{1(w/o)(1650^oC)} = 2.83(\pm 0.0070) + 0.116(\pm 0.0046)(w/oC) \qquad (3\text{-}13)$$

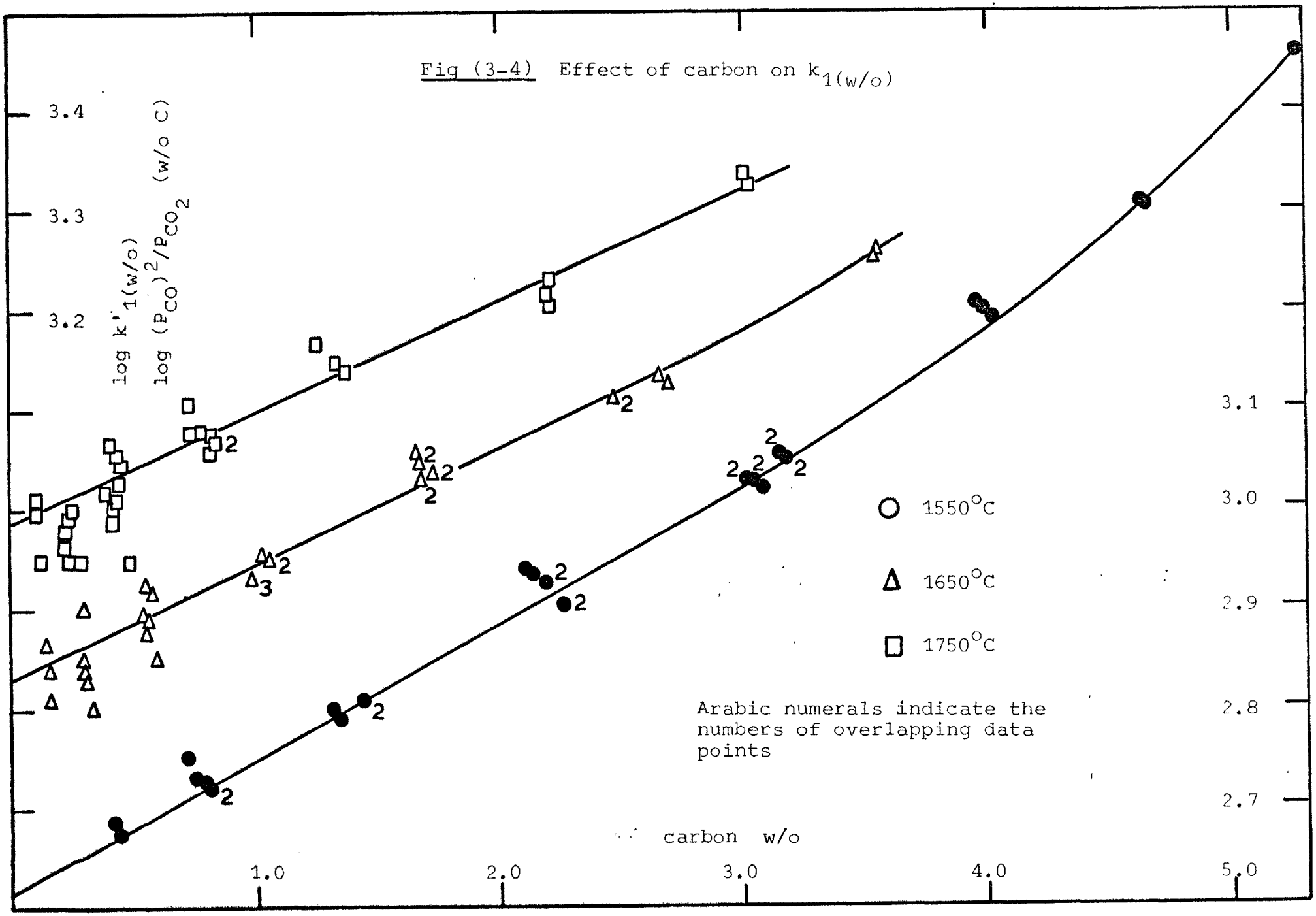
Fig (3-4) Effect of carbon on $k_{1(w/o)}$
log $k'_{1(w/o)}$ / log $(P_{CO})^2/P_{CO_2}$ (w/o C)
3.4
3.3
3.2
3.1
3.0
2.9
2.8
2.7
1550°C
1650°C
1750°C
Arabic numerals indicate the numbers of overlapping data points
carbon w/o
1.0
2.0
3.0
4.0
5.0

$$\text{Log } K'_{1(w/o)\ (1750^{o}C)} = 2.99(\pm 0.0080) + 0.110\ (\pm 0.0068)(w/oC) \quad (3\text{-}14)$$

The probable error given in brackets was due mainly to magnification of the error in the measured carbon since the plot involves (w/oC) on one axis and 1/(w/oC) on the other axis and is therefore sensitive to any small error in carbon below 1 w/o. The error limits quoted in the equations (3-12), (3-13) and (3-14) are therefore well above the error limits ascribed to the raw data and summarized in table (3-5). However the high error limits are taken in the subsequent derivation of thermodynamic quantities from the equations

The first terms on the right hand side of the equations are the logarithms of the true equilibrium constants of reaction (3-1). The variation of the equilibrium constant with temperature.

$$\frac{\delta \log K_{1(w/o)}}{\delta(1/T)} = \frac{\Delta H^{o}}{2.3\,R} \quad (3\text{-}15)$$

was obtained over the temperature range studied using the usual plot of $\log K_{1(w/o)}$ against 1/T, fig. (3-5). The straight line path through the accuracy limits of $\log K_{1(w/o)}$ was obtained using the method of least mean squares as:

$$\log K_{1(w/o)} = -6836\ (\pm 187)/T + 6.37\ (\pm 0.097) \quad (3\text{-}16)$$

$$\Delta F^{o}_{1(w/o)} = 31275\ (\pm 855) - 28.14\ (\pm 0.44)\ T \quad (3\text{-}17)$$

The second term on the right hand side of the equation is $\log f_{c}$. The logarithm of the activity coefficient shows

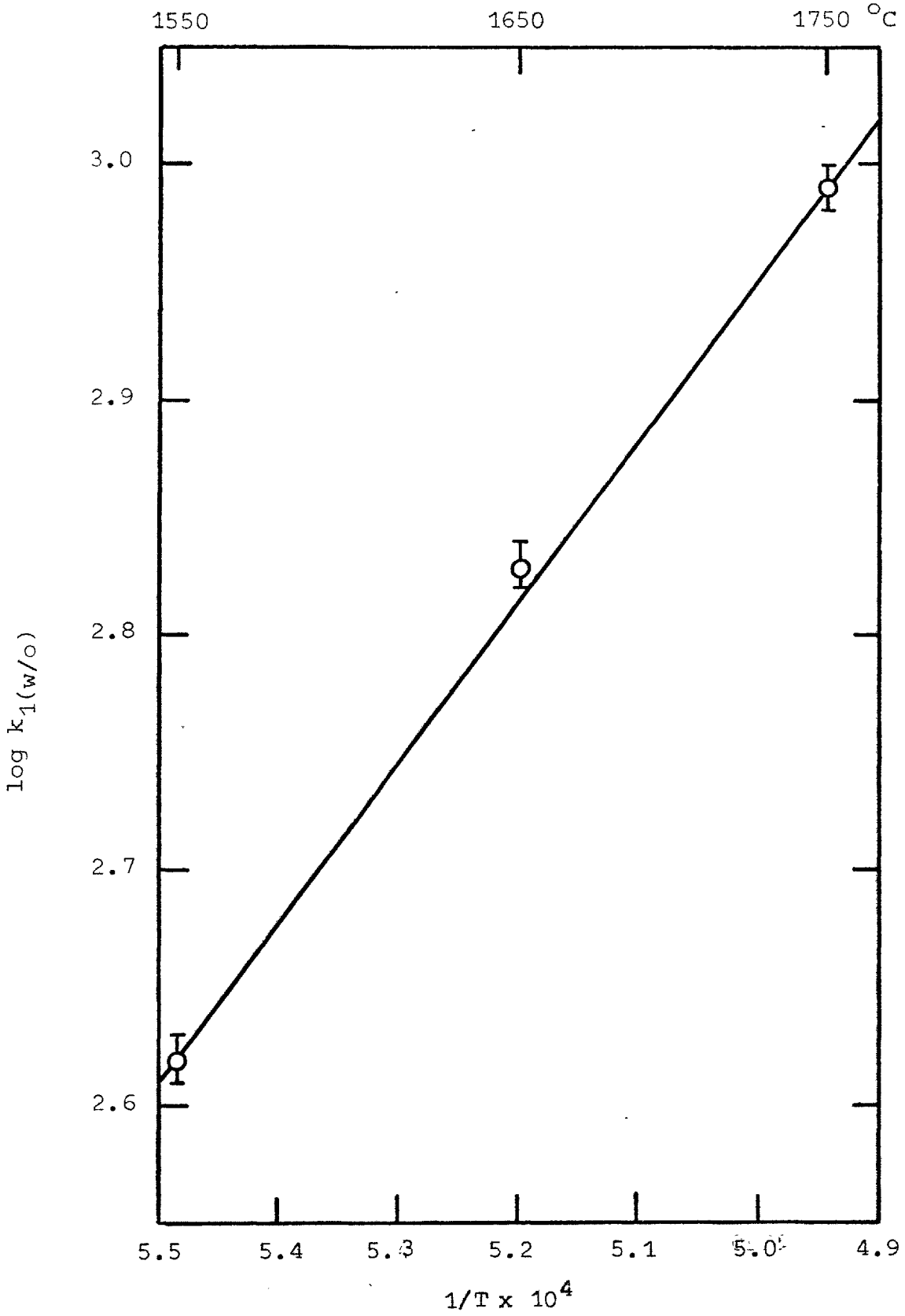

Fig (3-5)

Variation of $k_{1/w/o)}$ with temperature

a decrease with increasing temperature as would be expected following the treatment of Darken and Gurry (67). The dependence of log f_C on carbon concentration was measured at 1550°C where the results were accurate and covered the whole carbon range, fig. (3-4). It was found that log f_C is not a linear function of w/o carbon over the whole range. Non linear dependence suggests that higher order terms in carbon were necessary to represent log f_C. However up to 3.0 w/o carbon the data may be expressed with a first order term given in equation (3-12) as:

$$\text{Log } f_C = 0.135 \text{ (w/o C) at } 1550^{\circ}C \qquad (3-18)$$

and the experimental curve should be used at higher carbon concentration, fig. (3-4). At 1650 and 1750°C, log f_C is a linear function of carbon concentration over the carbon range studied and the dependence is obtained from equations (3-13) and (3-14).

The carbon activities computed from the activity coefficients at 1550°C and 1750°C are shown in fig. (3-6). Changing the temperature by 200°C has no practical effect on the position of the activity curves at low carbon, and the dependence of activity on temperature becomes obvious at higher carbon concentration. This change runs parallel with the corresponding increase in the limiting solubility of graphite in liquid iron with temperature. The fact that apparently the same activity was obtained at 1650 and 1750°C

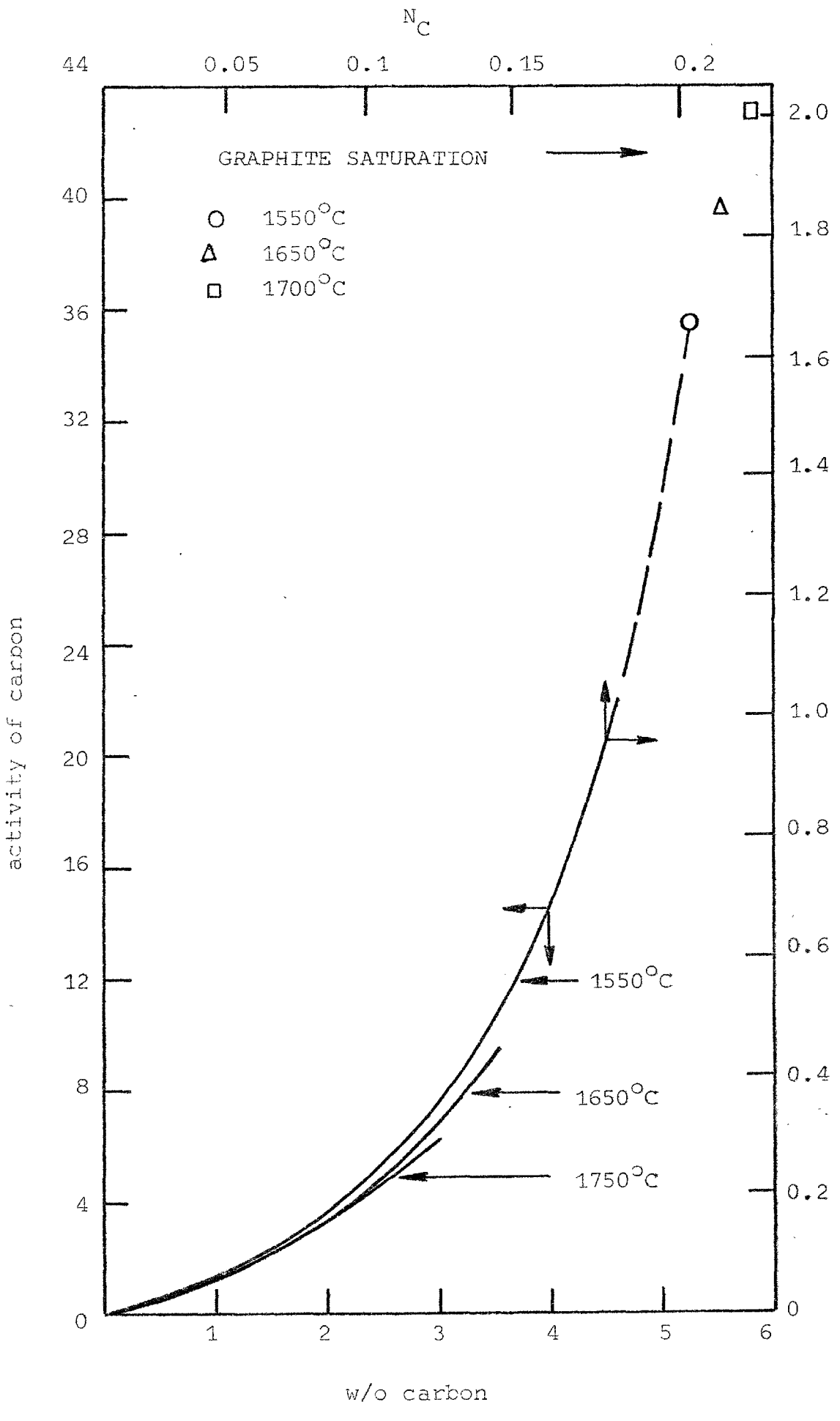

Fig (3-6) Activity of carbon in iron-carbon alloy, starder state is the infinitely dilute solution of carbon

is indicative of the large error limits of the measurements at high temperatures. It is apparent that deviations from Henry's Law are marked above 0.2 w/o carbon, and the activities increased markedly above 4.0 w/o carbon towards the solubility limit.

When carbon concentration was expressed in atom fraction at standard state of infinitely dilute solution ($a_C/N_C = 1$ at $N_C = 0$, and $a_C = \gamma_C N_C$) the resulting equation for $CO-CO_2$ equilibrium with carbon in molten iron becomes:

$$\log K_{1(N_C)} = -6836\ (\pm 187)/T + 7.70\ (\pm 0.097) \qquad (3\text{-}19)$$

$$\Delta F^{\circ}_{1(N_C)} = 31275\ (\pm 855) - 35.78(\pm 0.44)\ T \qquad (3\text{-}20)$$

The activity of carbon can be represented on fig. (3-6), with different numerical values on the axes.

In fig. (3-7) the logarithm of the activity coefficient $\log(\gamma_C)$ shows a linear relation with atomic fraction of carbon up to about 0.05. In dilute solution the activity coefficients in the linear part may be expressed as:

$$\text{Log}\ \gamma_C\ (1550^{\circ}C) = 2.90\ N_C \qquad (3\text{-}21)$$

$$\text{Log}\ \gamma_C\ (1650^{\circ}C) = 2.5\ N_C \qquad (3\text{-}22)$$

$$\text{Log}\ \gamma_C\ (1750^{\circ}C) = 2.38\ N_C \qquad (3\text{-}23)$$

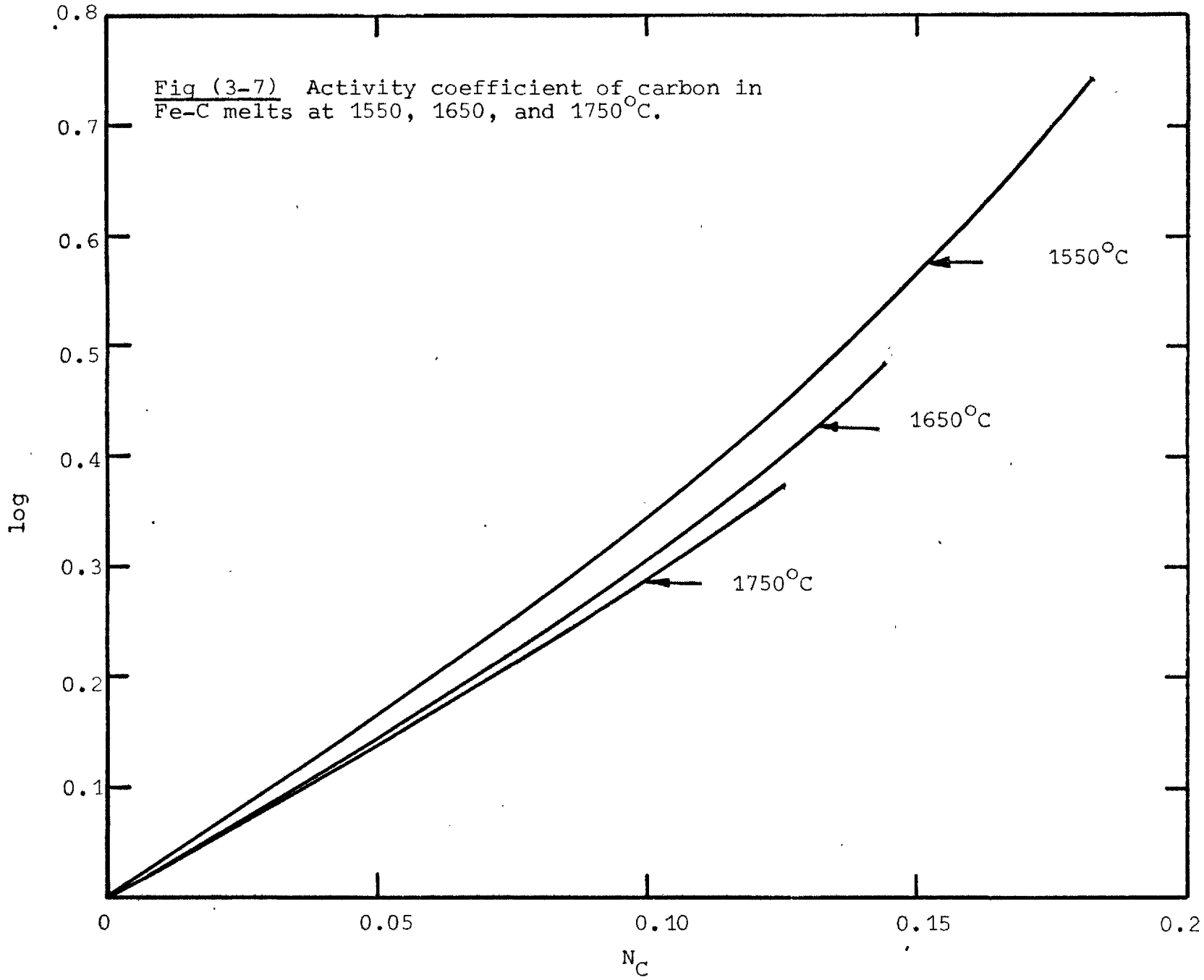

Fig (3-7) Activity coefficient of carbon in Fe-C melts at 1550, 1650, and 1750°C.

3-6.2 Thermodynamic properties of Fe-C melts

As is customary, pure liquid iron and β graphite were chosen as standard states of the solution, so that the activity of carbon will be unity at graphite saturation in molten iron

a) Activity of carbon

The activity of dissolved carbon in molten iron may be evaluated as

$$a_C^{(gr)} = \gamma_C^{(gr)} N_C = \gamma_C K_{1(N_C)} N_C / K_{(gr)} \qquad (3\text{-}24)$$

where $K_{(gr)}$ is the equilibrium constant of β graphite oxidation with $CO-CO_2$ gas mixtures.

$$C(\beta \text{ graphite}) + CO_2 \rightleftharpoons 2CO \qquad (3\text{-}25)$$

$$K_{(gr)} = (P_{CO})^2 / P_{CO_2} \qquad (3\text{-}25a)$$

This was evaluated from tabulated thermodynamic data (41), and it may be expressed as:

$$\text{Log } K_{(gr)} = -8347.5/T + 8.763 \qquad (3\text{-}26)$$

where the enthalpy term is an average between 38.632 kcal and 37.748 kcal at 1800° and 2100°K respectively. The activity coefficient of carbon becomes

$$\log \gamma_C^{(gr)} = \log \gamma_C + (1511.5/T - 1.063) \qquad (3\text{-}27)$$

The activity of carbon at 1550°C was evaluated from the equation (3-27) is shown in fig. (3-8).

b) Heat and entropy of mixing

The partial molar free energy for solution of carbon in molten iron is:

$$\Delta\overline{F}_C = \overline{F}_C - F^{\circ}_{(gr)} = RT\ln a_C^{(gr)} \qquad (3\text{-}28)$$

and its corresponding heat and entropy of mixing are

$$\Delta\overline{H}_C = \left\{\delta(\Delta\overline{F}_C/T)/\delta(1/T)\right\}_{N_C} \qquad (3\text{-}29)$$

$$\Delta\overline{S}_C = -\left\{\delta(\Delta\overline{F}\ )/\delta T\right\}_{N_C} \qquad (3\text{-}20)$$

The partial molar heat of mixing at infinitely dilute solution is the difference between the heat of reactions between $CO\text{-}CO_2$ gas mixture with β graphite and with carbon in liquid iron respectively. The difference was 6.915 ($\pm$2.0) kcal/mole . The observed dependence of the activity on concentration (at infinitely dilute solution as standard state) implies a variation of the partial molar heat of mixing with concentration. Plotting log $a_C^{(gr)}$ against 1/T at 0.08, 0.1, and 0.12 atomic fraction, fig. (3-9), the $\Delta\overline{H}_C$ from the slopes were 10.7, 11.79 and 12.97 ($\pm$2.0) k cal/mole respectively. Although the limits of uncertainty are fairly large, the values obtained justify the observed dependence of the activity coefficient on temperature. The partial molar heat of dissolved carbon increases linearly from 6.915

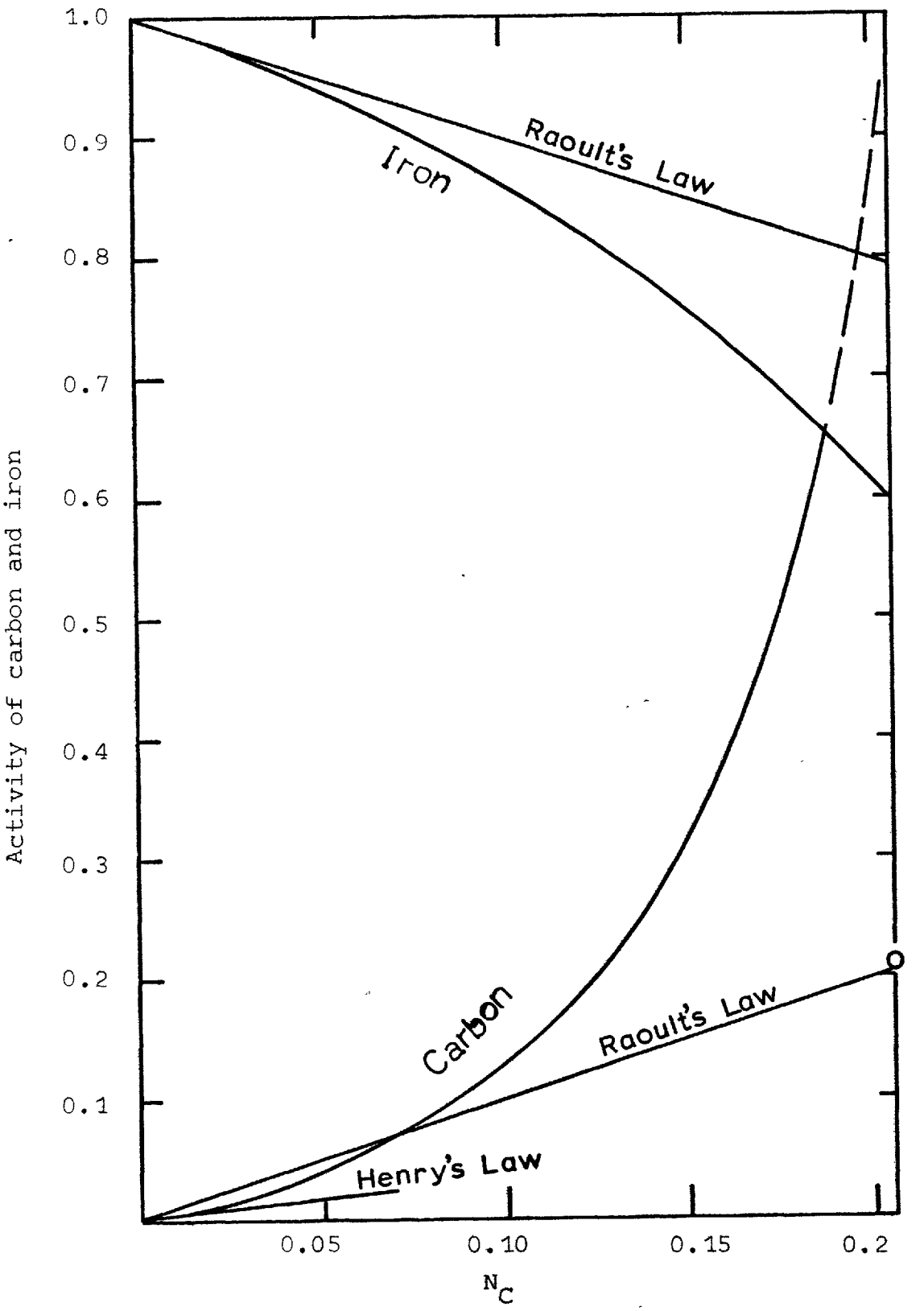

Fig (3-8) Activity of carbon and iron at 1550°C standard state being graphite and pure liquid iron

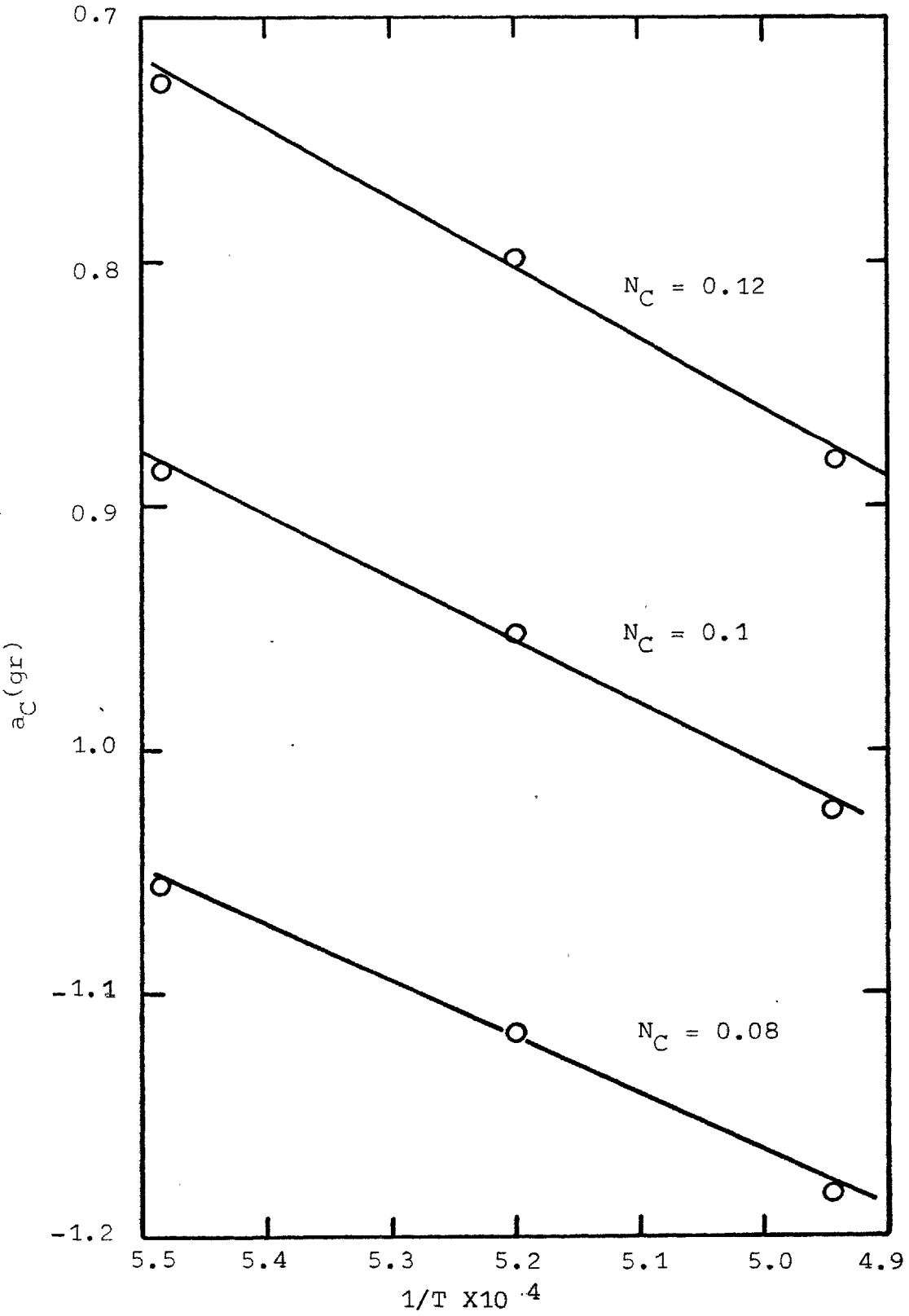

Fig (3-9) Plots of log carbon activity against 1/T at 1550, 1650, and 1750^{o}C at 0.08, 0.1, and 0.12 atomic fraction of carbon

at infinitely dilute solution to 12.97 kcal/mole at 0.12 carbon atomic fraction, fig. (3-10a). The partial molar entropy is shown in fig. (3-10b). The partial molar entropy of carbon for an ideal solution is also included in the same figure.

c) Activity of iron

The iron activities were obtained by numerical integration of the Gibbs-Duhem equation

$$N_1 \, d \ln a_1 + N_2 \, d \ln a_2 = 0 \qquad (3\text{-}31)$$

which may be rearranged to the following form

$$\log \gamma_{Fe} = - \int_0^{N_C} N_C \, d \log \gamma_C^{(gr)} / (1 - N_C) \qquad (3\text{-}32)$$

The activities of iron at 1550°C which cover the whole carbon range are given in fig. (3-8).

The findings in the thermodynamic properties of Fe-C melts at 1550°C are summarized in table (3-7).

3-6.3 Equilibrium of CO with carbon and oxygen in molten iron

The equilibrium constant of the carbon oxygen reaction in liquid iron (3-5) and (3-5a)

$$C \text{ (in iron)} + O \text{ (in iron)} \rightleftharpoons CO \qquad (3\text{-}5)$$

$$K_5 = P_{CO} / a_O \, a_C \qquad (3\text{-}5a)$$

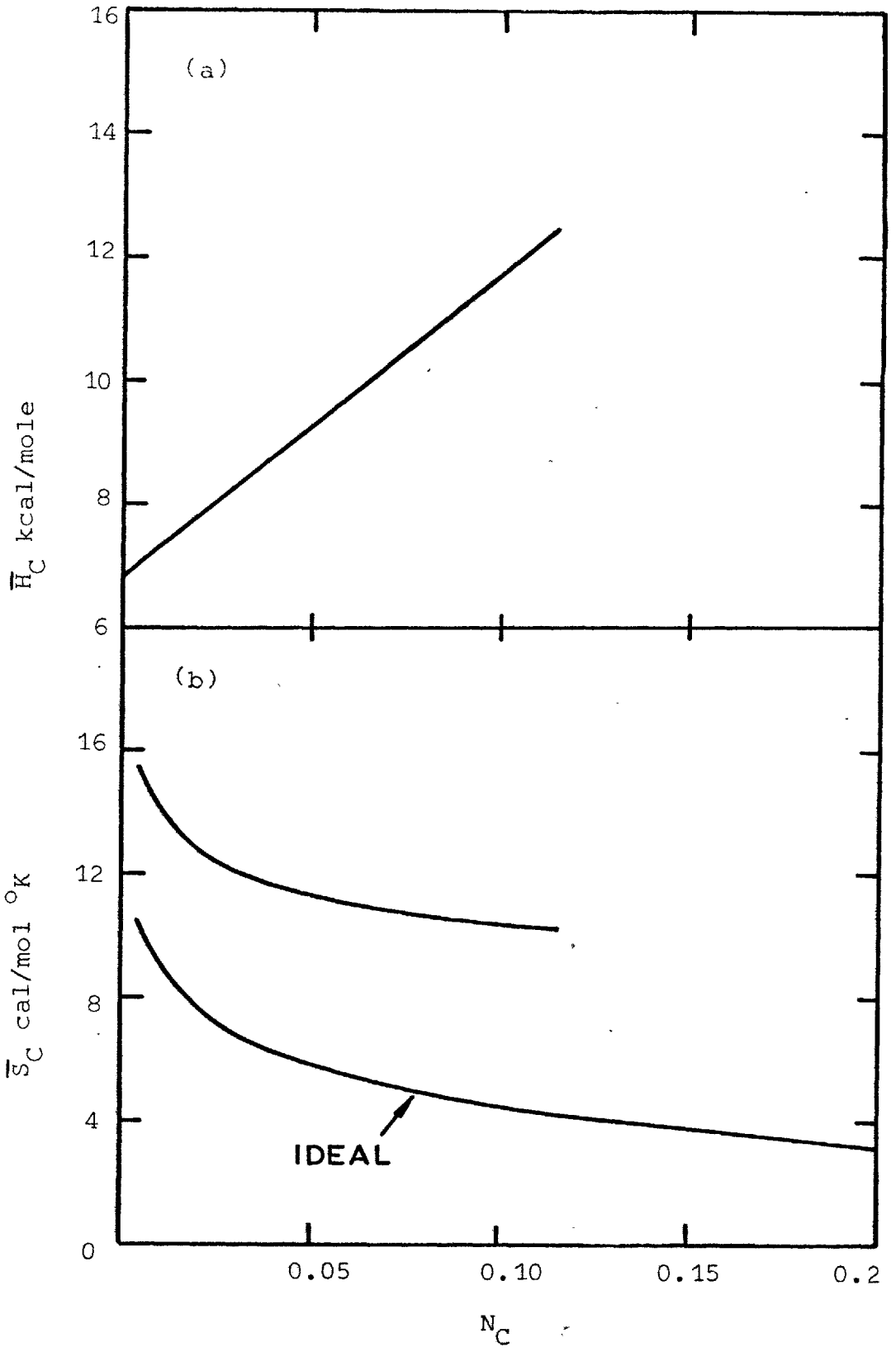

Fig (3-10)

Partial molar heat and entropy
of solution of carbon in molten iron

N_C	$\Delta\bar{S}_C$ cal/mole^oK	$\Delta\bar{H}_C$ k cal/mole	Activities of Carbon & Iron at 1550^oC	
			a_C	a_{Fe}
0		6.915	0	1.0
0.02	12.81	7.890	0.013	0.978
0.04	11.66	8.87	0.032	0.954
0.06	11.07	9.750	0.056	0.926
0.08	10.71	10.703	0.088	0.896
0.10	10.52	11.798	0.131	0.862
0.12	10.33	12.796	0.187	0.823
0.14			0.269	0.781
0.16			0.386	0.732
0.18			0.567	0.676
0.20			0.869	0.614
0.205			1.0	0.597

Table (3-7)

Thermodynamic properties

of Fe-C solution

was obtained from the equilibrium data of $CO-CO_2$ reaction with carbon equations (3-16) and (3-17) combined with the equilibrium data of the reaction (3-4) obtained by Tankins, Goken and Belton (58)

$$\text{Log } K_4 = 6817(\pm 72)/T - 3.13(\pm 0.039) \qquad (3\text{-}34)$$

$$\Delta F_4^o = -31.200(\pm 330) + 14.33(\pm 0.18)\ T \qquad (3\text{-}35)$$

converted to the corresponding values for $CO-CO_2$ reaction with dissolved oxygen reaction (3-3) by thermodynamic data for the water-gas reaction (3-6) (61).

$$\text{Log } K_6 = -1398/T + 1.38 \qquad (3\text{-}36)$$

$$\Delta F_6^o = 6400 - 6.30\ T \qquad (3\text{-}37)$$

as

$$\log K_5 = 1379(\pm 326)/T + 1.86(\pm 0.15) \qquad (3\text{-}38)$$

$$\Delta F_5^o = -6308(\pm 1500) - 8.51(\pm 0.69)T \qquad (3\text{-}39)$$

The activities of carbon and oxygen in the ternary molten Fe-C-O system may be described through the interaction parameter (68, 69). The activity coefficient is defined as

$$f_O = f_O^O\ f_O^C \qquad (3\text{-}40)$$

where f_O^O is the activity coefficient of binary iron-oxygen

melts and was found by Tankins et al (58) to be unity (oxygen obeys Henry's Law), and the interaction coefficient of carbon-oxygen f_O^C is given as

$$\log f_O^C = (w/oC)\ (\delta \log f_O/\delta(w/oC))_{(w/oC \rightarrow 0)}$$
$$= (w/oC)\ e_O^C \qquad (3\text{-}41)$$

where e_O^C is the interaction parameter of carbon on oxygen.

It follows from the oxygen results, which showed a decrease of oxygen by increasing carbon at constant oxygen activity, that carbon increases the activity coefficient of oxygen. Calculated activity coefficients from the results were plotted as log f_O against (w/oC) in fig. (3-11). A linear dependence may be drawn through the results from the reliable data at high carbon to the origin. The results which were obtained from deoxidized specimens follow the same line but with large scatter. The temperature has no effect on the slope (interaction paramter e_O^C) within the experimental error. The interaction parameter e_O^C is $+0.1(\pm 0.02)$, and the activity coefficient of oxygen in Fe-C-O melts can be obtained as

$$\log f_O = 0.1\ (w/oC) \qquad (3\text{-}42)$$

The activity coefficient of carbon is represented as

$$f_C = f_C^C\ f_C^O \qquad (3\text{-}43)$$

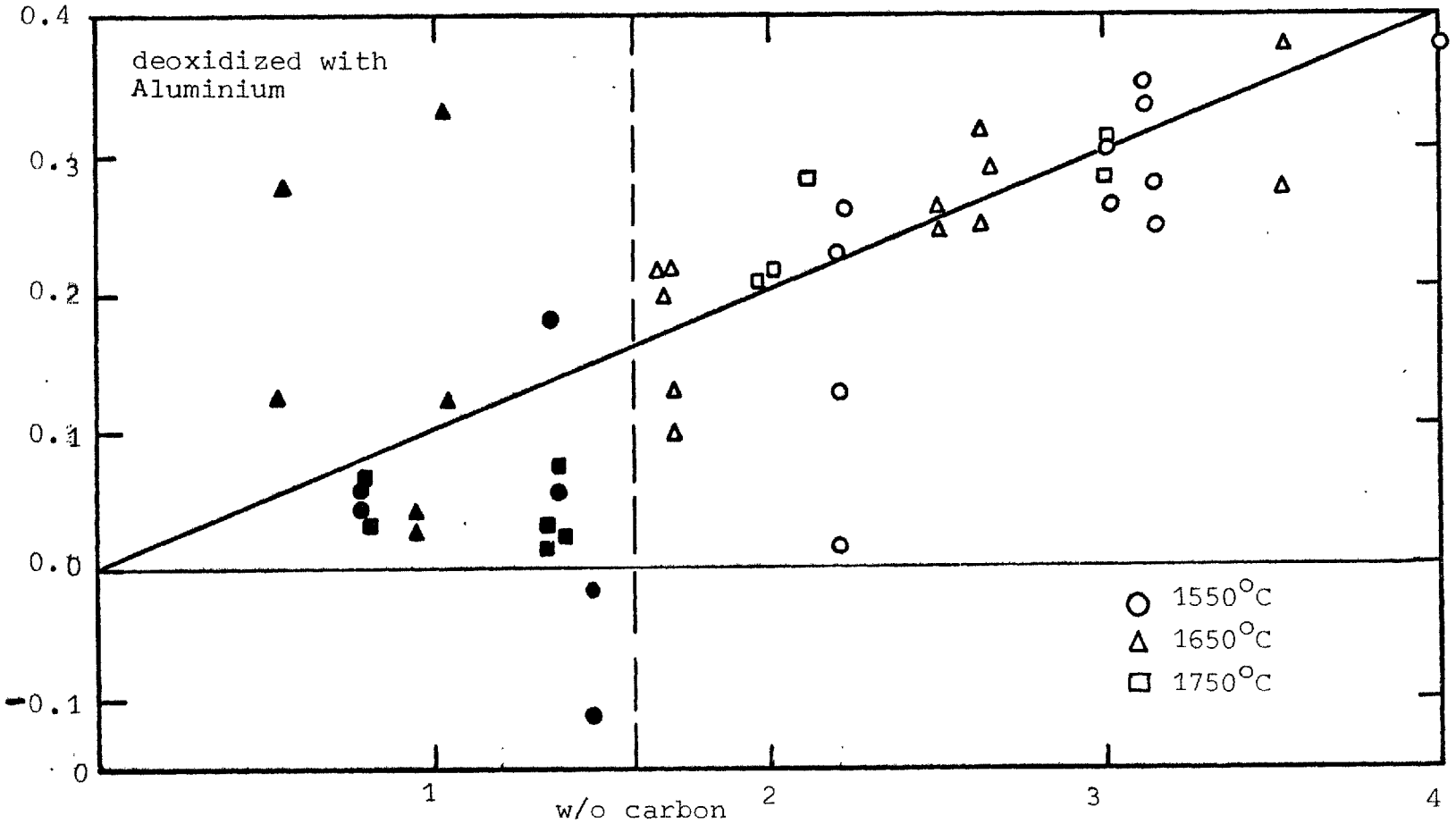

Fig (3-11) Effect of carbon on activity coefficient of dissolved oxygen at 1550, 1650 and 1750°C

where the interaction coefficient of oxygen on carbon f_C may be obtained by

$$\log f_C^O = e_C^O (w/o\ O) \qquad (3\text{-}44)$$

Since the interaction parameter of oxygen on carbon e_C^O is related to e_O^C at infinite dilution of carbon and oxygen by

$$e_C^O = (M_C/M_O)/e_O^C \qquad (3\text{-}45)$$

we obtain the interaction parameter of oxygen on carbon as

$$e_C^O = 0.075(\pm 0.015) \qquad (3\text{-}46)$$

When the concentration is expressed in atomic fraction, Lupis and Elliott (70) have shown that the value of ϵ_O^C can be determined from e_O^C as

$$\epsilon_O^C = 230(M_C/M_{Fe})e_O^C + (M_O - M_C)/M_{Fe} \qquad (3\text{-}47)$$

which gives the value of 5.0. The value of ϵ_C^O was shown by Wagner (68) is to be equal to ϵ_O^C at infinitely dilute solution.

3-7 Discussion

3-7.1 Introduction

In this work the thermodynamic measurements were made partly in an attempt to improve the knowledge of these systems, and partly in order to measure the ultimate equilibria reached in the kinetic runs and prior to bubble nucleation.

Because of the wide range of subjects covered in this thesis, it became impossible to deal with all the ramifications of all the results. No discussion of models of solutions of liquids (71) has been included.

In this discussion the thermodynamic data and properties evaluated in the previous section are only briefly dealt with, by comparing them with earlier results and discussing their accuracy. Tests on the correctness of the results using well known data (e.g. activity of carbon in austentite) have also been carried out.

The sources of error using conventional crucible techniques which have been discussed in section (3-2.5), yielded a wide variation in thermodynamic data and also limited studies to the low carbon region. The experimental technique which was adopted in this work was more suitable and allowed the measurements to be made at high carbon without losing any accuracy. The agreement between the observed and predicted levels of carbon saturation (within

the error limits due to thermal diffusion, see section 2-3) is good evidence of this. In the following sections the results obtained for each system (Fe-C and Fe-C-O) will be discussed from the thermodynamic point of view.

3-7.2 Binary Fe-C system

The results presented in this chapter have covered nearly the whole range of carbon at 1550°C, and were consistent with the approach to graphite solubility at that temperature. The results at 1650, and 1750°C also covered a large proportion of the carbon range, up to 3.5 w/o carbon.

The results of the previous studies by means of reaction (3-3) up to 1 w/o carbon at 1550°C are shown in fig. (3-12). The studies made by Dennis and Richardson (45) and Ban-Ya and Matoba (51) showed lower measured carbon than the present study.- about 15% and 20% relative in carbon at the same $(P_{CO})^2/P_{CO_2}$ respectively. Marshall and Chipman (48) on the other hand obtained higher carbon than the present work, about 20% relative higher, and their data also showed a large scatter.

There is no doubt that the present results are the most accurate. The sources of error discussed in section (3-2.5) and also by Chipman (63) have been eliminated almost completely in this work. It is interesting to note that all the previous studies, as well as the present work, nearly agree at very low carbon and the deviation increases as carbon increases.

This is because the errors become greater as % CO_2 in the gas mixture is decreases (see section (3-2.5) and reference (63)). The agreement at low carbon is also demonstrated by the fact that all investigators agree on the value of the equilibrium constant for the reaction

$$C(w/o \text{ in iron}) + CO_2 \rightleftharpoons 2CO \qquad (3\text{-}3.a)$$

This agreement over the whole temperature range is illustrated in fig. (3-13).

The agreement at different temperatures is another indication that the errors in temperature measurement were not outside the error limits of $\pm$ 10°C estimated earlier in section (1-4).

Following from the above discussion the derived activity of carbon in molten iron must be correct. When the standard state is expressed such that the activity approaches the atomic fraction at infinite dilution, the activity coefficient of carbon γ_C at 1550°C shows a better agreement with Dennis and Richardson's values than with any of the other work, fig. (3-14). Rist and Chipman's (50) extrapolation of Dennis and Richardson's results up to graphite saturation, by following the treatment of Darken and Gurry (67) assuming constant α function ($\log \gamma_C/(1-N_{Feb}^2)$) , gives greater deviations from the present measurements at high carbon. However such extrapolation is not too far out from the present

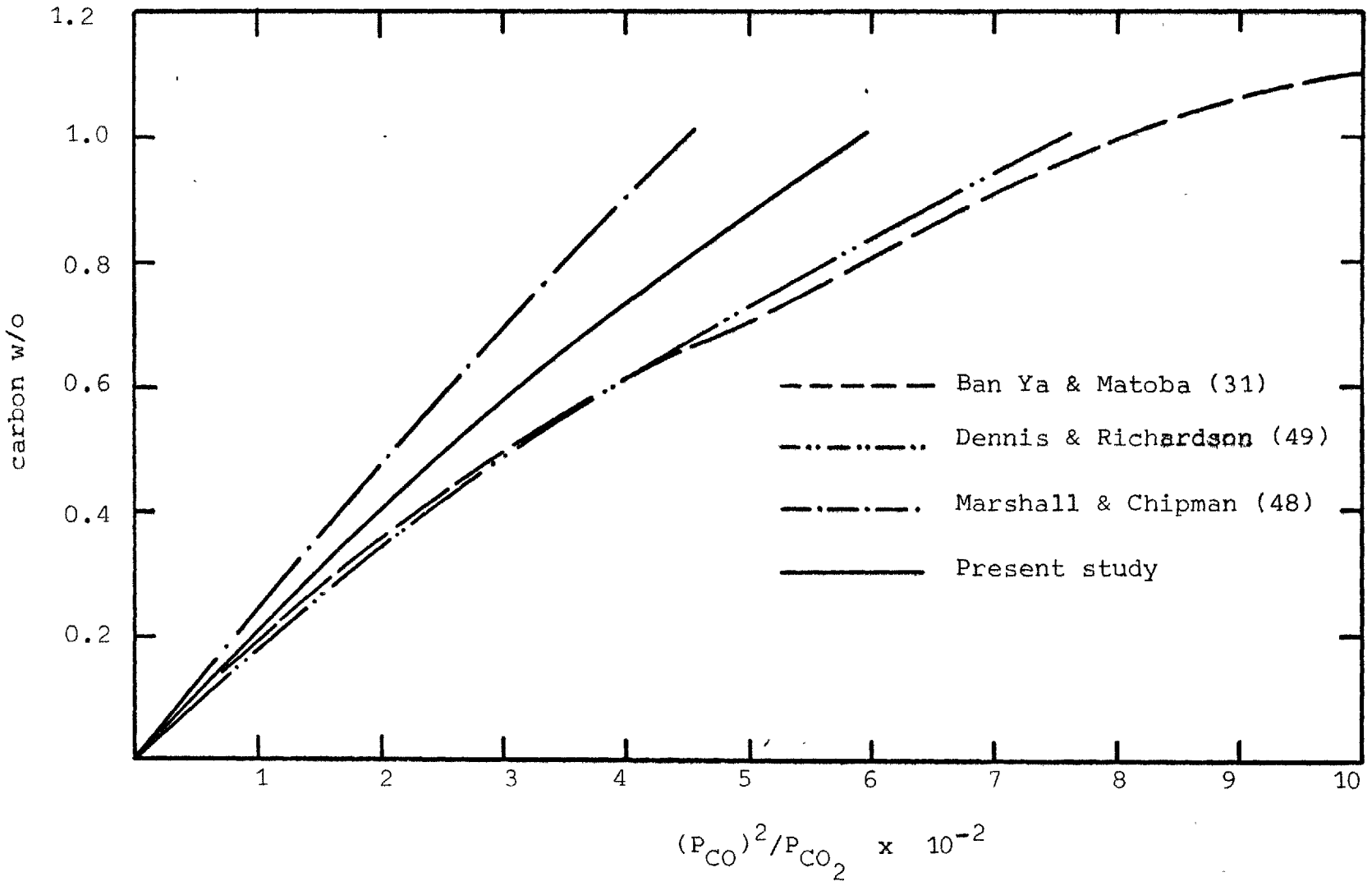

Fig (3-12) Equilibrium carbon measurements by various investigations

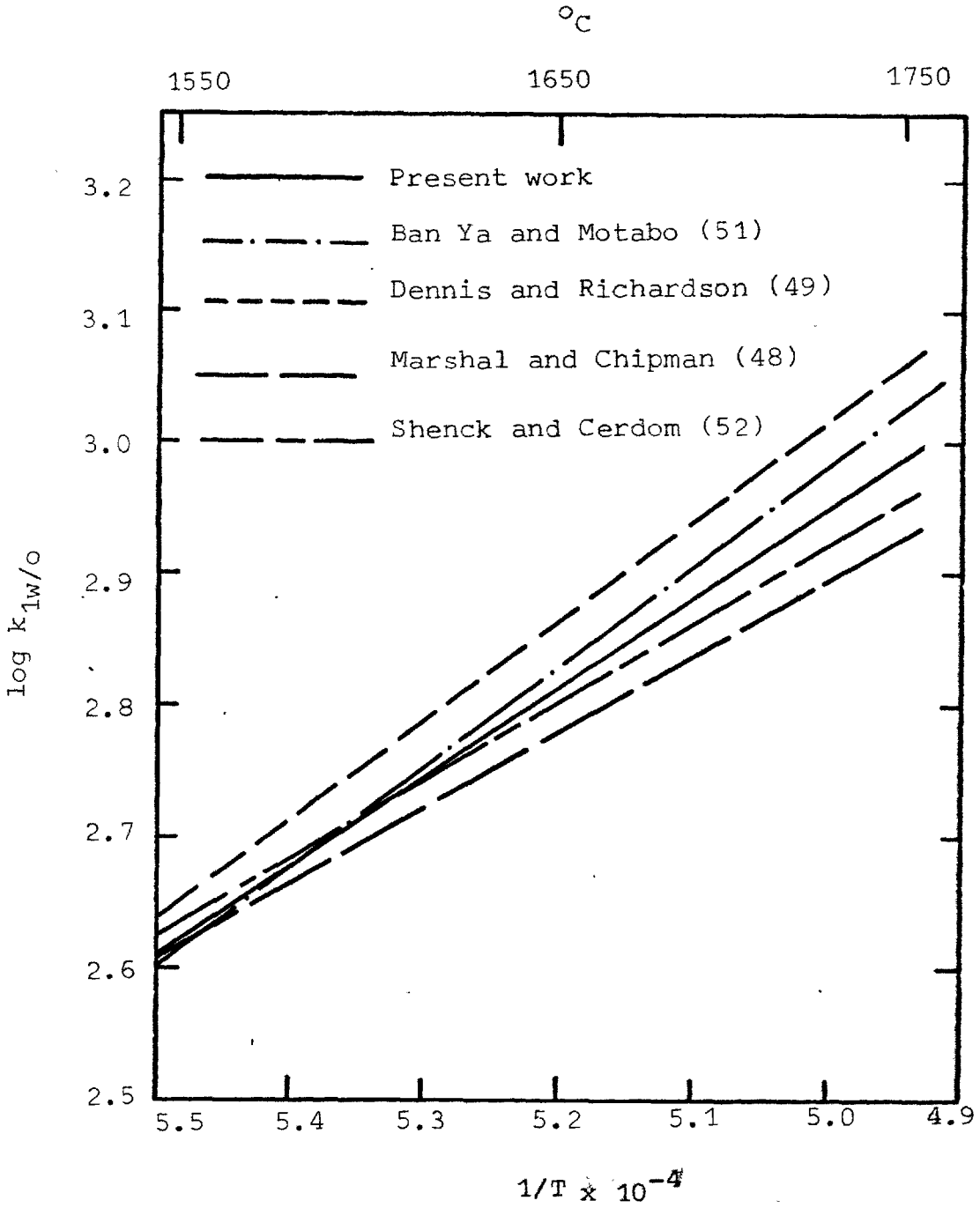

Fig (3-13)

Comparison of $k_{1(w/o)}$ with other investigations

measurements, and it was worth doing in the abscence of the data at high carbon.

The thermodynamic properties of carbon in liquid iron, i.e. partial molar heats, entropies and free energies, provided the method for interpolating or extrapolating the measurements to other temperatures. Choosing graphite as standard state ($a_C = N_C \gamma_C^{(gr)} = 1$ for liquid saturated with graphite at the particular temperature under consideration) as indicated in section (3-6.5), the partial molar properties for solution of carbon in iron may be calculated i.e.

$$\Delta \overline{F}_C = \Delta H_C + T\Delta \overline{S}_C = 2.303\ R\ T \log a_C^{(gr)} \qquad (3\text{-}48)$$

$$\Delta \overline{H}_C = 2.303\ R \left[d(\log a_C^{(gr)})/d(1/T) \right] \qquad (3\text{-}49)$$

$$\Delta \overline{S}_C = \Delta \overline{H}_C/T - 2.303\ R \log a_C^{(gr)} \qquad (3\text{-}50)$$

The results at 1650 and 1750°C did not extend over a sufficiently wide range of carbon concentration to obtain the partial molar quantities over the whole range. The partial molar heats in kcal/mole, fig. (3-10a), showed a linear dependence on carbon concentration and can be expressed over the measured range as

$$\Delta \overline{H}_C = 6.915 + 48.85\ N_C \qquad (3\text{-}51)$$

The excess partial molar entropy of carbon in solution

$$\Delta \overline{S}_C^{ex} = \Delta \overline{S}_C - \Delta \overline{S}_C^{ideal} \qquad (3\text{-}52)$$

was also found to have a linear dependence on carbon concentration, fig. (3-14). The entire partial molar entropies in cal/mol degree Kelvin may then be expressed over the range studied as,

$$\Delta \bar{S}_C = -2.303\ R \log N_C + 11.0\ N_C + 4.85 \qquad (3\text{-}53)$$

The first term in equation (3-53) is the ideal partial molar entropy of carbon in solution, while the last two terms represent the excess partial molar entropy.

The correctness of the measured thermodynamic properties has been tested by evaluating the activity of carbon along the liquidus line between austenite and liquid on the iron-carbon phase diagram. The following table compares the predicted activities at the liquidus from the present study with those obtained from the measurements of carbon activities in austenite (72).

Temperature ^{o}C	Liquidus Carbon atomic fraction	Activity of Carbon	
		Present work	from austenite data
1300	0.125	0.354	0.341
1350	0.1	0.198	0.216
1400	0.075	0.105	0.129
1450	0.05	0.0515	0.066
1493	0.027	0.0215	0.024

Table (3-8)

Activity of Carbon at the liquidus between austenite and liquid

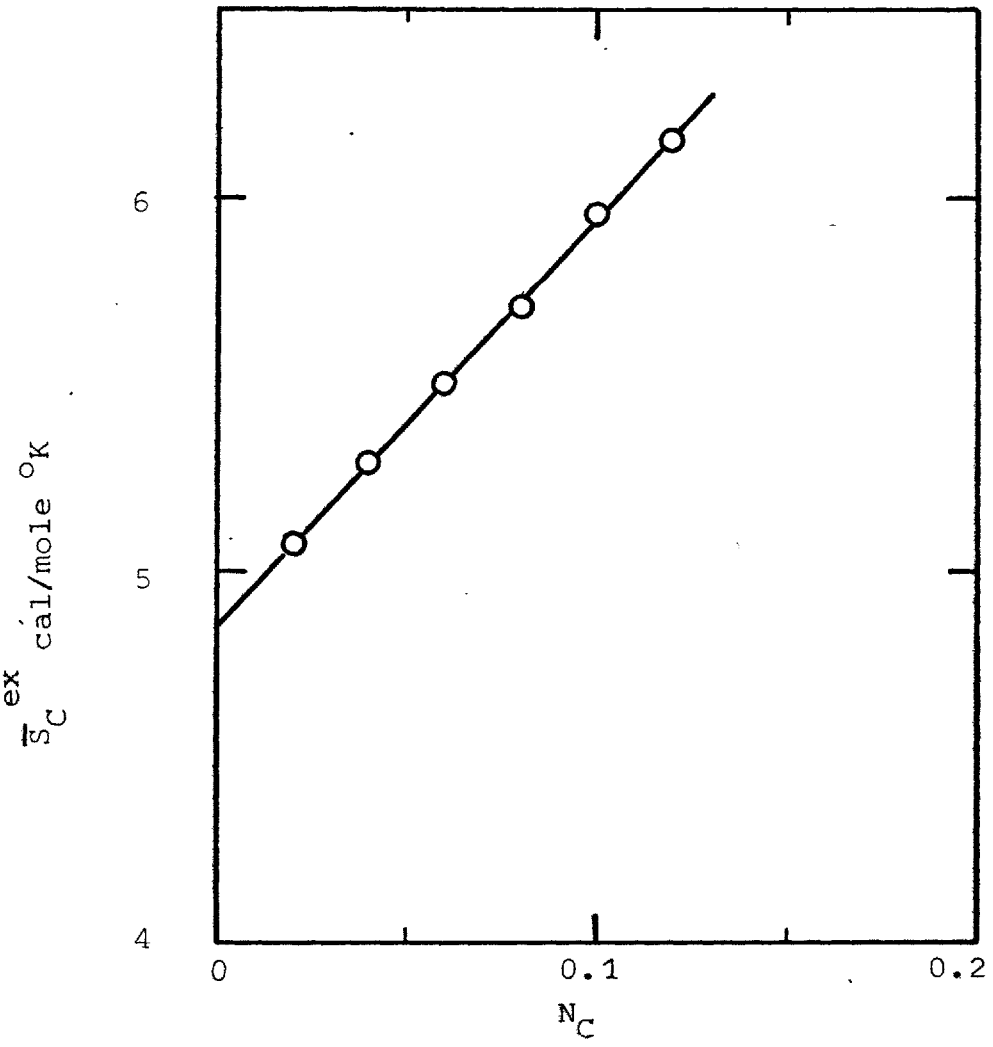

Fig (3-14) Excess partial molar entropy of carbon as function of carbon atomic fraction

The agreement is remarkably good, which implies the accuracy and validity of the derived thermodynamic properties. It should be emphasised that the derived thermodynamic properties of carbon apply only to the composition range over which they were measured i.e. up to 0.12 atomic fraction of carbon in molten iron.

The activity of iron at 1550°C computed from carbon by means of the Gibbs-Duhem equation is found to be in excellent agreement with the measured activity of iron in iron-carbon solutions (73), fig. (3-15).

3-7.3 Ternary Fe-C-O system

The results presented in section (3-5.2) and section (3-6.3) showed that carbon increased the activity coefficient of oxygen in Fe-C-O solution. The temperature was found to have no practical effect on the activity coefficient of oxygen in the Fe-C-O system. It was also shown that the carbon oxygen product decreased with higher carbon and was nearly independent of the temperature.

These findings are contradictory to all the previous investigations (48, 51, 53, 60, 61) except the work of Matsumoto (62). The majority measured a decrease in the activity coefficient of oxygen with carbon. It is important to realise that most of the previous investigators did not keep a constant oxygen potential and vary the carbon concentration as was done in this work, but they measured the carbon and oxygen in

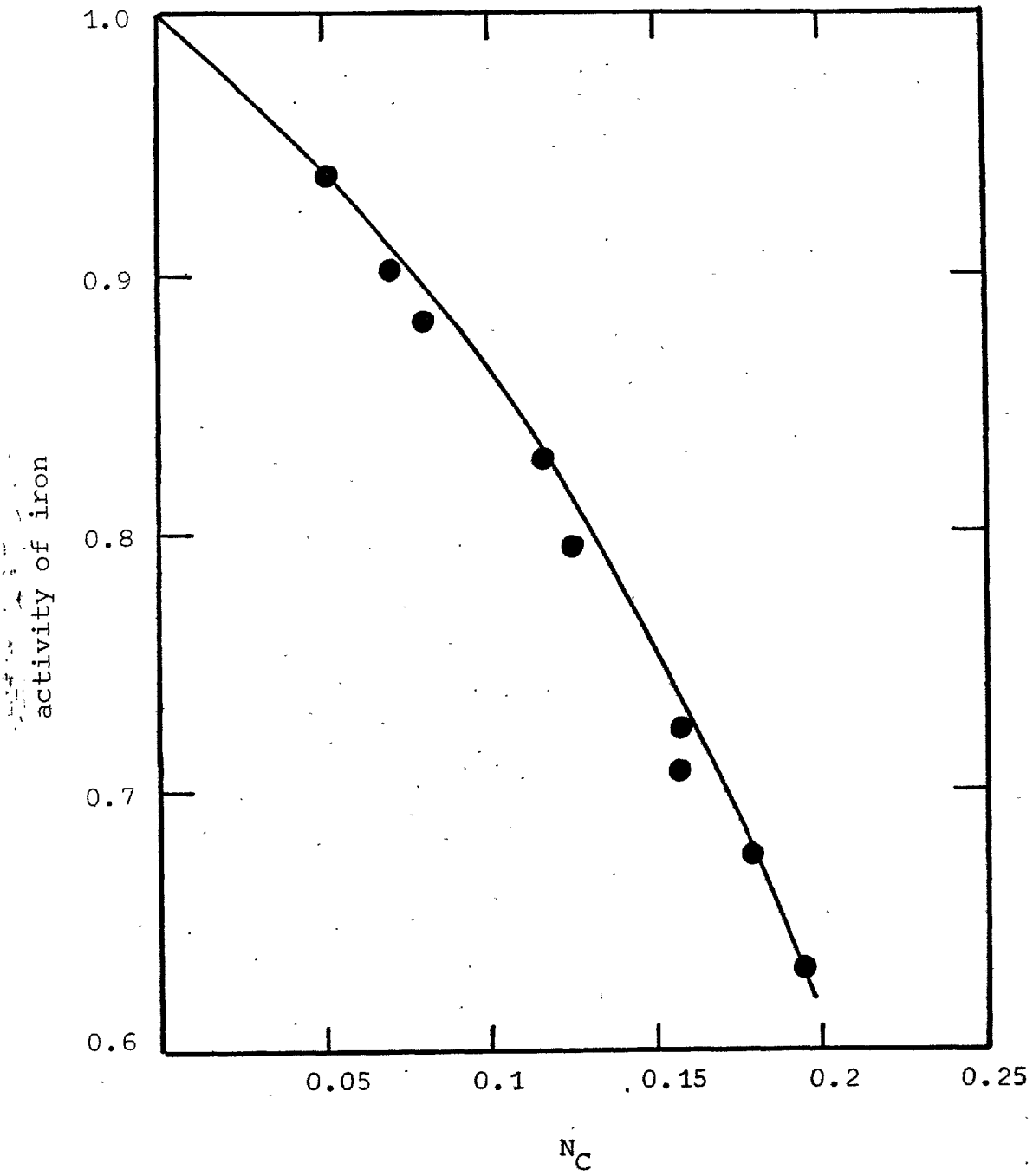

Fig (3-15) Activity of iron in Fe-C solution at 1550°C. Line integration of Gibbs-Duhem equation, points measurements (73)

equilibrium in $CO-CO_2$ gas mixtures at one pressure. This meant that even if the experimental data were quite accurate they then had difficulties in separating the carbon-oxygen interaction from the carbon-carbon and oxygen-oxygen interactions. Since the experimental errors progressively increase with carbon (as mentioned in section (3-2.5) their results were subjected to a large uncertainty at high carbon. This is shown by the widely different results obtained for the dependence of the activity coefficient of oxygen on carbon concentration, despite their agreement on carbon oxygen product at very low carbon. Errors which were particularly damaging in attempting to achieve the correct oxygen concentration in Fe-C-O alloys are discussed in the following paragraphs. It is important to realise that other sources of error were also present, and had an effect on the measurements.

1) Melt contamination with stable oxides, e.g. CaO, which will tend to increase the oxygen concentration in the analysis. The main sources of such oxides are the graphite used in the preparation of iron-carbon melts, and the erosion of the crucible. This error will be greatest at high carbon. Fuwa and Chipman (61) realised that specimens prepared in graphite crucibles contained up to 20 ppm excess oxygen, and they suggested that this was due to the adsorption of oxygen or water vapour on the graphite flakes in the specimen after sampling and prior to analysis. This error may well co-operate with ashes in the graphite to yield higher oxygen in the specimens. The erosion of oxide crucibles, particularly in

melts stirred by an electromagnetic field, is a common feature in high temperatures studies. This error may have had quite a measurable effect in crucible work, since attainment of the equilibrium took several hours. No account could be taken of such a phenomenon, since it is difficult to separate it from the side reaction with the melt (see (2) below).

2) Side reactions between oxide crucibles and carbon, by the reaction

$$C \text{ (in iron)} + MO \rightleftharpoons M \text{ (in iron)} + CO \qquad (3\text{-}54)$$

The dissolved element (e.g. Al) goes into solution in the melt and, since it must have a higher affinity for oxygen than iron it will decrease the activity coefficient of oxygen in the melt and the oxygen concentration will then rise by reaction with the gas phase. Turkdogan et al (60) used alumina crucibles, and they reported that no marked attack of the crucible occurred. However the study of absorption of CO in molten iron by Parlee et al (64), using a modified Sievert's apparatus, showed conclusively the dissolution of Al in the melt from the crucible. From the thermodynamic data for the Fe-Al-O system (65) 0.1 w/o Al decreases the activity of oxygen by a factor of ten. This level of aluminium was observed in all experiments using alumina crucibles at high carbon (61). Turkdogan's measurements are subject to a large error in oxygen due to dissolved Al. The results of Fuwa and Chipman (61), Ban-Ya and Matoba (51), and Schenck and Hinze (53) must have all suffered from

such error.

The work of Marshall and Chipman (48) and Matsumoto (62) must have been less affected by reaction (3-54) since it is pressure dependent, and the equilibrium dissolved metal should decrease by increasing the pressure. Matsumoto measured an increase in the activity coefficient of oxygen by carbon. The results of Marshall and Chipman were invalidated for the reason discussed below.

3) Absorption of oxygen from the $CO-CO_2$ mixture in contact with the melt after the addition of deoxidiser. Marshall and Chipman added Al to melts containing carbon up to 2 w/o in $CO-CO_2$ atmosphere to obtain sound specimens. They allowed a few minutes for stirring and this must have led to an increase of oxygen in the melt by reaction with the gas phase as in (2) above.

4) The errors in the composition of the gas mixtures generally tend to increase the oxygen potential in the gas phase, and this led investigators to relate the measured oxygen concentration to an oxygen potential in the gas phase lower than that actually present. This is particularly obvious in the case of Ban-Ya and Matoba (51), from their carbon measurements.

The second and third errors listed were the most damaging ones. The effect of these errors was to increase the apparent

oxygen with increasing carbon, which has led to the wrong belief that carbon decreases the activity coefficient of oxygen. Even if the error of oxygen is only of the order of tens of ppm too high, it has a tremendous effect in calculating the activity coefficient of oxygen.

The effect of carbon on oxygen observed in this work is analogous to previous measurements of the effect of carbon on sulphur (46) and tellurium on carbon (74) in molten iron. This makes the whole group (oxygen, sulphur, (selenium), tellurium, ...) in the periodic table have the same behaviour in the Fe-C-X system, and is consistent with the idea of "periodicity" (74).

Because of the difficulties associated with an adequate theory of the liquid state there is as yet no satisfactory theory of metal solution. As metallurgists it is useful to have a simple picture which, although it is qualitative and elementary, is in general agreement with the meagre information currently available. On the basis of the simple model employed by Chipman (75) and Richardson (76, 77), we shall predict the behaviour of the activity of oxygen in the Fe-C-O solution. This model considers the behaviour of the solutes using the energies associated with the bonds between similar and dissimilar atoms in a qualitative sense. In a binary mixture strong interaction between solvent and solute, which may gauged by the value of $\overline{H}_i$ (77), decreases the activity of the solute below the Raoultian value. If a thrid element is added the effect of the second element on it depends on the relative strength of the interactions.

between the three elements. Let us consider the behaviour of the well known Fe-C-Si ternary solution as an example. The Fe-C contact has higher potential energy than those of Fe-Fe and C-C contact since $\Delta\bar{H}_{C,Fe}$ is about +7 kcal/mole while Si-C and Si-Fe contacts have lower potential energies, since $\Delta\bar{H}_{Si,Fe}$ and ΔH_{SiC} (the heat of formation) are about -31.4, -12.4 kcal/mol respectively. The heat of formation has to be used where partial molar heats are not available. In the ternary solution of Fe-C-Si, as shown in fig. (6-15a) where iron is the solvent, Si atoms will be at lower potential

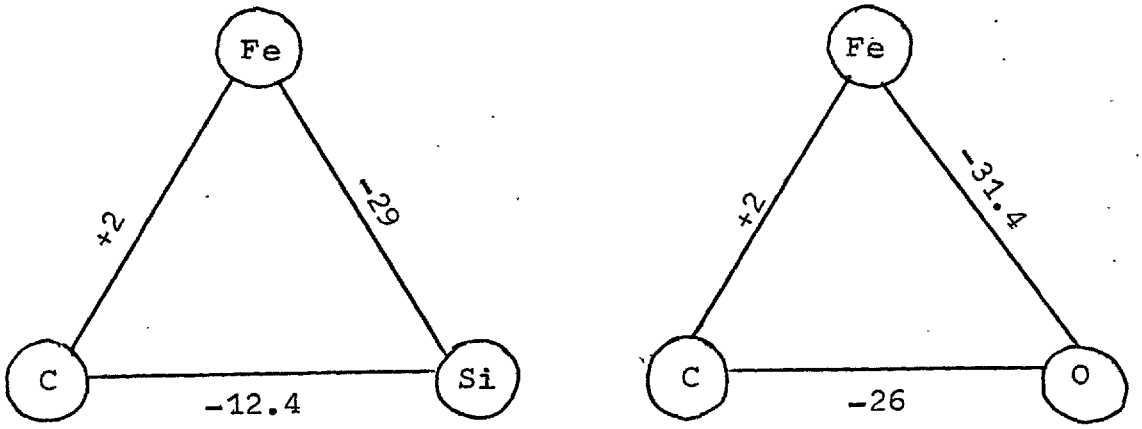

Fig. (3-16) Schematic representation of contact energy
a) Fe-C-Si solution b) Fe-C-O solution

energy if they are in contact with iron atoms rather than with carbon atoms, i.e. carbon reduces the capactiy of the melt to accomodate Si at low potential energy. This leads to an increase of the activities of the solutes relative to the binary. Such a prediction is confirmed by experiment.

For the Fe-C-O system, the potential energy of Fe-O is lower than that of C-O, as $\Delta\overline{H}_{O,Fe}$ is about -29 kcal/mole and ΔH_{CO} (from the heat of CO formation) is about -26 kcal/mole fig. (6-15.b). It follows by analogy with Fe-C-Si solution that we anticipate a decrease of oxygen activity by carbon relative to the binary, which was observed in the present study.

The interpretation in terms of a simple bond energy argument is not submitted as an adequate explanation of the observed facts, but it is used to show that the present measurements are consistent with commonsense arguments.

3-8 Conclusion

It is considered that the results of this investigation have improved on our knowledge of the Fe-C-O system. The experimental technique which was applied eliminates most of the sources of error which accompanied the previous investigations and allowed the measurements to be extended to very high carbon without a loss of accuracy. Obtaining the graphite saturation within the limits of error caused by thermal diffusion (see chapter 2) is good evidence of this. The technique also allowed the study of the effect of carbon on the activity coefficient of oxygen.

The equilibrium in the reaction between carbon in iron and $CO-CO_2$ gas mixtures was investigated over a wide temperature and composition range (1550-1750°C and 0-0.16 at % carbon).

The equilbrium constant and the free energy changes for that reaction over the temperature range are given by

$$\log K_{1(w/o)} = -6836\ (\pm 187)/T + 6.37\ (\pm 0.087) \quad (3\text{-}19)$$

$$\Delta F^{\circ}_{1(w/o)} = 31275\ (\pm 855) - 29.14\ (\pm 0.443)T \quad (3\text{-}20)$$

The activity of carbon increased by increasing carbon concentration. The activity coefficient expressed for infinite dilute solution depended on the temperature and was not linear

with carbon concentration over the whole carbon range studied. It may be expressed up to 3.0 w/o carbon at 1550°C as

$$\log f_C = 0.135 \text{ (w/o C)} \qquad (3\text{-}18)$$

The thermodynamic properties of Fe-C melt using β-graphite as standard state were tested by evaluating the activity of carbon at the liquidus between the austenite and liquid. The activities derived are in good agreement with the measurements of the activity of carbon in austenite.

The carbon oxygen product was decreased by increasing carbon and nearly independent of temperature and equal to 0.0024 at very low carbon at 1550°C, which is in agreement with all industrial and laboratory measurements. The results showed that carbon increased the activity coefficient of oxygen in molten iron. The activity coefficient of oxygen in Fe-C-O melt is given by

$$\log f_O = 0.1 \text{ (w/o C)} \qquad (3\text{-}42)$$

Assessment of the previous investigations showed that the sources of error present in them led to the wrong belief

that carbon decreased the activity coefficient of oxygen. The carbon has the same effect on oxygen as that on sulphur and tellerium, and this proves the idea of "periodicity". Simple explanations based on the bond energy argument are consistent with the findings of this work.

CHAPTER 4

KINETICS OF THE DECARBURIZATION, AND CARBURIZATION OF LIQUID IRON WITH $CO-CO_2$ GAS MIXTURE AT HIGH PRESSURES

4-1 Introduction

This work was undertaken to examine the effect of pressure on the kinetics of decarburization and carburization around levitated drops in $CO-CO_2$ gas mixtures. By carrying out the reactions at high pressure the importance of diffusion resistance in the liquid phase was magnified. A mixed control model based on the quasi-steady state assumption was developed. The high pressure also decreased the importance of the chemical step of the carburization reactions. The possible rate of the chemical step was examined from the results of this work and of previous studies.

The behaviour of diffusion in levitated drops observed in this study was applied successfully to other investigations.

4-2 Previous work

4-2.1 Decarburization of iron carbon melts

The rate of decarburisation of liquid iron in slag-free melts has been the subject of numerous investigations. However, there is a lack of general agreement in interpreting experimental results and several different views on the rate controlling step have been proposed. These mechanisms have been reviewed by Gunji (78).

Decarburisation of levitated molten iron-carbon drops was studied by Baker and co-workers (79, 80), Distin et al (81), Kaplan and Philbrook (82) and Robertson (5). They concluded that at high carbon (above 1-2 w/o) decarburization occurs by the reactions at the surface of the liquid metal drop

$$C \text{ (in iron)} + CO_2 = 2CO \qquad (4\text{-}1a)$$

$$C \text{ (in iron)} + \tfrac{1}{2}O_2 = CO \qquad (4\text{-}1b)$$

and that the rate was controlled by the mass transfer through the gas boundary layer around the drop. At lower carbon concentration the rates became a subject of controversy. This was mainly because of the complicated nature of decarburisation at low carbons owing to the formation of oxide and carbon monoxide gas bubbles. The critical carbon at which these phenomena occurred depended on the purity of the melts (5), and on the rate of decarburization which controlled the gradients of carbon and oxygen in the molten drops (81).

The work on decarburization of molten dorps during free fall in a column containing an oxidizing atmosphere (83-86) was in agreement with the conclusions drawn from the study of levitated drops.

Decarburization of iron-carbon melts in crucibles by CO_2 and oxygen has been extensively studied. It has been accepted by the majority of workers in the field that, for high carbon alloys, the rate is controlled by diffusion in the gas phase. In this connection reference should be made to the excellent recent works by Nomura and Mori (87), and Fruehan and Martonik (88). The work of Fruehan et al (88) has shown that the results of Swisher and Turkdogan (89) and Ghosh and Sen (90) were in fact consistent with control of the rate by gas phase mass transfer and therefore not determined by a chemical reaction step. They also demonstrated the importance of a resistance in the liquid phase at carbon levels less than 0.5 w/o to the overall rate. At carbons below 0.1 w/o the rates were primarily controlled by diffusion of carbon in the melt. On the other hand Nomura and Mori (91) have suggested that the chemical step is controlling rates at carbons below 0.05 w/o.

4-2.2 Carburization of molten iron

Carburization of liquid iron has not attracted the same degree of attention as decarburization and little work has been carried out on it. Parlee et al (64) measured the rate of carburization of liquid iron alloys containing from 0.15 to 4.4 w/o carbon by absorption of CO using a modified

$$CO \rightleftharpoons C(\text{in iron}) + O(\text{in iron}) \qquad (4\text{-}2)$$

Sieverts apparatus. Their rates, after correction for the side reaction of dissolved carbon in iron with the crucible, was consistent with control by the transport of oxygen in the liquid. King et al (92) also showed that the rates of absorption to alloys of low carbon (ranging from 0.2 - 0.04 w/o) were compatible with control by diffusion of oxygen in the melt.

Distin (93) measured the carburization of liquid iron by flowing pure CO around a levitated drop, through the reaction

$$2CO \rightleftharpoons C(\text{in iron}) + CO_2 \qquad (4\text{-}3)$$

His results were affected by thermal cracking of CO. However the equilibrium carbon concentrations reached for each flow rate were roughly consistent with the measured CO_2 in the exit gases. His interpretation of the results assumed that the rate was controlled by diffusion in the gas phase. His calculations of the mass transfer coefficient were in error and 5 to 7 times higher than the values predicted using the available correlations. This prevented him from drawing any conclusion about the rate controlling mechanism of the reaction.

4-3 Experimental technique

The experimental technique was exactly analogous to that described in the section (3-3) on the equilibrium measurements.

The specimens were kept at the reaction temperature in a flow of helium before introducing the reactant gas. A change of the specimen temperature was caused by introducing the reactant gas. The temperature was adjusted to the reaction temperature in about 10 seconds by the automatic temperature controller. This then maintained a constant temperature of the specimens during the reaction period. The specimens were quenched under pressure at various stages of the reaction, so that each point on the rate curve represents one levitation experiment.

Spec-pure iron specimens and two different batches of prepared Fe-C alloys containing 5.0 w/o and 5.5 w/o carbon were used in the experiments. Each reaction kinetic curve was established using specimens from the same batch.

4-4 Results

Decarburization and carburization reaction rate curves for one gram specimens at 1650°C were obtained from the reaction of iron drops in 1.1% and 2.15% CO_2 gas mixture at a total pressure around 40 atmosphere. The flow rate was fixed at 1 s.l.m. in all runs, to maintain fresh gas flowing past the specimen.

4-4.1 Decarburization by $CO-CO_2$ gas mixtures

As shown in fig. (4-1) the rate of decarburization was increased by increasing the CO_2 in the gas mixture. The time required to reach 80% decarburization toward the equilibrium value with 1.1% CO_2 was found to be twice the time with 2.15% CO_2. The rate of decarburization was not constant and decreased with the approach to the equilibrium.

4-4.2 Carburization by $CO-CO_2$ gas mixtures

The apparatus was not suitable for the study of fast reactions. Experiments could not be carried out with reaction times below 90 seconds, because this was the time required to control the specimen temperature and rotate the turn-table to introduce the quenching mould below the specimen.

In carburization of spec-pure iron, as shown in fig. (4-2), the carbon concentration has reached more than 1.0 w/o carbon in 90 seconds with both gas mixtures. It would appear that the initial rate was independent of the CO_2%. The rates then slowed down markedly as the reaction approached equilibrium. The equilibrium was attained with the 2.15% CO_2 gas mixture in about half the time of that for 1.1% CO_2.

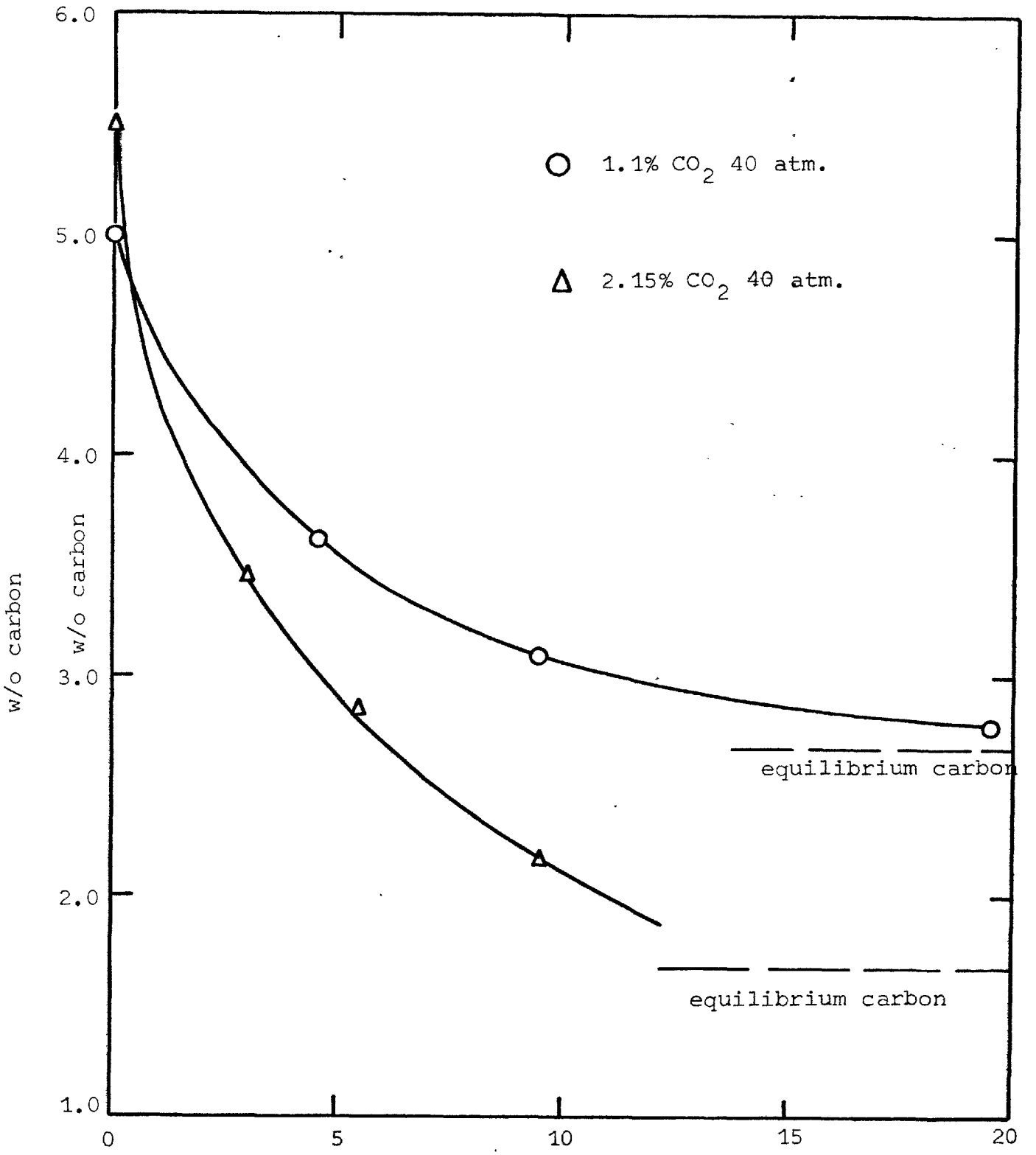

Fig (4-1) Decarburization of Fe-C alloys with CO-CO_2 gas mixture at 1650°C

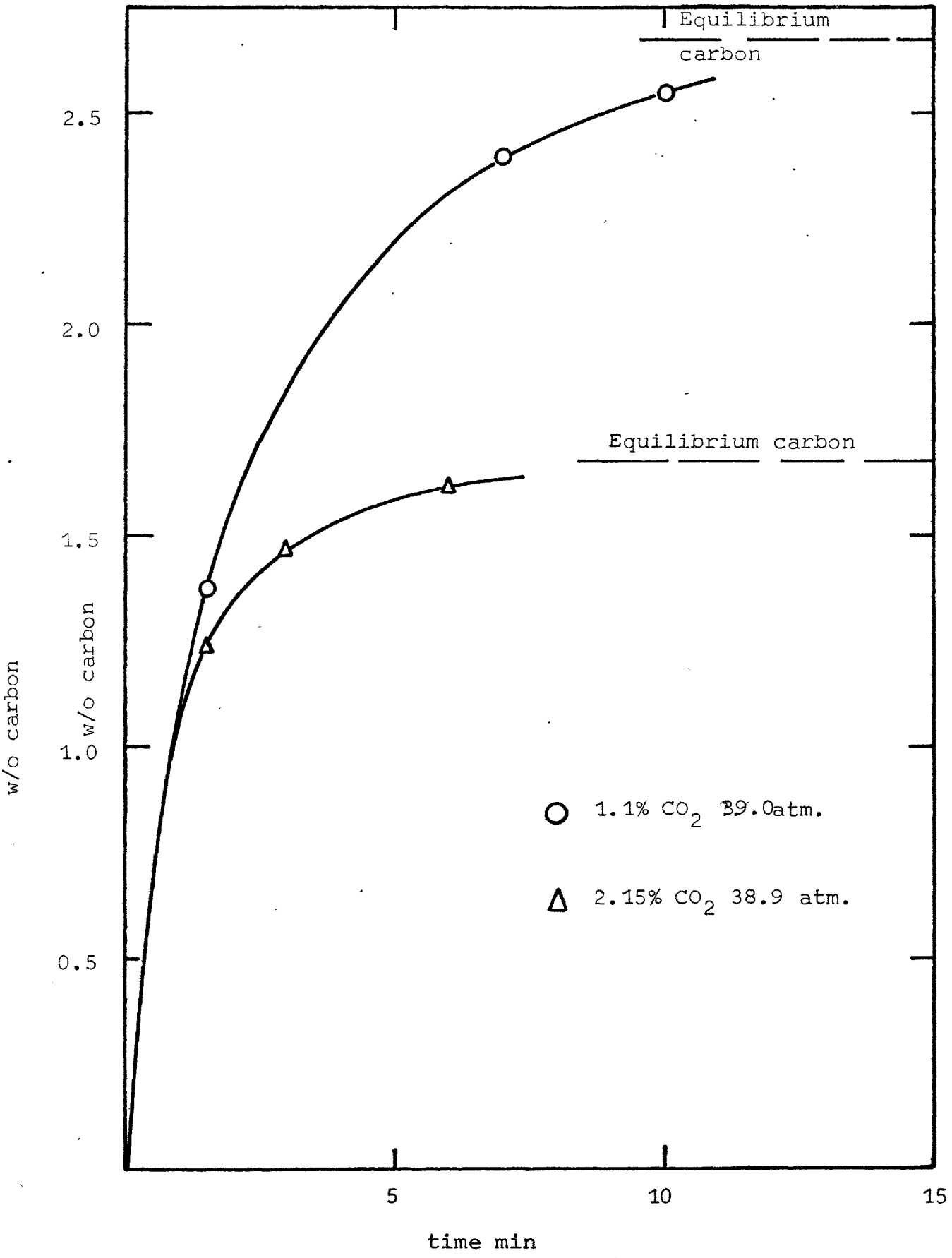

Fig (4-2) Carburization of 1gm iron drops with $CO-CO_2$ gas mixture at 1650°C

4-5 Interpretation of the results

4-5.1 Introduction

The reaction of $CO-CO_2$ gas mixture with molten iron drops either in carburization or decarburization was carried out with bulk gas compositions of lower oxygen potential than that necessary for FeO formation. The mechanism of the reaction

$$C(\text{in iron}) + CO_2 \rightleftharpoons 2CO \qquad (4-4)$$

must have included the following steps:

1) Diffusion of the gases in the boundary layer around the drop.
2) Chemical reaction at the surface of the drop.
3) Diffusion of dissolved carbon in the molten iron.

The measured rate may be determined by one or more of these steps. The mass transfer coefficients in the gas phase boundary layer may be estimated within ± 20 % from the correlation of convective mass transfer obtained in section (2-4.2). Although stirring was observed at the surface of the levitated drops, the characteristics of the stirring in the drops were not known and it was therefore not possible to predict the mass transfer coefficient or the eddy diffusivity in the liquid. However the minimum rate for diffusion in the liquid will be the one for a static sphere. It is interesting to note that, from the solution of the case of unsteady diffusion in a static sphere (94) for one gram drops using a value of 4×10^{-4} cm^2/sec for the molecular diffusivity of carbon in

liquid iron (95), 50% of the reaction would be completed in 6 seconds and 99% of the reaction in 90 seconds. The calculations were carried out assuming there was no resistance to transport in the gas phase or to chemical reaction. The high rate of static diffusion in the drops relates to the small capacity, small diffusion distances and high surface to volume ratio.

The chemical reaction step is the most difficult one to predict while there exist no direct measurements of the chemical rates and while the rate-determing step of the chemical reaction mechanism is unknown. However chemical reactions at high temperatures frequently have a very high rate constant, and may not play any part in determining overall reaction rates.

The results were therefore interpreted assuming that the rate was determined by one or both of the transport steps. If the results cannot be interpreted in this way, it is then usual to assume that a chemical step plays an important part in determining the rate.

4-5.2 Mass transfer in the gas boundary layer

The molar flux of the diffusing species relative to stationary coordinates for an isothermal binary mixtures (without external forces) is expressed as:

$$N_A = -CD\delta x_A/\delta r + x_A(N_A + N_B) \qquad (4-5)$$

The first term represents the diffusion flux due to the concentration gradient while the second term results from the bulk motion of the fluid.

The convective mass transfer around a sphere the velocity and concentration profiles cannot be determined from first principles, and the concept of a mass transfer coefficient is used. The molar flux in equation (4-5) may be represented as (96)

$$N_A = k_g \Delta x_A + x_{As} (N_A + N_B) \qquad (4-6)$$

where k_g is the mass transfer coefficient. As discussed in section (2-4.2) the value of k_g depends on the mass transfer rate and is equivalent to the heat transfer coefficient at the limit of zero flux.

At 40 atmosphere (the pressure at which the experiments were carried out) the gas flow in the boundary layer was found to be dominated by natural convection, and the value of k_g° at zero flux was found to be 4.7×10^{-4} mole/cm^2 sec. Such high mass transfer coefficients, compared with the relatively slow rates of carburization and decarburization observed, imply that the correction for mass transfer rate was negligible. However we shall examine the correction at the maximum rates obtained. The rate factors ϕ (96)

$$\phi = (N_{As} + N_{Bs})/k_g \qquad (4-7)$$

at the maximum rates obtained were -0.0265 and +0.0443 for decarburization and carburization respectively. The correction factors Θ for the effect of mass transfer rate on transfer coefficients

$$k_g^o = \Theta k_g \qquad (4-8)$$

were obtained from the solution of the laminar boundary layer theory for a plate (96), which is a good approximation for the natural convection flow around a sphere. These were 1.02 for decarburization and 0.98 for carburization at the values of ϕ given above. This implies a correction of 2% in the value of k_g. Since the error in estimating k_g could be $\pm$ 20% such a correction can be neglected.

The contribution of thermal diffusion flux N_A^{td} to the flux equations (4-5) and (4-6) due to the steep temperature gradient in the boundary layer (see equation 2-24) may be expressed by

$$N_A - x_A(N_A + N_B) = CD \left[(\delta x_A/\delta r) + K_T (\delta \ln T/\delta r) \right] \qquad (4-9)$$

For the CO-CO_2 mixtures where the Lewis number is nearly unity, the thermal and concentration boundary layer practically coincide, and $K_{(T)}$ is constant for a reacting gas mixture of given composition, (see section 2-3). In this case, integration of equation (4-9) yields:

$$N_A - x_{As}(N_A + N_B) = k_g \left[\Delta x_A + K_T \ln(T_s/T_b) \right] \qquad (4-10)$$

The term $K_T \ln(T_s/T_b)$ in equation (4-10) represents the contribution of the thermal diffusion flux to the mass transfer. The thermal diffusion contribution is therefore constant for any system at constant temperature gradient and reacting gas composition. This term can be represented as an equivalent concentration difference using equation (2-25) as:

$$K_{(\bar{T})} \ln(T_s/T_b) = (\Delta x)_A^{td} \qquad (4\text{-}11)$$

where $(\Delta x)_A^{td}$ is the concentration difference at equilibrium due to thermal diffusion. This term is particularly significant at low concentration differences where Δx_A is comparable with $(\Delta x)_A^{td}$. From equation (4-10) and (4-11) we obtain, for CO_2 represented as component A, that:

$$N_A - x_{As}(N_A + N_B) = k_g (\Delta x_A + (\Delta x)_A^{td}) \qquad (4\text{-}12)$$

equation (4-12) is analogous to equation (4-6). The driving force in equation (4-12) is best written as $(x_{Ab} + \Delta x_A^{td} - x_{As})$. The surface composition will be determined by the carbon concentration in the drop at the drop temperature, and the effect of thermal diffusion is taken account of by using the modified bulk composition x'_{Ab} $(= x_{Ab} + (\Delta x)_A^{td})$.

4-5.3 Mass transfer in levitated molten drops

Although levitated drops are characterised by electromagnetic stirring, the hydrodynamics of this are not known and hence neither is the rate of mass transfer in the liquid. However, the mass transfer coefficient for carbon in the molten drops k_L

$$N_L = k_L \Delta C \qquad (4\text{-}13)$$

will be taken as 0.032 cm sec^{-1}, from the value estimated by Distin et al (81) from his results obtained during decarburization.

The calculated rates of carburization and decarburization assuming no gas phases resistance and either k_L = 0.032 or molecular diffusion in a static drop were much faster than the measured values. However before reaching the conclusion that the mass transfer in the liquid had no effect on the rate the possibility of mixed control was examined.

4-5.4 Combined resistance to transport in two phases (mixed control)

In any gas liquid reaction, there must be a gradient in each phase.

In decarburization and carburization reactions the equilibrium relationship between the diffusing species on the gas (x_{CO_2}) and in the liquid (w/o carbon) is highly nonlinear. It is therefore difficult to make sensible guesses

about interfacial concentrations during reaction or to predict the controlling regime.

The conditions under which there will be mixed transport control have been worked out for reactions obeying Henry's Law (96) of the type

$$A(gas) \rightleftharpoons A(dissolved) \qquad (4\text{-}14)$$

and for reactions obeying Sievert's Law (97) of the type

$$A_2(gas) \rightleftharpoons 2A(dissolved) \qquad (4\text{-}15)$$

and for the reactions between gases and liquid of the type (98)

$$A(gas) + B(dissolved) \rightleftharpoons AB(gas) \qquad (4\text{-}16)$$

e.g.
$$CO + O(in\ copper) \rightleftharpoons CO_2 \qquad (4\text{-}17)$$

In treating the reaction of carbon in iron with CO-CO_2 gas mixtures, equation (4-4), which is in the category

$$A(gas) + B(dissolved) \rightleftharpoons 2AB(gas) \qquad (4\text{-}18)$$

we assume for the reaction at the quasi-steady state condition

1) Instantaneous chemical reaction, i.e. equilibrium between the gas and carbon at the interface.

2) The mass transfer coefficients in the gas and the liquid phases were the same at all the points on the interface.

3) The ratio of k_g/k_L remains constant during the reaction.

The equilbrium curve at 1650°C and 39 atmosphere is shown in fig.(4-3) and was computed from thermodynamic data in section (3-6). In fig.(4-4), which is drawn for a decarburization experiment, the bulk gas composition in an isothermal system at the temperature of the drop is represented by gg, and its equilibrium carbon concentration is the point of intersection of gg and the equilibrium curve at G. The bulk metal carbon concentration is represented by the point L on the line ll. The surface concentration in each phase can be represented by the point s.

From the stoichiometric relation of the reaction (4-4) it follows that $N_C = -N_{CO_2}$ and $N_{CO} = 2N_{CO_2}$. Since the rates of mass transfer in each phase are equal (steady state assumption), so the relation between k_g and k'_L is given as

$$k_g \, (x'_{CO_2 b} - x_{CO_2 s})/(1 + x_{CO_2 s}) = k'_L \, (w/oC_b - w/oC_s) \qquad (4\text{-}15)$$

where k'_L has the units $mol/cm^2 sec$ $\left[w/oC\right]$, since it is convenient to represent carbon concentration in weight percent. The term $(1 + x_s)$ represents the contribution of bulk flow. As shown in fig.(4-3) this term is nearly unity above 0.4 w/o carbon and will be neglected.

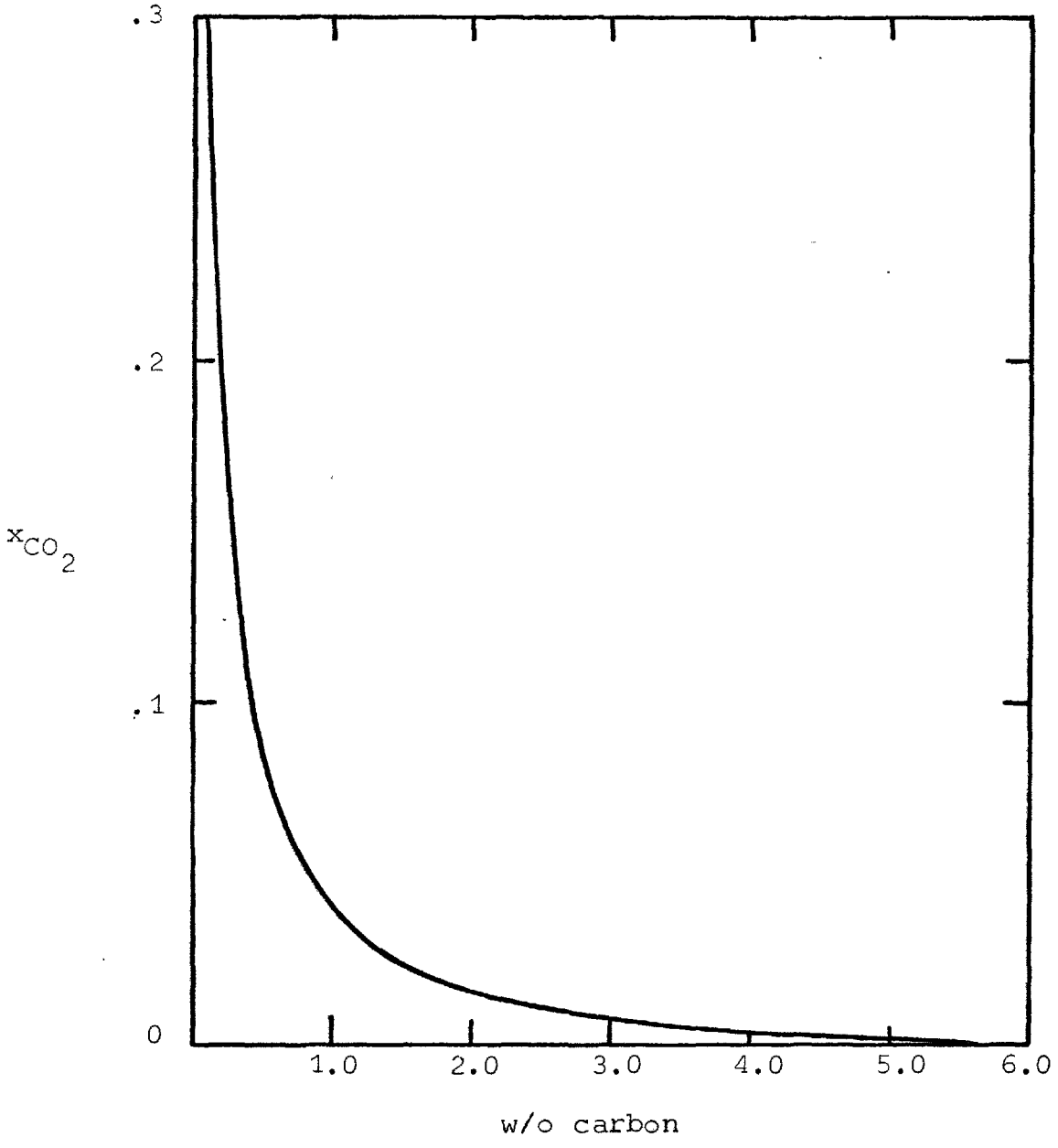

Fig (4-3)

Equilibrium curve of carbon dioxide mole fraction and w/o carbon in molten iron at 1650°C and 39 atmospheres total pressure

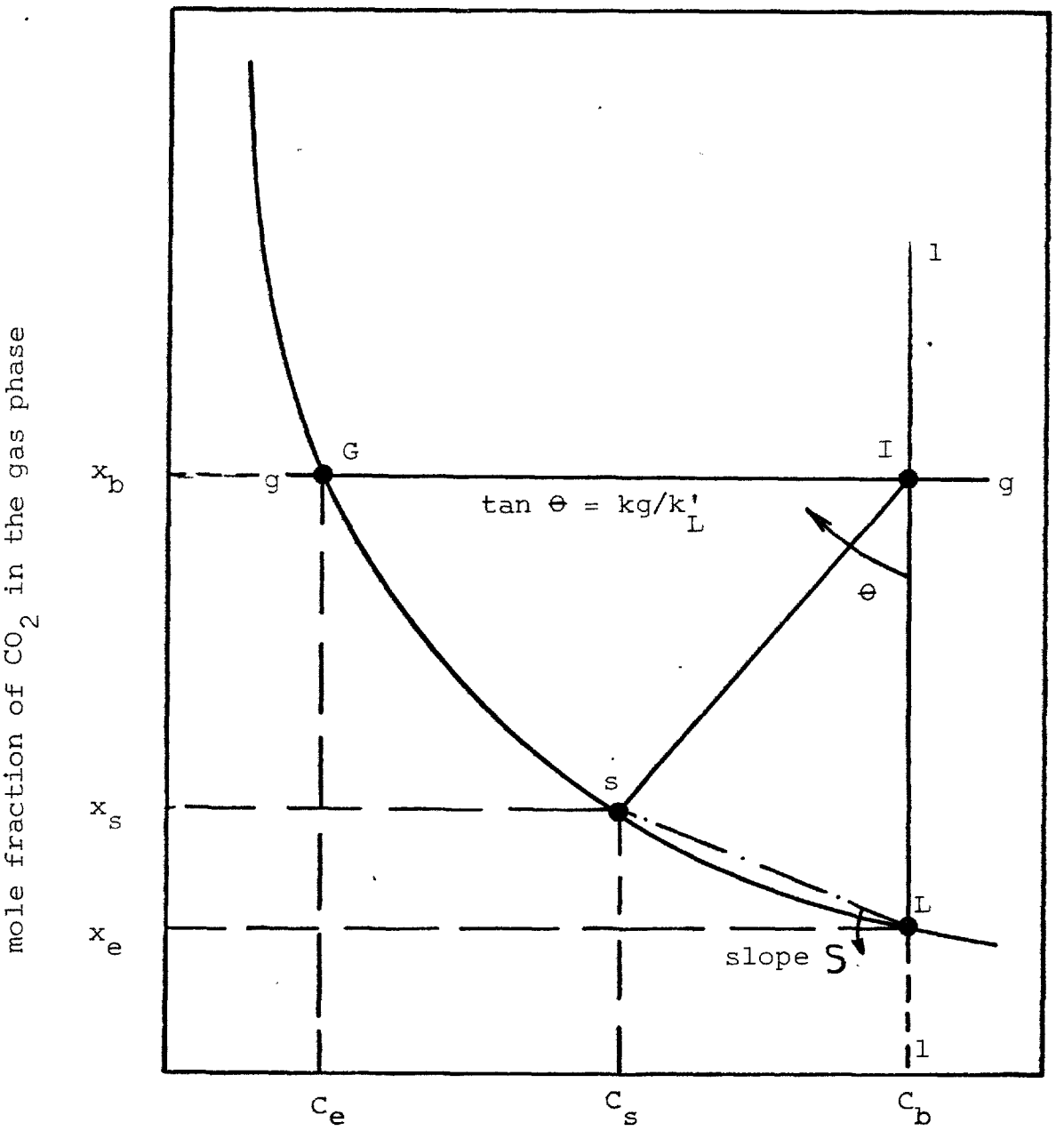

Fig (4-4) Driving forces in interphase mass transfer during decarburization

Equation (3-19) becomes

$$N = k_g(x_b' - x_s) = k_L'(w/oC_b - w/oC_s) \qquad (4\text{-}20)$$

We determine the position of s graphically by drawing a line of slope k_L'/k_g from the point of intersection of ll and gg (I) to intersect the equilibrium line. Rearranging equation (4-20) and writing $w/oC \equiv C$

$$k_g(x_b' - x_e) + k_g(x_e - x_s) = k_L'(C_b - C_s) \qquad (4\text{-}21)$$

$$\frac{k_g(x_b' - x_e)}{k_L'(C_b - C_s)} + \frac{k_g(x_e - x_s)}{k_L'(C_b - C_s)} = 1 \qquad (4\text{-}22)$$

$$(x_b' - x_e)/(x_b' - x_s) = 1 - (k_g/k_L')S \qquad (4\text{-}23)$$

where $$S = (x_e - x_s)/(C_b - C_s) \qquad (4\text{-}24)$$

Here S is now the slope of a line joining the bulk and surface liquid concentrations.

Since the overall coefficient in the gas phase $\overline{k}_g$ is defined by the equation

$$N = \overline{k}_g(x_b' - x_e)$$

the right hand term in equation (4-23) is equal to the ratio $(k_g/\overline{k}_g)$. The reciprocal of this ratio will be defined as η_g.

$$\eta_g = \overline{k}_g/k_g \qquad (4\text{-}25)$$

η_g is a very useful quantity because it defines the extent to which the rate deviates from the value it would have if it were determined purely by transport in the gas phase. In levitation work the fluid dynamics of flow around the drop are well understood and k_g can be accurately predicted from correlations or measured by simple experiments. For this reason results of mixed control are interpreted using η_g and choosing values of k_L to suit. Equation (4-23) becomes

$$\eta_g = 1/(1 - (k_g/k_L')S) \qquad (4\text{-}26)$$

Since the slopes are negative we write

$$\eta_g = 1/(1 + (k_g/k_L')|S|) \qquad (4\text{-}27)$$

From equation (4-27) it follows that when $k_g/k_L'|S|$ approaches zero, η_g is nearly unity and hence transport in the gas phase controls the rate. At high values of $k_g/k_L'|S|$, η_g becomes less than unity and mass transfer in the liquid phase affects the rate. The ratio of k_g/k_L' is in general constant for any system and defined from the physical properties and the flow characteristics of the gas and liquid phases. The parameter S is defined mainly from the equilibrium relation of the reactant species, and its limit for small concentration gradients (close to equilibrium) is the slope of the equilibrium curve at the point under consideration.

The graphical procedure is not convenient for the evaluation of S and η_g from equations (4-24) and (4-27) respectively during the course of the reaction. The interfacial concentrations can be evaluated from the following relations. The surface and bulk concentration of carbon are related by

$$C_b = C_s + (k_g Z/k_L'^2)(1 - \sqrt{4/Z + 1} - (C_s f_s/C_e f_e)(1 - \sqrt{(4C_e f_e/C_s f_s Z) + 1})) \qquad (4\text{-}28)$$

where Z defines the composition of the reacting $CO-CO_2$ gas mixture

$$Z = (x_{CO})^2/x_{CO_2} \qquad (4\text{-}29)$$

and f is the activity coefficient of carbon and can be evaluated from (see section (2-6))

$$\log f = 0.116 \quad (w/o\ C) \qquad (4\text{-}30)$$

At higher carbon concentration above 3 w/o equation (4-30) is not valid, and the values of f_c must be obtained from fig.(3-4). However the near linear slope of the equilibrium curve at this carbon range provides a constant value of S.

The values of the mole fraction of CO_2 can be obtained from carbon concentration as

$$x_{CO_2} = 1 + \frac{Cf\,K}{2P_t}\left[1 - \sqrt{4P_t/Cf\,K + 1}\right] \qquad (4\text{-}31)$$

where k is the equilibrium constant of the reaction (4-4).

A final point about the mixed control model discussed on the previous page is the effect of total pressure on the η_{kg} value. From equation (4-27) at constant (k_g/k_L'), η_g is affected by the slope of a line joining bulk and surface liquid concentrations S which depends on the shape of the equilibrium curve. Since the reaction is pressure dependent the shape of the equilibrium curve not only depends on the equilibrium constant but also on the pressure, equation (4-31), i.e. the ratio of K/P_t. It can be shown that as the ratio K/P_t increases the curve is shifted toward lower carbons and shows a steeper transition. Therefore η_g will have a steeper change from nearly zero value initially liquid carbon (transport control in the liquid) to unity at about 0.1 w/o carbon (gas phase control). The effect of total pressure is to determine the concentration at which the transition from pure liquid phase to pure gas phase control occurs and the sharpness of that transition.

For the purposes of the following paragraph we will discuss mixed control using the experimental conditions of 1.1 and 2.15% CO_2 gas mixture and 39 atmosphere total pressure. at 1650°C with (k_g/k_L') of 2.5 w/o.

The values of η_g were computed from equations (4-27) to (4-31), and are given in fig. (4-5). η_g was found to be effectively the same for both gas mixtures.

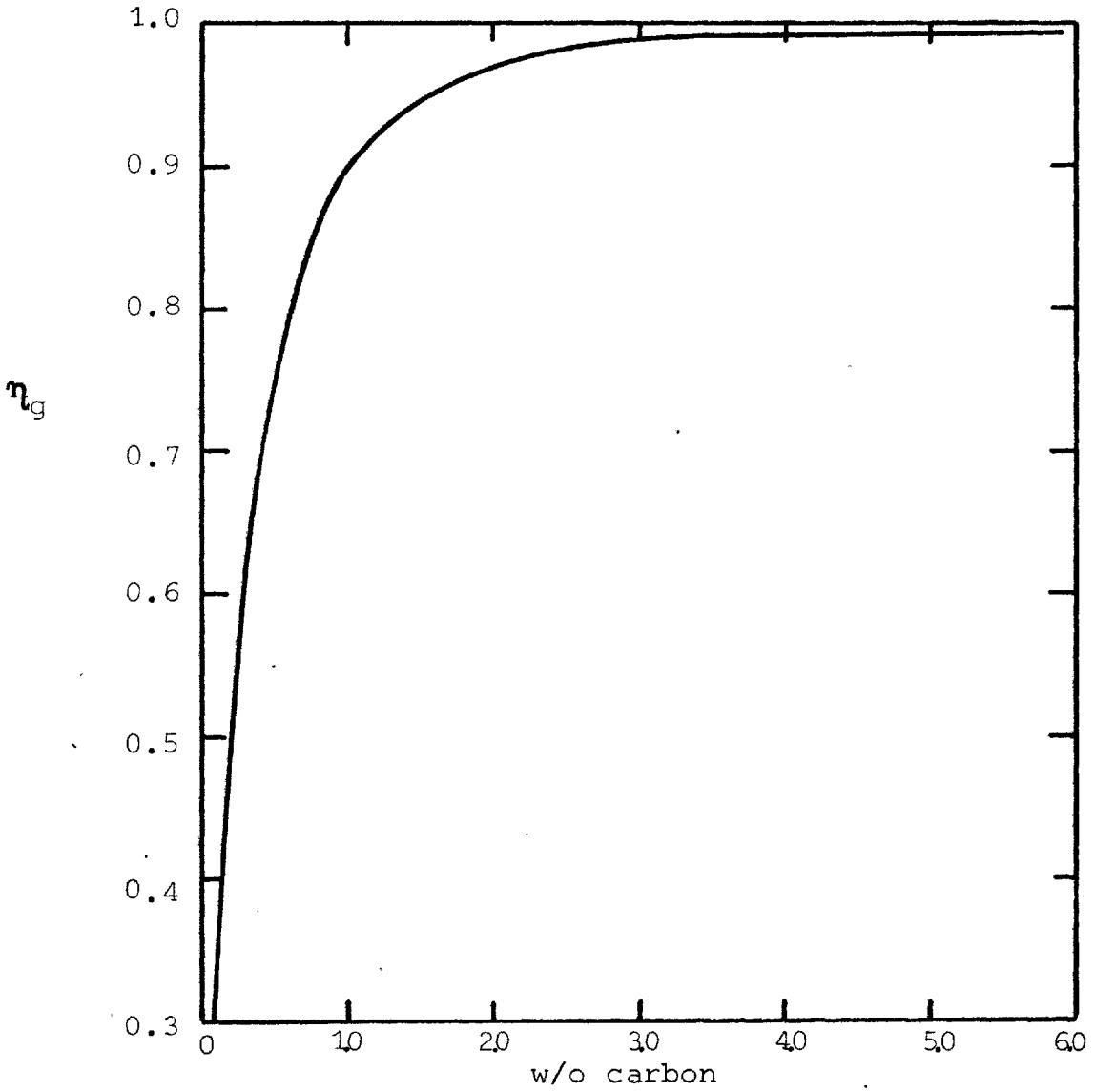

Fig (4-5)

Overall to the actual gas phase mass transfer coefficient against w/o carbon at 1650°C and 40 atmospheres total pressure for 1.1 and 2.15% CO_2

In the decarburization situation (C>3.0 w/o) the values of η_g were constant and nearly unity and the reaction rate will be gas phase controlled. The small change in the overall gas phase mass transfer coefficient of about 5% was much smaller than the error in estimating k_g from the correlation, and can be neglected.

In carburization η_g is small at very low carbon, but as the reaction proceeds it will progressively increase until close to equilibrium it is nearly unity. Thus the importance of gas phase control will progressively increase from the start of the reaction and certainly exhibits perfect mixed control over some part.

4-5.5 Decarburization results

From the previous discussion, the rate of decarburization will be controlled by diffusion in the gas phase for carbon concentrations above 3 w/o if the chemical step is fast. The decarburization rate of the iron-carbon drops is given by

$$dC_b/dt = 1200A\, N_C/w \qquad (4\text{-}32)$$

$$= \frac{1200\, A\, \bar{k}_g}{\omega} (x'_{CO_2 b} - x_{CO_2 e}) \qquad (4\text{-}33)$$

$\bar{k}_g$ is equal to $\eta_g k_g$ and figure 4.5 shows that η_g is close to unity above 3 w/o carbon.

The condition of interfacial equilibrium relates x_{CO_2e} to bulk carbon concentration of the drop by equation (4-31). Equation (4-33) may be rewritten as

$$\frac{\omega}{1200A}\int_{C=C_0}^{C=C}\frac{dC}{x'_{CO_2b} - f(C)} = \eta_g k_g \int_0^t dt \qquad (4\text{-}34)$$

The gas phase mass transfer coefficient was obtained by comparing the experiment rate curve with the computed rates from solving equation (4-34) at all times for different values of k_g with η_g equal to unity. The left hand term in equation (4-34) was integrated numerically since $f(C_b)$ is a complicated function (see equation (4-31)) and no analytical solution can be obtained for the integral. The resulting plots are given in fig.(4-6) and fig.(4-7) for 1.1% and 2.15% CO_2 respectively.

The results of decarburization with 1.1% CO_2 were found to be in good agreement over the whole length of the predicted rate curve at k_g of 4.5×10^{-4}, fig. (4-6). The k_g value is nearly equal to the estimated value obtained from convective mass transfer correlations (see section 4-5.2)). Equally good agreement was found between the experimental points of decarburization with 2.15% CO_2 above 3 w/o carbon and the predicted rate curve at the same value of k_g - fig.(4-7). The experimental points below carbon levels of 3 w/o showed a decrease of the value of k_g to a value of 3.5×10^{-4} near the equilibrium. This was running parallel with the decrease of η_g below 3 w/o carbon, fig. (4-5). But the extent of decrease

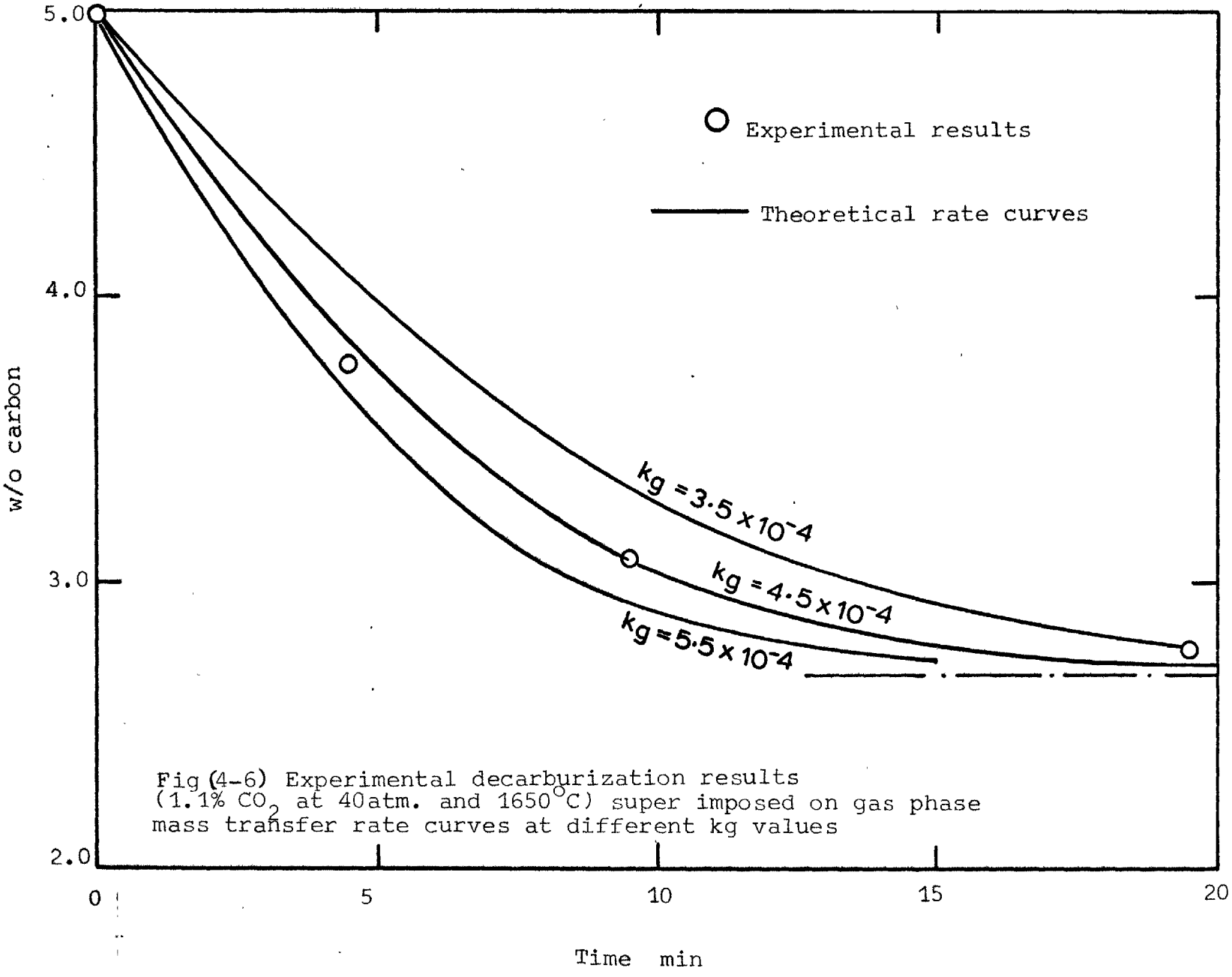

Fig (4-6) Experimental decarburization results (1.1% CO_2 at 40atm. and 1650°C) super imposed on gas phase mass transfer rate curves at different kg values

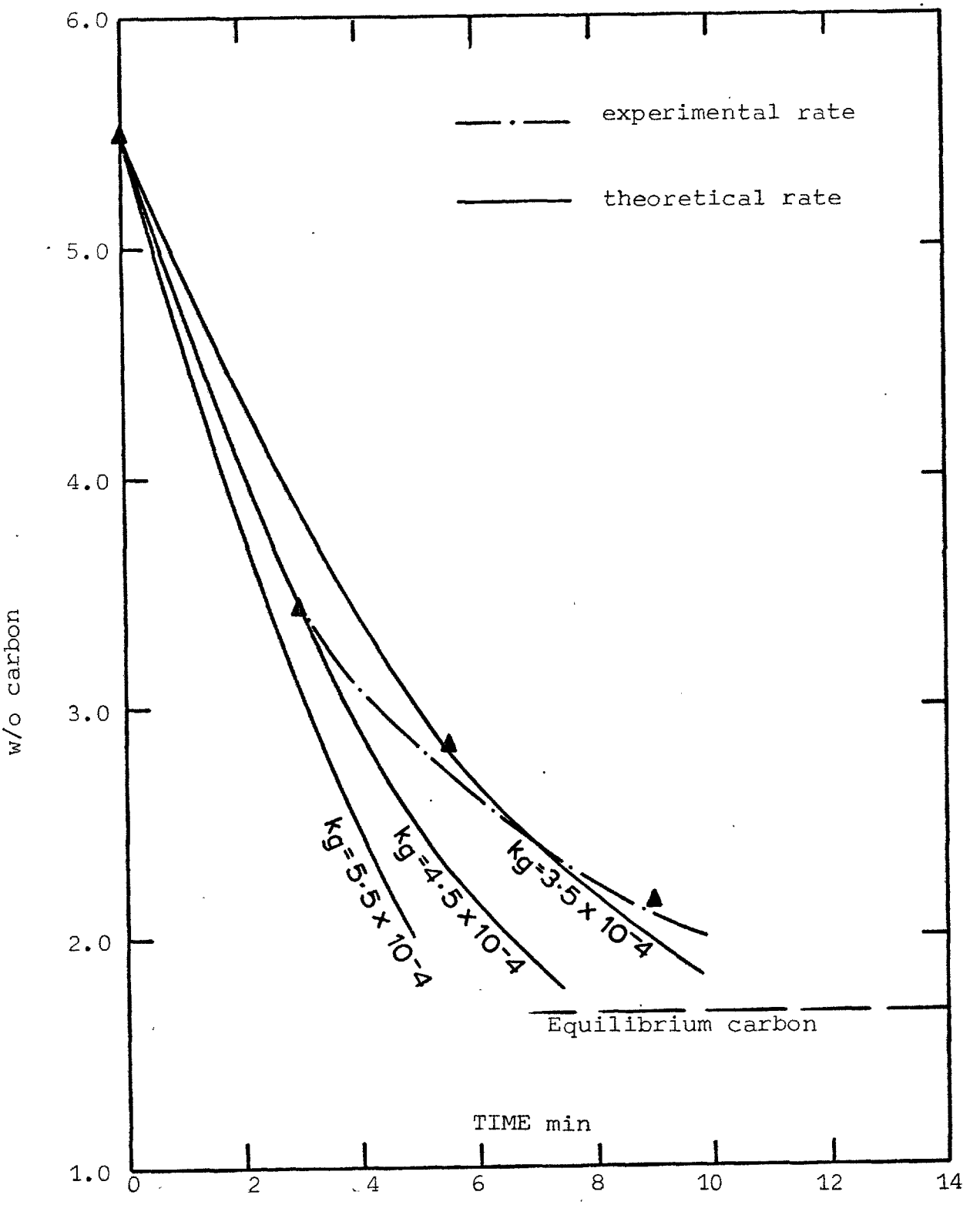

Fig (4-7) Experimental decarburization results (2.15% CO_2 at 40 atm. and 1650°C) super imposed on gas phase mass transfer rate curves at different kg values

in η_g predicted was not as great as observed. One explanation for this discrepancy could be that k_L was lower than the value of 0.032 cm/sec. This could not affect the situation at carbon concentration above 3 w/o where η_g is close to unity even for k_L of 0.0032.

4-5.6 Carburization results

During carburization the liquid phase resistance could not be ignored when interpreting the results, assuming the rate to be determined by a transport mechanism. It follows from conservation of mass that

$$\frac{dC_b}{dt} = - \frac{1200\ A}{\omega} N_C \qquad (4-35)$$

where N_C is defined by equation (4-20), and may be represented as

$$N_C = k_g \eta_g \left[x_{CO_2 e} - x'_{CO_2 b} \right] \qquad (4-36)$$

where η_g is a continuous function of bulk carbon concentration fig.(4-5), and k_g has a value of 4.5×10^{-4} mol/cm^2 sec., which was obtained from decarburization experiments. k_g/k'_L was taken as 2.5 on a first assumption.

The experimental rates for carburization with 1.1% and 2.15% CO_2 were slower than the calculated rates under these conditions, fig. (4-8) and fig.(4-9). Since k'_L was the only unknown parameter, solution of the equations was carried out

for different values of k_g/k'_L, and the experimental results were reproduced with k_g/k'_L in the range of 20 to 25 (k_L = 3.2 - 2.7 x 10^{-3} cm/sec). Although this value seems to be low for a stirred liquid, the abscence of any information concerning the stirring of the levitated drop makes it impossible to assess this value. However the minimum rate of the transport mechanism would be that for unsteady state diffusion in a stagnant drop (sphere) with variable surface concentration defined by the flux in the gas phase and gives a clear cut model for comparisons with the results. If the measured rate is below the rate predicted for static diffusion in the drop plus convection in the gas phase then a chemical step must be rate controlling.

The minimum rate of transport was obtained by solving the radial diffusion equation in a sphere

$$\frac{\delta C}{\delta t} = D\left(\frac{\delta^2 C}{\delta r^2} + \frac{2}{r}\frac{\delta C}{\delta r}\right) \qquad (4\text{-}37)$$

with the flux equation

$$N_C = -N_{CO_2} = -D\left(\frac{\delta C}{\delta r}\right)_{r=a} = k_g(x_{CO_2 s} - x_{CO_2 b}) \qquad (4\text{-}38)$$

where the boundary conditions were

$t = 0$	$0 \leqslant 1 \leqslant a$	$C = 0$
$t \geqslant 0$	$r = a$	$C_a = f(x_{CO_2 s})$

These equations were solved numerically using the finite difference method developed by Crank and Nicolson (94,99). The method of solution is given in Appendix (4-1). The curves for carburization showed a remarkable agreement with carburization by 1.1% CO_2, fig.(4-8) and a slightly slower rate than that observed with 2.15% CO_2, fig.(4-9).

The results do not firmly prove where the control step lies, whether in chemical reaction or mass transfer. This point will be taken up in the discussion, section (4.6).

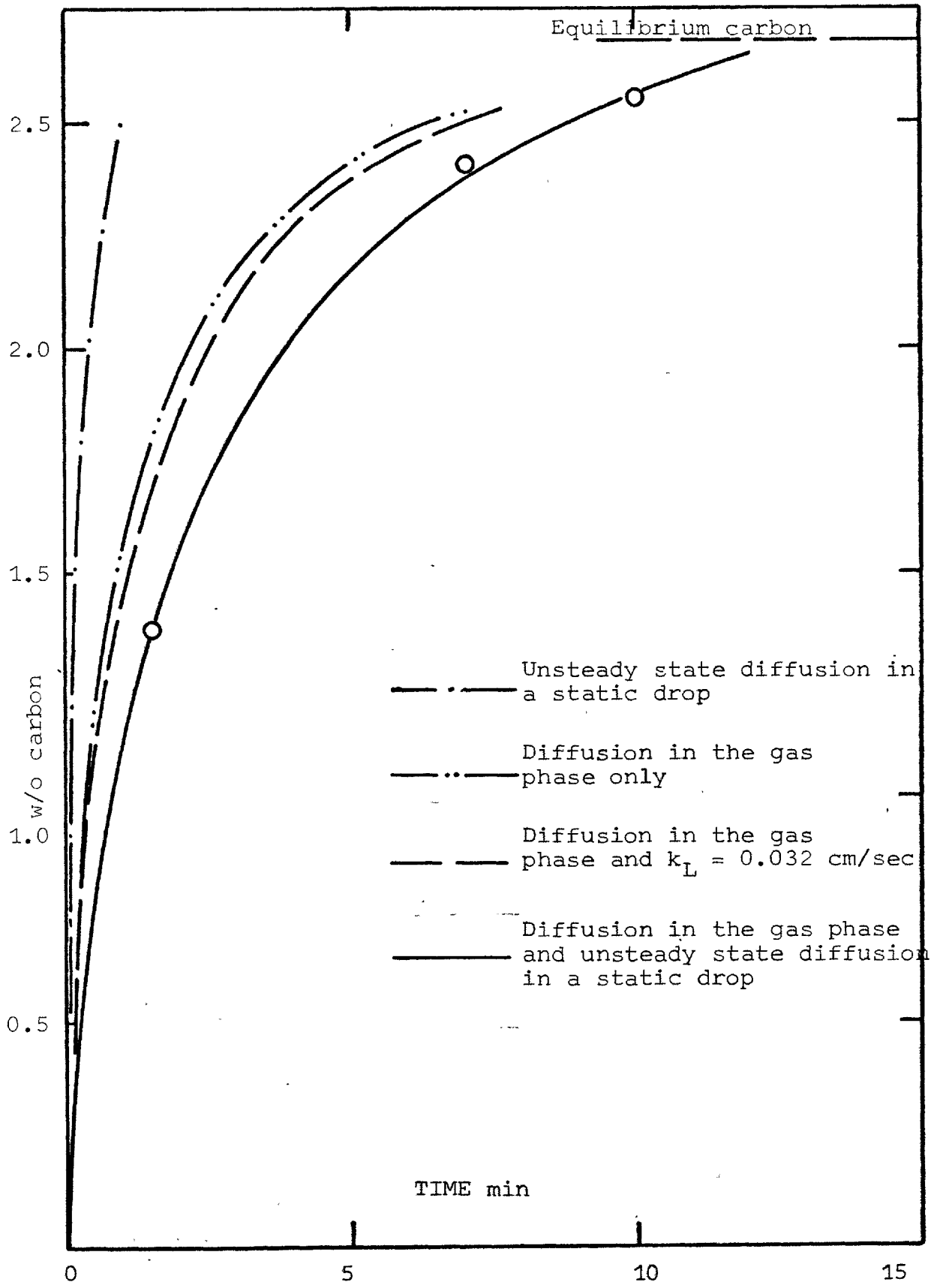

Fig (4-8) Experimental carburization results (1.1% CO_2 at 39 atm and 1650°C) compared with theoretical rates for different transport models

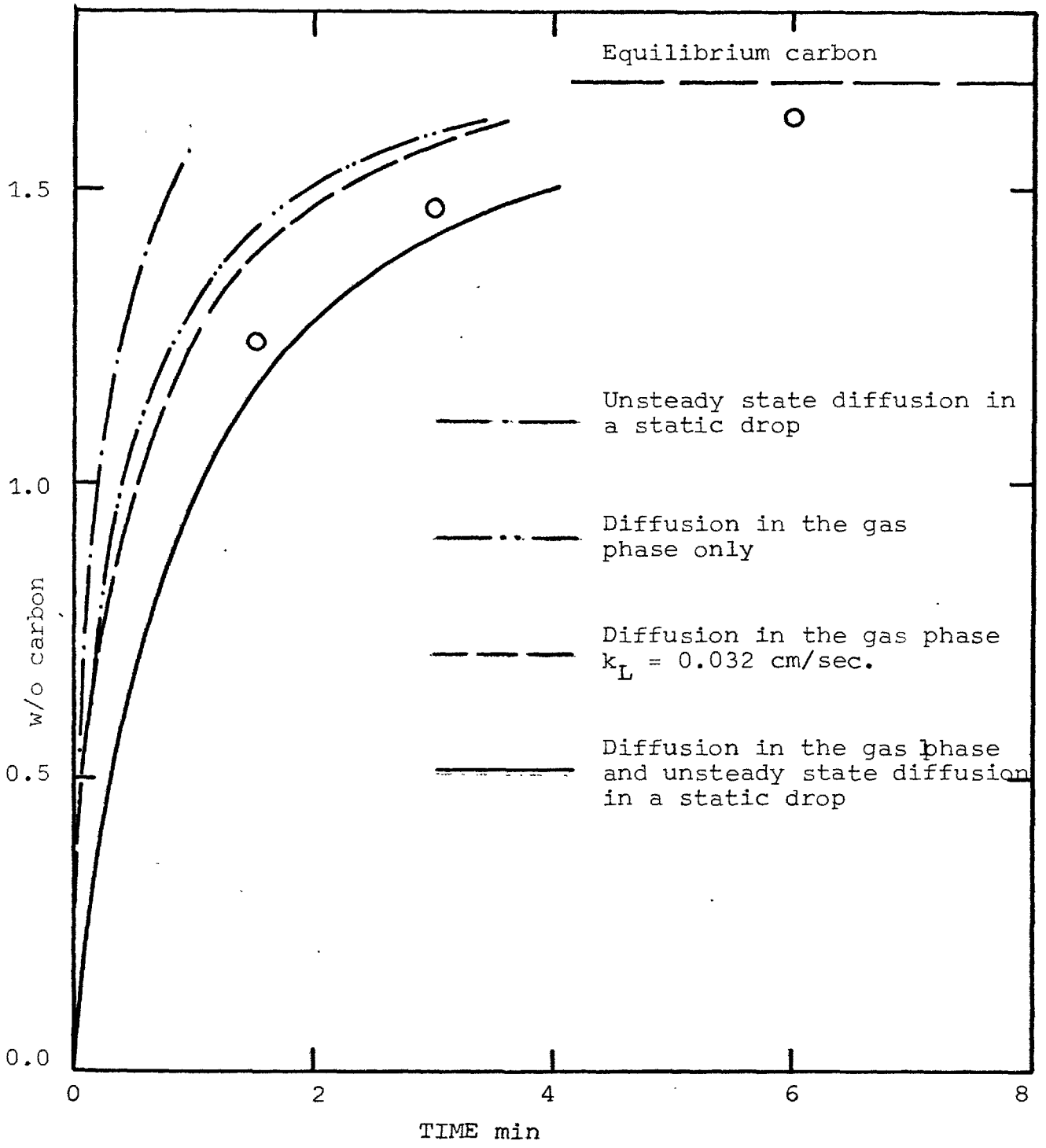

Fig (4-9) Experimental carburization results (2.15% CO_2 at 38.9 atm and 1650°C) compared with theoretical rates for different transport models

4-6 Discussion

4-6.1 Introduction

The aim of this work was to examine the carburization and decarburization reaction mechanism under the experimental conditions of high pressures and high gas phase mass transfer coefficients. These conditions enhance the importance of the liquid phase resistance. At one atmosphere transport in the gas phase has already been established as the rate controlling step in decarburization of high carbon alloys (particularly for levitated drops) as well as for the carburization reaction after recalculation of Distin's rates (93). For this reason the study of the kinetics of carburization and decarburization in this research was not comprehensive. However the work provided a sound basis for accurate prediction of the time required for the specimen to attain the equilibrium in the thermodynamic measurements and prior to bubble nucleation.

The few experiments which were carried out in decarburization were enough to satisfy the purpose of this study. On the other hand the carburization experiments were not sufficient to give a complete picture of the importance of the diffusion behaviour in levitated drops. For this reason the possibility that the chemical reaction might be the rate controlling step is discussed. Data from other sources were used to provide more information.

4-6.2 Kinetics of decarburization of Fe-C drops

The interpretation of the decarburization results in section (4-5.5) conclusively showed that the process of gaseous diffusion controls the overall rate, at high carbon, as would be expected from the previous investigations. The results with 2.15% CO_2 gas mixtures show the importance of the diffusion in the liquid phase at carbon below 3 w/o by lowering the overall mass transfer coefficient in the gas phase $\overline{k}_g$, as shown by the combined diffusion model section (4-5.4). In order to reproduce the experimental results using the mixed control model the liquid phase mass transfer coefficient k_L must be lower than the value of 0.032 cm/sec obtained by Distin et al (81). It is interesting to note that the lower k_L in levitated drops observed in this work has no effect on the rates of decarburization observed by Baker (29) or Distin (81) at one atmosphere. This is primarily due to the effect of the ratio K/P_t in the mixed control model (see section (4-5.4)). At 1 atm. K/P_t becomes large and hence $1S1$ is of the order of 10^{-3}, above 1 w/o carbon. This means that values of (k_g/k'_L) as large as 40 (i.e. k_L 0.0015), have practically no effect on the value of η_g which is unity. It is important to realise that liquid phase mass transfer coefficient cannot be decreased indefinitely, since the assumptions inherent in its use fail when the flux becomes comparable with the molecular diffusion flux.

The experimental conditions of this work at high pressures and high carbons nearly simulate those at atmospheric pressure and low carbons. The observed importance of liquid phase

resistance must act in slowing down the measured decarburization rates at one atmosphere from fast gas phase to slow liquid phase as decarburization proceeds. This may settle the controversy in the interpretation of rates of decarburization at low carbons. It is worth mentioning that in order to interpret thier results during the transition from gas phase control Nomura and Mori (91) used the criteria, such as flow rate and gas composition, which control the transition towards liquid phase control. They interpreted their results as showing a transition towards chemical control but this may not be correct.

4-6.3 Kinetics of carburization of Fe-C drops

The carburization, results, as shown in section (4-5.6) could not be explained in terms of the transport in the gas phase alone, where the gas phase mass transfer coefficient k_g was well known (see section (2-4.2)) and showed a good agreement with decarburization rate measurements. This was due to the effect of a resistance in the liquid phase which must be included in the mixed control model, section (4-5.4). In order to interpret the results with the mixed control model, k_L must be much lower than the Distin value of 0.032 cm/sec. This is also observed in the decarburization results. Combining quasi-steady state mass transfer in the gas phase with unsteady state molecular diffusion in a static sphere gave remarkable agreement with the measurements. It has hitherto been assumed that the surface movement of levitated drops implied a vigorous stirring in the bulk of the drops, so before introducing the idea that

levitated drops behave as unstirred spheres the possibility of the chemical step controlling the rate in carburization must be examined.

In the absence of measurements of the chemical rate of carburization of liquid iron in $CO-CO_2$ atmospheres, we may seek the information from carburization of austenite. Grabke (100) described the mechansim of carburization (or decarburization) by the two elementary steps

$$CO_2 \underset{k'_1}{\overset{k_1}{\rightleftharpoons}} CO + O \text{ (ads.)} \qquad (4\text{-}39)$$

$$O \text{ (ads.)} + C \text{ (in iron)} \underset{k'_2}{\overset{k_2}{\rightleftharpoons}} CO \qquad (4\text{-}40)$$

where k_1, k_2 are the rate of forward reactions, and k'_1, k'_2 are the rate of backward reactions. The rate of carburization may then be represented as

$$N_C = k_1 P_{CO_2} (C_e/C - 1) \qquad (4\text{-}41)$$

From equation (4.41) the rate of the reaction depends on k_1 and total pressure of CO_2 at any extent of the reaction. Increasing the pressure of CO_2 increases the rate of reaction relative to one atmosphere. k_1 was found to be 10^{-3} at 1650°C (100) and at fourty atmospheres and 1650°C gives a rate much higher than the rate for either pure gas phase control or static diffusion alone in the drop.

So in the present work at about 40 atmospheres and 1650°C the chemical rate must have been so high that it has no effect on kinetics of carburization.

On the other hand increasing the pressure acts to magnify the effect of the liquid phase resistance by decreasing K/P_t (see section 4-5.4). This makes Distin's (93) measurements of carburization at one atmosphere another test on the chemical rate. If carburization is chemically controlled the rate will be much slower than that for gas phase control, but if its transport controlled it it will be equal to the gas phase control rate since the liquid phase resistance has nearly no effect on carbons above 0.1 w/o, as deduced from the combined diffusion model. From his results Distin (93) calculated gas phase mass transfer coefficients which were five to seven times greater than the values estimated either using the mass transfer correlations or the values obtained from the decarburization experiments. These calculations were in fact subject to error due to assumptions used to simplify the rate equation (equation 4-33). These assumptions were made so that the equation would be amenable to analytical integration. There was also an error in the integrated form of the equation. Recalculation of Distin's (93) carburization rates using equations for the gas phase mass transfer given in section(4-5.2)were carried out with no simplification of the rate equation (4-35), by numerical integration. The predicted gas phase mass transfer rates at the experimental conditions given by Distin were in general agreement with his results, taking into account the inconsistency of CO_2 measurements with the obtained equilibrium carbon, fig.(4-10). This

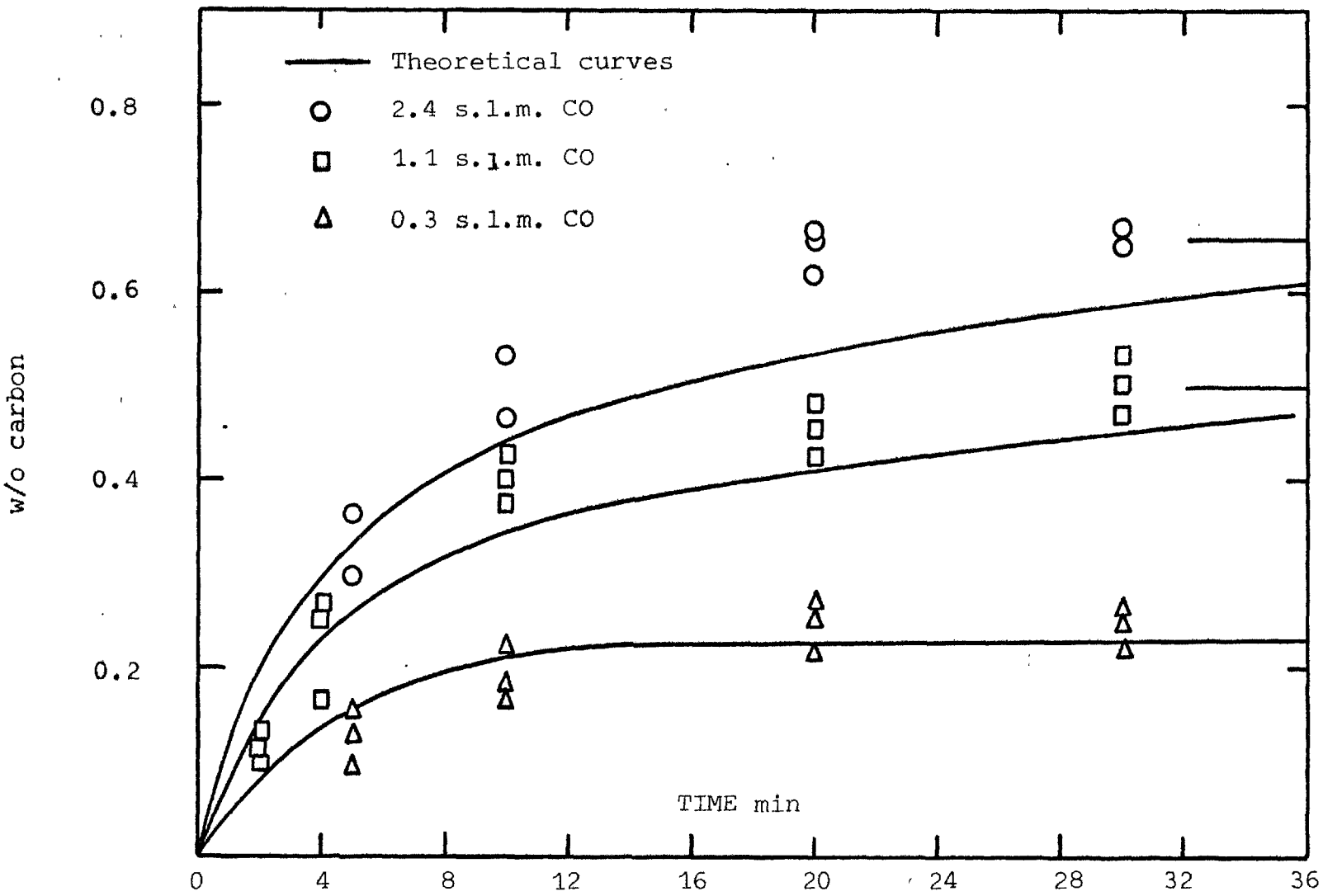

Fig (4-10) Carburization of levitated molten drops in CO by Distin (93)

confirms that the chemical rate was not controlling in the present measurements of carburization at high pressures.

From the above discussion, all the evidence indicates that levitated drops ($<$1 cm diameter) behave as though they are static with respect to internal diffusion. Because of their small size even static diffusion is a rapid process and this has mislead many investigators into believing that the drop is well stirred. There are no examples in all the published work on gas-liquid metal reactions using the levitation technique, and in which the reaction mechanism is that described in section (4-5.1), where the measured rates are higher than those for mixed control with static diffusion in the drop. Forster and Richardson (101) studied oxidation and deoxidation of molten copper and nickel using $CO-CO_2$ gas mixtures. They measured rates less than the rate of diffusion in the gas phase as well as in the liquid phase using the k_L of 0.032 cm/sec. obtained by Distin et al (81). The possibility of mixed control was not considered, and they went ahead to interpret the results as chemically controlled. It was found, from examining the oxidation reaction by the mixed control model, that it should exhibit perfect mixed control over some part of the reaction. Reinterpretation of Forster and Richardson's results (101) using the mixed control model with static diffusion are shown in figs. (4-11) to (4-14). The theoretical curves have been drawn for the starting and finishing temperatures reported by Forster and Richardson.

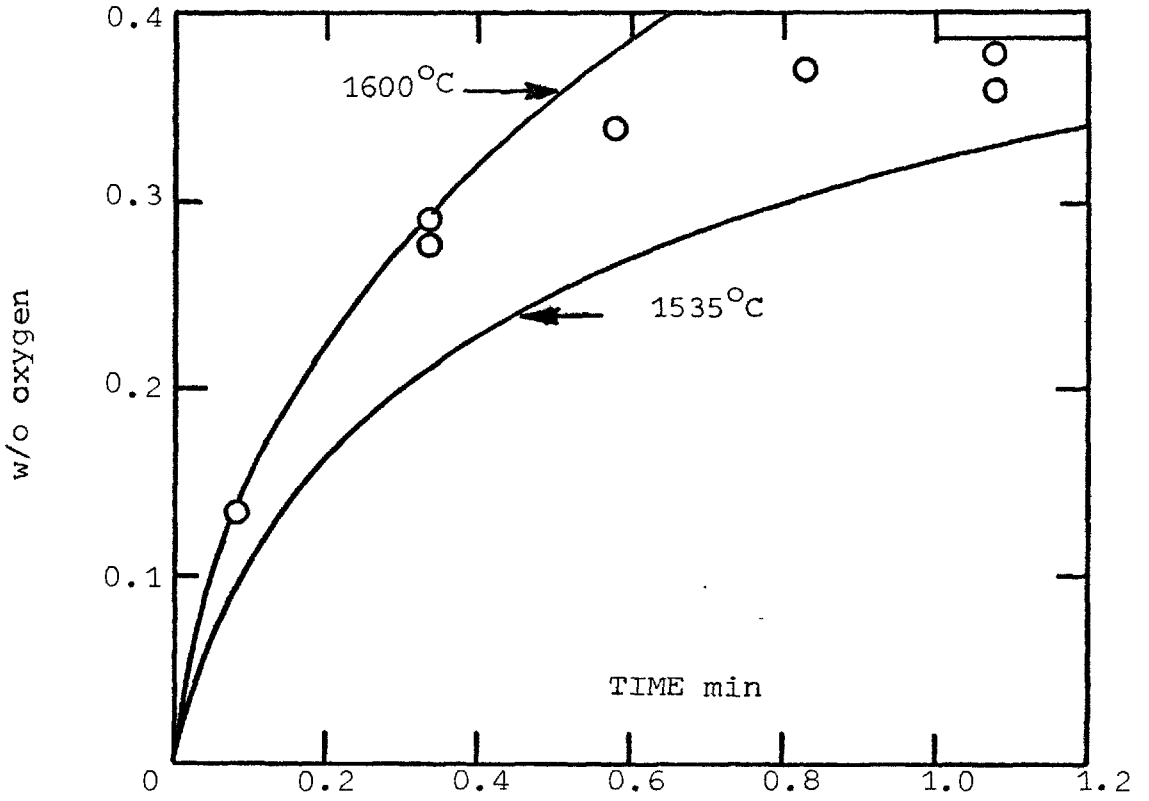

(a)

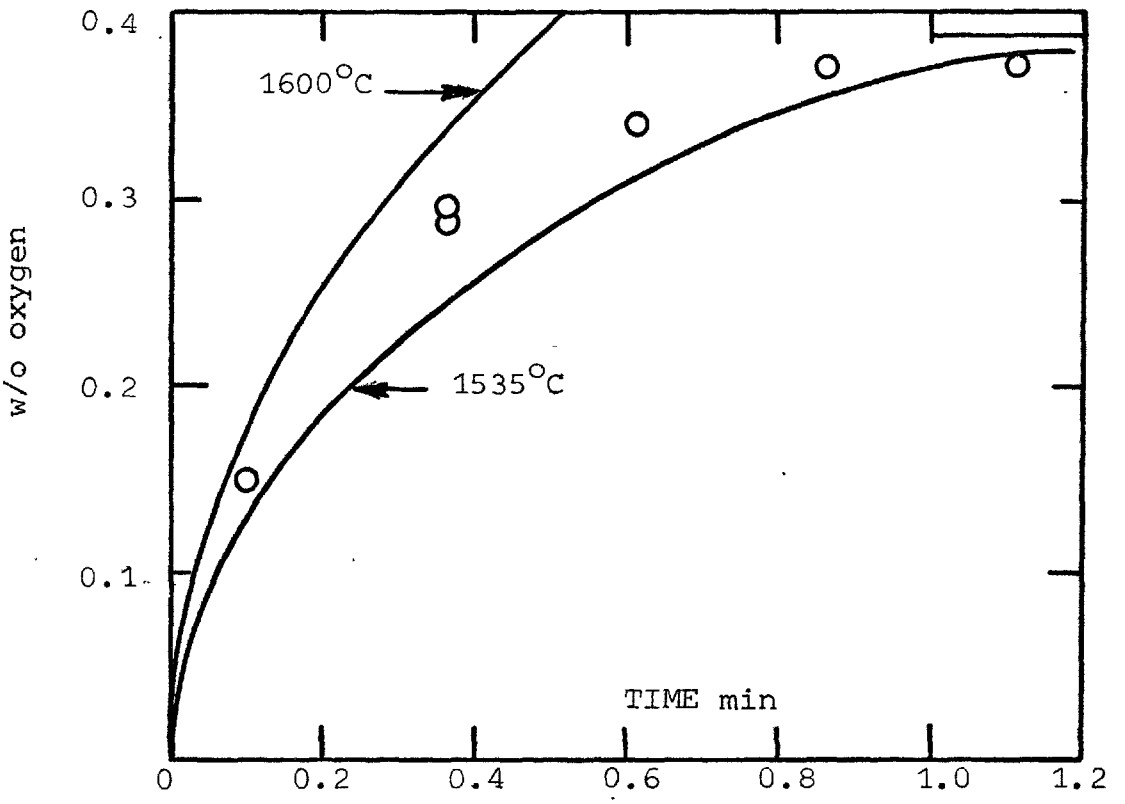

(b)

Fig (4-11) Transfer of oxygen to 0.5gm copper drops with CO/CO_2 = 1/50

(a) 5.1 s.l.m. (b) 12.065 s.l.m.

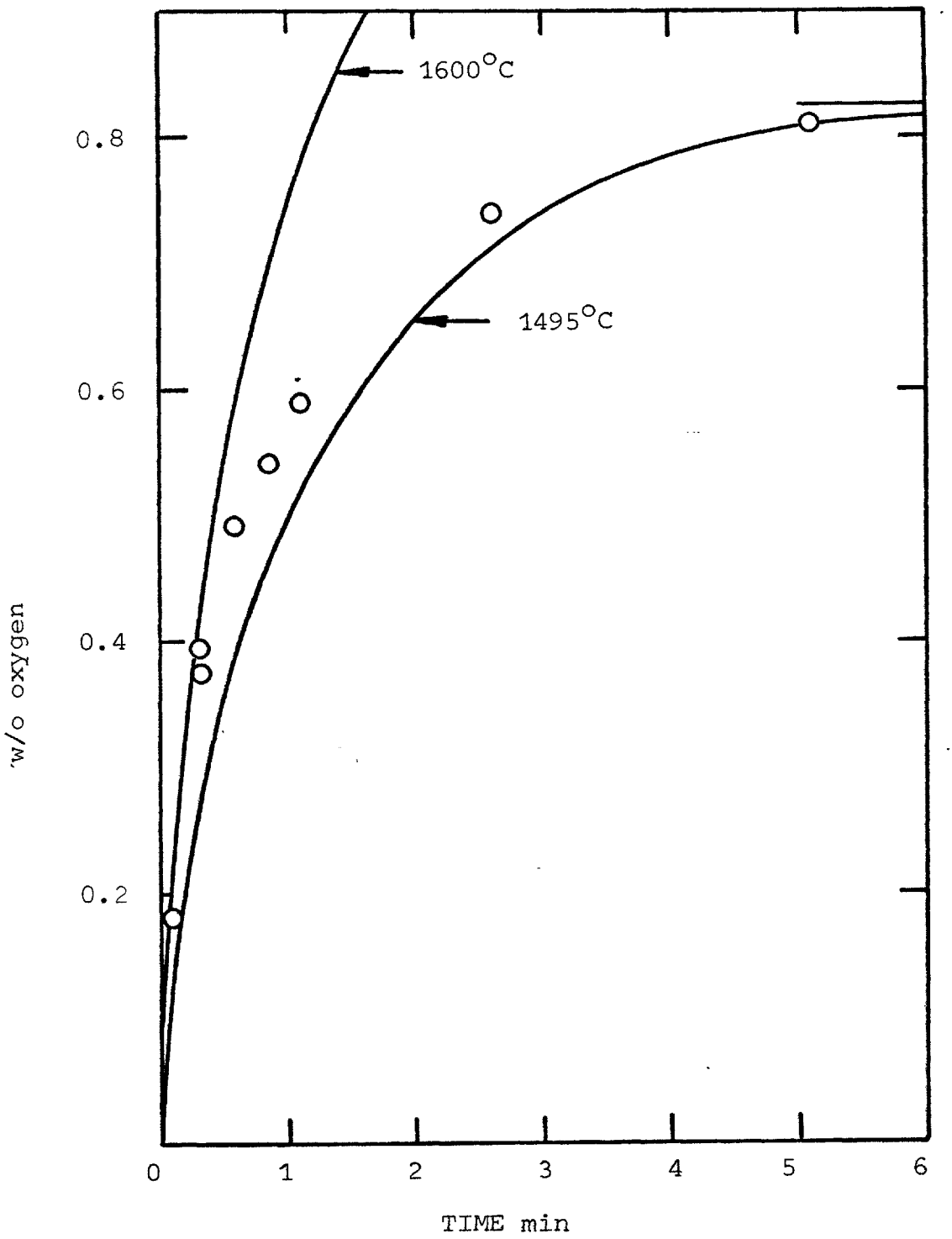

Fig (4-12) Transfer of oxygen to 0.5g. copper drops with CO/CO_2 = 1/130; flow 8.767 s.l.m.

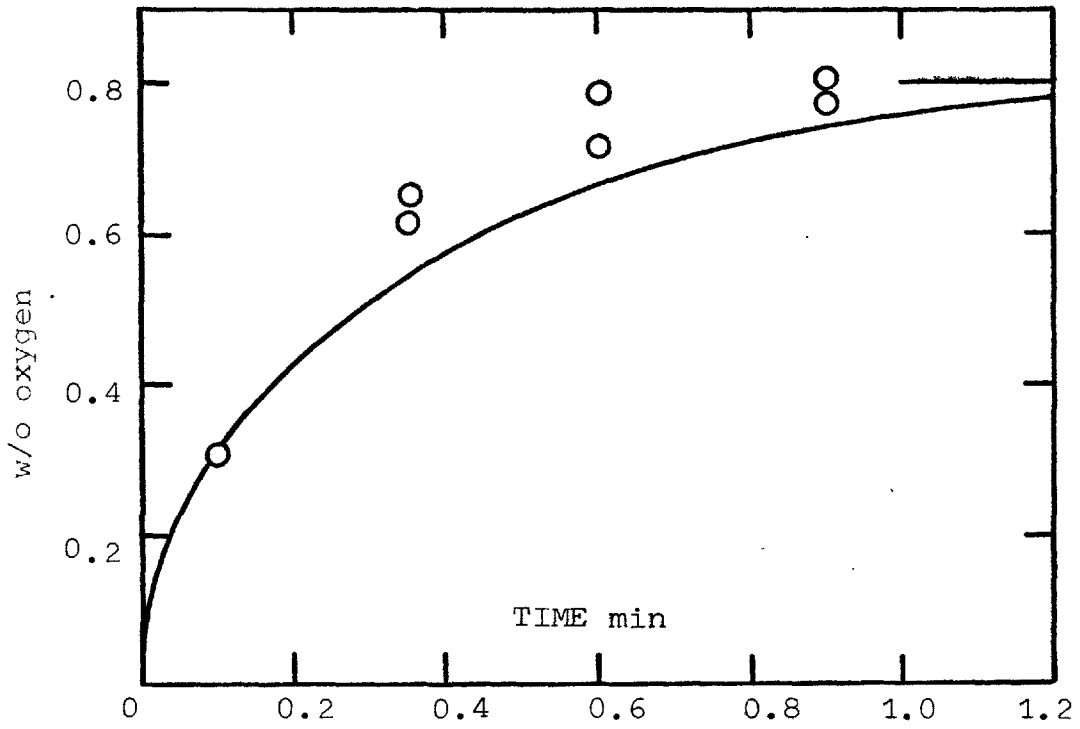

Fig (4-13) Transfer of oxygen to 0.5g. nickel drops with CO/CO_2 = 1/72, flow, 12.59 s.l.m. at 1750°C

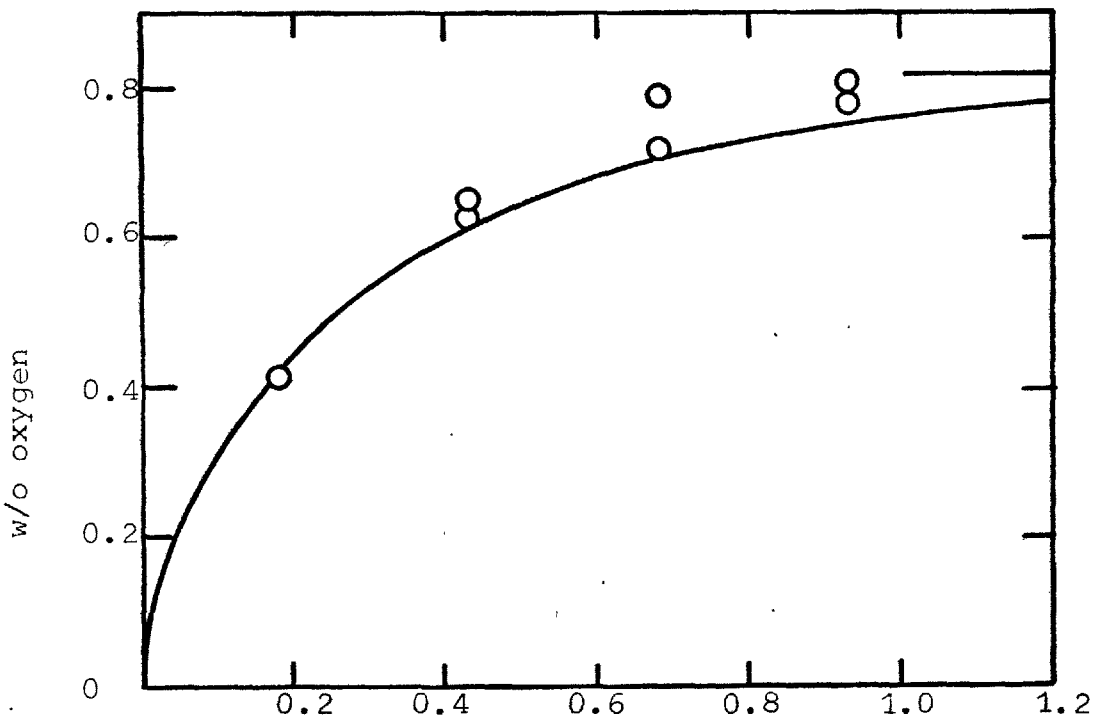

Fig (4-14) Transfer of oxygen to 0.5g nickel drops with CO/CO_2 = 1/59; flow, 11.99 s.l.m. at 1750°C

As shown in figs. (4-11) to (4-14) their results agree well with the mixed control model with static diffusion. The validity of assuming the static behaviour of levitated drops in interpreting independent measurements on three different melts (iron, copper, and nickel) using different reactions implies that it is the actual behaviour. Such behaviour indicates that although high circumferential velocities are observed at the surface, there are no radial velocity components to cause transfer of the diffusing substance into the bulk of the drop by convection.

This finding is particularly interesting from the point of view of levitation technique, since it makes this technique a powerful tool in the study of gas-liquid reactions, because the rates are then well defined in both gas and liquid phases.

4-7 Conclusion

The work reported in this chapter has extended our knowledge of the reaction of liquid iron-carbon alloys in oxidizing gas ($CO-CO_2$ mixtures) by using high pressure. The work examined the possibility of mixed control of the transport steps. It was found that diffusion in the liquid phase plays an important part during carburization and decarburization at relatively low carbons at high pressures.

The results obtained for decarburization confirm the observed fact that the diffusion in the gas phase is the rate controlling step at high carbon. It was also shown that, at relatively low carbons, diffusion in the liquid phase affects the overall mass transfer rate. This tends to support the diffusion of carbon in liquid as the rate controlling step in decarburization at very low carbon below 0.1 w/o at one atmosphere rather than the chemical reaction.

The possibility of the chemical reaction controlling the rate of carburization was examined and the chemical step was found to be very fast, particularly at high pressures. The rate must be interpreted in terms of combined transport mechanisms, particularly at high pressures. The measurements give a remarkable agreement with theory, by assuming the levitated drops behave as static spheres.

Despite the observed circumferential velocity observed on the surface of levitated drops, the results of the present

study and of other studies can be interpreted by treating the levitated drops as unstirred. This suggests that such behaviour does occur in levitated drops.

CHAPTER 5

HOMOGENEOUS NUCLEATION OF CARBON MONOXIDE BUBBLES IN MOLTEN IRON

5-1 Introduction

The work presented in this chapter is the first study specifically on the homogeneous nucleation phenomena of gases in molten metals. The experimental technique of levitation at high pressure provided the tool for this study. The super-saturation was achieved by a sudden change of the ambient pressure. Nucleation of carbon monoxide gas bubbles in molten iron was investigated over a wide range of oxygen activities. Experiments on nitrogen were also performed.

A clear picture of the nucleation phenomena was obtained. Theories on nucleation were reviewed and discussed on the basis of the results. The adsorbed surface-active oxygen was found to play an important role in nucleation.

5-2 Theories of homogeneous nucleation of gas bubbles in liquid metals

5-2.1 Introduction

The formation of gas bubbles in supersaturated liquids occurs by nucleation and growth of the gas phase. If this happens when the liquid is under positive pressure (compression) the phenomenon is called ebullition. When the corresponding process occurs in liquids under negative pressure (tension) it is called cavitation. Since homogeneous nucleation is only of interest in this work the growth of bubbles will not be mentioned.

The origin of the classical theory of nucleation can be attributed to Gibbs (102) who developed the thermodynamics of heterogeneous systems. As a consequence he showed for the first time the importance of the idea of "work of formation" of a new phase in an existing phase. He calculated the reversible work required to form a critical sized nucleus which is in metastable equilibrium with the bulk phase as

$$\Delta F^{*} = \tfrac{1}{3}\sigma A^{*} \qquad (5-1)$$

where A^{*} is the surface area of the critical nucleus and σ is the effective surface tension. Volmer and Weber (103) recognised that the stability of the supersaturated phase is a question of kinetics and according to fluctuation theory the probability of having a critical nucleus depends on the work of formation of the critical nucleus . By analogy with Boltzmann statistics,

they
/ related the rate of formation of critical nuclei in the system I to ΔF^* by the equation

$$I\alpha \exp.(-\Delta F^*/kT) \qquad (5\text{-}2)$$

This exponential term, which dominates the theory of homogeneous nucleation, is still present in the most modern theories. The homogeneous nucleation theory for the formation of gas bubbles in a liquid phase predicts the critical supersaturation for gas bubble nucleation in ebullition and the negative pressure in the liquid at which cavitation can occur i.e. fracture pressure of the liquid.

Dean's theory (104) on nucleation by cavitation is an alternative to the homogeneous nucleation theory in supersaturated stirred liquids.

5-2.2 Classical theory of nucleation

This theory is based on two main points. First the work of formation of a new phase is evaluated for the critical nucleus size, at which it can grow. The argument here involves the thermodynamics of the heterogeneous system and a detailed understanding is necessary. It should be noted that it was assumed that the macroscopic thermodynamic properties may be used to describe the small nuclei ($r^* \simeq 10^{-6}$cm). The second part is concerned with the rate of critical size nucleus formation through the kinetic model of capturing and losing molecules from the newly-formed phase (embryos).

5-5.2.1 Thermodynamics of liquid-gas bubble system

For a liquid-gas bubble system, the gas (β-phase) in the form of a homogeneous spherical bubble, embedded in a homogeneous liquid (α-phase), there is a thin/non homogeneous transition layer separating them. This transition layer is referred to as the surface of separation, or the interface, fig. (5-1). The concentrations in the interface are not constant, but vary continuously through its thickness (fig. (5-2a)) due to the fact of different attractive forces between the molecules in the liquid and gas phase. However, it is more convenient to choose a dividing surface (Gibbs model) fig. (5-2b) for relating surface phenomena. This dividing surface is called the "surface of tension". For the model to be stoichiometrically equivalent to the actual system, it is necessary to attribute a mass to the dividing surface N^S and in an analogous manner we define the surface energy U^S and surface entropy S^S. So the interfacial properties relate to the surface area since they are confined to a layer of zero thickness. The total number of molecules in the system

$$N = N^{\alpha} + N^{\beta} + N^{S} \qquad (5-3)$$

and the state functions, the internal energy and entropy, are

$$U = U^{\alpha} + U^{\beta} + U^{S} \qquad (5-4)$$

$$S = S^{\alpha} + S^{\beta} + S^{S} \qquad (5-5)$$

For the thermodynamic system composed of components (1 ... i) the energies of each phase are (105, 106):

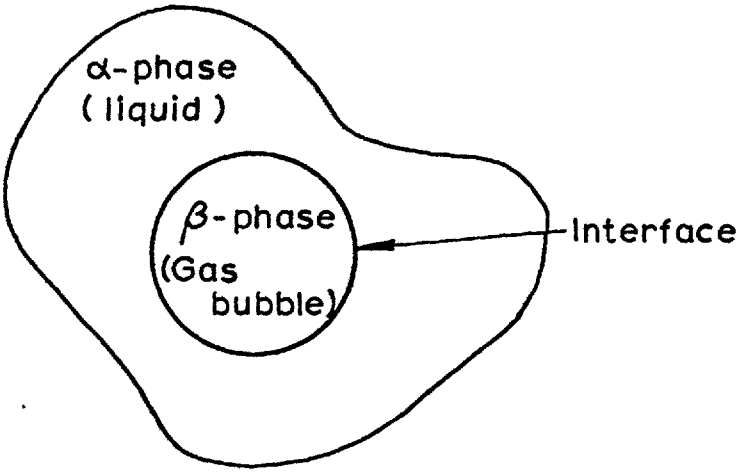

Fig (5-1) The thermodynamic system is composed of an β-phase (gas bubble) a α-phase (liquid and the interface separating the two phases.

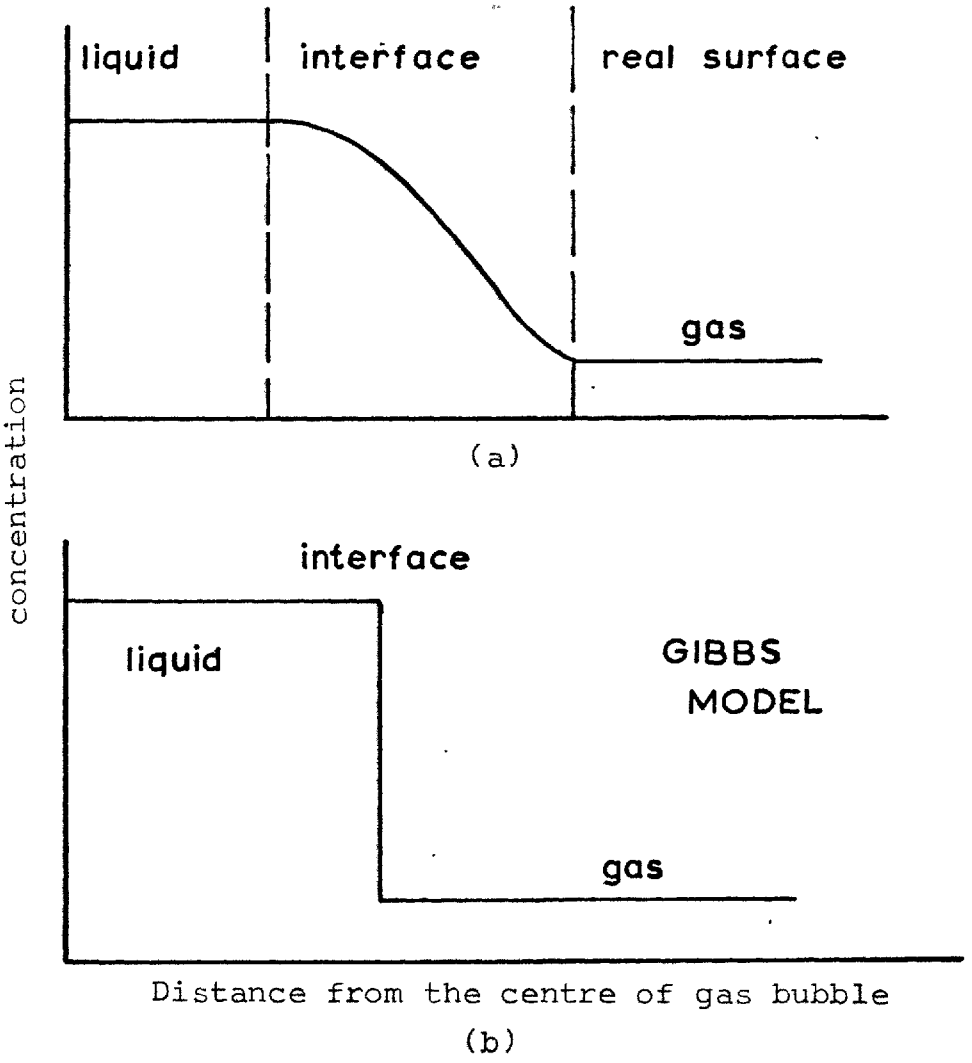

Fig (5-2) (a) Real surface ditribution of concentration
(b) The Gibbs model surface, equivalent to the real surface

$$U^{\alpha} = -P^{\alpha}V^{\alpha} + TS^{\alpha} + \sum_{i=1}^{i} n_i^{\alpha} \mu^{\alpha}{}_i \qquad (5-6)$$

$$U^{\beta} = -P^{\beta}V^{\beta} + TS^{\beta} + \sum_{i=1}^{i} n_i^{\beta} \mu_i^{\beta} \qquad (5-7)$$

$$U^{s} = \sigma A + TS^{s} + \sum_{i=1}^{i} n_i^{s} \mu_i^{s} \qquad (5-8)$$

where σ is the additional potential energy per unit surface which is $(\delta U^s/\delta A)_{S s_N s}$ and called surface tension.

From the second law of thermodynamics, the criterion of equilibrium is

$$(dU)_{S,V} = (dF)_{T,V} = (dG)_{T,P} = 0 \qquad (5-9)$$

Since the physico-chemical change in our system takes place at constant temperature and volume so the Helmholtz potential should be used for the study of that system. For an isothermal system, the physico-chemical equilibrium condition is given by

$$\mu_i{}^{\alpha} = \mu_i{}^{\beta} = \mu_i{}^{s} \qquad (5-10)$$

Mechanical Equilibrium (Laplace Equation)

The surface energy σ can be considered as a tension acting parallel to the surface from a mechanical stand point. The mechanical equilibrium condition for a spherical surface (gas bubble in the liquid) is given by the well-known relationship

$$P^{\beta} - P^{\alpha} = \frac{2\sigma}{r} \qquad (5-11)$$

Equation (5-11) can also be obtained from the thermodynamic considerations for the system under equilibrium (107).

Effect of curvature on the equilibrium state (Kelvin equation)

The influence of curvature on the equilibrium pressure of components in the gas bubble gives additional information about our composite system. Since at the equilibrium both the mechanical and physico-chemical conditions are satisfied, P^{α} and P^{β} satisfy the equation

$$\mu_i^{\beta}(P^{\beta}, T) = \mu_i^{\alpha}(P^{\alpha}, T) \qquad (5\text{-}12)$$

Using the fact that $P^{\beta} = P^{\alpha}$ for a planar interface, so

$$\mu_i(P_{\infty}^{\beta}, T) = \mu_i(P_{\infty}^{\alpha}, T) \qquad (5\text{-}13)$$

Subtracting the two equations we have

$$\mu_i^{\alpha}(P^{\alpha}, T) - \mu_i(P_{\infty}^{\beta}, T) = \mu_i^{\beta}(P^{\beta}, T) - \mu_i(P_{\infty}^{\beta}, T) \qquad (5\text{-}14)$$

The variation of the chemical potential with pressure at constant temperature and concentration of other components (106) is

$$\begin{aligned} (\delta\mu_i^{\alpha}/\delta P^{\alpha})_{T_1 x_2 \cdots} &= v_i^{\alpha} \\ (\delta\mu_i^{\beta}/\delta P^{\beta})_{T_1, x_2 \cdots} &= v_i^{\beta} \end{aligned} \qquad (5\text{-}15)$$

so for the liquid phase α,

$$\mu_i^{\alpha}(P^{\alpha}, T) - \mu_i^{\alpha}(P_{\infty}^{\beta}, T) = v_i^{\alpha}(P^{\alpha} - P_{\infty}^{\beta}) \qquad (5\text{-}16)$$

and for the gas phase

$$\mu_i^{\beta}(P^{\beta},T) - \mu_i(P^{\beta},T) = RT \ln(P_i^{\beta}/P_{\infty}^{\beta}) \qquad (5\text{-}17)$$

from equation (5-11), (5-14), (5-16), and (5-17) we obtain

$$\frac{2\sigma}{r} = (P^{\beta} - P_{\infty}^{\beta}) - (RT/v^{\alpha}_i) \ln(P_i^{\beta}/P_{i\infty}^{\beta}) \qquad (5\text{-}18)$$

Equation (5-18) shows that increasing the curvature decreases the equilibrium pressure below that for a flat interface, which explains the existence of supersaturated liquid.

Work of Formation of gas bubble phase

In the process of new phase formation in the pre-existing phase, a new surface is formed. Such a surface can be formed only at the cost of energy and in proprotion to the surface area. On the other hand the new phase formation is accompanied by a decrease of the energy of the system relative to the previous state. The balance between these two energies determines the activation energy of nucleation. This energy is the work which must be done to form the new phase. Owing to the large size of the pre-existing phase the volume of the system remains effectively constant and the system is thermally isolated, the work performed by the system is equal to the change of the free energy (Helmholtz free energy).

$$(\Delta F)_{T,V} = -(P^{\beta} - P^{\alpha})V^{\beta} + \sum_{i=1}^{i} n_i^{\beta}(\mu_i^{\beta} - \mu_i^{\infty}) + \sum_{i=1}^{i} n^{s}{}_i(\mu^{s}{}_i - \mu^{\alpha}{}_i) + \sigma A \qquad (5\text{-}19)$$

Since the critical nucleus is in equilibrium, the free energy of nucleation of a critical nucleus is

$$\Delta F^* = -(P^{\beta *} - P^{\alpha})\, V^{\beta *} + \sigma A^* = \tfrac{1}{3}\sigma A^* = 16\pi\sigma^3/3(P^{\beta *} - P^{\alpha})^2 \qquad (5\text{-}20)$$

Equation (5-120) was obtained by combining equation (5-19) with the physico-chemical equilibrium equation (5-10) and mechanical equilibrium equation (5-11). The term $(P^{\beta *} - P^{\alpha})$ in equation (5-20) is nearly the difference between the dissolved gas pressure in the liquid phase (see Kelvin equation (5-18)) and liquid phase pressure. The pressure difference is called the supersaturation pressure. Increasing the supersaturation pressure leads to a decrease in the work of formation of the critical nucleus. For a gas bubble below its critical size the general expression for the work of formation, (equation (5-19)) must be used, since neither the mechanical equilibrium (108) nor the physico-chemical equilibrium conditions can be applied. However to simplify the calculation, we can neglect $n_i^s\ (\mu_i^s - \mu_i^{\alpha})$ in comparison with $n_i^{(\beta)}(\mu_i^{\beta} - \mu_i^{\alpha})$. This reduces equation (5-19) to

$$\Delta F = -(P^{\beta} - P^{\alpha})V^{\beta} + \sum n_i^{\beta}(\mu_i^{\beta} - \mu_i^{\alpha}) + \sigma A \qquad (5\text{-}21)$$

for the critical nucleus

$$\mu_i^{\beta *}\ (P^{\beta *},\ T) = \mu_i^{\alpha}\ (P_i^{\alpha},\ T) \qquad (5\text{-}22)$$

and from equations (5-15) and (5-17) we have

$$\mu_i^{\beta}(P^{\beta},T) = \mu_i^{\beta^*}(P^{\beta^*},T) + kT \ln (P_i^{\beta}/P_i^{\beta^*}) \qquad (5\text{-}23)$$

so we may write equation (5-21) as follows

$$\Delta F = -(\tfrac{4}{3})\pi r^3 (P^{\beta} - P^{\alpha}) + \sum n_i^{\beta} kT \ln(P_i^{\beta}/P_i^{\beta^*}) + 4\pi r^2\sigma \qquad (5\text{-}24)$$

From equation (5-24) it follows that to determine the free energy charge for a sub-critical nucleus it is necessary to know simultaneously both P (or n^{β}) and r. The relationship between these two parameters is not defined in the case of gas bubble nucleation.

5-2.2.2 The kinetic theory of nucleation

Although Volmer and Weber (103) obtained the relationship between the work of formation of the critical nucleus and its rate of formation, they did not discuss the kinetic model. Farkes (109), working from an idea of Szilard's, gave a kinetic mechanism of homogeneous nucleation which has served as the basis of all subsequent development. Farkes assumed that formation of the embryos of the new phase of all sizes (up to the critical size) occurred by a series of intermediate reactions of capturing or losing a single molecule. The kinetic mechanism describing the system is thus

$$m\alpha_1 \rightleftharpoons B_m$$

$$B_m + \alpha_1 \rightleftharpoons B_{m+1}$$

$$B_{j-1} + \alpha_1 \rightleftharpoons B_j$$

$$B_j + \alpha_1 \rightleftharpoons B_{j+1}$$

If we consider that f_j, the concentration of embryos of size j at any instant t, we have

$$\delta f_j/\delta t = I_{j-1} - I_j \qquad (5\text{-}26)$$

and

$$I_j = \vec{\omega}_j f_j - \overleftarrow{\omega}_{j+1} f_{j+1} \qquad (5\text{-}27)$$

where $\vec{\omega}_j$ is the frequency of capturing a molecule by an embryo M_j and $\overleftarrow{\omega}_j$ is the frequency of losing a molecule from M_j and I_j is the rate of the reaction. For the steady case, f_j does not change with time and I has one and the same value for all sizes of embryo. The frequencies of capturing and losing molecules depend only on the diffusion of molecules in the liquid and on the pressure in the gas respectively (as well as the surface area) and are independent of the embryo population.

The relation between both frequencies can be obtained at the equilibrium population (i.e. I is zero) by writing

$$n_j \vec{\omega}_j = n_{j+1} \overleftarrow{\omega}_{j+1} \qquad (5\text{-}28)$$

where n_j is the equilibrium concentration of embryos of size j_i. From equation (5-27) and (5-28), the steady state rate of

nucleation is given by

$$I = (f_j/n_j - f_{j+1}/n_{j+1}) \vec{\omega}_j n_j \qquad (5\text{-}29)$$

and this equation can be converted into differential equation by writing

$$I = - \vec{\omega}_j n_j \delta(f_j/n_j)/\delta j \qquad (5\text{-}30)$$

From the boundary conditions fig.(5-3)

$$f_j/n_j = 1 \qquad j \rightarrow m$$
$$f_j/n_j = 0 \qquad j \rightarrow \infty \qquad (5\text{-}31)$$

equation (5-30) becomes

$$I = 1/ \int_{m}^{\infty} (\delta j/ \vec{\omega}_j n_j) \qquad (5\text{-}32)$$

where the equilibrium concentration of embryos of component i which participate in nucleation (105) is given as

$$n_{j_i} = (\dot{C}_{im} + \dot{C}_i) \exp (- \Delta F_j/kT) \qquad (5\text{-}33)$$

Integration of equation (5-32) has been the subject of many studies (110-114). However the nucleation rate is generally expressed as the product of the equilibrium concentration of critical nuclei n_j^*, the frequency of capturing molecules at the critical nucleus size and the non-equilbrium factor Z which

expresses the departure of the actual concentration (f_j^*) and the gradient of concentration at the critical nucleus size, from the equilibrium value, fig.(5-3):

$$I = Z \overrightarrow{\omega}_{(j^*)} n_{(j^*)} \qquad (5\text{-}34)$$

From equations (5-33) and (5-34), the rate of nucleation has the following relation

$$I = Z \overrightarrow{\omega}_{j^*} (\dot{C}_1 + \dot{C}_2) \exp(-\Delta F_j^*/kT) \qquad (5\text{-}35)$$

This result is consistent with Volmer's supposition that the expression for the number of critical nuclei contains this exponential factor. The pre-exponential term is nearly independent of supersaturation and depends on the physical properties of the system e.g. viscosity, diffusivity, molar concentration of liquid, etc. Figure (5-4) shows how the nucleation rate behaves as a function of supersaturation pressure ΔP. The rate increases without limit after the critical supersaturation has been reached, and decreases without limit below it. The critical supersaturation is that which gives a nucleation rate of one bubble in a reasonable time - say one bubble per cm^3 per second. It should be emphasised that the exponential term dominates the theory of homogeneous nucleation.

In the present case of homogeneous nucleation of gas bubbles of dissolved gases equation (5-35) may be expressed as (108)

$$I = (2(\dot{C}_1 + \dot{C}_2) \sqrt{\textstyle\sum_i} \gamma I_L^{\alpha})(\sigma/kT)^{\frac{1}{2}} \exp(-\Delta F_d/kT) \exp(-\Delta F^*/kT) \qquad (5\text{-}36)$$

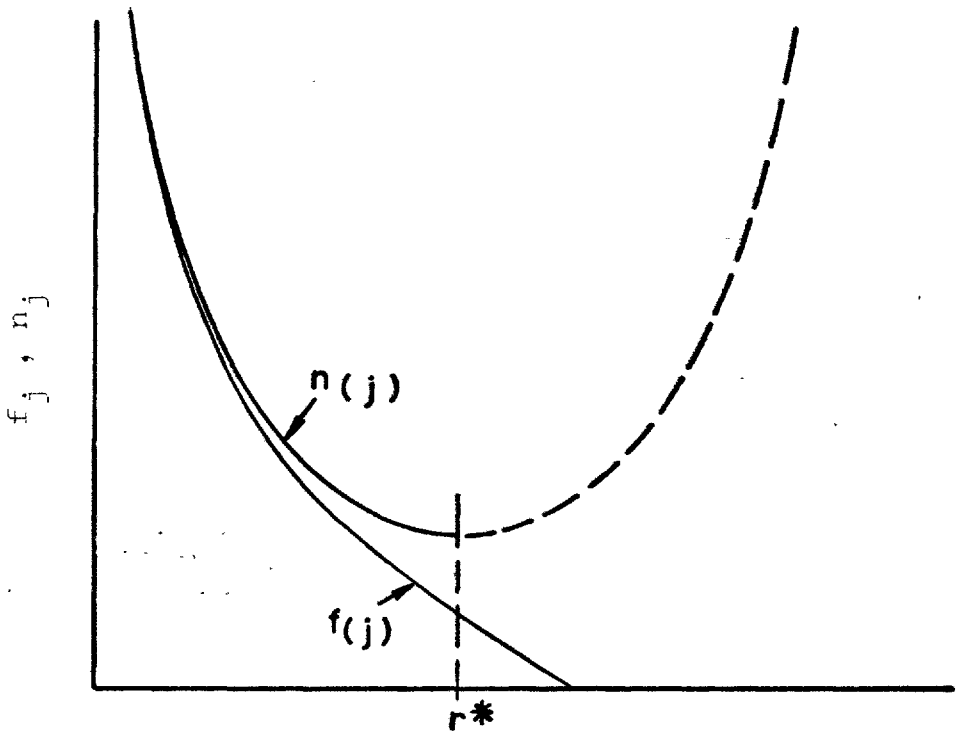

Fig (5-3) Concentration of the gas bubble in the liquid

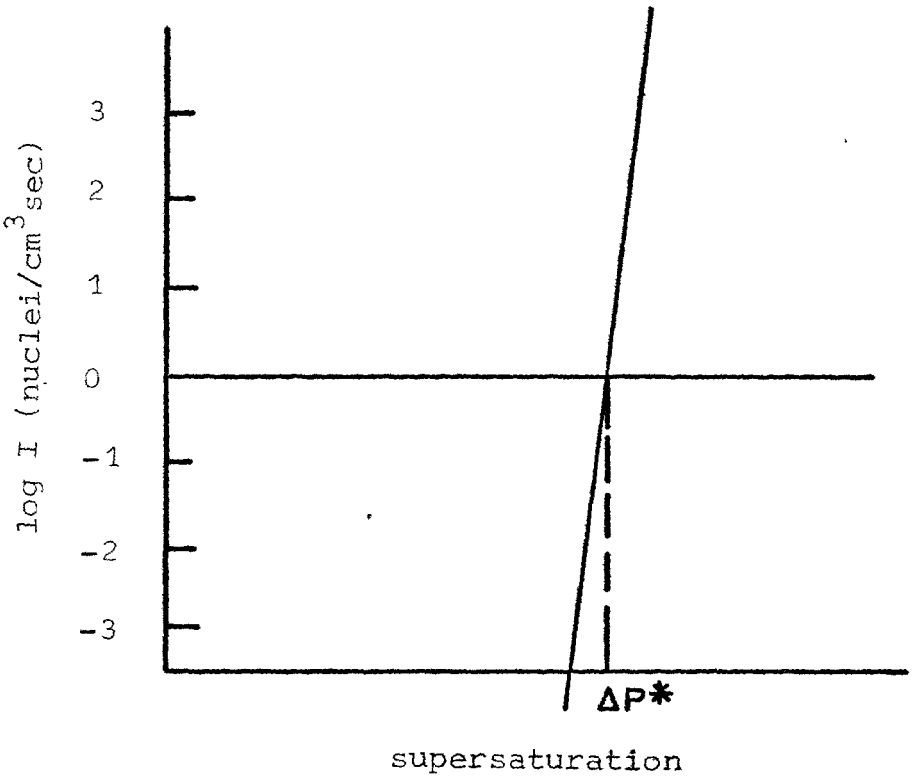

Fig (5-4) Steady state nucleation rate as function of supersaturation

where Γ_i is the relative adsorption of the solute, γ is Debye maximum frequency of vibration of liquid molecules, ΔF_d is activational energy for diffusion of the solute in the liquid.

5-2.3 Nucleation by cavitation, Dean's Theory

Dean (104) postulated that the turbulence in the fluid forms free vortices. Following this hypothesis he showed that the negative pressure (hydrostatic tension) is sufficiently large, close to the centre of the free vortex to cause fracture of the liquid and form a cavity into which the dissolved gases (and the vapour of the liquid) could diffuse. The equilibrium vapour pressure inside a cavity is

$$P_v = -(\phi^2\rho/8\pi^2r^2) + (2\sigma/r) \qquad (5-37)$$

where ϕ is the vortex circulation and ρ is the liquid density. From the plot of P_v as function of bubble radius and vortex circulation fig. (5-5), it is shown that the gas bubble will grow once the bubble size passes the maximum. This is the condition for gas bubble growth in a liquid. In order to do so, the dissolved gas pressure in the liquid i.e. the pressure of gases in the cavity must be equal or greater than the maximum pressure at the plateau. If the pressure of the gas in the cavity is less than the maximum pressure the cavity will expand to the radius (below the critical one) at which the mechanical equilibrium is established. The cavity will remain at that size and will disappear when the vortex decays. It is also shown

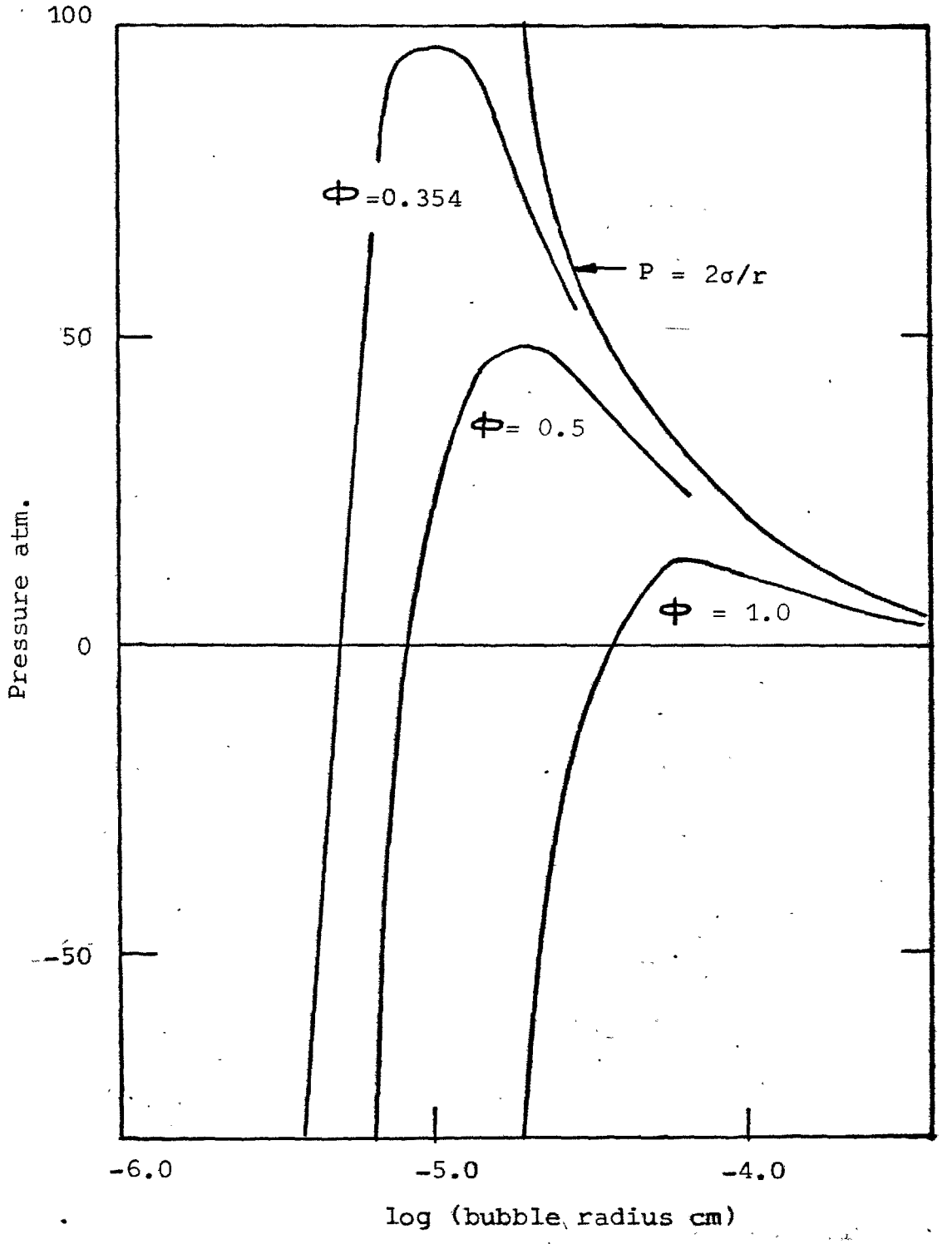

Fig (5-5) Pressure on spherical bubble in molten iron (σ = 1000dyne/cm) at the centre of vortex circulation Φ

that the more active vortices which have greater circulation have the lower maximum pressures. Hence a lower pressure of dissolved gas is required to form a permanent bubble when the vortices are very active. The main criticism of the theory is that small free vortices with high circulation must decay very rapidly (5).

5-3 Previous work

No experimental work has been carried out which has been specifically designed to study homogeneous nucleation of gas bubbles in liquid metals. This has been because the nucleation theories predict that very high supersaturations are required to initiate nucleation and because there are substantial experimental difficulties involved in carrying out such experiments. One paper worthy of mention is that by Korber and Oelsen (115) who studied the nucleation of carbon monoxide in molten iron held in a crucible coated with fluid slag layer to eliminate gas bubble formation in the solid-liquid interface pores. They found that bubble formation in the liquid steel or at the slag/metal interface did not occur until the degree of supersaturation was over 20 atmosphere.

After the establishment of levitation melting as a simple known technique where the specimen can be held in a gas by the aid of an electromagnetic field (1960), gas bubble nucleation was observed in levitated drops during the study of gas metal reactions, particularly during decarburization of iron-carbon alloys. Baker et al (80) observed CO gas bubble formation at 0.5 w/o carbon. Their results suggested bubble formation occurred after oxide formation on the surface. They estimated a super-saturation of 50 atmospheres by postulating that the mechanism of surface renewal by eddy diffusion dragged volume elements from the surface, which were saturated with oxygen, to the bulk of the drop at high carbon concentration to give local high supersaturation. They suggested that such supersaturation was required for homogeneous nucleation.

Distin et al (81) found that carbon boil in the levitated drops started as soon as oxide phase appeared on the surface. The carbon concentrations at which the oxide phase was formed varied from 1 w/o to 0.2 w/o carbon, depending on the decarburization rate. Supersaturations of 10-40 atmospheres were deduced from the amounts of carbon and oxygen in drops when they began to boil. They suggested that CO bubbles were nucleated heterogeneously at the metal/oxide interface.

Robertson (5) took high speed films of decarburization at very high rates and found that CO nucleation occurred without any formation of oxide phase. He suggested that CO bubble nucleation occurred by vortex cavitation, with the vortices formed by intense surface turbulence in the liquid caused by chemical reaction.

Nucleation of SO_2 gas bubbles was also observed during desulphurization of iron sulphur (116) and nickel sulphur (117) levitated drops.

Gas bubbles nucleation was also observed in gas liquid reactions during free falling in a reaction column (analagous in many respects to the levitation technique from the homogeneous nucleation point of view). During decarburization of iron-carbon alloys CO formation was observed at all levels of carbon concentration from 0.5 to 4 w/o carbon, depending on the rate of decarburization, without observing oxide phase formation (84-86). These workers suggested either the Baker et al mechanism (80) or Robertson mechanism (5) for gas bubble nucleation.

5-4 Experimental technique

One gram drops of either spec-pure iron or iron-carbon alloy were brought to equilibrium with gases at high pressures and at temperatures around 1600°C. Gas-liquid equilibrium was acheived using the technique described in chapter 3. The molten iron was then supersaturated with respect to the dissolved gas by a sudden drop of the gas pressure. The observation of the gas bubble nucleation phenomenon was recorded on cinefilms.

Nucleation of gases was studied with nitrogen and forming gas (N_2-10%H_2) in spec-pure iron and CO in iron-carbon alloys at different oxygen activities defined by the CO-CO_2 ratio. In the experiments with forming gas the same specimen was used several times at different supersaturations before quenching, while in the experiments with CO-CO_2 gas mixtures the specimens were quenched after dropping the pressure and filming. Carbon analyses of the specimens were carried out as a check to show that the equilibrium had been achieved at high pressures.

5-4.1 Pressure decrease of HPLA

The pressure decrease caused the supersaturation of the gases in the drop. Supersaturation may be defined as the pressure difference between the initial (equilibrium) and final (ambient) pressures. The initial pressure was measured accurately from the pressure transducer using a potentiometer. The final pressure of the helium atmosphere was adjusted to the required pressure (usually about one atmosphere) by the pressure

regulator on the helium cylinder (working range up to 14 atmosphere), and measured by the pressure transducer at the end of the run.

Dropping the pressure was carried out by switching off the solenoid valve to cut the gas supply from the cylinder to the HPLA, and bleeding the gas in the HPLA by opening fully the needle valve at the end of the high pressure line at the same time. Helium flowed through the check valve, which operated with a differential pressure as low as 1 psi, at the required final pressure in the HPLA. Bleeding the gases took about 3 seconds, and this time was nearly independent on the initial pressures. Fig (5-6) is a copy of a typical pressure transducer chart record showing the pressure charge in HPLA with time during bleeding of the gases.

5-4.2 Temperature control

The rapid change of the pressure, during bleeding the gases from the HPLA, had a significant effect on the convective heat transfer, and hence on the temperature of the drop during the nucleation period. The work on the nucleation of N_2-10% H_2 gas mixture was carried out before the apparatus was equipped with the automatic temperature control system. Temperature adjustment was carried out manually. The response time of the operator was not adequate to cope with the vast change in flow conditions (convective heat transfer) over the short time of dropping the pressure and subsequent bubble nucleation (about 6 seconds). The increase of the temperature of the drops was kept within 75°C.

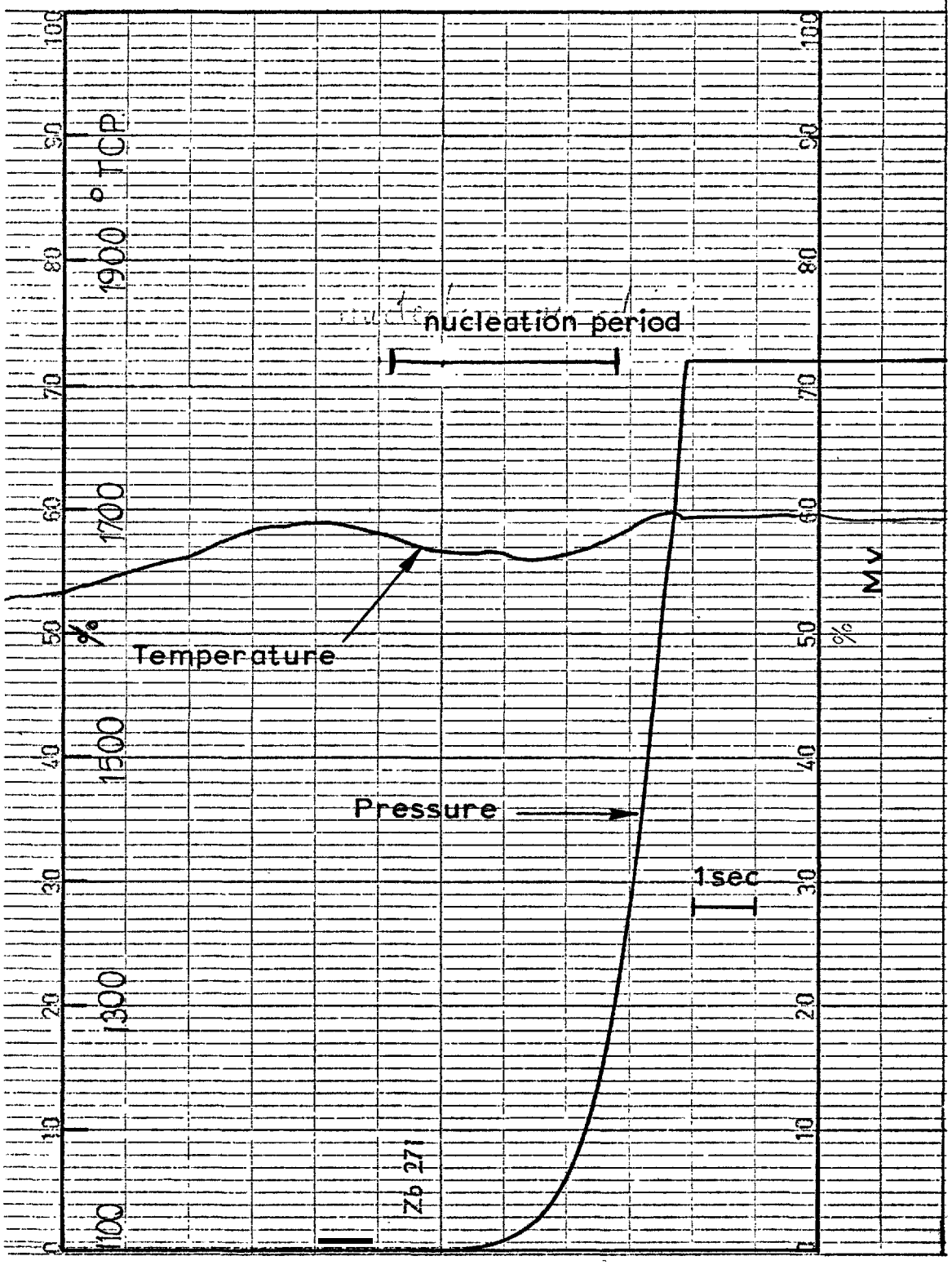

Fig (5-6) A copy of the chart record of run CN48, showing the pressure and temperature changes during rapid decrease of the pressure

Nucleation of CO gas bubbles was carried out while using the automatic temperature controller, which gave much better control of the temperature, $\pm$ 25°C. A copy of a temperature chart output from the TCP during the nucleation period using the automatic controller is shown in fig. (5-6).

5-4.3 Cinematography

It was essential in nucleation runs to determine whether nucleation had occurred or not without relying on the usual "impression" of the operator. A "Bolex" cine camera was used to take pictures at a speed of 64 picture per second. A 75 mm, "Cannon" lens, with suitable close-up lenses, was used to get a field of view covering the whole area within the 12.5mm bore alumina tube. A photograph of the apparatus and cine camera is given in Fig (5-7). The filming was carried out from the upper window, while the temperature was measured from the bottom one. Filming was started at exactly the same time as the pressure drop was initiated. Adequate records were obtained of the nucleation phenomena by this camera.

5-5 Results

5-5.1 Nucleation of N_2 and N_2-10% H_2 in pure iron

Although the final conclusion drawn from the results was that nucleation of N_2 and of N_2-10% H_2 in pure iron was not observed up to supersaturations of $(P_I - P_f) \simeq 100$ atmosphere (maximum working pressure of the apparatus), the results obtained during overcoming the experimental difficulties had important

Fig (5-7) Photograph of the aparatus and cine camera

features which lead to a better understanding of the nucleation phenomena (see discussion, section 5.6). For this reason all the results will be given.

For the first run NN1, oxygen-free nitrogen was used. Forming gas (75% N_2-25% H_2) was used to remove any oxygen from the drop before pressurizing the HPLA with N_2. No N_2 nucleation was observed up to supersaturation of 100 atmosphere, the details of the run are given in table (5-1).

In run NN2 the specimen was levitated using helium as coolant gas. The apparatus was then pressurized using forming gas (90% N_2-10% H_2). Forming gas was used in place of oxygen-free nitrogen in an attempt to ensure that the specimen did not contain any dissolved oxygen. The results of run NN2 at supersaturations up to 74 atmosphere showed no nucleation. The first pressure drop in run NN3 at a supersaturation of 76 atmospheresshowed nucleation with the ejection of metal droplets from the specimen. Surprisingly the same specimen in the same run at a higher supersaturation of 95 atmosphere showed no nucleation. Experiments with forming gas were repeated to clarify this point in runs NN4, NN5, NN6. No nucleation was observed in runs NN4 and NN6, but vigorous nucleation was observed in the first pressure drop at supersaturation of 55 atmosphere in run NN5, but there was no nucleation afterwards at higher supersaturations. The details of these runs are given in table (5-2).

Run	Temperature °C	Initial (Equilibrium) atm.	Final press. atm.	Supersaturation pressure atm.	Observation
Run NN1					
Oxygen-free Nitrogen	1690	22.32	1.30	21.02	no nucleation
	1690	41.62	"	40.32	"
	1690	62.13	"	60.83	"
	1690	81.19	"	79.89	"
	1675	100.89	"	99.59	"

Table (5-1)

Results of nitrogen

nucleation in molten iron

Run	Temp °C	Initial (Equilibrium) pressure atm.	final pressure atm.	supersaturation pressure atm.	Observation
Run NN2					
N_2-10% H_2	1640	34.72	1.30	33.42	no nucleation
	1635	56.69	"	55.39	"
	1620	74.31	"	73.01	"
Run NN3	1620	77.64	"	76.34	nucleation
N_2-10% H_2	1630	94.97	"	93.37	no nucleation
	1620	95.30	"	94.00	"
Run NN4					
	1625	55.43	1.30	54.13	no nucleation
	1625	55.43	"	54.13	"
	1620	62.00	"	60.70	"
	1620	68.57	"	67.27	"
	1620	74.9	"	73.60	"
	1620	77.03	"	75.73	"
Run NN5					
	1620	54.34	1.30	53.04	nucleation
	"	62.02	"	60.72	no nucleation
	"	67.98	"	65.68	"
	"	74.76	"	73.46	"
	"	80.74	"	79.44	"
	"	89.08	"	87.78	"

Table (5-2) Results of Nucleation experiment in N_2-10% H_2 gas mixture

Run	Temp °C	Initial (Equilibrium) pressure atm.	final pressure atm.	supersaturation pressure atm.	Observation
Run NN6					
	1620	34.91	1.30	33.61	no nucleation
	"	41.91	"	40.61	"
	"	48.09	"	46.79	"
	"	51.30	"	50.00	"
	"	54.56	"	53.26	"
	"	58.22	"	56.92	"

Table (5-2)
(continued)

Observing the nucleation in the first pressure drop at supersaturation above 55 atmosphere only and following the suggestion that oxygen may play a significant role in gas bubble nucleation in molten iron (124), it appeared likely that/during the first 10 minutes oxygen may not have been removed completely allowed to attain the equilibrium with gas at high pressure. Supporting evidence for this hypothesis was obtained by measuring the oxygen in spec-pure iron levitated at different times in the same gas - table (5-3)

Run No	Temperature	Time min.	Oxygen content ppm.
01	1600	10	10
02	1600	10	9
03	1600	30	5
04	1600	30	7
Analysis for oxygen in spec-pure iron rods			59 61

Table (5-3)

Oxygen content in the spec-pure iron levitated in forming gas

For a pure forming gas, containing no water vapour or oxygen as impurities, the final oxygen level would be fractions of a ppm and this would be acheived after, at most, 2 minutes. The much lower rate of oxygen removal observed and the high final level of about 6 ppm may be attributed to the impurities in the gas, mainly oxygen and water vapour.

For Run NN7, the forming gas was purified from O_2 and H_2O by passing it through a high pressure vessle containing "Deoxo" catalyst and molecular sieve. The final oxygen and water vapour levels of the gas purified in this way should have been less than 1 vpm. Forming gas was also used as coolant gas during the initial levitation, to remove most of the oxygen from the drops before increasing the pressure. The results of these runs showed no gas bubble nucleation in the drop, table (5-4) These results were not conclusive, because the first initial pressure was not above 55 atm.

Experiments on the homogeneous nucleation of nitrogen bubbles in iron drops containing controlled oxygen concentrations will be carried out in the future.

5-5.2 Nucleation of CO in Fe-C-O alloys

5-5.2.1 Nature of CO bubble formation

The results obtained with $CO-CO_2$ gas mixtures showed reproducible CO gas bubble formation. The $CO-CO_2$ gas mixtures fix the oxygen potential in the drop, which was independent of the pressure. These gas mixtures had lower oxygen potentials than that for the formation of iron oxide, and the measurements of oxygen concentration in the drop in chapter 3 prove this. This implies that the nucleation of the gas bubbles must have occurred in one single liquid phase i.e. homogeneous nucleation.

The whole sequence of observing the nucleation event of CO gas bubbles is illustrated in fig (5-8) run CN48. The temperature and pressure record is given in fig (5-6). In this example the drop was equilibrated with 8% CO_2 in CO gas mixture at 31.15 atmospheres and the pressure was dropped to 1.08 atm. No nucleation was observed for 0.8 seconds after operating the

Run	Temperature	Initial (equilibrium) pressure atm.	Final Pressure atm.	Supersaturation pressure atm.	Observation
Run NN7					
N_2-10% H_2	1660	34.61	1.3	34.31	No nucleation
	1650	44.80	"	43.50	"
	1645	54.36	"	53.06	"
	1625	64.70	"	63.40	"
	1610	74.60	"	73.30	"

Table (5-4)

Results of nucleation experiments in purified N_2-10% H_2 gas mixtures

cinecamera. Assuming that nucleation also occurred 0.8 seconds after the start of the pressure drop ebullition first occurred at a pressure of 15 atmosphere and lasted for 3.5 seconds.

The pictures taken during the intial pressure drop were not in focus. This was mainly due to the dependence of the focal length on the density of the gas and the high flow rate of the gas past the drop during rapid bleeding of the HPLA, as well as a shimmering effect due to a large density difference between the gas in the bulk and at the surface of the drop.

The first boil occurred without appreciable growth of the nucleating bubbles and small particles were ejected at high velocity from the drop. Fractions of a second later growth of the bubbles became pronounced. This was identified by the swelling and deformation of the drop. After one second the ebullition became vigorous as shown by the large number of gas bubbles coming out from the surface and the tremendous swelling. The diameter of the drop became comparable with the inner diameter of the alumina tube (12.5 mm). Towards the end of the nucleation event ejection of metal droplets characterized the ebullition. After nucleation (about 45 seconds) the levitated drop became quiescent and returned to its original size.

These features of ebullition were our evidence of homogeneous nucleation of gases in molten drops. Not all these features were observed in every "nucleation" run but one or more of these phenomena occurred. The extent of ebullition,

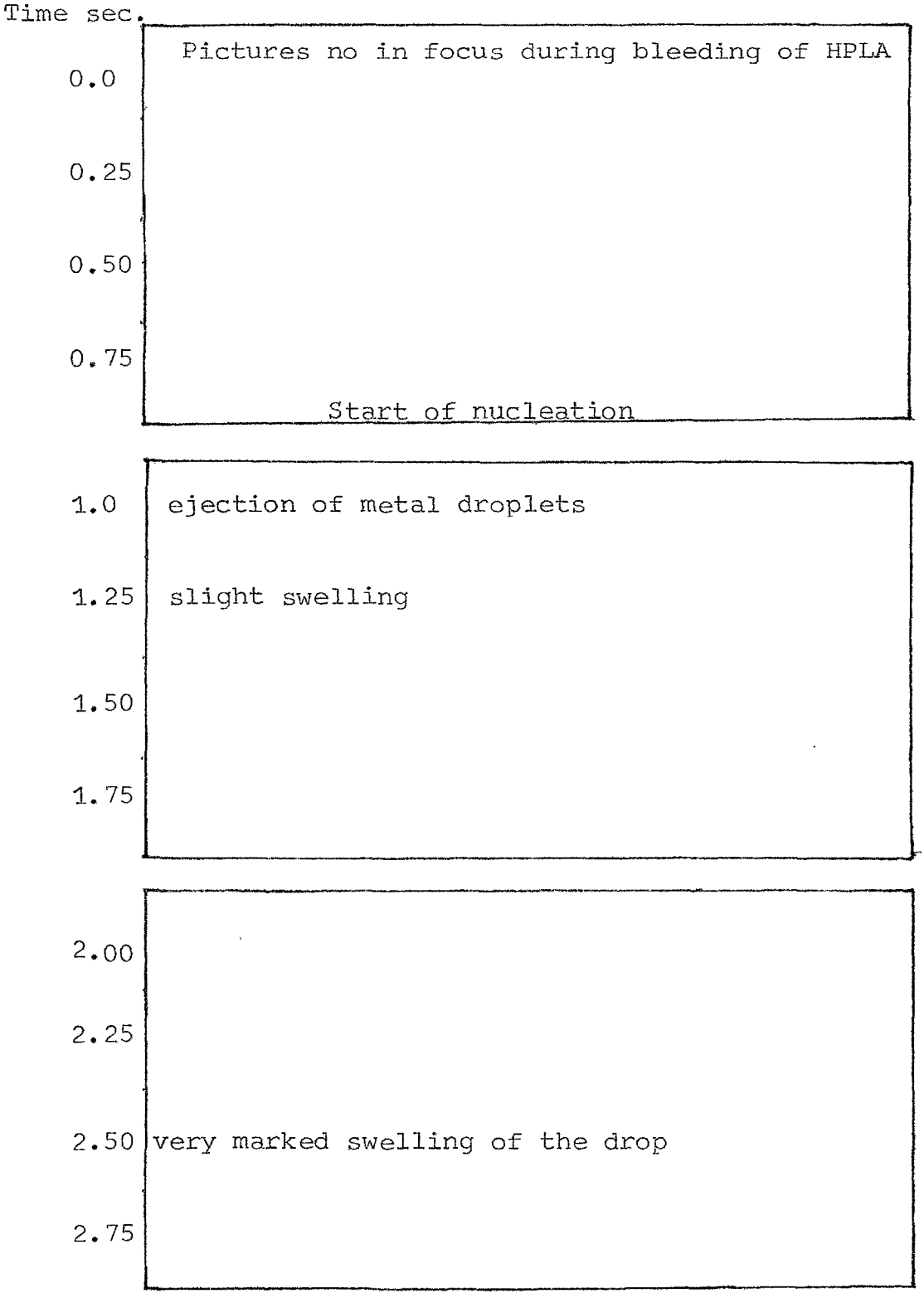

Fig (5-8) A typical film record of gas bubble nucleation in molten iron, Run CN48

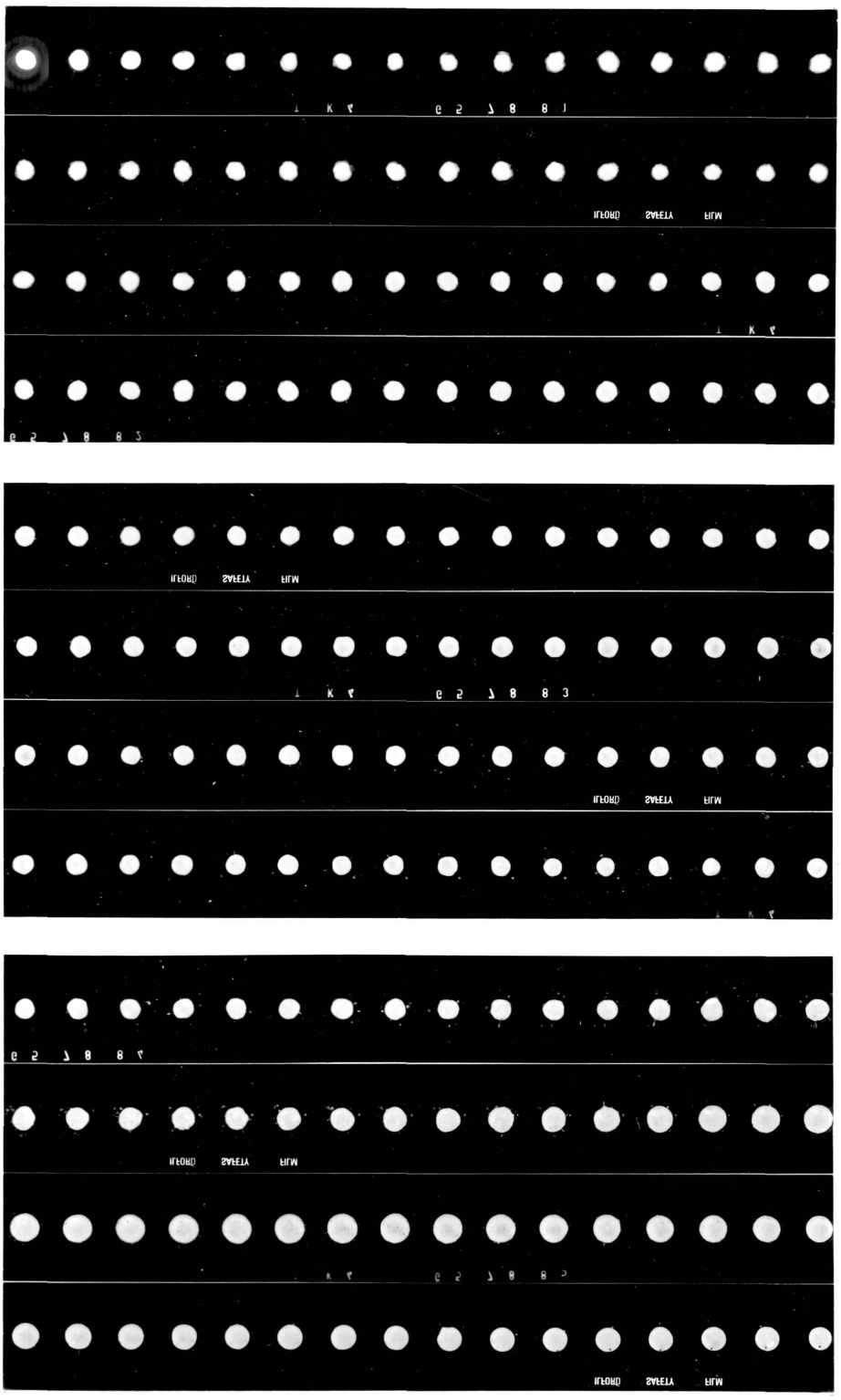

3.0	Bubble nucleation. The particle ejection and swelling can be seen
3.25	
3.5	
3.75	
4.0	Occasional ejections
4.25	
4.5	End of nucleation
4.75	
5.0	
5.25	The droplet remained quiescent to the end of the film (9 sec.)

Fig (3-8) continued

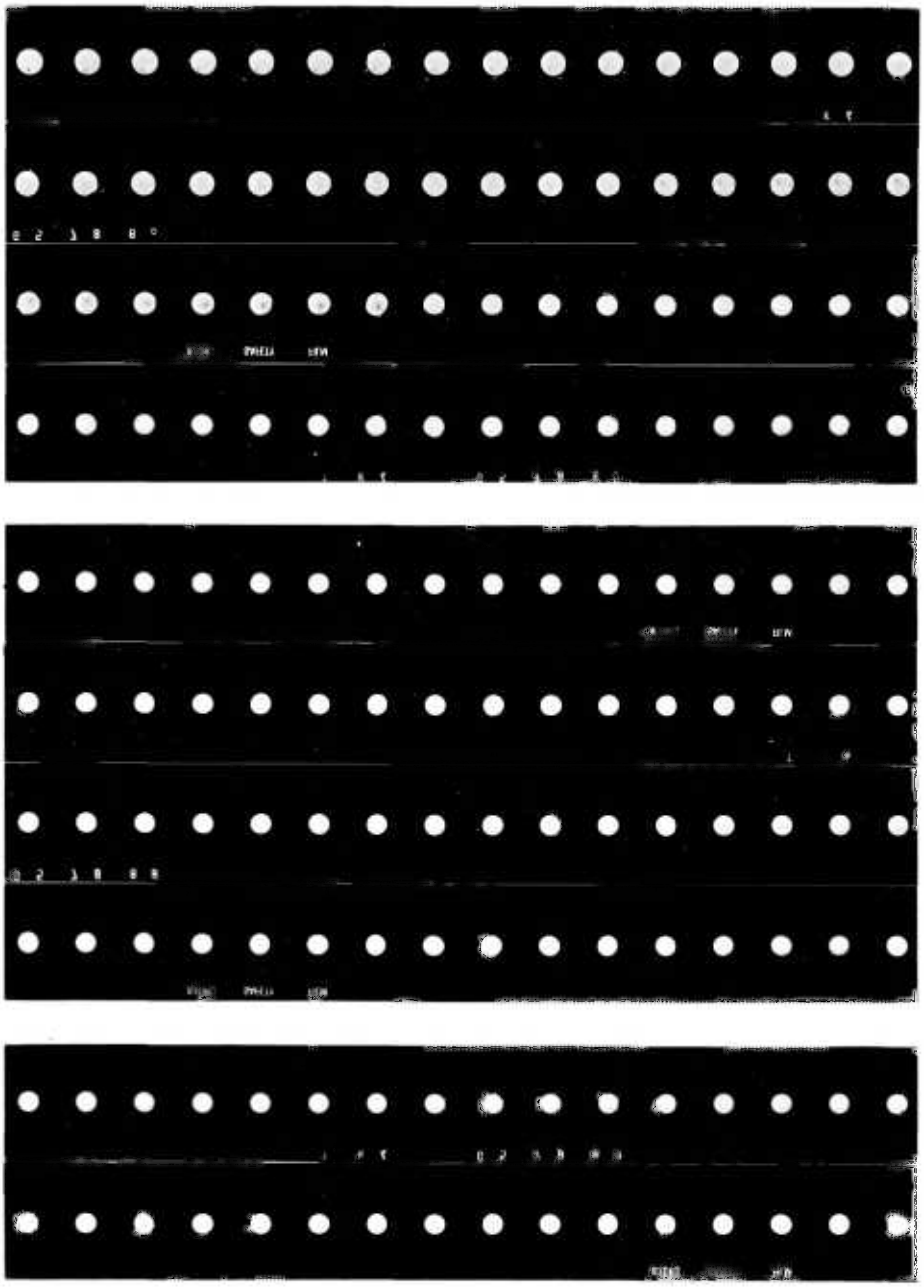

i.e. frequency of nucleus formation, depended on the degree of supersaturation of the drop. Ejection of metal droplets was a feature of the CO bubble formation near the critical supersaturation limits of homogeneous nucleation. The behaviour of the boil at different oxygen potentials is illustrated for 2.15% CO_2 run 36, 2.3% CO_2 run 57, and 4.58% CO_2 run 44, in fig (5-9), fig (5-10) and fig (5-11) respectively. Ejections were common at all the oxygen potentials, but the growth and swelling had different features.

At low oxygen concentrations (CO_2 less than 2.3% in CO gas mixtures) it appeared that only one or two nuclei grew and caused the swelling. Just before escaping from the surface of the drop a gas bubble can be identified by the dark spot on the surface of the drop, fig (5-9) and fig (5-10), which disappeared after the gas bubble escaped from the surface of the drop and the specimen had returned to its original size. The dark spots implied less brightness density at that part of the drop, i.e. a lower temperature. This was due to different heating by the electromagnetic field of the thin skin of melt between the gas bubbles and the atmosphere compared to the heating in the bulk of the drop. At higher oxygen potentials, above 2.8% CO_2, a large number of the nuclei grew at the same time and caused a frothy drop. This is shown by the large number of gas bubbles escaping from the surface of the drop for 4% CO_2 in fig (5-11).

Fig (5-12) shows an interesting series of photographs of drops which solidified during ebullition. These drops had the spherical shape of molten drops and showed tremendous swelling

Time from start of
the run, sec.

3.0 Pictures of levitated molten iron illustrating the size of the levitated drop before nucleation

4.0 After nucleation started the swelling of the drop showed the growth of gas bubbles

The dark spot which appeared on the surface indicated that a gas bubble is just below the surface of the drop

/4.8 Escape of the gas bubble from the surface of the drop. After the collapse of the drop new gas bubble nuclei are spontaneously formed as indicated by the sudden increase of the drop size

Ejection of a metal particle from the surface of the drop.

Fig (5-9) Run CN36, illustrating CO gas bubble nucleation in molten iron, 2.15% CO_2 Picture speed 64 f.p.s.

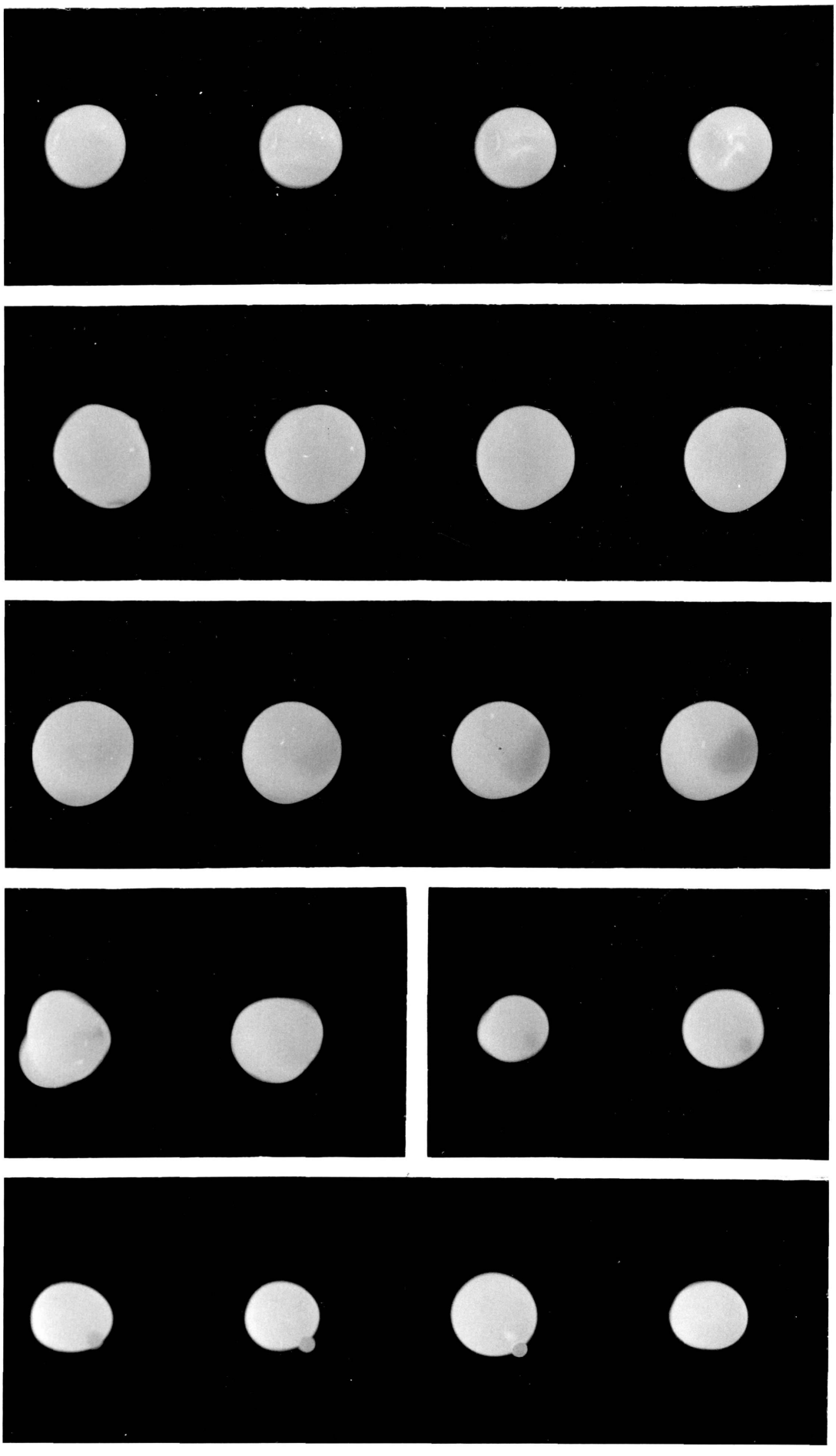

Time from start of the run, sec.

5.0/ 5.8 First two frames illustrate the size of the levitated drop before nucleation. The drop after nucleation showed the growth of gas bubbles

Escape of the gas bubble in the second frame accompanied by ejection of a relatively large metal droplet.

6.6 The dark spot disappeared from the surface after the escape of a gas bubble from the surface

7.3 Escape of a gas bubble leading to deformation of the molten drop

8.1 The large dark area with the gradient of the brightness around its centre indicated that the swelling was caused by one bubble

Fig (5-10) Run CN57, illustrating CO gas bubble nucleation in molten iron, 2.3% CO_2 Picture speed 64 f.p.s.

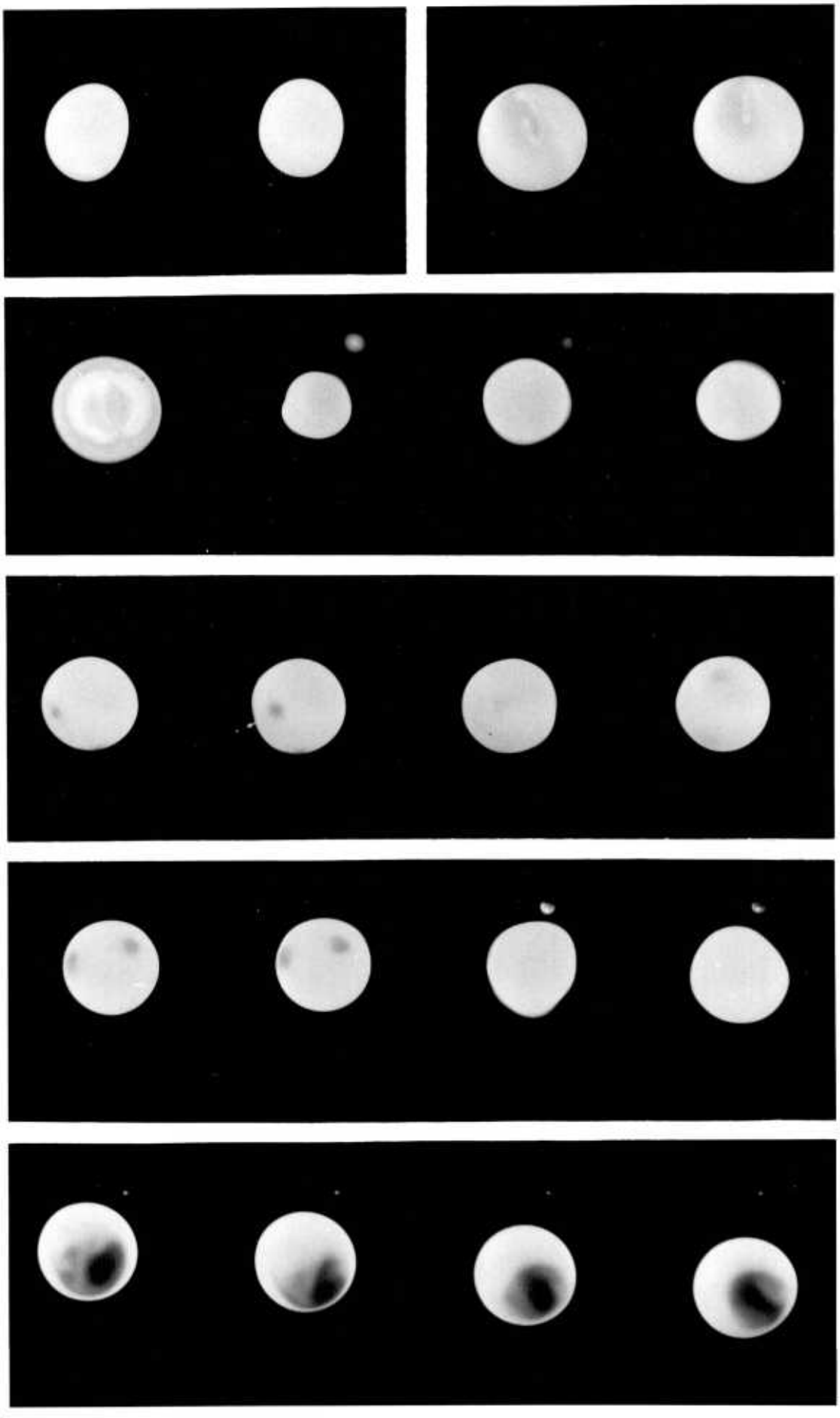

Time from start
of run, sec.

1.6 Nucleation started with ejection of metal droplets

2.4 Drop is undergoing deformation due to the escape of large gas bubbles

Considerable rate of CO bubble nucleation

2.42/
2.54 Drop suffused with CO bubbles

Fig (5-11) Run 44, illustrates CO gas bubbles nucleation in molten iron, 4.58% CO_2 Picture speed 64 f.p.s.

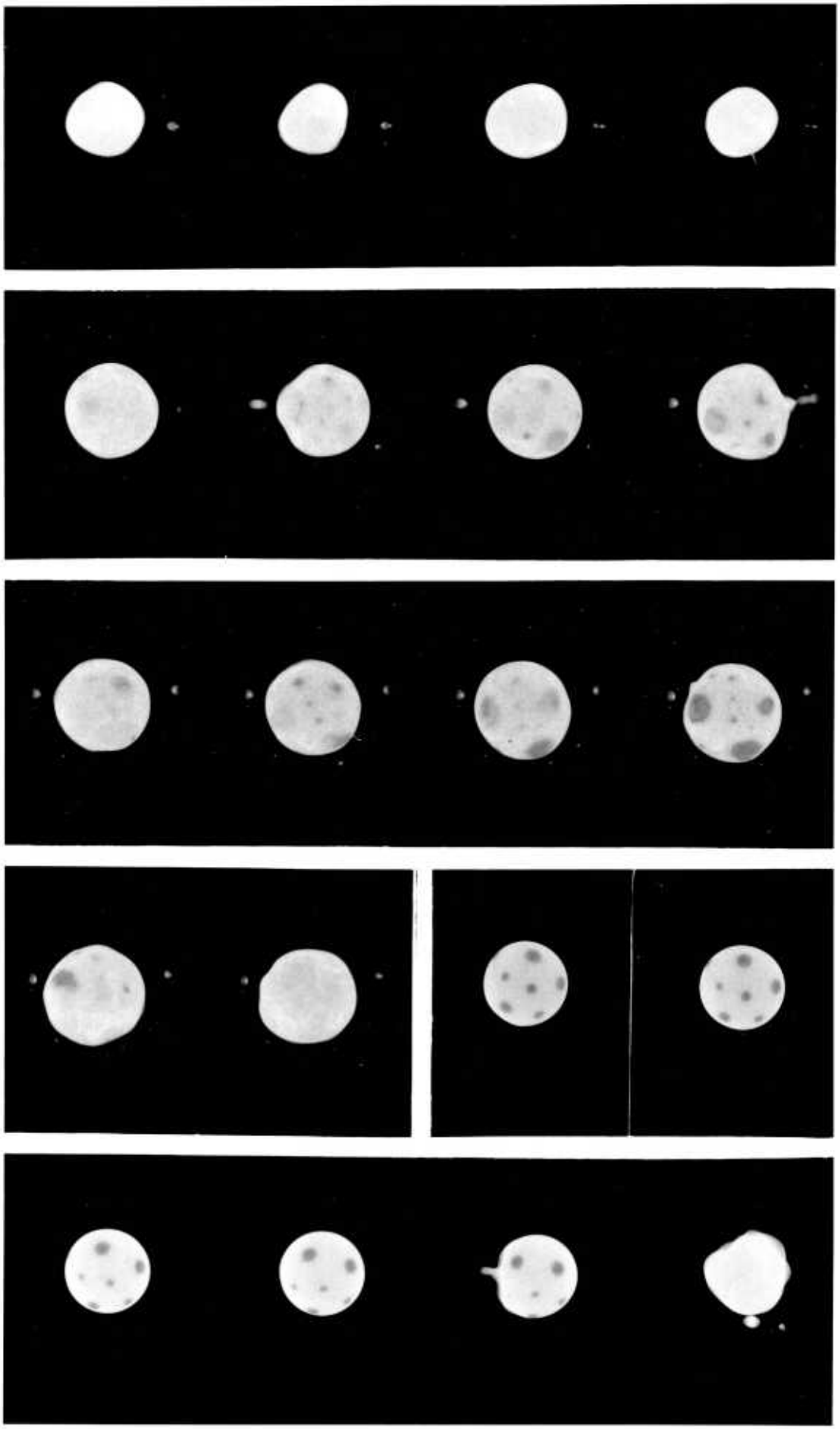

(a)

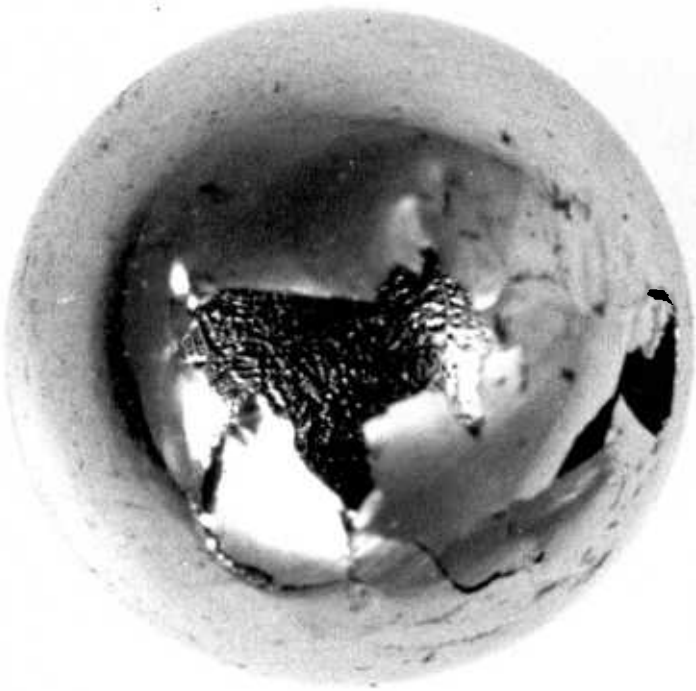

(b)

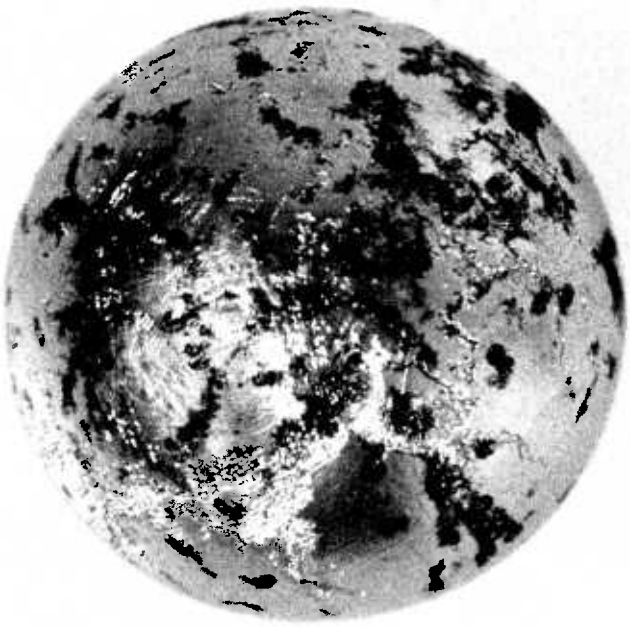

Fig (5-12) Shows solidified drops during ebullition (1gm iron r=6.4mm)

a) CN9 illustrates the swelling and a large cavity below the broken shell

b) Run CN15, illustrates the swelling

(1 gram molten iron has 6.4 mm diameter). They were obtained from the preliminary runs CN9 with 1.9% CO_2 fig (5-12a) and CN15 with 4.5% CO_2 fig (5-12b)using manual power control.. Solidification occurred due to the large increase of radi ative heat transfer caused by the swelling (doubling the surface area of the drop) without a corresponding increase of heat input to the drop by the eddy currents. Fig (5-12a) suggests that the swelling was caused by one gas bubble, which is another piece of evidence of formation of one gas bubble at a time at low oxygen concentration, while fig (5-12b) shows the formation of the gas bubbles in the drops. These figures give another piece of evidence of homogeneous gas bubble formation of CO in molten iron.

5-5.2.2 Supersaturation pressure for CO bubble nucleation

Carbon monoxide gas bubble formation in molten iron was observed only when the supersaturation pressure was sufficient to cause an observable rate, which may be defined by the formation of one nucleus/sec cm^3. The supersaturation limits were found to depend on the oxygen concentration in the drops. They were obtained for each oxygen potential (CO-CO_2 gas mixture) by scanning all over the supersaturation pressures experimentally possible (up to 100 atmosphere) for gas bubble nucleation. It was possible to obtain the supersaturation limit to within one atmosphere pressure difference.

The results of all the runs are given in table (5-5). The carbon analyses of the drops after quenching were consistent

with the estimated equilibrium values at the intial high pressure for all CO-CO_2 gas mixtures. The reproducibility of the gas bubble formation, specially near the supersaturation limits, was remarkable. The critical supersaturation limit as a function of oxygen activity in the drop is plotted in fig (5-13). The supersaturation pressure decreases rapidly from 72 atmosphere at oxygen activity defined by the 2.15% CO_2 gas mixture to 15 atmosphere at that of the 4% CO_2 mixture. At higher oxygen activites the supersaturation pressure shows no significant change (10 atmosphere at 8% CO_2). It is interesting to note that at lower oxygen activities than that of the 2.15%CO_2 in CO gas mixture superaturation of hundreds of atmospheres would be required for nucleation.

A few experiments were carried out at final pressures of 5 and 10 atmospheres with the 8% CO_2 gas mixture. The higher final pressure showed no effect on the nucleation phenomena. These results are given in table (5-5). These experiments confirm that the supersaturation pressure (P_i-P_f) for any oxygen activity fixes the nucleation behaviour.

Fig (5-13) Supersaturation for nucleation of CO bubbles in Fe-C-O at 1600°C

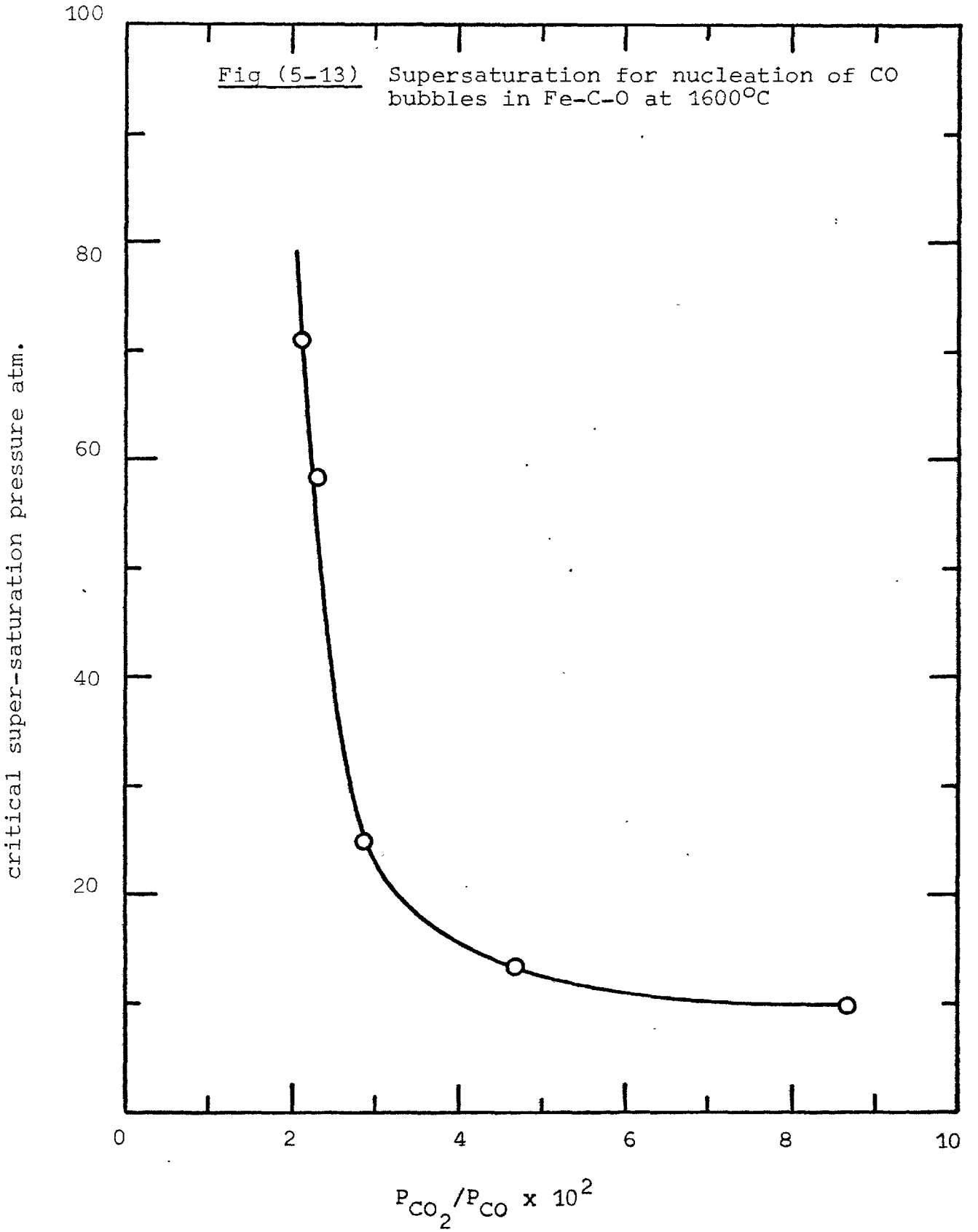

Run No	gas mixture	initial (equilibrium) press. atm.	final press. atm.	temp. °C	w/o carbon	super-saturation pressure	observation	notes
CN6	CO-1.9% CO_2	66.04	1.30	1550	3.28	64.74	no nucleation	(visual observation)
7	"	66.77	"	1650	2.57	65.47	"	
8	"	66.17	"	1750	2.10	64.87	"	
9	"	66.68	"	1550	--	65.38	nucleation	
10	"	68.09	"	1650	2.64	66.79	"	
11	"	67.14	"	1550	3.31	65.84	no nucleation	
12	"	67.52	"	1750	2.11	66.22		(film record manual temp. control
CN14	CO-4.58% CO_2	56.54	"	1600	1.26	56.24	nucleation	
15	"	56.38	"	"	"	56.08	"	
16	"	50.37	"	"	1.36	49.07	"	
17	"	45.75	"	"	1.19	44.45	"	
18	"	45.10	"	"	1.24	43.80	no nucleation	
19	"	40.17	"	"	0.929	38.87	"	

Table (5-5) Results of carbon monoxide nucleation in molten iron

Run No	gas mixture	initial (equilibrium) press. atm.	final press. atm.	temp. °C	w/o carbon	super-saturation pressure	observation	notes
CN20	CO-4.5% CO_2	47.19	1.30	1600	1.18	45.89	nucleation	film record-manual temp. control
21	"	39.96	"	"	1.09	38.66	"	film record-manual temp control
CN23	CO-8.21% CO_2	45.55	1.30	1600	0.57	44.77	nucleation	film record-automatic temp. control
24	"	39.73	"	"	—	38.45	"	
25	"	49.42	10.14	"	0.70	39.28	no nucleation	
26	"	59.77	10.25	"	0.86	49.51	nucleation	
27	"	70.10	10.19	"	0.94	59.91	"	
28	"	79.63	10.25	"	1.12	69.38	"	
29	"	75.70	10.25	"	1.04	65.45	"	
30	"	75.27	10.25	"	0.71	65.02	"	carbon much less than equilibrium
31	"	55.25	5.65	"	0.81	49.60	"	film record automatic temp control

Table (5-5)
(continued)

Run No	gas mixture	initial (equilibrium) press. atm.	final press. atm.	temp ^{o}C	w/o carbon	super-saturation pressure	observation	notes
CN32	CO-8.21% CO_2	50.86	5.65	1600	0.825	45.21	nucleation	
33	"	45.10	5.65	"	0.70	39.45	"	
34	"	41.54	5.65	"	0.62	35.89	"	
CN35	CO-2.15% CO_2	71.23	1.30	1600	2.86	69.93	no nucleation	film record automatic temp control
36	"	78.92	"	"	2.95	77.62	nucleation	
37	"	76.08	"	"	2.85	74.78	"	
38	"	73.17	"	"	2.67	71.87	"	
CN39	CO-4.58% CO_2	39.44	1.1	1600	0.924	38.34	nucleation	
40	"	34.83	"	"	0.88	32.73	"	
41	"	30.56	"	"	0.75	29.46	"	
42	"	25.87	"	"	0.64	24.77	"	
43	"	20.52	"	"	0.58	19.42	"	
44	"	16.89	"	"	0.42	15.79	"	
45	"	14.29	"	"	0.42	13.19	no nucleation	

Table (5-5)
(continued)

Run No	gas mixture	initial (equilibrium) press. atm.	final press. atm.	temp. ^{o}C	w/o carbon	super-saturation pressure	observation	notes
CN46	CO-4.58% CO_2	15.18	1.1	1600	0.41	14.08	nucleation	film record automatic temp control
47	"	13.82	"	"	0.35	12.72	no nucleation	
CN48	CO-8.21% CO_2	31.14	1.10	1600	0.36	30.04	nucleation	film record automatic temp control
49	"	20.91	"	"	0.23	19.81	"	
50	"	11.82	"	"	0.15	10.72	"	
51	"	11.29	"	"	0.09	10.19	"	
52	"	10.02	"	"	0.10	8.92	no nucleation	
53	"	10.76	"	"	0.13	9.66	"	
54	"	11.31	"	"	0.097	10.21	nucleation	
CN55	CO-2.3% CO_2	59.34	1.1	1600	2.31	58.24	no nucleation	film record automatic temp control
56	"	60.19	"	"	2.36	59.09	nucleation	
57	"	60.44	"	"	--	59.34	"	

Table (5-5)
(continued)

Run No	gas mixture	initial (equilibrium) press. atm.	final press. atm.	temp. ^{o}C	w/o carbon	super-saturation pressure	observation	notes
CN58	CO-2.3% CO_2	58.47	1.1	1600	2.24	57.24	no nucleation	film record automatic temp. control
59	"	58.53	"	"	2.30	57.43	"	
CN60	CO-2.8% CO_2	22.90	1.1	"	--	21.80	no nucleation	film record automatic temp control
61	"	16.20	"	"	--	15.10	"	
CN62	CO-8.21% CO_2	20.20	1.1	1600	1.337	19.10	nucleation	high speed films automatic temp control
63	"	20.20	1.1	1600	--	19.10	nucleation	

Table (5-5)
(continued)

Run No	gas mixture	initial (equilibrium) press. atm.	final press. atm.	temp. ^{o}C	w/o carbon	super-saturation pressure	observation	notes
CN64	CO-2.9% CO_2	30.20	1.1	1600	1.16	29.1	nucleation	film record automatic temp control
65	"	27.65	"	"	1.001	26.55	"	
66	"	27.85	"	"	1.05	26.75	"	
67	"	27.25	"	"	1.02	26.15	"	
68	"	25.75	"	"	0.95	24.65	"	(only one ejection was observed)
69	"	26.50	"	"	1.00	25.40	"	

Table (5-5)
(continued)

5-6 Discussion

5-6.1 Remarks on gas bubble nucleation phenomena in molten iron

The object of the following paragraph is to summarize briefly the features of gas bubble nucleation in levitated molten iron drops observed in this work. This gives a reasonably clear picture on nucleation phenomena in molten iron.

The results reported in section (5-5) showed that gas bubble formation can occur in liquid metal, when no second phase is present at the surface, at supersaturation pressures as low as 10 atmospheres, under particular conditions. The results also showed that supersaturation pressures above those which could be obtained experimentally are required in order to initiate nucleation under other conditions.

The supersaturation pressures at which the nucleation can be observed depend on oxygen activity in the Fe-C-O system, and on the presence of oxygen in the Fe-N system. (The study of the Fe-N-O was qualitative, and only showed that dissolved oxygen enhanced the nucleation of dissolved nitrogen in molten iron). No nucleation was observed in the Fe-N or Fe-C-O systems up to supersaturation pressures of 100 atmosphere at sufficiently low oxygen activities, fig (5-13). From the summary of experimental observations of nucleation it seems clear that the presence of dissolved oxygen in molten iron is essential to initiate gas bubble nucleation in molten iron in these systems.

As discussed in section (5-2.2) the work required to form a new surface is proportional to the surface tension. From this point we shall examine the effect of dissolved elements on the

surface tension of molten iron using the surface tension measurements on liquid iron in the presence of added elements (118-120). It is well known that dissolved oxygen decreases the surface tension of molten iron tremendously, while nitrogen has a smaller effect fig (5-14). Fig (5-14) shows the surface tension in the Fe-O system as a function of CO/CO_2 ratio and the surface tension in the Fe-N system as a function of nitrogen pressure. (The data for nitrogen is based on an extrapolation of measurements at pressures of up to 1 atmosphere and may be subject to considerable error.) This was done since it is convenient in this study to express the results in terms of gas pressures.

Iron-nitrogen solutions at 100 atmosphere pressure of nitrogen would be expected to have a surface tension comparable with that of Fe-O solutions in equilibrium with 8% CO_2 in CO gas mixtures. (Carbon has little effect on the surface tension of molten iron in the binary Fe-C system). Despite the fact that surface tensions were similar in the Fe-N (N_2 at 100 atm) and Fe-C-O (8% CO_2 in CO) systems no nucleation was observed in the first system, while the critical supersaturation pressure in the second case was extremely small (about 10 atmosphere). From these facts we may conclude that the <u>decrease of surface tension by the presence of a surface active element is not the only important factor in gas bubble nucleation in molten iron</u>.

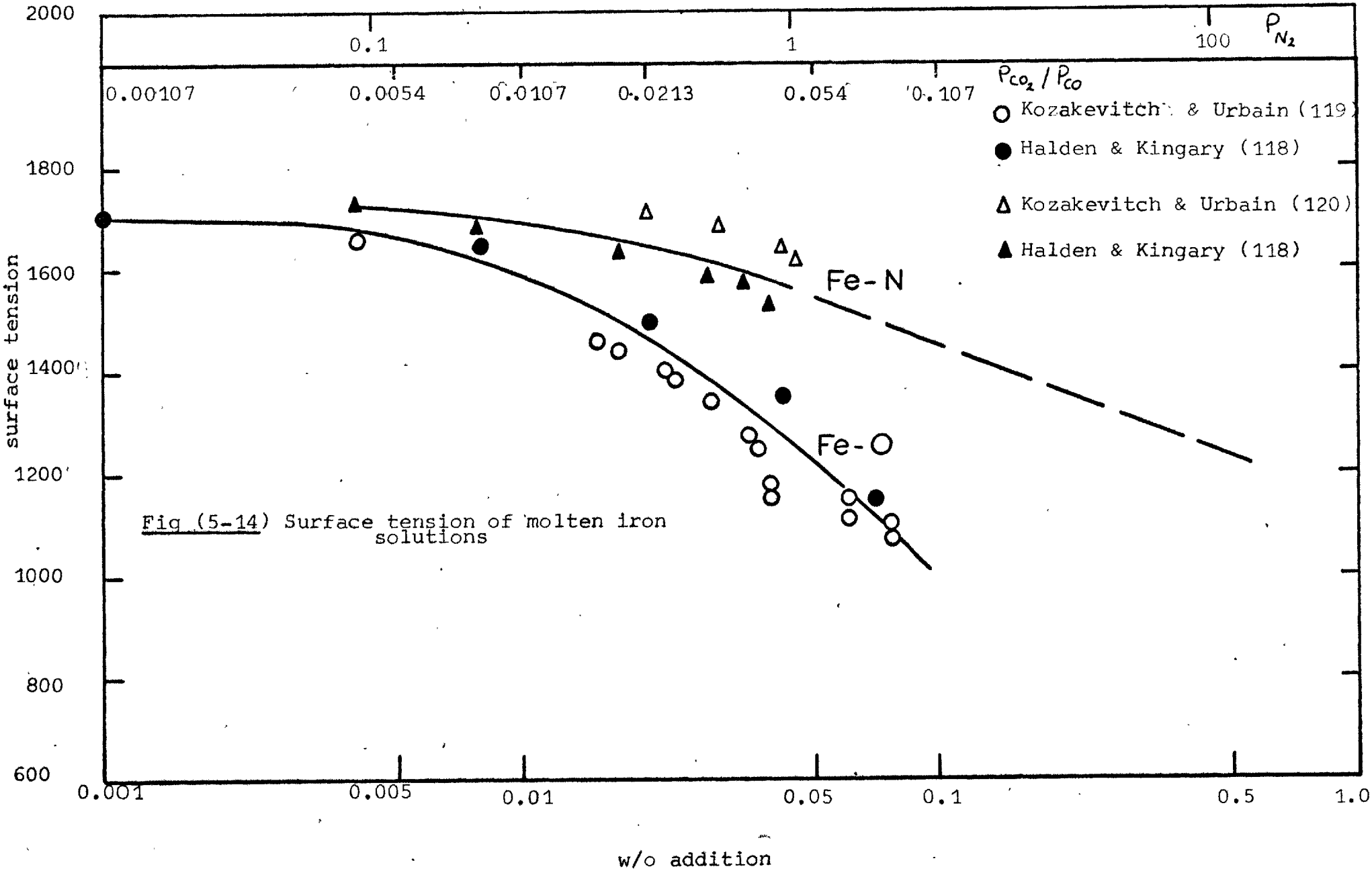

Fig (5-14) Surface tension of molten iron solutions

It was interesting to find that the critical supersaturation pressure was nearly independent on oxygen activity above the values corresponding to the 4% CO_2 gas mixture. This observation is in line with a nearly constant relative adsorption (excess surface concentration) of oxygen, from the surface tension measurements. The dramatic change in the critical supersaturation pressure with lower oxygen matches the decrease of the excess surface concentration, fig (5-15). The relative adsoprtion of nitrogen is less than that of oxygen fig (5-15). The value of relative adsoprtion corresponding to any nitrogen pressure above 1 atm. is less than the value from oxygen corresponding to 2% CO_2 or above. We may conclude from these facts that the number and nature of the adsorbed molecules at the surface play an important role in the nucleation phenomena. The fact that nucleation of nitrogen bubbles becomes possible with traces of oxygen confirms this. The effect of adsorbed species in the surface layer has already acted to decrease the surface tension of even flat surfaces. However such decreases in surface tension are not adequate to give homogeneous nucleation. (Even a surface tension of 100 dynes/cm represents an enormous barrier to nucleation according to the classical theory). Therefore the effect of the adsorbed layer on the nucleation phenomena must in my view be related to the sharp curvature of the surface (gas bubble nucleus has a spherical shape and $r^* \simeq 10^{-6}$cm).

We may summarise the main features of gas bubble nucleation in liquid iron in the systems studied as follows.

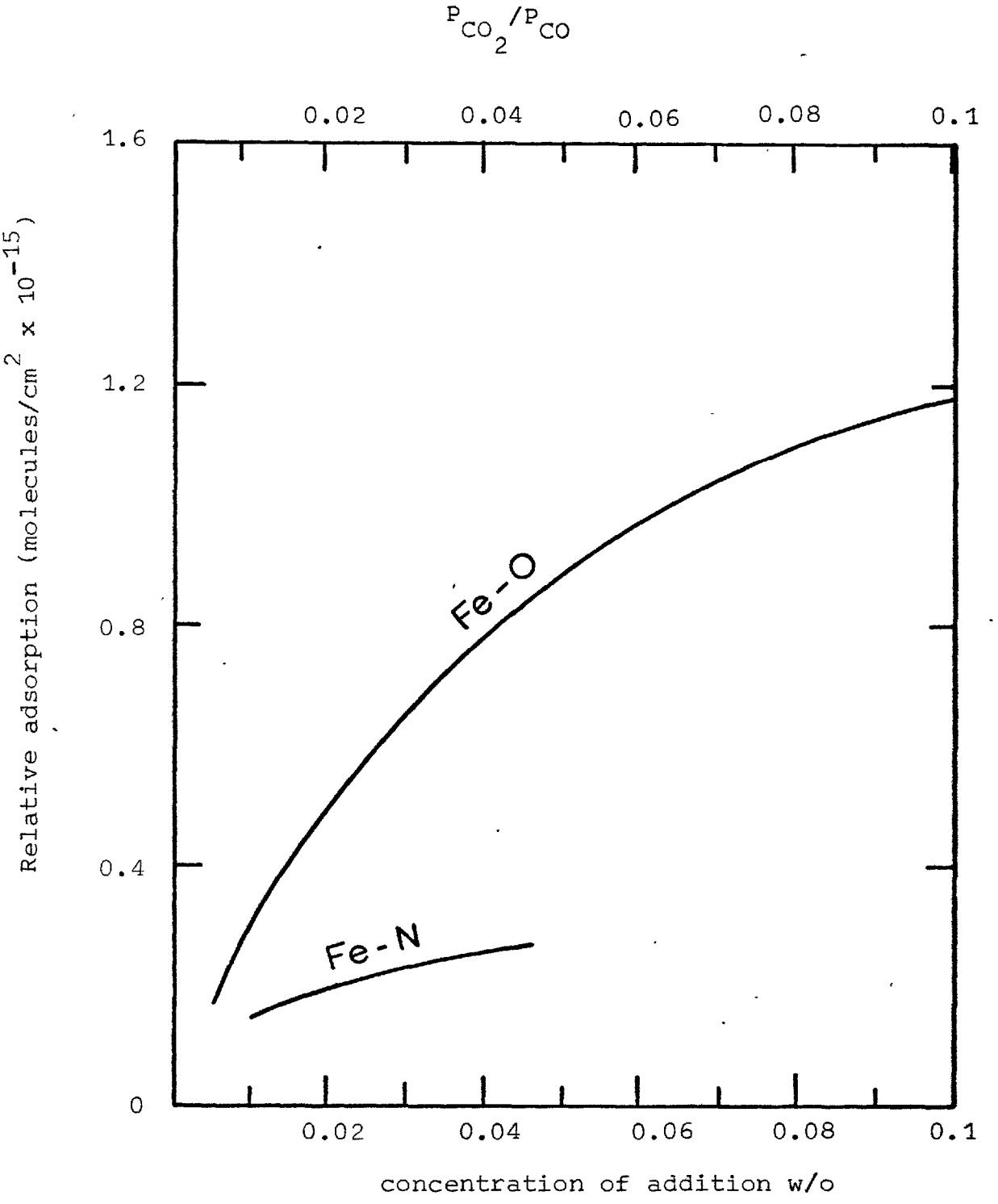

Fig (5-15) Relative adsorption of additions to iron at 1550°C

1) Critical supersaturation pressure in Fe-C-O system varies from a hundred or more to ten atmospheres, depending on oxygen potential in molten metal, while in the Fe-N system no nucleation was observed up to 100 atmosphere but the presence of oxygen caused nucleation at lower pressures.

2) The decrease of surface tension of liquid iron solutions is not the important factor in dropping the critical supersaturation pressure.

3) The nature and concentration of adsorbed oxygen the surface layer of the spherical gas bubble plays the major role in gas bubble nucleation phenomena in molten iron.

These points, which are drawn from the experimental facts, must be considered in any explanation of this phenomenon.

5-6.2 Discussion of nucleation theories

In the light of the above conclusions it is possible to confirm or deny the application and the validity of the previous theories in the case of gas nucleation in liquid metals.

Nucleation by cavitation, Dean's theory

This theory (see section (5-2.3)) has gathered a wide support from the previous investigators (5, 85, 121) as the explanation of carbon monoxide gas bubble formation in levitated or free fall molten iron drops during decarburization. The idea at that time was the observed high circumferential velocities at the surface of the drop during decarburization lead to formation of free vortices.

If we accept that there is a high level of turbulence in this work as a result of flow induced by the eddy currents in the drops (in the experiments there was no observed interfacial turbulence due to chemical reactions) there must be a nearly constant value of the main vortex circulation. According to the theory we may therefore expect a constant critical supersaturation pressure for all dissolved gases at all conditions (see fig (5-5)). This is inconsistent with the observed facts.

Classical theory of nucleation

The critical supersaturation pressure required to nucleate a single gas bubble in Fe-C-O molten drop at 1600°C was calculated by the equation (5-36), as a function of oxygen activity (represented by CO/CO_2 ratio) fig (5-16). These results are based on assumed values of $\gamma = 10^{13}$ sec^{-1} and ΔF_d = 15 k cal/mol. It is important to realise that the pre-exponential term in the classical rate equation

$$I = A \exp (\Delta F^*/kT) \qquad (5-38)$$

is nearly constant over the whole range and about 10^{35}. As illustrated in fig (5-16), the required supersaturation pressure for carbon monoxide bubble nucleation is extremely high. The value is about 10^4 atmospheres at very low oxygen and does not change much be decreasing the surface tension of the molten iron solution by dissolved oxygen.

One of the strongest pieces of evidence that the results of this work are significant is that they show a trend towards very

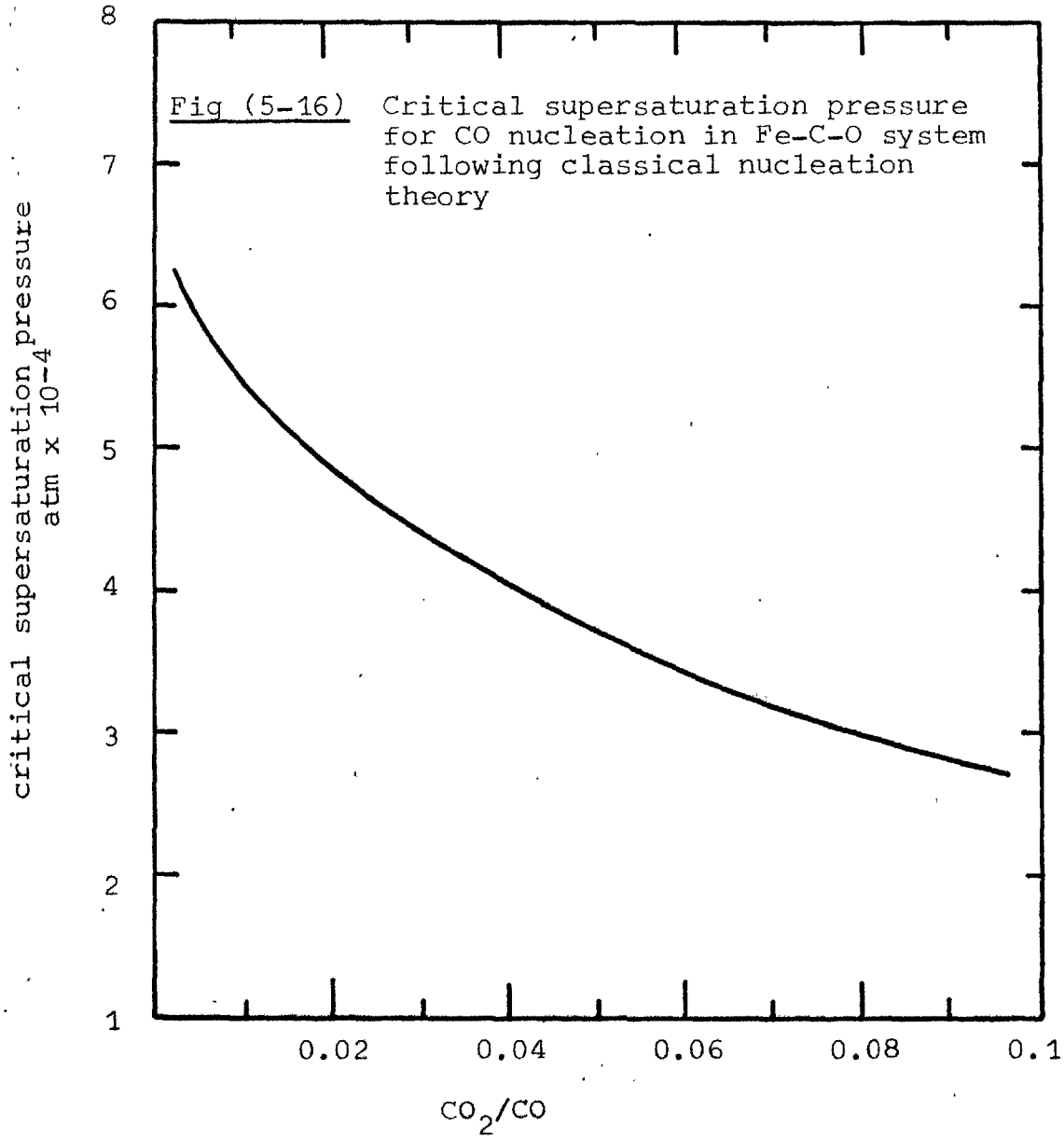

Fig (5-16) Critical supersaturation pressure for CO nucleation in Fe-C-O system following classical nucleation theory

supersatuations in iron free of dissolved oxygen. The data are therefore consistent with the predictions of the classical theory under the conditions where there are no possiblities of additional effects being important. In other words the classical theory is basically valid. This leads to the belief that the adsorbed layer does work on the system which must be added to the work of formation of the new phase. This work must be related to curvature, since the effect of the adsorbed layer on the flat surface is already taken account of by the observed decrease of surface tension of molten iron.

5-6.3 Speculation on surface structure

Recently, it was recognized that the surface structure of embryonic liquid drops, which differs from the structure of the flat surface of the bulk liquid, may resolve the disagreement between the theory of vapour condensation and experiments (107). In this section a similar approach is considered for gas bubble nuclei in an attempt to resolve the disagreement between the measurements and the theory. The experimental observations back this hypothesis. In the following paragraphs the nature of adsorbed oxygen is considered and its role in gas bubble nucleation is examined.

It is well known that an adsorbed film of nonmetallic atoms on a solid metal surface possesses a certain degree of ionicity according to the relative electronegativities of the adsorbed atoms and the metal in question (122). The ionic character, which implies a dipole moment is a result of a-symmetry of the atoms at the surface. The adsorbed atoms on the surface of

molten metal may also possess a dipole moment. Also the dramatic decrease of the surface tension by the presence of adsorbed surface active species in molten iron implies a certain degree of orientation of dipoles at the surface, because repulsion between like charges at the surface decreases the work done in extending the surface area. This simple picture of surface structure of molten iron has been considered as the basis of the following discussion.

Levine (123, 124, 125, 126) recognized the importance of the role of the dipole layer on nucleation during the combustion in oxygen-nitrogen mixtures of zirconium droplets and during decarburization of iron-carbon alloys. Regrettably his treatment of the equation for the work of formation (equation (5-19)) is not correct and his paper does not provide an explanation of the nucleation phenomena. He violated the condition of equilibrium, equation (5-10), as a result of misusing the electrochemical potential of the oxygen at the surface

$$\bar{\mu}_o = \mu_o + z e x \qquad (5\text{-}39)$$

where z is number of charge, e is the electron charge, and x is the surface potential. The contribution of μ_o to the electro-chemical potential depends not only on the temperature and local concentration but also on the electric field at the point considered, as emphasised by Defay et al (105). Levine erroneously obtained an extra work term in ΔF^* which he related to the electro static effect caused by a dipole layer of adsorbed oxygen. As a result his calculation on nucleation showed that at

oxygen activites above those corresponding to a value of 14ppm dissolved oxygen ΔF^* is zero i.e. no work is required to form a new surface. This does not make sense and completely contradicts the present measurements on CO nucleation in molten iron.

Abraham (107) introduced a fascinating idea on the effect of curvature on dipole-dipole interaction energy; he demonstrated that the surface free energy of drops is increased from that of the plane surface by rotating dipoles toward each other. The ends of the dipole in the surface are considered to remain at the same spacing irrespective of curvature. The angle of rotation is directly related to the radius of the droplet fig (5-17b)

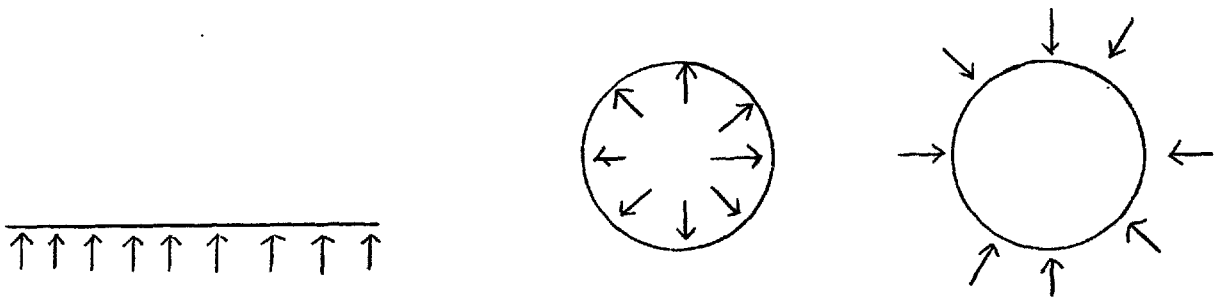

(a) (b) (c)

Fig (5-17)

Illustration of a polar molecule with dipole alignment at either (a) a flat plane, (b) a liquid drop, (c) a gas bubble

The increase of the potential energy according to classical electrostatic theory is given by

$$\overline{U}^{s} = 2P^2 n/r_o^3 \qquad (5\text{-}40)$$

where P is dipole moment of a molecule, n is the number of surface nearest neighbours and r_o is the distance between the nearest neighbours.

In the case of a bubble the effect of curvature acts to decrease the potential energy, fig (5-17c). The total surface energy of a bubble of surface A is

$$\Delta F^{(s)} = \sigma A - \bar{U}^{s} = \sigma(r)A \qquad (5\text{-}41)$$

where σ is the flat plane surface tension and r is the bubble radius.

Calculations assuming that all the adsorbed oxygen is completely polarized and orientated normal to the surface give $\bar{U}^{s}$ about 10^{-10} erg. This decreases the critical supersaturation pressure from about 3×10^{4} to about 5×10^{3} atmosphere. Despite this decrease the supersaturation pressure does not approach the levels of supersaturation observed experimentally. However the effect does demonstrate the important role of the surface structure on the nucleation phenomena.

5-6.4 Significance of the results

This study provided unique data on the supersaturation required for the carbon oxygen reaction in molten iron. This has a fundamental importance in understanding the decarburization reaction in steelmaking and in soldification of rimmming steel. It also provides useful information for vacuum degassing of liquid iron.

The results confirm the possiblity of the homogeneous CO bubble formation observed during decarburization, particularly the work on levitated drops and in free fall (5, 80 - 86). They can also provide a quantitative prediction for the carbon and oxygen levels at which the carbon boil will start during decarburization and hence a complete analysis of the decarburization reaction.

These results also tie in with the visual observations on the reaction of iron carbon alloy drops in slag (127), which simulate one of the decarburization mechanisms in the L.D. process (128, 129). Previous calculations on the heterogeneous nucleation rate at the iron-iron oxide interface (130) rejected this possibility as a mechanism of decarburization of levitated drops. However the calculations were based on the classical theory which, as we have seen, predicts very high supersaturations. The results of this work show that nucleation, whether homogeneous or heterogeneous, will occur at low carbon (high oxygen).

The results on homogeneous nucleation of carbon monoxide gas bubbles in molten iron may provide information towards understanding the surface phenomena of molten metals. They also demonstrated that under certain conditions the barrier to gas bubble nucleation is not tremendously large as was believed before. This may lead to a better understanding of gas-metal reactions.

5-7 Conclusion

The work reported in this chapter has extended the knowledge of homogeneous nucleation of gases in molten iron, particularly carbon-oxygen reaction. The techniques which were applied provide a correct and accurate approach to gas bubble nucleation studies in molten metals.

This work has tested the previous nucleation theories and has enabled their application to molten metals to be studied. It has demonstrated that adsorbed oxygen is the most important factor in the nucleation phenomena. At very low oxygen activity in molten iron very high supersaturation was required for homogeneous nucleation, which is basically in agreement with classical nucleation theory. The supersaturation was found to decrease dramatically by increasing the oxygen activity. At relatively high oxygen activity a low and nearly constant supersaturation was required for nucleation. The change of supersaturation with oxygen in molten iron was thought to depend on some effect arising from the high relative adsorption of oxygen on the surface layer. This effect was not taken into account in the classical nucleation theory. The experimental facts were found to be inconsistent with Dean's theory of nucleation by cavitation. Levine's theory, which considered the structure and properties of the interface, was found to have been incorrectly formulated. Although Abraham's approach to the dipole-dipole interaction is basically correct such interactions would have a relatively small effect on the nucleation rate.

The results provided the first quantitative results on the homogeneous nucleation of carbon monoxide in molten iron. They give the basic information required in understanding carbon-oxygen reactions in molten iron and hence the decarburization reaction, which is one of the most important reactions in steelmaking processes.

Conclusion

In the understanding of the kinetics of decarburization reactions in steel making processes, the thermodynamic data of the Fe-C-O system must be established first and then the processes by which the reaction occurs must be defined. Great stress has been laid in this thesis on the thermodynamics of the Fe-C-O system, the kinetics of decarburization by oxidizing gas at the surface of molten iron and the carbon-oxygen reaction in molten iron via homogeneous nucleation of carbon monoxide bubbles.

The simple geometry of almost spherical drops suspended in a gas stream during levitation provide an ideal system for such a study. The new technique adopted in this work involving the use of high pressure eliminated the disadvantage of levitation melting at one atmosphere. These are temperature control and enhanced vaporization of the metal. It became possible by using the high pressure to measure the heat transfer in the gas phase in all convective regimes. The transfer coefficient in the gas phase were evaluated for levitated drops, where there are steep temperature gradients in the gas phase, and there are no previous studies under these conditions.

Segregation of the gas mixture across the gas phase boundary layer due to the steep temperature gradient can be accurately

defined using the technique of Sunderland et al. For $CO-CO_2$ gas mixtures where there was not a large difference between the molecular weight of the two gases the thermal diffusion was only a small effect in dilute mixtures. It was possible to measure the thermal diffusion by using high pressures. This was acheived by relying on very accurate equilibrium data (graphite equilibrium with $CO-CO_2$ gas mixtures, and the solubility of carbon in molten iron). The accurate knowledge of gas composition at the surface of the drop, together with the advantages of the levitation technique, provided an accurate and practical method for thermodynamic measurements. By the use of high pressure, the thermodynamic measurements on the Fe-C-O system the data were extended over a very wide range carbon and it was possible to study the Fe-C-O system under well defined conditions.

Besides accurately defining transport phenomena in the gas phase, this work has shown that the levitated drop can be treated as a static sphere as regards diffusion in the liquid. This solved one important kinetic aspect in the study of gas-metal reactions using the levitation technique.

A new technique was developed for the study of homogeneous nucleation of dissolved gases in molten metal. This technique has been applied successfully to the study of carbon monoxide

nucleation in molten iron. The first quantitative data on carbon oxygen reaction in a single phase Fe-C-O system were obtained. The work also showed that the nucleation barrier in molten metals (under certain conditons) was not as high as was beleived before. This may lead to a better understanding of nucleation of gas bubbles in molten metals.

APPENDICES

Appendix 1

High frequency generator and its power control.

The main stages in the generation of high frequency power shown in fig. (A1-1) are

1) Producing A.C. high voltage from main 3-phase 440 volt A.C. by step-up transformer.
2) Rectification of A.C. to D.C. high voltage.
3) The high D.C. voltage supplied the power to the anode of the oscillator valve which produces the high frequency power.
4) The high frequency power is fed via a high frequency transformer to the induction coil.

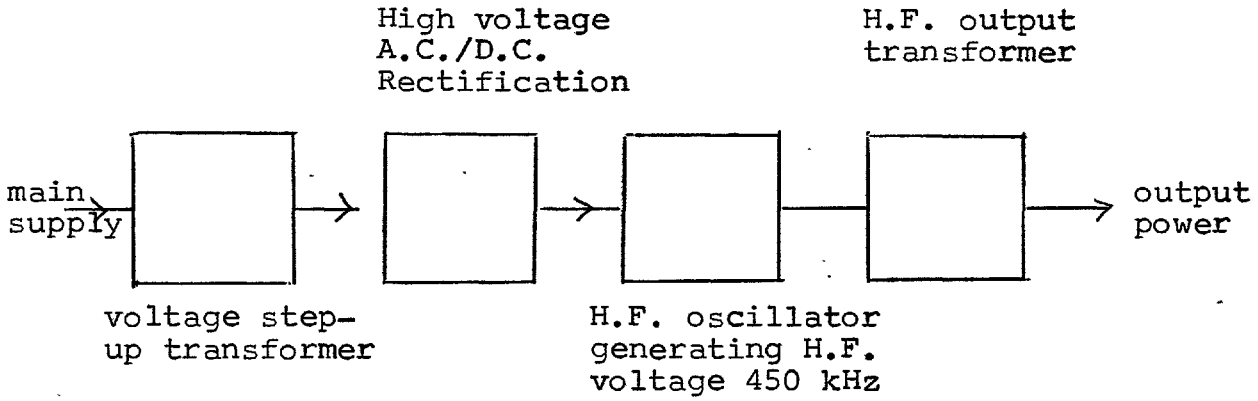

Fig (A1-1)

Stages in generation of

high frequency power

The output power is controlled either by the variable high frequency transformer or by altering the supplied high voltage to the oscillator. The first method is provided by the generator and operated manually. The second method was adopted for automatic control of the power, simply by controlling the main supplied voltage. This was achieved by the electronic circuit fig (A1-2) supplied by "Eurotherm". It functioned as follows. The temperature reading from the T.C.P. as mV output 0-9.99 mV. was converted in the digital set-point controller into 5-0 volt inverted output. The output voltage was fed to a synchronised three phase thyristor controlled system. This comprised of three individual driving units of 0-24 volt output, and three thyristor units rated for 25 A each, with a filter. This system controlled the three phase A.C. voltage input to the high frequency generator.

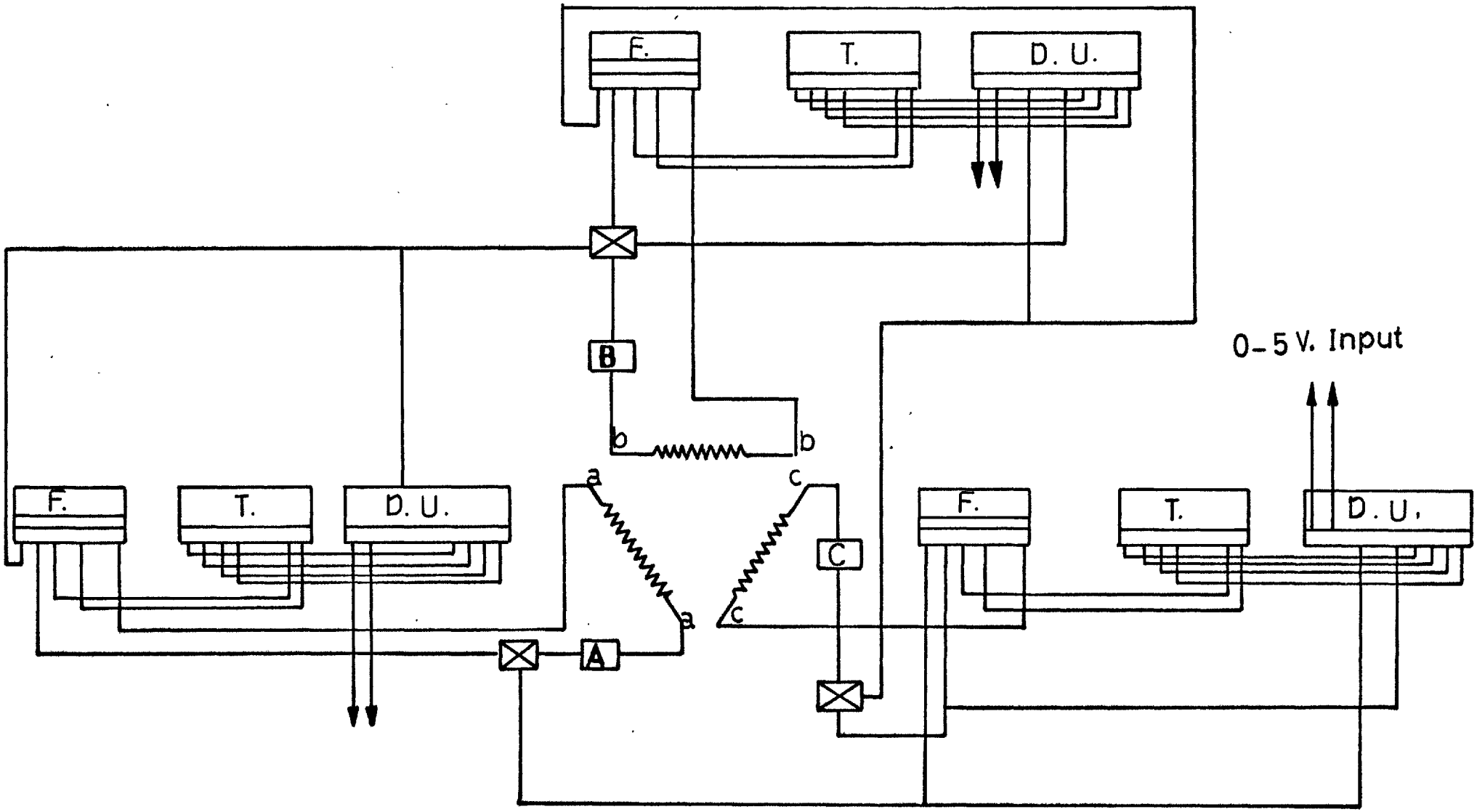

Fig (A1-2)

Temperature controller equipment wire diagram

Appendix 2

Calculation of convective heat transfer around a sphere.

In the abscence of a satisfactory solution of convective heat transfer problems (as in the present study) the heat flow across the interface can be expressed by "Newton's Law of cooling" as

$$Q_{CONV} = A\, h_m \Delta T \qquad \text{(A2-1)}$$

where h_m is the mean heat transfer coefficient. When there are steep temperature gradients so that the properties of the fluid vary across the boundary layer, the arithmetic mean temperature

$$T_f = (T_s + T_b)/2 \qquad \text{(A2-2)}$$

is used to define the property values. The mean heat transfer coefficient is thus given as

$$h_m = Nu_m\, k_f/d \qquad \text{(A2-3)}$$

where Nu_m is dimensionless and called the Nusselt number, k_f is the thermal conductivity at the film temperature and d is the hydrodynamic characteristic length of the system - the diameter for a sphere.

From Dimensional Analysis Nu_m is a function of the fluid hydrodynamics, that is the dimensionless groups Reynolds number (Re) and Grashof number (Gr), as well as the ratio of the thermal

to the velocity gradients defined by Prandtl number (Pr). The groups are defined as (96)

$$Re = \rho_f V_c d/\mu_f \qquad (A2-4)$$

$$Gr = \rho_f^2 gd^3 \Delta T/T_f \mu_f^2 \qquad (A2-5)$$

$$Pr = C_p \cdot \mu_f/k_f \qquad (A2-6)$$

where V_c is a corrected approach velocity at the bulk temperature calculated from the tube blockage (see equation (2-15)), μ is the viscosity of the fluid, g is the acceleration due to gravity and C_p is the heat capacity of the fluid at constant pressure per unit mass.

For heat transfer to argon, which is a monatomic gas and was used in this study, the transport properties such as viscosity (μ) in gr/cm sec and thermal conductivity (k) in cal/cm sec ^{o}K can be evaluated very accurately from the kinetic theory of gases (29). They are given as (29,96) as

$$\mu = 2.6693 \times 10^{-5} \sqrt{M\ T}\ /\sigma^2\ \Omega^{(2,2)*} \qquad (A2-7)$$

$$k = 1.9891 \times 10^{-4} \sqrt{T/M}\ /\sigma^2\ \Omega^{(2,2)*} \qquad (A2-8)$$

where M, and σ are the molecular weight and molecular diameter ($\mathring{A}$) of the gas respectively and $\Omega^{(2,2)*}$ is the collision integral relative to idealised rigid-sphere model.

Appendix 3

Frankel's Elementary Theory of Thermal Diffusion

This appednix has been written as a physical explanation of thermal diffusion in gases because the complexity of the phenomenon is not properly understood in the metallurgical literature, and over simplifications have often been made with the result that wrong conclusions have been drawn. We follow the elementary approach developed by Frankel, which is based on the momentum transfer method of Maxwell and Stefan.

In the following paragraphs the basic idea of momentum transfer approach will be given, which shows that a concentration gradient in the gas phase implies net momentum transfer by collision between the unlike molecules.

For a homogeneous binary gas mixture with no bulk flow, the total components of momentum in any direction of the all molecules, as well as for each type of molecule in any volume element, are the same (uniform total and partial pressure in the system). The existence of a concentration gradient implies a gradient in the partial pressure of each gas since $P_i = n_i KT$ and the total pressure $P = P_1 + P_2$ is uniform. For simplicity if we consider the concentration gradient in one direction say the x direction, the pressure gradient in x is

$$(dP_1/dx) = kT(dn_1/dx) \qquad (A3-1)$$

The gradient of partial pressure of component 1 is equal to the time rate of change per unit volume of momentum of component 1 in x direction. Since there is no net transfer of momentum in collisions between identical molecules, according to the law of conservation of momentum, we conclude that the transfer of momentum is a result of momentum transfer in x direction from gas 1 to gas 2 per unit value per unit time (M_{12}). It follows that

$$(dP_1/dx) = kT(dn_i/dx) = -M_{12} \qquad \text{(A3-2)}$$

As shown above there must be a continual net transfer of momentum from one gas to the other to support a partial pressure gradient and hence a concentration gradient.

The momentum transfer method of treating thermal diffusion is based on (A3-2) and involves calculation of M_{12}. For simplicity Frankel (34) assumed that the molecules of one gas are so heavy that their motion can be neglected, and that the molecules of the other gas are composed of two streams with uniform velocities moving toward the cold and hot side respectively. In effect we consider one dimensional flow in the x-direction with the temperature gradient also along the x axis and positive in the positive x direction. In steady state where there is no net molecular flow ($n_1^+ v_1^+ = n_1^- v_1^-$) writing

$$n_1^+ m_1 v_1^+ = n_1^- m_1 v_1^- \qquad \text{(A3-3)}$$

we see that both streams must carry the same momentum per unit volume. The momentum transfer per unit volume per unit time by unlike collisions is the product of the average number of collisions and the average momentum transfer per collision. Therefore M_{12} for each stream is given by

$$M_{12}^{+} = n_1^{+} n_2 v_1^{+} \sigma_{12}(v_1^{+}) m_1 v_1^{+} \qquad \text{(A3-4)}$$

$$-M_{12}^{-} = n_1^{-} n_2 v_1^{-} \sigma_{12}(v_1^{-}) m_1 v_1^{-} \qquad \text{(A3-5)}$$

The net rate transfer of momentum by unlike collisions becomes

$$\begin{aligned} M_{12} &= M_{12}^{+} + M_{12}^{-} \\ &= n_2 n_1^{+} m^{+}{}_1 v_1 \left[v_1^{+} \sigma_{12}(v_1^{+}) - v_2^{-} \sigma_{12}(v_2^{-}) \right] \end{aligned} \qquad \text{(A3-6)}$$

Since the velocity of the stream coming from the hot side in somewhat greater than the velocity of the other stream M_{12} will be -ve. There will be a net transfer of momentum by unlike collisions against the temperature gradient. and hence a concentration gradient of the light molecules in the positive direction (equation (A3-2). This means that the light molecules (species 1) will be concentrated in the hot region. Equation (A3-6) showed the importance of the intermolecular force law, which appears in the effective cross-section for unlike collisions.

The general case in which account is taken of the three dimensional nature of molecular motion as well as the distribution in the velocity was considered by Furry (33). However the momentum transfer method is only useful to show the physical picture of this phenomenon and the rigorous kinetic theory of gases (29) must be used for quantitative calculations (see appendix 4).

Appendix 4

Calculation of the thermal diffusion ratio

From the kinetic theory of gases (28,29) the first approximation to thermal diffusion ratio K_T for a binary gas mixture is given by the following expression

$$K_{T_1} = (6C^*_{12} - 5)\, x_1x_2(S_1x_1 - S_2x_2)/6k_{12}(x + y) \qquad (A4\text{-}1)$$

where

$$S_1 = (M_1 + M_2)\, k_{12}/2M_2k_1 - (15/4)A^*_{12}((M_2 - M_1)/2M_2) - 1 \qquad (A4\text{-}2)$$

$$S_2 = (M_2 + M_1)k_{12}/2M_1k_2 - (15/4)A^*_{12}((M_1 - M_2))/(2M_2) - 1 \qquad (A4\text{-}3)$$

$$X = x_1^2/k_1 + 2x_1x_2/k_{12} + x_2^2/k_2 \qquad (A4\text{-}3)$$

$$Y = x_1^2\, U_1/k_1 + 2x_1x_2\, U_{12}/k_{12} + x_2^2\, U_2/k_2 \qquad (A4\text{-}5)$$

$$U_1 = 4A^*_{12}/15 - (12B^*_{12}/5 + 1)\, M_1/12M_2 + (M_1 - M_2)^2/2M_1M_2 \qquad (A4\text{-}6)$$

$$U_2 = 4A^*_{12}/15 - (12B^*_{12}/5 + 1)\, M_2/12M_1 + (M_2 - M_1)^2/2M_1M_2 \qquad (A4\text{-}7)$$

$$U_{12} = A^*_{12}k^2_{12}\,(M_1 + M_2)^2/15M_1M_2\, k_1k_2 - (12B^*_{12}/5 + 1)/12 - 5(12B^*_{12}/5 - 5)(M_1 - M_2)^2/32A^*_{12}\, M_1M_2 \qquad (A4\text{-}8)$$

x_1, x_2 is mole fractions of species 1, 2.

M_1, M_2 is molecular weight of species 1, 2.

A^*_{12}, B^*_{12} and C^*_{12} are the collision integral functions relative to indealised rigid sphere model; they are

$$A^*_{12} = \Omega^{(2,2)*} / \Omega^{(1,1)*} \qquad \text{(A4-9)}$$

$$B^*_{12} = (5\Omega^{(1,2)*} - 4\Omega^{(1,3)*}) / \Omega^{(1-1)*} \qquad \text{(A4-10)}$$

$$C^*_{12} = \Omega^{(1,2)*} / \Omega^{(1,1)*} \qquad \text{(A4-11)}$$

k_1 and k_2 are the thermal conductivity of species 1, 2.

For polyatomic molecules (CO, CO_2) where there is a transfer of energy on collision between translation and internal degrees of freedom the thermal conductivity may be expressed by

$$k = (C_p + 5R/4M)\mu \qquad \text{(A4-12)}$$

where the viscosity μ is defined by equation (A2-7). k_{12} is the thermal conductivity of the gas mixture and is given for a binary mixture as

$$k_{12} = x_1 k_1 + x_2 k_2 \,/ x_2 \phi_{12} + x_1 \phi_{21} \qquad \text{(A4-13)}$$

$$\phi_{ij} = (1 + M_i/M_j)^{-\frac{1}{2}} \left[1 + (\mu_i/\mu_j)^{\frac{1}{2}} (M_j/M_i)^{1/4}\right]^2 / \sqrt{8} \qquad \text{(A4-14)}$$

The thermal diffusion ratio is thus a very complex function of temperature, concentration, and the molecular weight, and depends parametrically on the force law of the molecule.

The primary concentration dependence is given by x_1, x_2 and to a lesser extent by $(S_1x_1 - S_2x_2)$. The main dependence on the masses of the molecules is given by S_1 and S_2. The temperature dependence appears in the thermal conductivity terms and the collision integral functions A^*_{12}, B^*_{12}, and C^*_{12}. The dominant effect of the law of interaction of the molecules on thermal diffusion appears in the $(6C^*_{12} - 5)$ term. It is worth emphasising the importance of intermolecular interaction. For molecules which interact with inverse power repulsion only (the force between unlike molecules at distance r being $F \propto r^{-\delta}$) the term $(6C^*_{12} - 5)$ is given as

$$(6C^*_{12} - 5) = \delta - 5/(\delta - 1) \qquad \text{(A4-15)}$$

From equation (A4-15) when $\delta = 5$ (Maxwellian molecules) the term $(6C^*_{12} - 5)$ becomes zero, and hence the thermal diffusion vanishes.

The knowledge of the quantities A^*_{12}, B^*_{12} and C^*_{12} for a specific molecular model is essential to calculate the thermal diffusion ratio. For a special simple case, rigid elastic sphere model, these quantities are equal to unity. For the Lennard-Jones (6-12) model, which is commonly used in the prediction of the transport properties of gases, the integral functions are well known and given by Hirschfelder et al (29).

Appendix 5

Solution of unsteady diffusion in a rigid sphere

Basic equations

For heterogeneous reaction of CO gas at the surface of a molten iron drop, the resultant carbon will diffuse in the drop. The rate of carbon accumulation for diffusion in a static sphere is given by

$$\delta c/dt = D\left[(\delta^2 c/\delta r^2) + 2(\delta c/\delta r)/r\right] \qquad \text{(A5-1)}$$

On putting $R = r/a$, $T = Dt/a^2$, $C^* = C/C_e$ where a is the diameter of the drop and C_e is the equilibrium concentration, equation (5A-1) becomes dimensionless and has the following form

$$\delta C^*/\delta T = \left[\delta^2 C^*/\delta R^2 + 2(\delta C^*/\delta R)/R\right] \qquad \text{(A5-2)}$$

The rate of diffusion in the drop is equal to the rate of diffusion of the resultant CO_2 gas out of the gas phase boundary layer. The boundary condition involving the rate of transfer of carbon diffusing across the surface is given by

$$N_{CO_2} = D(\delta c/\delta r)_s = 1200kg\ (x_{CO_2 S} - x_{CO_2 b})/\rho_{Fe} \qquad \text{(A5-3)}$$

in $$(\delta C^*/\delta R)_s = A\ (x_{CO_{2s}} - x_{CO_{2b}}) \qquad \text{(A5-4)}$$

where A = 1200 a kg/CeDρ_{Fe}

kg is the gas phase mass transfer coefficient in mol/cm^2 sec.,

ρ is the density of the molten drop, g/cm^3.

Method of solution

Solution of the differential equation (A5-2) with the boundary condition given by equation (A5-4) was carried out using the finite difference approximation. This was done by dividing the drop into a number of layers of equal intervals δR, and the time into intervals δT. We denote by C^*_{m-1}, C^*_m, C^*_{m+1}, the concentrations at the points $(m-1)\delta R$, $m\delta R$, $(m+1)\delta R$ respectively at time $T = n\delta T$, and by C^{+*}_m, C^{-*}_m the corresponding values at $R = m\delta R$ at times $(n+1)\delta T$ and $(n-1)\delta T$ respectively. Then using Taylor's expansion theorem we have

$$C^*_{m+1} = C^*_m + \delta R(\delta C^*/\delta R) + \tfrac{1}{2}(\delta R)^2(\delta^2 C^*/\delta R^2) + \cdots \qquad \text{(A5-4)}$$

$$C^*_{m-1} = C^*_m - \delta R(\delta C^*/\delta R) + \tfrac{1}{2}(\delta R)^2(\delta^2 C^*/\delta R^2) - \cdots \qquad \text{(A5-6)}$$

so we get at point in $m\delta R$, and time T that

$$(\delta^2 C^*/\delta R^2)_m = (C^*_{m+1} - 2C^*_m + C^*_{m-1})/(\delta R)^2 \qquad \text{(A5-7)}$$

$$(\delta C^*/\delta R)_m = (C^*_{m+1} - C^*_{m-1})/2\delta R \qquad \text{(A5-8)}$$

The corresponding approximation for $\delta C/\delta T$ is (94,99)

$$(\delta C^*/\delta T)_m = (C^{+*}_m - C^*_m)/\delta T \text{ at } T + \tfrac{1}{2}\delta T \qquad \text{(A5-9)}$$

From the equations (5A-2) and (5A-7) to (A5-9) the corresponding result at T + δT is given by

$$C_m^{*+} = C_m^* + \frac{\delta T}{2m\delta R}\left[(m+1)(C_{m+1}^* + C_{m+1}^{*+}) - 2m(C_m^* + C_m^{*+}) + (m-1)(C_{m-1}^* + C_{m-1}^{*+})\right] \quad \text{(A5-10)}$$

for the centre of the sphere, m = 0, equation (A5-10) becomes (94)

$$C_o^{*+} = C_o^* + 3\frac{\delta T}{(\delta R)^2}(C_1^* + C_1^{*+} - C_o^* - C_o^{*+}) \quad \text{(A5-11)}$$

The boundary condition given by equation (A5-4) defines the surface concentration at any time T. If we imagine the drop extended one interval δR beyond the real surface R_s to $R_s + \delta R$, so for the point at the surface (m = s) we have

$$\left(\frac{\delta C_s^*}{\delta T}\right) = \frac{1}{s(\delta R)^2}\left[(m+1)\,C_{m+1}^* - 2mC_m^* + (m-1)\,C_{m-1}^*\right] \quad \text{(A5-12)}$$

and

$$\left(\frac{\delta C^*}{\delta R}\right)_s = (C_{s+1}^* - C_{s-1}^*)/2\delta R \quad \text{(A5-13)}$$

From equation (A5-4) and (A5-13) we get

$$C_{s+1}^* = C_{s-1}^* + 2\delta R\, A(x_{CO_2 S} - x_{CO_2 b}) \quad \text{(A5-14)}$$

By eliminating the fictitious concentration $C_{(s+1)}^*$ from equation (A5-12), the corresponding result at time interval

$$C_s^{*+} = C_s^* + \frac{\delta T}{(\delta R)^2}\left[C_{s-1}^* + C_{s-1}^{*+} - C_s^* - C_s^{*+} + \delta R\left(\frac{s+1}{s}\right) A\left[(x_{CO_2 s} - x_{CO_2 b})^- + (x_{CO_2 s} - x_{CO_2})^+\right]\right] \quad \text{(A5-15)}$$

In this method we have a one equation for each layer, and the solution of these equations simultaneously gives the concentration gradient at time T + δT. The time interval δT is determined by the selected value of $\delta T/(\delta R)^2$.
The initial boundary conditions were

$t < 0$	$C_m^* = 0$	$m = 0$ to s
$t = 0$	$C_s^* = 1$, $C_m^* = 0$	$m = 0$ to $(s - 1)$

All computation was carried out on a CDC 6400 computer using Fortran IV. The solution of the m simultaneous equations (A5-10), (A5-11), and (A5-15) was performed by NAG4F library subroutine labelled F04AEF. A block diagram of the computer program is given in fig (A5-1).

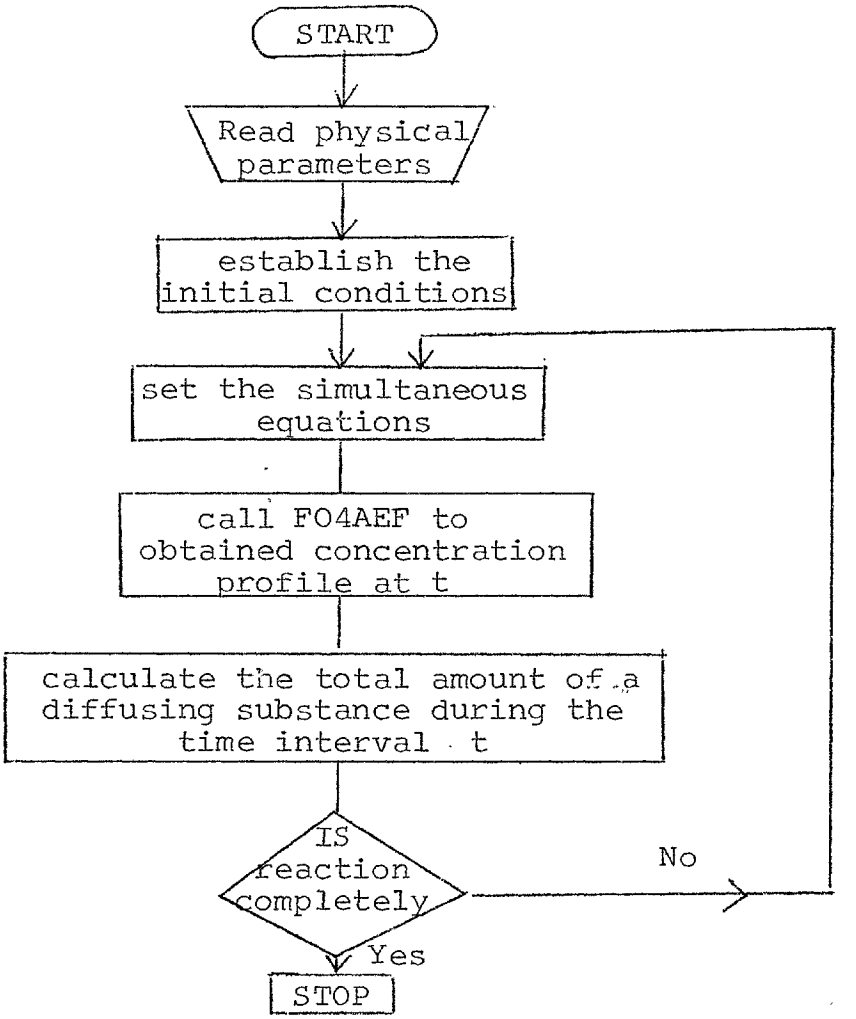

Fig (A5-1)

Block diagram of
computer programme

Acknowledgements

Grateful acknowledgement is made to my supervisor Dr. D.G.C. Robertson for the invaluable advice, assistance and encouragement received throughout the work. I am indebted to Professor F.D. Richardson for his guidance, encouragement and financial support.

This work has been partially supported by the Science Research Council. I am grateful for the award of an Andrew Carnegie Bursary from the Iron and Steel Institute during 1973-1974. I am also grateful for the award of a Bursary from the British Steel Corporation during 1974-1975.

My thanks go to Mr. J. Haynes and Mr. P. Brindley who assisted in the construction of the apparatus, to Mr. M. Hayward who did the film printing, to Mr. A.J. Tipple who drew the diagrams, and to Miss G. Page for typing the thesis so carefully.

I am also especially grateful to my father, Mr. H.A. El-Kaddah for the financial assistance to enable me to complete this thesis in the United Kingdom.

List of symbols

Symbol	Definition
Roman	
A	surface area
a	activity
C	concentration of the solute in liquid in weight percent
C	molar density of the gas
$\dot{C}$	concentration in molecules per unit volume
C_p	heat capacity at constant pressure
D	diameter of the tube
D_{12}	binary diffusion coefficient
D^T	thermal diffusion coefficient
d	diameter of levitated drops
e	total emissivity of a surface
e	interaction parameter (concentration in weight percent)
e	electron charge
F	intermolecular forces
ΔF	free energy
$\Delta \overline{F}$	partial molar free energy
ΔF_d	activation energy for diffusion in liquid
f	activity coefficient (concentration in weight percent)
f	distribution function of the embryos in the liquid during nucleation
ΔH	enthalpy
$\Delta \overline{H}$	partial molar enthalpy
h	heat transfer coefficient
I	nucleation rate nuclei/cm^3
J	mass flux vector

K	chemical rate constant
K	equilibrium constant of the reaction
K'	apparant equilibrium constant
K_T	thermal diffusion ratio
k	Boltzmann constant
k	thermal conductivity
k_g	mass transfer coefficient in the gas (mole/cm^{2}sec.)
k_g^o	mass transfer coefficient at zero flux
$\overline{k}_g$	overall mass transfer coefficient
k_L	mass transfer coefficient in the liquid (cm/sec)
k'_L	mass transfer coefficient in the liquid (mole/cm^2 sec. w/o)
M	molecular weight of a component.
m	mass of a molecule
N	molar flux with respect to stationary coordinates
N	atomic fraction
N	number of the molecules in the phase
n	number density (number of molecules/cm^3)
n	equilibrium distribution function of the embryos in the liquid
P	pressure
Q	energy flow across the surface/or energy transferred to the drop
R	the gas constant
R_T	thermal separation ratio
r	coordinate of the system
r	radius of the embryo
ΔS	entropy
$\Delta\overline{S}$	partial molar entropy

T	temperature ^{o}K
t	temperature ^{o}C
t	time
U	potential energy
$\overline{U}$	change of potential energy for an embryo with respect to planar surface
V	velocity
V	volume
v	molar volume
w	weight of the drop
X	external forces
x	mole fraction
Z	Zeldovich non-equilbrium factor
z	number of charge

Greek

Γ	relative adsorption
γ	activity coefficient (concentration in atomic fraction)
γ	Debey maximum frequency of vibration
δ	intermolecular force index
ϵ	interaction parameter (concentration in atomic fraction)
θ	correction factor of mass transfer coefficient
η_g	overall to actual mass transfer coefficient
μ	viscosity coefficient
μ	chemical potential
$\tilde{\mu}$	electro-chemical potential
ρ	mass density
σ	Stefan-Boltzmann constat
σ	surface tension

Φ	rate factor of mass flux
$\emptyset$	vortex circulation
x	surface potential
ω	rate in the growth of embryos

superscript

td	thermal diffusion contribution to mutual diffusion
'	corrected bulk gas composition from thermal diffusion flux
*	critical value for homogeneous nucleation
$\rightarrow$	forward
$\leftarrow$	backward

subscripts

b	bulk value
c	corrected gas velocity
CONV	for heat transfer by convection
EC	for heat generated by eddy current
e	equilibrium value
f	property at the film temperature
m	mean value
Rad	for heat transfer by radiation
S	surface value
∞	for approach gas stream

Dimensionless Groups

E	Eckert number
Gr	Grashof number for heat transfer

Gr_{12}	Grashof number for mass transfer
Nu	Nusselt number
Pr	Prandtl number
Re	Reynolds number
Sc	Schmidt number
Le	Lewis number
T	Time parameter of dimensionless unsteady state diffusion equation

Abbreviations

expt	experimental
gr	graphite
HPLA	high pressure levitation apparatus
HPLC	high pressure levitation cell
rig. sph.	rigid sphere
s.l.m.	standard litres per minute
TCP	two colour pyrometer
w/o	weight percent

List of References

1) Jenkins A.E. Harris B. and Baker L.A.,
Electromagnetic levitation and its use in physico-chemical studies at high temperature.
Symposium on metallurgy at high pressures and high temperatures Met. Soc. AIME conference Gordon Brench Sci Publ.(1964), 22, 23-43.

2) Peifer W.A.,
Levitation melting - survey of the state of the art.
J. of Metals (1965) May 487-493.

3) Rostron A.J.,
Levitation melting
Science J. (1967) July 69-73).

4) Tweeddale J.G.,
Practical mechanical design.
Iliffe Books (1963) London

5) Robertson D.G.C.,
Heterogeneous reactions and mass transfer from liquid metal drops in gases.
Ph.D. Thesis University of New South Wales, Australia (1968).

6) Schlichting, H.,
Boundary layer theory.
McGraw Hill, New York (1955).

7) Bayley F.J. Owen J. and Turner A.B.,
Heat Transfer.
Nelson (1972) London.

8) Szekely J., and Themelis N.J.,
Rate Phenomena in Process Metallurgy.
John Wiley, New York (1971).

9) Ranz W.E., and Marshall Jr., W.R.,
Evaporation from drops II .
Chem. Eng. Progr. (1952), 48, 173-180.

10) Mathers W.G., Madden A.J. and Piret E.C.,
Simultaneous heat and mass transfer in free convection .
Ind. Eng. Chem. (1957) 49 961-968.

11) Frossling N.,
Evaporation heat transfer and velocity distribution in two-dimensional and rotating symmetrical laminar boundary layer flow,
Lund Univ. Årsskrift N.F. (1940), 2, 36.
English translation in NACA TM (1958), 14-32.

12) Rowe P.N., Claxton K.T. and Lewis J.B.,
Heat and mass transfer from a single sphere in an extensive flowing fluid.
Trans. Inst. Chem. Eng. (1965), 43, T14-31.

13) White R.R. and Churchill S.W.,

A.I. Ch.E.J. (1959), 5, 354.

14) Xenakis G., Amerman A.E., and Michelson R.W.,
An investigation of the heat transfer characteristics of spheres in forced convection.
Wright Air Development Center, Ohio (1955) TR52,117.

15) Frossling N.,
Uber die Verdunstung Fallenden
Trpfen, Beitr. Geophys. (1938), 52, 170-216.

16) Lee K. and Barrow H.,
Transport processes in flow around a sphere with particular reference to the transfer of mass,
Int. J. of Heat and Mass Transfer, (1968), 11, 1013-1026.

17) Merck H.J. and Prins J.A.,
Thermal convection in laminar boundary layers III.
Appl. Sci. Res. (1954), 4A, 207-221.

18) Lienhart, J.H.,
On the commonality of equations for natural convection from immersed bodies.
Int. J. of Heat and Mass Transfer (1973), 16, 2121.

19) Yuge T.,
Experiments on heat transfer from spheres including combined natural and forced convection.
J. of Heat transfer (1960), C82,214-220.

20) Broham R.J. and Mayhew Y.R.,
Free convection from spheres in air.
Int. J. of Heat and Mass Transfer (1962), 5, 82-83.

21) McAdams W.H.,
Heat transmission.
3 ed. McGraw Hill, New York (1954).

22) Steinberger R.L. and Treybal R.E.,
Mass transfer from a solid soluble sphere to a flowing liquid stream.
A.I. Ch.E. (1963), 6, 227-232

23) Pei D.C.T., Narasimham C., and Gauvin W.H.,
Evaporation from drops and particles in high temperature surroundings.
Interaction between fluids and particles symp. Instn. Chem. Engrs. London (1962), 243-249.

24) Pei D.C.T.,
Heat transfer from spheres under combined forced and natural convection.
Ch.Eng. Progr. Symp. Series No 59,(1965), 61, 57-63.

25) Brown, W.S., Pitts, C.C. Leppert G.,
Forced convective heat transfer from a uniformly heated sphere.
J. Heat Transfer (1962), C84, 133-140.

26) Pei D.C.T.,
Effect of tunnel blockage and support in the heat transfer from spheres.
Int. J. of Heat and Mass Transfer (1969), 12, 1707-1709

27) d'Entremont J.C.,
Optical temperature measurements for liquid iron.
Trans. AIME, (1963), 227, 482-485.

28) Chapman S. and Cowling T.G.,
The mathematical theory of non-uniform gases.
Cambridge Univ. press (1939)

29) Hirschfelder J.O. Curtiss C.F. and Bird R.B.,
Molecular theory of gases and liquids.
John Wiley New York (1964).

30) Present R.D.,
Kinetic theory of gases.
McGraw Hill (1958).

31) Gillespie L.J.,
A simple theory for separation of gases by thermal diffusion.
J. of Ch. Phy. (1939), 7, 530-535.

32) Fürth R.,
An elementary theory of thermal diffusion.
Proc. Roy. Soc. (1942) A179, 461-469.

33) Furry, W.H.,
On the elementary explanation of diffusion phenomena in gases.
American J. of Phys. (1948), 16, 63-78.

34) Frankel S.P.,
Elementary derivation of thermal diffusion.
Phys. Rev. (1940), 57, 661

35) Sunderland M., Hamielec A.E., Lu W.K., and McLean A.,
Thermal diffusion in kinetics and equilibrium measurements.
by levitation techniques.
Met. Trans. (1973), 4, 575-583.

36) Laiche F.C.L. and McLean A.,
The determination of chromium-oxygen interactions in levitated iron alloy droplets.
Trans. Iron and Steel Inst. of Japan, (1973), 13, 71-77.

37) Grew E.K. and Ibbs T.L.,
Thermal diffusion in gases.
Cambridge Univ Press (1952).

38) Grew E.K., Johanson F.A. and Neal W.E.J.,
Thermal diffusion factor and temperature.
Proc. Roy. Soc. London (1954), A224, 513-526.

39) Humphreys A.E. and Grey P.,
Thermal diffusion as a probe of binary diffusion coefficients at elevated temperatures.
Proc. Roy. Soc. London (1970), A320, 397-415.

40) Becker E.W., Z. Natusforsch, (1950), SA, 457
Effect of pressure on thermal diffusion in gases.
J. Chem. Phys. (1951), 19, 131-132

41) JANAF, Thermodynamic tables,
2 ed NSRDS - NB537 (1971)

42) Chipman J., Alfred R.M., Cott L.W., Small R.B., Wilson D.M., Thomson C.N., Guernsey D.L. and Fulton J.C.,
The solubility of carbon in molten iron and in iron-silicon and iron-manganese alloys.
Trans. Am. Soc. Metals, (1952) 44, 1215-1232

43) Hamielec A.E. Lu W.K., and McLean A.,
Interpretation of kinetic data for the decarburization of iron droplets.
Can. Met. Quart. (1968), 7, 27-33

44) Baker L.A.,
Discussion,
Ibid (1968), 7, 217-221

45) Perry J.H.,
Chemical Engineer's Handbook
4th ed. (1963), McGraw Hill.

46) Bodsworth C., and Bell H.B.,
Physical chemistry of iron and steel manufacture.
2nd ed. Longman (1972)

47) Vacher H.C. and Hamilton E.H.,
The carbon-oxygen equilibrium in liquid iron.
Trans. AIME (1931), 95, 124.

48) Marshall S. and Chipman J.,
The carbon-oxygen equilibrium in liquid iron.
ASM Trans. (1942), 30, 695-746.

49) Richardson F.D. and Dennis W.E.,
Thermodynamic study of dilute solutions of carbon in molten iron.
Trans. Faraday Soc., (1953), 49, 171-180.

50) Rist A. and Chipman J.,
Activity of carbon in liquid iron-carbon solutions.
Physical chemistry of iron and steel making,
John Wiley, New York (1958), 3-12.

51) Ban-Ya S. and Matoba S.,
Activity of carbon and oxygen in liquid iron,
Phsycial Chemistry of Process Metallurgy,
Interscience Publication New York (1961), 373-401.

52) Schenck H. and Gerdon G.H.,
Arch. für das Eisenhüttenwesen (1959) 30, 451-460.

53) Schenck H., and Hinze H.,
Ibid (1966), 37, 545-550.

54) Turkdogan E.T., Leake L.E., and Masson C.R.,
Thermodynamics of iron carbon melts,
Acta Met. (1956), 4 396-406.

55) Gokcen, N.A.,
Equilibrium in reaction of hydrogen and carbon monoxide with dissolved oxygen in liquid iron; equilibrium in reduction of ferrous oxide with the hydrogen and solubility of oxygen in liquid iron.
Trans. AIME (1956), 296, 1558-1567.

56) Floridis T.P., and Chipman J.,
Activity of iron in liquid iron alloys.
Trans. AIME (1958), 212, 549-553

57) Sakao H. and Sano K.,

Japan Inst. Metals Trans., (1960), 1, 38.

58) Tankins E.S., Gokcen N.A. and Belton G.R.,
The activity and solubility of oxygen in liquid iron, nickel and cobalt.
Trans. AIME, (1964), 230, 820-827.

59) Schenck H. and Steinmetz E.,
Archiv für das Eisenhüttenwesen, (1957), 38, 1-7.

60) Turkdogan E.T., Davis L.S., Leake L.E., and Stevens, C.G.,
The reaction of carbon and oxygen in molten iron.
J.I.S.I. (1955), 181, 123-128

61) Fuwa T. and Chipman J.,
The carbon-oxygen equilibria in liquid iron.
Trans. AIME (1960), 218, 887-891.

62) Matsumoto N.,
Equilibrium between carbon and oxygen in liquid iron and carbon monoxide under high pressure.
Sci. Rept. Res. Inst. Tohoku Univ. (1970).

63) Chipman J.,
Thermodynamics of liquid Fe-C solutions.
Met. Trans. (1970), 1, 2163-2168.

64) Parlee N.A., Seagle S.R. and Schuhmann Jr. R.,
Rate of carbon-oxygen reaction in liquid iron.
Trans. AIME (1958), 212, 132-138.

65) Fruehan R.J.,
Activities in liquid Fe-Al-O and Fe-Ti-O alloys.
Met. Trans (1970), 1, 3403-3410.

66) Bale C.W. and Pelton A.D.,
Mathematical representation of thermodynamic properties in binary systems and solution of Gibbs-Duhem equation.
Met. Trans. (1974), 5, 2323-2337.

67) Darken L.S. and Gurry,
Phsycial chemistry of metals.
McGraw Hill, (1952).

68) Wagner C.,
Thermodynamics of alloys.
Addison Wesley (1952).

69) Chipman J.,
Atomic interaction in molten alloy steel.
J.I.S.I. (1955), 180, 97-106.

70) Lupis H.P. and Elliot J.F.,
The relationship between the interaction coefficient ε and e.
Trans. A.I.M.E. (1965), 233, 257-258.

71) Richardson F.D.,
Phsyical chemistry of melts in metallurgy.
Vol 1 Academic Press, London and New York (1974).

72) Ban-Ya S., Elliott J.F., and Chipman J.,
Thermodynamics of autenitis Fe-C alloys.
Met. Trans. (1970),1,1313-1320.

73) Syn T., Polyakov A.V., and Samaria A.M.,
Tzv Vysshikh, Ucheben Zavendenii, Chem. Met., (1959), 11, 3-12

74) Schenck H. and Frohberg M.G.,
The charge in the activities of dissolved substances by additional solute elements and their position in the periodic system.
The Chipman conference, The MIT Press (1965), 95-101.

75) Chipman J.,
Another look at the problem of steel deoxidation.
Metal Progress (1949), 56, 211-221.

76) Richardson F.D.,
Principles underlying refining processes. The principles of extraction and refining of metals.
Inst. Metall. London (1950) 83-102

77) Richardson F.D.,
The properties and structures of phases and their relevance to processes in steel-making.
The Chipman Conference, the MIT Press (1965), 65-76.

78) Gunji K.,
Kinetics of decarburization of liquid iron in an oxidizing atmosphere.
Trans. ISIJ. (1970), 10, 1-12.

79) Baker L.A., Warner N.A. and Jenkins A.E.,
Kinetics of decarburization of liquid iron in an oxidizing atmosphere using the levitation technique.
Trans. AIME (1964), 230, 1228-1235.

80) Baker L.A., Warner N.A. and Jenkins A.E.,
Decarburization of a levitated iron droplet in oxygen.
Trans. AIME (1967), 239, 857-864.

81) Distin P.A., Hallett, G.D. and Richardson F.D.,
Some reactions between drops of iron and flowing gases.
J.I.S.I. (1968), 206, 821-833.

82) Kaplan R.S. and Philbrook W.O.,
The kinetics of gaseous oxidation of binary and ternary alloys of liquid iron.
Trans. AIME (1969) 245, 2195-2204

83) Baker R.,
Oxidation studies of molten iron alloy drops.
J.I.S.I. (1967), 205, 637-641

84) Baker L.A. and Ward R.G.,
Reaction of an iron-carbon droplet during free fall through oxygen.
Ibid (1967), 205, 714-717.

85) See J.B. and Warner N.A.,
Reaction of iron alloy drops in free fall through oxidizing gases.
Ibid (1973), 211, 44-52.

86) Roddis P.G.,
Mechanism of decarburization of iron-carbon alloy during falling through an oxidizing gas.
Ibid (1973), 211, 53-58.

87) Nomura H. and Mori K.,
Kinetics of decarburization of liquid iron with high concentration of carbon.
Trans. ISIJ, (1973), 13, 265-273.

88) Fruehan, R.J. and Martonik L.J.,
The rate of decarburization of liquid iron by CO_2 and H_2.
Met. Trans. (1974), 5, 1027-1032.

89) Swisher J.H. and Turkdogan E.T.,
Decarburization of iron-carbon melts in CO_2-CO atmospheres; kinetics of gas-metal surface reaction.
Trans. AIME (1967), 239, 602-610.

90) Ghosh D.N. and Sen P.K.,
Kinetics of decarburization of iron-carbon melts in oxidizing gas atmospheres.J.I.S.I. (1970), 208, 911-916.

91) Nomura H. and Mori K.,
Kinetics of decarburization of liquid iron at low concentrations of carbon,
Trans.I.S.I.J. (1973), 13, 325-332.

92) King T.B. Karaser R.A. and Dastur P.,
The interaction of carbon monoxide and liquid iron. Heterogeneous kinetics at elevated temperatures.
Plenum Press (1970), 409-432

93) Distin P.A.,
Reactions between levitated iron-carbon alloys and flowing gases.
Ph.D. Thesis, Imperial College, London (1967)

94) Crank J.,
The mathematics of diffusion,
Oxford Univ. Press. (1956)

95) Solar M.Y. and Guthrie R.I.L.,
Kinetics of the carbon-oxygen reaction.
Met. Trans. (1972), 3, 713-721.

96) Bird R.B., Stewart W.E. and Lightfoot E.N.,
Transport Phenomena.
John Wiley (1960)

97) Chatterjee A. and Bradshaw A.V.,
The influence of gas phase resistance on mass transfer to a liquid metal.
Met. Trans. (1973), 4, 1359-1363

98) El-Kaddah N.H. and Robertson D.G.C.,
unpublished work

99) Crank J. and Nicolson P.,
A practical method for numerical evaluation of solutions of partial differential equations of the heat conduction type.
Proc. Cambridge Phi. Soc. (1947), 43, 50-67.

100) Grabke H.J.,
Kinetics of oxygen transfer from carbon dioxide to the surface of iron.
Proceed III Internat. Cong. on Catalysis (1965), S.928
928-937 North Holland, Amsterdam

101) Forster A and Richardson F.D.,
Oxidation of copper and nickel drops by carbon dioxide.
Trans. Instn. Min. Metall. (1975), 84, C116-122

102) Gibbs J.W.
Collected works,
Vol 1 "Thermodynamics" Yale Univ. Press., New Haven,
Connecticut (1948)

103) Volmer M and Weber A.,

Z. phys. chem. (Leipzig) (1926), 119, 227

104) Dean R.B.,
The formation of bubbles.
J. of Appl. Phys. (1944), 15, 446-451.

105) Defay R., Prigogine I., Bellemans A. and Everett D.,
Surface tension and adsorption.
Longmans (1966)

106) Prigogine I., Defay R. and Everett D.,
Chemical thermodynamics.
Longmans (1954).

107) Abraham F.F.,
Homogeneous nucleation theory.
Academic Press (1974).

108) Hirth J.P., Pound G.M. and St. Pierre G.R.,
Bubble nucleation.
Met. Trans. (1970), 1, 939-945.

109) Farks L.,
z. phys. chem. (Leipzig) (1927) A125, 236.

110) Frankel J.,
Kinetic theory of liquids.
Oxford Univ. Press, (1946).

111) Zeldovich J.B.,
On the theory of new phase formation; cavitation
Acta Physicochemica URSS, (1943), 18, 1-22.

112) Volmer M.,
Kinetik der phasenbildung.
Dresden Leipizg, Therodo steinkopoff, (1939).

113) Kagan Yu.,
The kinetics of boiling of a pure liquid.
Russian J. of Phy. Chem (1960), 34, 42-46.

114) Katz J.L. and Blander M.,
Condensation and boiling: correction to homogeneous nucleation theory for non ideal gases.
J. of Coll. and Interface Sci. (1972), 42, 496-502

115) Korber F. and Oelsen W.,
The action of carbon as a reducing agent in the reations of the steelmaking processes with acid slags.
Mitteilungen aus dem kaiser Wilhelm Institute für Eisenforschung, (1935), 17 39-61, English translation 315 (1947)

116) Roberts O.C.,
Ph.D. Thesis,
University of New South Wales, Australia (1973).

117) Palmer R.,
Ph.D. Thesis
Imperial College, London (1971).

118) Halden F.A. and Kingery W.D.,
Surface tension at elevated temperatures: II Effect of C.N.S. and S on liquid iron surface tension and interfacial energy with Al_2O_3.
J. Phys. Chem. (1955), 59, 557-559.

119) Kozakevitch P. and Urbain G.,
Rev. Met. (1961) 58, 517-534.

120) Kozakevitch P. and Urbain G.,
Ibid (1961), 58, 931-947.

121) See J.B.,
Discussion of homogeneous nucleation of CO bubbles in Fe-C-O melts.
Met. Trans, (1973), 4, 2000-2001.

122) Burdert M.,
Heterogeneity of metal surface.
J. Amer. Chem. Soc. (1952), 74, 3556-3561.

123) Levine H.S.,
On the initiation mechanism for explosion during combustion of metal droplets.
High Temp. Sci (1971), 3, 237-243

124) Levine H.S.,
Formation of vapour nuclei in high temperature melts.
J. of Phys. Chem. (1972), 76, 2609-2614.

125) Levine H.S.,
Homogeneous nucleation of CO bubbles in Fe-C-O melts.
Met. Trans., (1973), 4, 777-782.

126) Levine H.S.,
Surface structure concepts in the theory of homogeneous bubble nucleation.
Ibid, (1974), 5, 953-955.

127) Mulholland E.W., Hazeldean G.S.F. and Davies, M.W.,
Visualization of slag-metal reactions by x-ray fluoroscopy: Decarburization in basic oxygen steel making.
J.I.S.I. (1973) 211, 632-639.

128) Mayer H.W., Porter W.F., Smith G.C. and Szekely J.,
Slag-metal emulsions and their importance in BOF steelmaking.
J. of Metals (1968), 20,(7), 35-42.

129) Trentini B.,
Comments on oxygen steel making.
Trans. AIME (1968), 242, 2377-2388.

130) Kaplan R.S. and Philbrook W.O.,
The rate of CO bubble nucleation at oxide metal interface within liquid iron alloys.
Met. Trans. (1972), 3, 483-487.